An ultrasonic study of phase transformations in indium alloys.

Madhava, Melkote Ramaswamy

Award date:
1977

Awarding institution:
University of Bath

AN ULTRASONIC STUDY OF PHASE TRANSFORMATIONS IN INDIUM ALLOYS

submitted by Melkote Ramaswamy Madhava

for the degree of Doctor of Philosophy

of the University of Bath

1977

Copyright

M. R. Madhava.

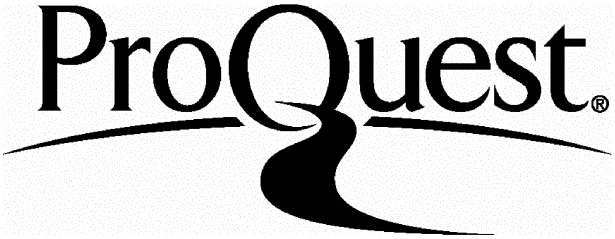

ABSTRACT

An ultrasonic study of the elastic behaviour and phase stabilities of single crystals of In alloys - many grown and characterised for the first time - with Cd, Tl and Pb is presented.

In both the fct and fcc In-Cd alloys, the shear modulus $\frac{1}{2}(C_{11} - C_{12})$ is much smaller than in In and tends to even smaller values as the fct-fcc structural transformation is approached from either the tetragonal or the cubic phase: the onset of instability is manifested as softening of the $[110]$, $q \,//\, [1\bar{1}0]$ acoustic phonon mode near the Brillouin zone centre. However, in contrast to its behaviour in the In-rich, In-Tl alloys, $\frac{1}{2}(C_{11} - C_{12})$ does not go to zero in the In-Cd alloys. This finding corresponds to the more recognisable first-order character of the transformation in the In-Cd compared to that in In-Tl alloys. Calorimetric measurements indicate enhancement of the fusion entropies due to the acoustic phonon mode softening.

In the primary solid solution range (fct, $c/a > 1$), addition of tetravalent Pb to In (valency 3) also reduces the shear modulus $\frac{1}{2}(C_{11} - C_{12})$. But in contrast to that of the divalent Cd and trivalent Tl alloys, this modulus is much larger than that of In in the other fct ($c/a < 1$) phase; neither is mode softening evident in the Pb-rich fcc phase - the anisotropy ratio A ($= 2C_{44}/(C_{11} - C_{12})$) is close to unity and the elastic behaviour is isotropic.

The shear constants of bcc Tl-rich, In-Tl alloys are in agreement with Zener's prediction namely that $\frac{1}{2}(C_{11} - C_{12})$ should be small compared with C_{44} for a closed ion shell bcc material.

The alloy data has been used to obtain the first estimate of the elastic constants of the high temperature bcc polymorph of Tl. The stability of this polymorph has been found to be - in accordance with Zener's arguments - due to its lower Debye temperature and consequently greater entropy than that of the normally occurring hcp form.

ACKNOWLEDGEMENTS

I am most grateful to my supervisor, Professor G.A. Saunders, for imparting knowledge and enthusiasm without which it would not have been possible to pursue this research.

An initial part of this work was done at the Department of Applied Physics and Electronics, University of Durham during my supervisor's tenure there and I take this opportunity to express my gratitude to former colleagues Dr. D.Y. Chung, Mr. T. Seddon and Mr. R. Waite for help and advice.

My thanks are also extended to my present colleagues in the School of Physics for their cheerful involvement with my experimental work. In this connection, particular mention must be made of Mr. B.F. Chapman for performing the calorimetric measurements and Mr. R.C.J. Draper for general assistance.

I am grateful to many others for their help in the execution of this work: Mrs. Susan Rigg for her careful typing of the thesis, Mr. G. Love of the School of Materials Science for electron probe microanalysis of the alloy specimens and Dr. J.R. Evans, also of the School of Materials Science, for advice on Differential Scanning Calorimetry.

Finally, I thank the Ministry of Education, Government of India and the British Council for financial support.

This research was supported in part by the Procurement Executive, Ministry of Defence.

CONTENTS

C H A P T E R 1

INTRODUCTION

Indium crystallises with tetragonal symmetry (fct, point group 4/mmm) with an atomic arrangement which differs only slightly from the cubic close-packed structure. At room temperature the c/a ratio is 1.08 and although this decreases with rise in temperature (Pearson 1967) it remains greater than unity right up to the melting point (T_m = 429.5°K); also no transformations take place down to 4.2°K (Swenson 1955) or up to ~300kbar (Vereshchagin, Kabalkina and Troitskaya 1964, Vaygham and Drickamer 1965). This makes In the stablest of the group IIIB metals inspite of the softening of the $[110]$, $\underline{q}//[1\bar{1}0]$ acoustic phonon mode near the Brillouin zone centre (Gunton and Saunders 1973). The elastic constant $\frac{1}{2}(C_{11} - C_{12})$ associated with this mode is a measure of the resistance to deformation when a shear stress is applied across a (110) plane in a $[1\bar{1}0]$ direction and its small value and rapid decrease with rise in temperature strongly suggests a shear assisted displacive transformation to an fcc (point group m3m) structure at high temperature; indeed, Chung, Gunton and Saunders (1976) have argued on the basis of ultrasonic measurements that this transformation would have taken place if melting did not occur first. Alloying with the isoelectronic element Tl further reduces the shear stability of In : In-rich, In-Tl alloys exhibit a soft mode transformation. The shear modulus $\frac{1}{2}(C_{11} - C_{12})$ tends to zero within experimental error as the fct to fcc displacive transformation, which is of the martensitic type, is approached from either the tetragonal or the cubic phase (Pace and Saunders 1972, Gunton and Saunders 1974).

It is possible that the enhancement of the acoustic mode softening and shear instability of In upon addition of Tl arises from a strong electron-phonon interaction; if this is so, then alteration

of the shape and size of the Fermi surface by alloying with an element of different valency, together with ion size effects should strongly influence the phase stability. This thesis presents an experimental study of the role of valency of the alloying element on the mode softening in In and the stability of the alloy phases by measuring for the first time ultrasonic wave velocities in single crystals of In alloys with divalent Cd (Group IIB) and tetravalent Pb (Group IVB). Cd and Pb have been chosen as alloying elements because they belong to the same Hume-Rothery intermediate class of metals as In and therefore the ion size effects (Hume-Rothery and Raynor 1962) are expected to be small.

Possible implications of acoustic phonon mode softening on the melting process in In alloys have been examined by measuring ultrasonic wave velocities in the vicinity of melting point in In-Cd alloys and from calorimetric determination of fusion entropies of In-Cd and In-Tl alloys.

Like In, the next group IIIB metal Tl, which crystallises in the hcp (point group 6/mmm) structure also displays a weak resistance to shear - the shear modulus $C_{66} = \frac{1}{2}(C_{11} - C_{12})$ is small (Ferris, Shepard and Smith 1963). The shear stability deteriorates with increasing temperatures and (unlike In) Tl transforms (Pearson 1967) to a bcc structure at 507°K close to the melting point ($T_m = 577^{\circ}K$). At the present very little is known about this transformation and in the absence of elastic constant data for the bcc phase - this phase cannot be retained at room temperature even with fast quenching techniques (Luo and Willens 1967) - a proper assessment of the relative stabilities of the hcp and bcc forms has

been difficult to make. However, the bcc phase can be stabilised at room temperature by alloying with In and we have grown for the first time large single crystals of bcc In-Tl alloys around the eutectoidal composition (∿17 - 24 at% In). The components of the elastic stiffness tensor have been obtained for the alloy compositions 18.5 and 23.5 at% In from ultrasonic wave velocity measurements. A linear extrapolation of the elastic constants of the alloys to vanishing solute concentration has been used to estimate the elastic constants of bcc Tl itself. The measured elastic constants of the bcc In-Tl alloys and the estimated values of bcc Tl have been used to test Zener's hypotheses (Zener 1947, 1948, 1967): (i) $\frac{1}{2}(C_{11} - C_{12})$ should be small in comparison with C_{44} for a bcc material comprised of closed ion shells and (ii) the stability of the bcc structure found at high temperature for many metals is due to a comparatively large vibrational entropy contribution.

In addition to the study of phase stabilities, a number of metallurgical problems associated with the structure and nature of In solid solutions have been resolved and many ambiguities in the alloy phase diagrams have now been removed.

C H A P T E R 2

PHASE TRANSFORMATIONS IN INDIUM ALLOYS

2.1 Introduction

The phase diagrams of In-Cd, In-Tl and In-Pb alloy systems will be described in this Chapter. In addition, some of the concepts underlying structural phase transformations will be introduced; their implications with regard to phase transformations in In alloys in the light of the experimental results of the present study will be discussed in Chapters 6, 7 and 8.

2.2 Phase diagrams of In-Cd, In-Tl and In-Pb alloy systems

A phase diagram may be defined (Pelton and Thompson 1975) as a geometrical representation of the loci of thermodynamic parameters when equilibrium between different phases under a specified set of conditions is established. The parameters employed in classical thermodynamic treatments are the temperature (T), pressure (P) and concentrations (X) of independent chemical variables. The underlying thermodynamic principle governing the construction of the phase diagram is contained in the Gibbs's phase rule which states: the maximum number of phases p which can coexist in an alloy, plus the number of degrees of freedom f is equal to the sum of the components c of the system plus 2. That is,

$$p + f = c + 2 \qquad (2.1)$$

f, the degree of freedom indicates the number of parameters that must be specified simultaneously in order to establish unambiguously the state of a system. Thus, in a binary alloy phase diagram there are three degrees of freedom set by pressure, temperature and alloy concentration. However, an isobaric two-dimensional description of the two component In alloy phase diagrams will be given here.

2.2.1 In-Cd System

The salient features of the In-Cd alloy phase diagram described here represent the results of the present investigation (Chapters 4 and 6) and those of the past forty years (Wilson and Wick 1937, Betteridge 1938, Valentiner 1943, Carapella and Peretti 1951, Heumann and Predel 1959a, 1959b and 1962, Predel 1964, Predel and Sandig 1970, Straumanis, Rao and James 1971 and Polovov and Ponyatovskii 1973). For the sake of completeness the entire range- 0 to 100 at% Cd-will be covered although the emphasis will be on the In rich end extending up to about 12 at% Cd - a portion that is relevant to the present study.

The complete phase diagram is given in Figure 2.1 and the In-rich portion covering the composition range of the present study in Figure 2.2. Up to about 4 at% Cd, In forms primary solid solutions i.e., the alloys freeze in the fct (point group 4/mmm) In structure. These alloys retain the fct structure right up to the melting point but the $\frac{c}{a}$ ratio decreases with Cd concentration (Chapter 4). When the Cd concentration is higher than about 5.9 at%, alloys freeze at room temperature ($20^{\circ}C$) in fcc (point group m3m) form. In the 4 - 5.9 at% Cd composition range, the alloys when cooled from the melt first freeze in the fcc phase but before reaching room temperature transform to the fct phase. This fct - fcc transformation involves a two phase region (Straumanis, Rao and James 1971) and its significance will be considered in Chapter 6 in discussing the order of the phase transformation. Also, according to Heumann and Predel (1962), in this range (4 - 5.9 at% Cd) there is a peritectic reaction (Rhines 1956): $L + \text{fct} \underset{\text{heating}}{\overset{\text{cooling}}{\rightleftharpoons}} \text{fcc}$ i.e., upon addition of increasing

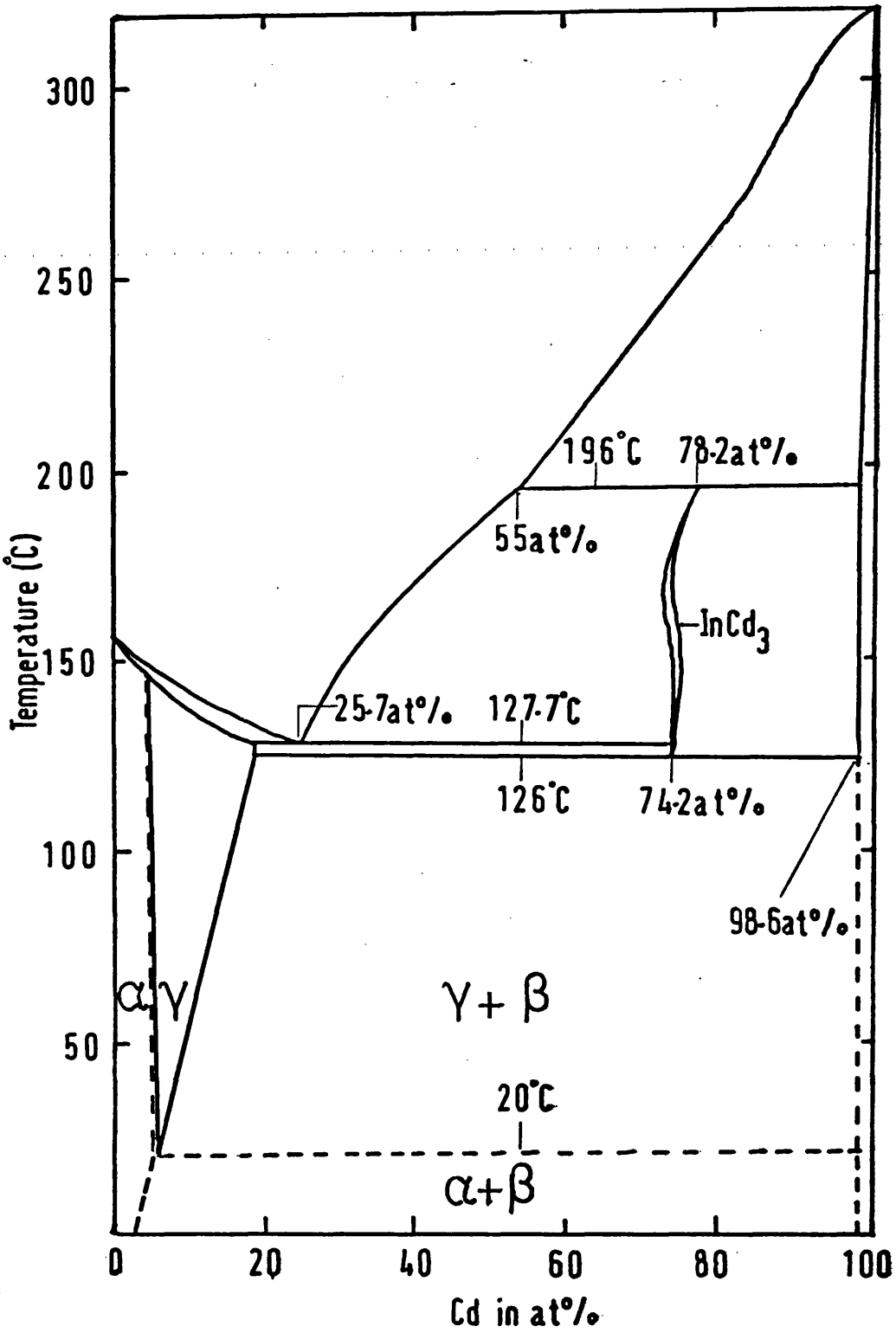

Figure 2.1: Phase diagram of the In-Cd system (Heumann and Predel 1962). α, β and γ denote fct, hcp and fcc phases respectively. The low temperature limit of the γ phase found here is at variance with that of the present study (Figure 2.2).

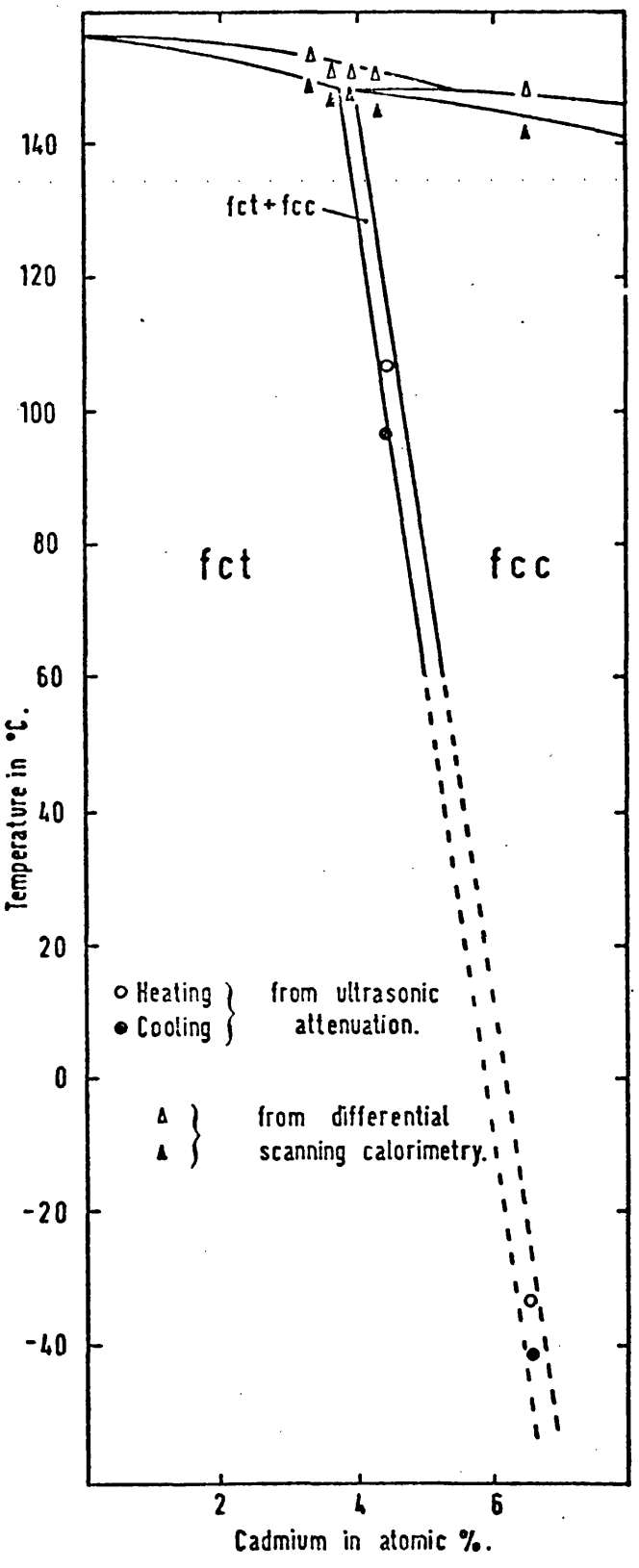

Figure 2.2: In-rich end of the In-Cd phase diagram. The lines above 60°C marking the phase boundary are due to Heumann and Predel (1962). The points are results obtained from the present work.

amounts of Cd, the tetragonal solid solution reacts with Cd forming some cubic alloy and partially reacting with the remaining tetragonal form with rapid decrease in $\frac{c}{a}$ value. The fcc - fct transformation itself has been studied by metallographic, thermal, X-ray and other methods and these investigations have already been cited at the beginning of this Section, and the broad consensus is that the fcc - fct structural transformation is diffusionless and probably of the martensitic type. However, no previous elastic constant study of this transformation has been made nor is there any discussion pertaining to the origins of the structural transformation at the atomic level. This gap has been filled by the present study (Chapter 6). The fcc phase starting at about 5.9 at% extends up to about 12 at% Cd at room temperature. Ultrasonic measurements performed on a 6.5 at% Cd fcc alloy has shown that this alloy transforms on cooling below room temperature. The transformation temperature is in good agreement with the extrapolated phase boundary (Figure 2.2) of the existing phase diagram - the low temperature region of the fcc/fct phase boundary has now been extended. The alloys up to about 12 at% Cd are homogeneous substitutional solid solutions. As part of the present contribution this has been corroborated from the single crystal studies (Chapter 4).

Although, In and Cd are completely miscible in each other in all proportions in the liquid state, the solid solubility is limited - about 12 at% Cd at 20^{o}C (Straumanis, Rao and James 1971). Further addition of Cd results in the precipitation of the hcp Cd phase along with the fcc phase. This precipitation progressively increases until at 98.6 at% Cd the alloy phase is entirely hcp. In the compo-

sition range 12 - 100 at% Cd there are two special features (Heumann and Predel 1959b): (i) a eutectic is formed at 25.7 at% Cd which melts at 127.7°C and (ii) in addition to the eutectic temperature arrest, there are two more temperature arrests at 126°C (74.2 at% Cd) and 196°C (78.2 at% Cd). The effect at 196°C is due to yet another peritectic reaction by which an fcc intermetallic phase $InCd_3$ is formed from the melt and the Cd-rich solid solution. The thermal effect at 126°C is due to the decomposition of the intermetallic phase into In-rich and Cd-rich solid solutions.

2.2.2 In-Tl System

The composite phase diagram given by Hansen and Anderko (1958) is reproduced in Figure 2.3. Since the compilation of this diagram, further studies have been reported (Meyerhoff and Smith 1963, Adler and Margolin 1966 and Pollock and King 1968). Of these, the former two include the pressure effects on the alloy system. Concerning the present work, the bcc phase of the Tl-rich end of the phase diagram is by far the most important region, although low temperature (down to 4.2°K) elastic constants of some fcc alloys pertaining to the fcc/fct phase boundary have been measured here (Chapter 7) to complement the previous work (Gunton and Saunders 1974).

At room temperature (20°C) the fct (point group 4/mmm) primary solid solution range extends up to about 23 at% Tl. In common with the In-Cd system, in this range the $\frac{c}{a}$ ratio decreases with Tl concentration (Chapter 4) but in contrast, the transformation into the fcc (point group m3m) phase above about 23 at% Tl is not preceded by a two phase region (Guttman 1950). The fcc phase is terminated by a peritectic at about 40 at% Tl and 170°C. However,

at room temperature the fcc phase extends up to about 60 at% Tl. The fcc alloys up to about 31 at% Tl transform below room temperature to the fct phase and the fcc/fct phase boundary has been well studied down to 3°K (see, for example, Pollock and King 1968 and Luo, Hagen and Merriam 1965) including by elastic constant measurements (Pace and Saunders 1972, Gunton and Saunders 1974 and Chung, Gunton and Saunders 1976). The fcc - fct transformation has been well established as being diffusionless martensitic type and the physics of it has been discussed in detail (Gunton and Saunders 1973). Above about 60 at% Tl one gets into the Tl-rich realm. The character of this region is strongly influenced by the polymorphs of Tl itself. At about 76 at% Tl and 20°C there is a eutectoid with a central bcc phase flanked by mixed phases -(bcc + fcc) from about 60 - 75 at% Tl and (bcc + hcp) from about 77 - 85 at% Tl. Above about 85 at% Tl and up to 100 at% Tl the alloys are entirely in the hcp ε Tl phase. Unlike the fcc/fct boundary of the In rich end, the eutectoid and the boundaries of the coexisting phases are not firmly established. In particular, the sluggish nature of the eutectoid reaction (see Chapter 7) leads to the situation wherein it is possible to have alloys at room temperature entirely in the bcc phase over a range that could cover almost 70 - 85 at% Tl. No previous elastic constant measurements of this bcc β Tl phase has been made, although such measurements can provide valuable information on the polymorphic transformations in Tl. It is with this in view the elastic constant measurements reported in Chapter 7 were undertaken.

2.2.3 In-Pb system

The description of the phase diagram (Hansen and Anderko 1958) again starts with the fct (point group 4/mmm) In primary solid

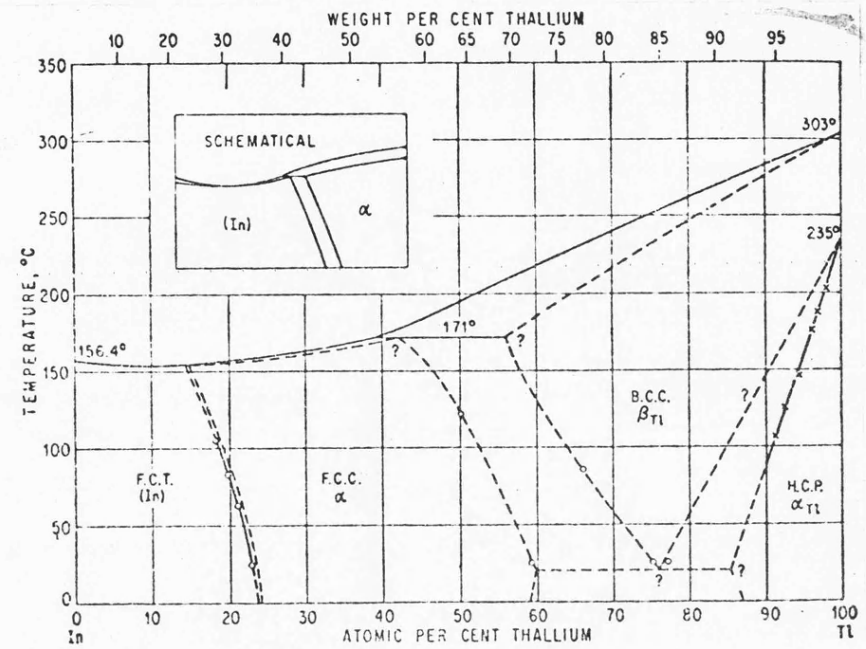

Figure 2.3: Phase diagram of the In-Tl system (Hansen and Anderko 1958). The two-phase region (inset) is not present according to Guttman (1950).

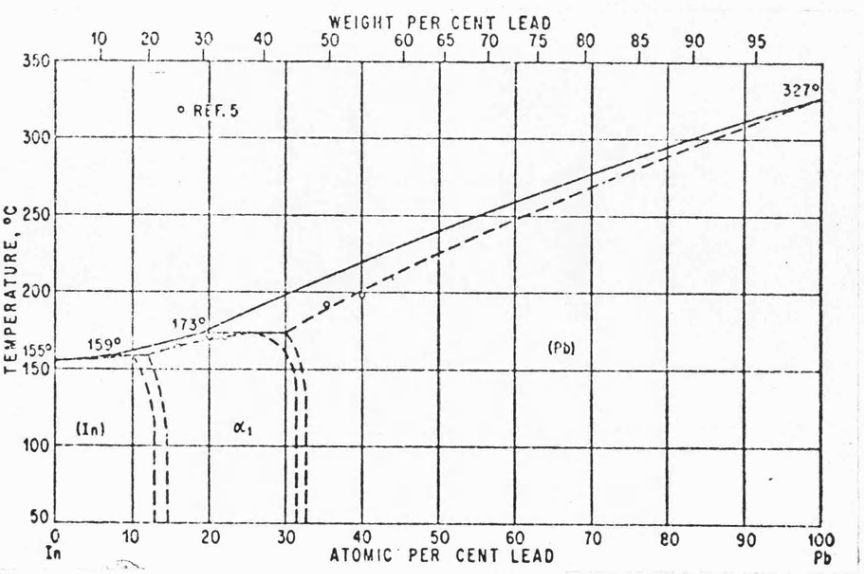

Figure 2.4; Phase diagram of the In-Pb system (Hansen and Anderko 1958). α_1 is the fct phase with c/a < 1.

solutions which extend up to about 12.7 at% Pb at 20°C (Figure 2.4). In this range, in contrast with the In-Cd and In-Tl systems the $\frac{c}{a}$ ratio of In (1.08) progressively increases (see Chapter 4) upon addition of Pb - at about 12.3 at% Pb the $\frac{c}{a}$ ratio is $\sim$ 1.09. Further increase of Pb does not lead to a fcc phase like in In-Cd and In-Tl alloys, but to yet another fct (α_1) phase; this time with $\frac{c}{a} < 1$. The α_1 phase exists between about 13.7 and 31 at% Pb with the $\frac{c}{a}$ ratio progressively decreasing from about 0.934 to 0.928 (Chapter 4). Beyond this, the fcc (point group m3m) Pb phase starts and extends right up to 100 at% Pb. The fct ($\frac{c}{a} > 1$) - fct ($\frac{c}{a} < 1$) transformation involves a two phase region with the mixed phase existing between 12.7 and 13.7 at% Pb at 20°C. The transformation from α_1 (fct, $\frac{c}{a} < 1$) to fcc phase is also preceded by a mixed phase region but its width has not been firmly established. The fct ($\frac{c}{a} > 1$) - fct ($\frac{c}{a} < 1$) transformation has been the subject of a detailed X-ray examination by Tyzack and Raynor (1954a) and Moore et al (1955), and they describe it as diffusionless second order. No previous elastic constant data of the fct phases is available but the elastic constants of Pb-rich fcc alloys have been measured by van der Planken, Greiner and Smith (1971). The elastic constant results of the two fct phases and the fcc phase of the present study will be discussed in Chapter 8. Other features of the In-Pb phase diagram include two peritectic horizontals - one at about 159°C (8-12 at% Pb) and the other at about 173°C (20 - 30 at% Pb). Also, Heumann and Predel (1966) indicate a eutectoid at -15°C in the range of Pb-rich solid solutions. This finding has not been elaborated.

2.3 Phase transformations in the solid state

A widely accepted categorisation of solid state phase trans-

formations in metallic systems is to group them into two main classes: (i) nucleation and growth transformations and (ii) martensitic transformations (see Table 2.1). In (i), the transformation process may be completed isothermally with thermal activation and diffusion playing an important role whereas in (ii), thermal activation has little effect on the transformation process - these transformations are athermal and diffusionless. A classification that provides a better insight into transformation mechanisms has been made by Buerger (1951) on the basis of crystallographic aspects of phase transformations.

2.3.1 Buerger's Classification

The rate at which a solid state phase transformation takes place depends on the energy barriers resisting the process. That is to say, an activation energy must in general be available to bring about a transformation. The changes in energy occurring in a transformation reflect the changes in bonding of atoms in the structure. When assessed from a structural point of view, bonding changes mean changes in the interaction between neighbouring atoms - nearest and more distant neighbours. On the basis of this description, solid state phase transformations fall into four categories:

(i) Secondary co-ordination or network transformations (Displacive and Reconstructive)

(ii) Disorder transformations (Rotational and Substitutional)

(iii) Primary co-ordination transformations (Dilatational and Reconstructive)

and (iv) Bond type transformations.

The fcc - fct transformations in In-Cd and In-Tl alloys studied here

can be placed under category (i) with a displacive character and hence this particular type of transformation will be described here in more detail than the others.

2.3.1.1 Secondary co-ordination transformations

Here, there is no change in primary or first co-ordination of atoms; the energy change is due to change in co-ordination of non-nearest neighbours. Since it is commonly assumed that the major contribution to the energy of a crystal comes from the contacting atoms of the first co-ordination, secondary co-ordination transformation represents a change in the residual co-ordination energy. There are two possible ways of moving from one kind of secondary co-ordination to another, leading to'Displacive' and 'Reconstructive' transformations.

2.3.1.2 Displacive transformations

As illustrated in Figure 2.5, atoms of any crystal structure can at least in theory be displaced in such a way as to leave the contacting atoms of the primary co-ordination intact, but yet resulting in a distorted structure due to the displacement of non-contacting atoms of the secondary co-ordination. The distorted structure can be regarded as a space network with the displacement bringing in a systematic distortion of the net without changing the linkage of the net. A net distortion of this nature is subjected to no energy barrier. Displacive transformations can therefore take place very rapidly - as in the martensitic transformation of In-Tl alloys (Pace and Saunders 1972a).

2.3.1.3 Reconstructive transformation

Changes in the non-contacting atoms of the secondary co-ordination can also be brought about by a process of delinking and relinking of the network, always leaving the primary co-ordination unchanged (Figure 2.5). However, this reconstructive process of transformation does involve a temporary disruption of the primary co-ordination before this is set right in the new structure. This means there is a high energy barrier unlike in the displacive transformation. Reconstructive transformations are therefore generally very sluggish.

2.3.1.4 Characteristics of displacive transformation

Certain general characteristics of displacive transformations are contained in Buerger's (1951) description of the transformation mechanism. This will now be illustrated with reference to the configurations given in Figure 2.5. Here, (c) represents the undistorted high temperature form and (b) is the low temperature distorted form. The network (b) is nothing but the displacive equivalent of (c). In (b), the second nearest neighbours of A and B atoms are closer than in (c). This means that the undistorted form (c) has a higher residual energy than the distorted form (b) and therefore (b) is more stable in the vicinity of $0^{\circ}K$. For the purposes of illustrating the point, if the A atoms of (b) are more or less fixed while the B atoms of the opposite kind predominantly vibrate, then when the temperature and hence the thermal agitation on (b) increases, the B atoms like B_1 move in the direction of the arrow (Figure 2.5). In doing so B_1 comes across B_2 and B_3 which it repels and allows B_2 and B_3 to move on in the direction of the arrows shown. Thus, an agitation of a single B atom gets communicated to all nearest B atoms

which in turn communicate the motion to their nearest B neighbours resulting in a co-operative distortion of the neighbourhood. When the thermal agitation on (b) further increases, a temperature is finally reached wherein the distorted neighbourhood gets enough energy to successfully oppose the secondary co-ordination non-nearest neighbour attractions and ends up in the reversed configuration (d). The displacive transformation is said to have ensued at that temperature (T_c) at which the network configuration is made up of equal amounts of (b) and (d). This high temperature transformed form is undistorted because the time average of the position of every B atom in this form is the same as the position of the B atom in the static form (c). The high temperature transformed form has the higher symmetry because this form is an average of the obversed (b) and reversed (d) forms. Again, the symmetry of the low temperature distorted form (b) is a sub-group of the symmetry of the undistorted form (c). This means that a down-temperature transformation often results in twins (Figure 2.6). This twinning in the case of structural transformation in In-Cd alloys is discussed in Chapter 6.

2.3.2 Disorder transformations (Rotational and Substitutional)

The order-disorder transformations - a common occurrence in many metal alloy systems belongs to this category. This class of transformation has been described elsewhere (Barrett and Massalski 1966) and will not be elaborated here.

2.3.3 Primary co-ordination transformations (Dilatational and Reconstructive)

Primary co-ordination changes can result from a reconstructive

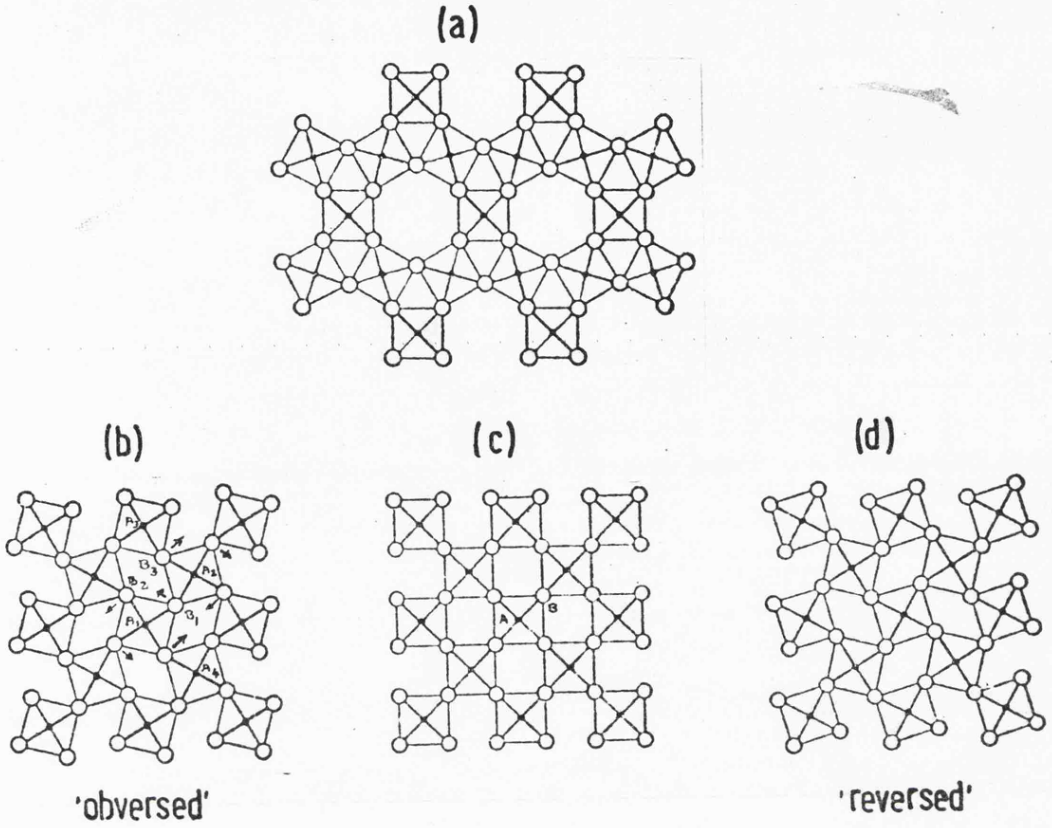

Figure 2.5: Secondary co-ordination transformation (Buerger 1951). Reconstructive transformation between (a) and (c) leaves the primary co-ordination unchanged yet the two networks are very different. The transformation between (b) and (c) also leaves the first co-ordination intact but the networks are related - the 'collapsed' form of (b) is the displacive equivalent of the 'open' form of (c).

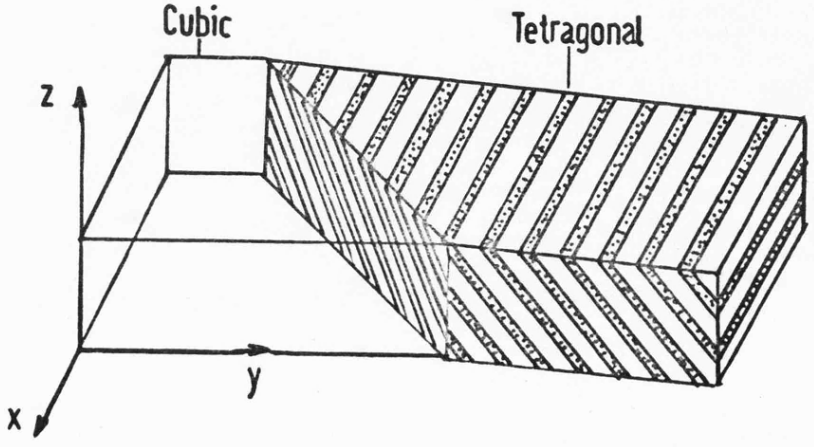

Figure 2.6: Partially transformed In-Tl alloy. The ridges indicate twin related lamellae.

process wherein the primary co-ordination bonds are broken and re-formed. These transformations involve high activation energies and are usually sluggish. Primary co-ordination changes can also take place by a dilatational process in which case the transformation is more rapid.

2.3.4 Bond type transformations

Lastly, in many polymorphic transformations the polymorphs are characterised by very different bonding - diamond and graphite, for example. The bond type transformations are again comparatively sluggish. Further discussion will be presented in Chapter 7 in dealing with the polymorphic transformations in Thallium.

2.4 Martensitic transformations

Martensitic transformations come under the category of displacive transformation. In addition to the general characteristics outlined in Section 2.3.1.4, there are many transformation features which are unique to any given material. Christian (1965) has reviewed these special features of martensitic transformations occurring in a number of metal and alloy systems including In-Tl (see also Table 2.1).

2.5 Soft mode concept of elastic phase transformations

Structural phase transformations are described in terms of establishing or destroying some kind of order. Destruction of order leads to a change of symmetry. Buerger's crystallographic approach (Section 2.3.1) provides this description in an elegant systematic manner. This description has become more and more refined in the recent past as a result of theoretical concepts introduced by Landau

Table 2.1

Martensitic transformations in non-ferrous materials

Material	Structural change
Ag-Cd	bcc to orthorhombic
Au-Cd	bcc to orthorhombic
Cu-Al-Mn	bcc to orthorhombic
Cu-Al-Ni	bcc to orthorhombic
Cu-Ga	bcc to fcc (faulted)
	bcc to orthorhombic
Cu-Sn	bcc to orthorhombic
	bcc to fcc (faulted)
Cu-Zn	bcc to orthorhombic
Hf	bcc to hcp
Hg	rhombohedral to bct
In-Tl	fcc to fct
Li	bcc to hcp
Mn-Cu	fcc to fct
Na	bcc to hcp
Nb_3Sn	cubic to tetragonal
Ti	bcc to hcp
Ti-Mn	bcc to hcp
Ti-Mo	bcc to hcp
Ti-Nb	bcc to orthorhombic
V_3Si	cubic to tetragonal
Zr	bcc to hcp

(see Landau and Lifshitz 1959) and Cochran (1960, 1961) which are widely applicable. Cochran's approach recognises the fact that structural phase transformations can be the result of an instability of the crystal against a soft mode. His analysis based on displacive transformations in ferroelectric crystals was essentially restricted to soft optic modes (Figure 2.7). Recently (see for example Folk, Iro and Schwabl 1976) the soft mode concept has again been used in the study of a class of structural phase transformations called 'Elastic phase transformations'. For an elastic phase transformation, the parameter designating order - the order parameter - is a component of the strain tensor and the soft mode is an acoustic phonon. The soft mode is a particular mode of vibration of the crystal whose characteristic frequency ω drastically decreases as the transformation is approached and whose eigenvector (array of atomic displacements) represents the distortion that the new structure imposes upon the old. The soft mode thus contains both dynamic and static information on the impending transformation. The soft mode concept has been invoked to answer the three basic questions pertaining to the structural phase transformation namely: (i) why do the transformations take place (ii) what is the transformation temperature T_c and (iii) what is the structure of the new phase? These questions are all answered in terms of the presence of the soft mode. Thus, the phase transformation occurs because of the instability of the crystal against the soft mode. This instability occurs because anharmonic interactions in the crystal cause a temperature renormalisation of the phonon frequencies. The transformation temperature T_c is then that temperature at which the temperature assisted phonon renormalisation is complete. The structure of the transformed phase is determined by the structure of the old phase and the eigenvector

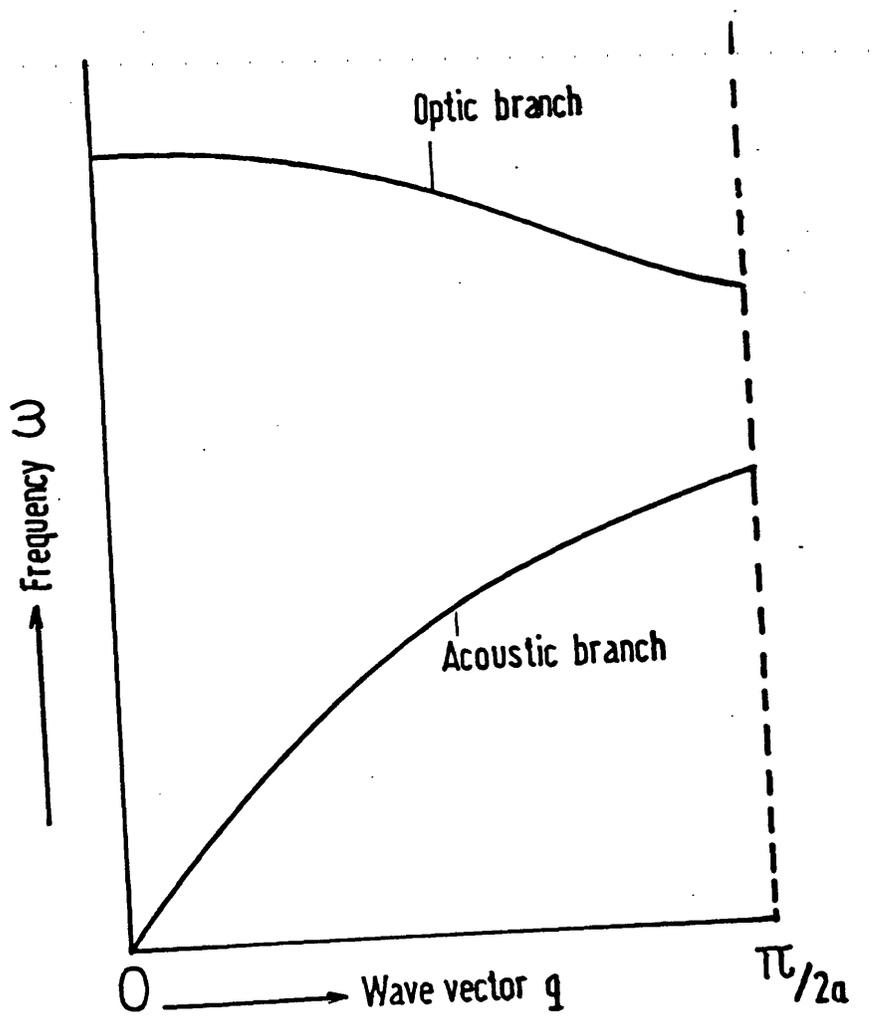

Figure 2.7: Optic and acoustic branches of the phonon dispersion curve of a linear diatomic lattice. In the case of fcc and fct In alloys - with one atom in the unit cell - the optic branch is absent.

of the soft mode.

Previously, optimised model potential calculation of the phonon dispersion curves of In-Tl alloys (Gunton and Saunders 1973)- reproduced in Figure 2.8-has shown that the $[110]$, $\underline{q}$ // $[1\bar{1}0]$ acoustic phonon mode softens near the Brillouin zone centre and its presence is responsible for the fcc-fct martensitic transformation. An elegant experimental way of studying the acoustic phonon mode softening behaviour near the Brillouin zone centre is to measure the elastic wave velocities of this regime (slope of the phonon dispersion curves, see Figures 2.7 and 2.8). This has been done here by ultrasonic techniques. The ultrasonic measurements have shown for the first time that the fcc-fct structural transformation in In-Cd alloys is due to the presence of a soft acoustic mode - $[110]$, $\underline{q}$ // $[1\bar{1}0]$. The results of this study will be discussed in Chapter 6. Before concluding this Section, some of the more recent reviews concerning the soft mode aspects of structural phase transformations may be listed. They include: Fleury (1972, a, b, 1973 and 1976), Nakanishi (1972), Rehwald (1973) and Shirane (1974).

2.6 Thermodynamics of structural phase transformations

Under this heading, the order of the phase transformation will be discussed, but before that, the inter-relationship between the various thermodynamic variables will be outlined and the significance of the Gibbs free energy G in the study of phase changes will be examined. The treatment follows the methods adopted by Bridgman (1925a) and Slater (1939).

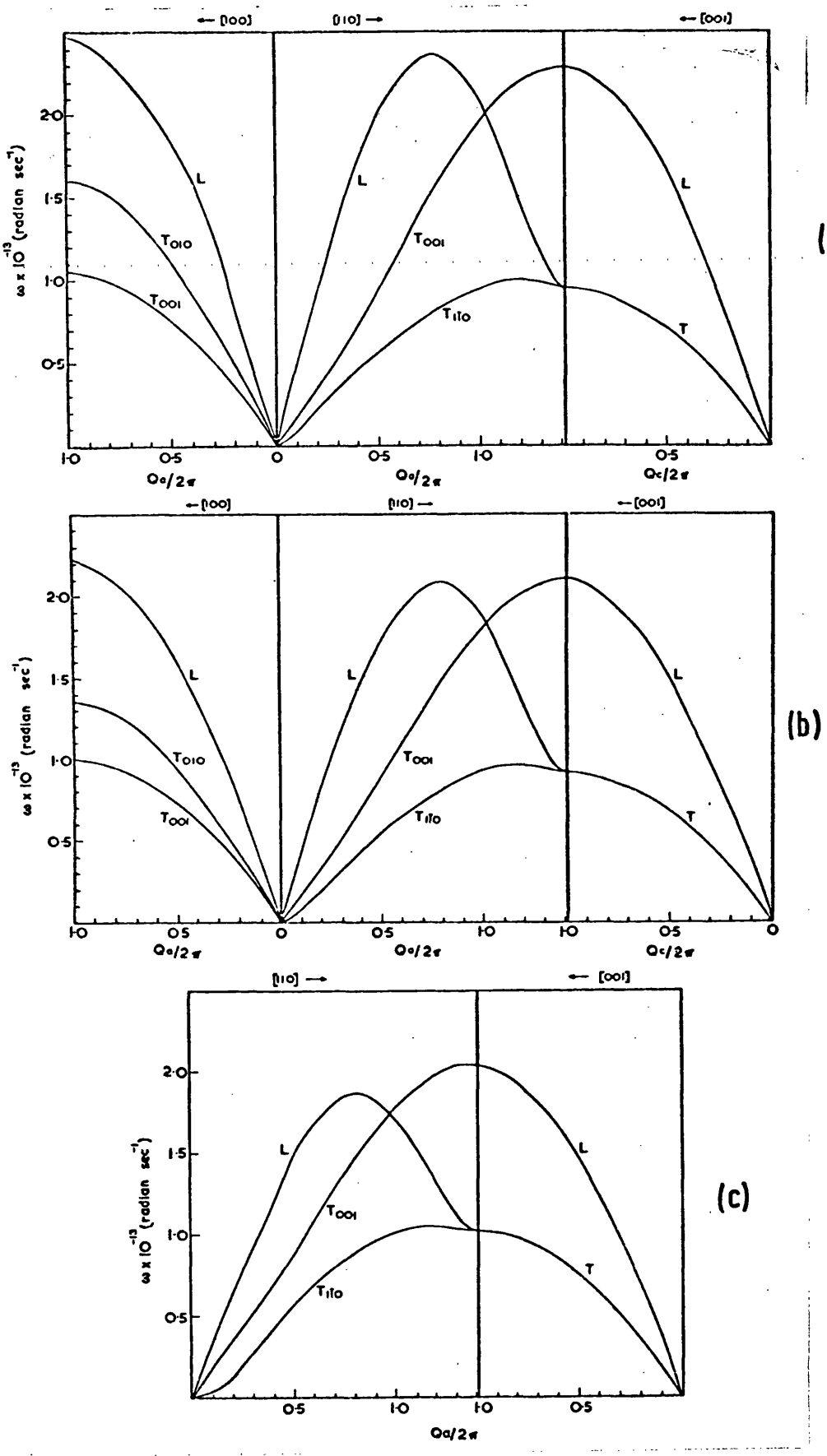

Figure 2.8: Phonon dispersion curves of In-Tl alloys showing the pronounced softening of the $[110]$, // $[1\bar{1}0]$ transverse acoustic mode near the Brillouin zone centre Q = 0. (a) fct In (b) fct In - 15 at% Tl (c) fcc In-25 at% Tl. L (longitudinal) and T (transverse) indicates the polarisations (Gunton and Saunders 1973).

2.6.1 Thermodynamic relations and the significance of G in the study of phase changes

P = Pressure

V = Volume

T = Temperature

S = Entropy

U = Internal energy

H = Enthalpy

A = Helmholtz free energy

G = Gibbs free energy

The analysis will first be restricted to the five thermodynamic variables P, V, T, S and U. Of these any two are independent. Some of the partial derivatives of these variables which lead to experimentally measurable quantities will now be given. They include:

$$\text{Thermal expansion} = \frac{1}{V}\left(\frac{\partial V}{\partial T}\right)_P \tag{2.2}$$

$$\text{Isothermal compressibility} = -\frac{1}{V}\left(\frac{\partial V}{\partial P}\right)_T \tag{2.3}$$

$$\text{Adiabatic compressibility} = -\frac{1}{V}\left(\frac{\partial V}{\partial P}\right)_S \tag{2.4}$$

Specific heat at constant volume

$$= C_V = \left(\frac{\partial U}{\partial T}\right)_V = T\left(\frac{\partial S}{\partial T}\right)_V \tag{2.5}$$

Specific heat at constant pressure

$$= C_P = T\left(\frac{\partial S}{\partial T}\right)_P = \tag{2.6}$$

$$\left(\frac{\partial U}{\partial T}\right)_P + P\left(\frac{\partial V}{\partial T}\right)_P \tag{2.7}$$

Except for C_P, all the other partial derivative relationships are very simple and straightforward. To tackle this point, the variable

H is introduced. The introduction of the other two variables A and G will also become clear soon.

C_P in equation (2.7) can be written as:

$$C_P = \left[\frac{\partial (U + PV)}{\partial T} \right]_P \tag{2.8}$$

Since the quantity (U + PV) appears fairly frequently it is customary to give a specific name for this. It is called enthalpy and is denoted by H. Thus,

$$H = U + PV$$

$$dH = dU + PdV + VdP = TdS + VdP \tag{2.9}$$

From equation (2.9) it is seen that if dP = 0, that is if the process is taking place at constant pressure, the change of enthalpy equals the heat absorbed. Since a number of actual experiments are isobaric in nature, enthalpy is an important quantity. Using the variable, H, the specific heat at constant pressure becomes,

$$C_P = \left(\frac{\partial H}{\partial T} \right)_P \tag{2.10}$$

From the first and second laws of thermodynamics we have,

$$dU = TdS - PdV \tag{2.11}$$

which leads to

$$\left(\frac{\partial U}{\partial S} \right)_V = T \tag{2.12}$$

$$\left(\frac{\partial U}{\partial V} \right)_S = - P \tag{2.13}$$

The quantity TS gives the energy bound as heat which means that U - TS should give the mechanical part of the energy. This mechanical

part is again frequently encountered and a special name has therefore been given. This is called the Helmholtz free energy and is denoted by A. Thus,

$$A = U - TS$$

$$dA = dU - TdS - SdT \tag{2.14}$$

and using the second law of thermodynamics

$$dA \leq -dW - SdT$$

$$\text{or } -dA \geq dW + SdT \tag{2.15}$$

where W is the work. Equation (2.15) for a system in equilibrium under hydrostatic pressure can be written as

$$dA = -PdV - SdT \tag{2.16}$$

$$\text{Also, } \left(\frac{\partial A}{\partial V}\right)_T = -P \text{ and } \left(\frac{\partial A}{\partial T}\right)_V = -S \tag{2.17}$$

These equations indicate that volume and temperature are the convenient variables to designate the Helmholtz free energy. However, it is frequently required to treat pressure and temperature as variables. In such instances the use of Helmholtz free energy A will be clumsy. For this reason the Gibbs free energy G is used instead. G is given by,

$$G = H - TS = U + PV - TS = A + PV \tag{2.18}$$

It again follows that

$$\left(\frac{\partial G}{\partial P}\right)_T = V \text{ and } \left(\frac{\partial G}{\partial T}\right)_P = -S \tag{2.19}$$

The Gibbs free energy G is by far the most important thermodynamic variable. This is because most actual physical processes occur at

constant pressure and temperature. Considering phase changes, for example, if unit mass of a substance changes phase reversibly at constant temperature and pressure the total Gibbs free energy must remain the same - in equilibrium G per unit mass must be the same for both the phases. At a temperature and pressure away from equilibrium, G per unit mass will be different for the two phases. In this case, the phase with the lower G is the stable phase. If the system finds itself in the phase having the higher G, it will be unstable and will transform to the other phase with the lower G. The elastic constants C_{ij} are intimately connected with the thermodynamic potentials - being related to the internal energy U by,

$$C_{ij} = \frac{\partial^2 U}{\partial x_i \partial x_j} \quad \text{where } x_i, x_j \text{ are strains} \qquad (2.20)$$

and hence provide valuable information in the study of phase changes. A comprehensive list of thermodynamic relations is also collected in Table 2.2.

2.6.2 Order of the phase transformation

There are a number of ways of looking at the order of a structural transformation - for example, Landau (Landau 1937a, b and Landau and Lifshitz 1959) defines a first order transformation as resulting in a discontinuous change in the state of the body with a gradual reconstruction of the lattice whereas in a second order transformation there is a continuous change in the state of the body and the symmetry undergoes a sudden change at the transition point. However, all the definitions depend upon the fact that in a first order transformation there are discontinuities in the first derivatives of the Gibbs free energy G and in the case of a second order transformation there are discontinuities in the second derivatives of G;

Table 2.2

Thermodynamic Relations

$$\left(\frac{\partial V}{\partial T}\right)_P = \left(\frac{\partial V}{\partial T}\right)_P$$

$$\left(\frac{\partial S}{\partial T}\right)_P = \frac{C_P}{T}$$

$$\left(\frac{\partial U}{\partial T}\right)_P = C_P - P\left(\frac{\partial V}{\partial T}\right)_P$$

$$\left(\frac{\partial H}{\partial T}\right)_P = C_P$$

$$\left(\frac{\partial A}{\partial T}\right)_P = -P\left(\frac{\partial V}{\partial T}\right)_P - S$$

$$\left(\frac{\partial G}{\partial T}\right)_P = -S$$

$$\left(\frac{\partial V}{\partial P}\right)_T = \left(\frac{\partial V}{\partial P}\right)_T$$

$$\left(\frac{\partial S}{\partial P}\right)_T = -\left(\frac{\partial V}{\partial T}\right)_P$$

$$\left(\frac{\partial U}{\partial P}\right)_T = -T\left(\frac{\partial V}{\partial T}\right)_P - P\left(\frac{\partial V}{\partial P}\right)_T$$

$$\left(\frac{\partial H}{\partial P}\right)_T = V - T\left(\frac{\partial V}{\partial T}\right)_P$$

$$\left(\frac{\partial A}{\partial P}\right)_T = -P\left(\frac{\partial V}{\partial P}\right)_T$$

$$\left(\frac{\partial G}{\partial P}\right)_T = V$$

$$\left(\frac{\partial P}{\partial T}\right)_V = -\frac{\left(\frac{\partial V}{\partial T}\right)_P}{\left(\frac{\partial V}{\partial P}\right)_T}$$

$$\left(\frac{\partial S}{\partial T}\right)_V = \frac{C_V}{T} = \frac{C_P}{T} + \frac{\left(\frac{\partial V}{\partial T}\right)_P^2}{\left(\frac{\partial V}{\partial P}\right)_T}$$

$$\left(\frac{\partial U}{\partial T}\right)_V = C_V = C_P + T\frac{\left(\frac{\partial V}{\partial T}\right)_P^2}{\left(\frac{\partial V}{\partial P}\right)_T}$$

$$\left(\frac{\partial H}{\partial T}\right)_V = C_V - V\frac{\left(\frac{\partial V}{\partial T}\right)_P}{\left(\frac{\partial V}{\partial P}\right)_T} = C_P + T\frac{\left(\frac{\partial V}{\partial T}\right)_P^2}{\left(\frac{\partial V}{\partial P}\right)_T} - V\frac{\left(\frac{\partial V}{\partial T}\right)_P}{\left(\frac{\partial V}{\partial P}\right)_T}$$

Table 2.2 continued

$$\left(\frac{\partial A}{\partial T}\right)_V = -S$$

$$\left(\frac{\partial G}{\partial T}\right)_V = -S - V\frac{\left(\frac{\partial V}{\partial T}\right)_P}{\left(\frac{\partial V}{\partial P}\right)_T}$$

$$\left(\frac{\partial P}{\partial T}\right)_S = \frac{C_P}{T\left(\frac{\partial V}{\partial T}\right)_P}$$

$$\left(\frac{\partial V}{\partial T}\right)_S = \frac{\left(\frac{\partial V}{\partial P}\right)_T}{\left(\frac{\partial V}{\partial T}\right)_P}\frac{C_V}{T} = \frac{\left(\frac{\partial V}{\partial P}\right)_T}{\left(\frac{\partial V}{\partial T}\right)_P}\left[\frac{C_P}{T} + \frac{\left(\frac{\partial V}{\partial T}\right)_P^2}{\left(\frac{\partial V}{\partial P}\right)_T}\right]$$

$$\left(\frac{\partial U}{\partial T}\right)_S = -P\frac{\left(\frac{\partial V}{\partial P}\right)_T}{\left(\frac{\partial V}{\partial T}\right)_P}\frac{C_V}{T} = -P\frac{\left(\frac{\partial V}{\partial P}\right)_T}{\left(\frac{\partial V}{\partial T}\right)_P}\left[\frac{C_P}{T} + \frac{\left(\frac{\partial V}{\partial T}\right)_P^2}{\left(\frac{\partial V}{\partial P}\right)_T}\right]$$

$$\left(\frac{\partial H}{\partial T}\right)_S = \frac{VC_P}{T\left(\frac{\partial V}{\partial T}\right)_P}$$

$$\left(\frac{\partial A}{\partial T}\right)_S = -P\frac{\left(\frac{\partial V}{\partial P}\right)_T}{\left(\frac{\partial V}{\partial T}\right)_P}\frac{C_V}{T} - S$$

$$= -P\frac{\left(\frac{\partial V}{\partial P}\right)_T}{\left(\frac{\partial V}{\partial T}\right)_P}\left[\frac{C_P}{T} + \frac{\left(\frac{\partial V}{\partial T}\right)_P^2}{\left(\frac{\partial V}{\partial P}\right)_T}\right] - S$$

$$\left(\frac{\partial G}{\partial T}\right)_S = \frac{VC_P}{T\left(\frac{\partial V}{\partial T}\right)_P} - S$$

in both cases G itself varies continuously. This means that there are discontinuities in volume and entropy at a first order transformation and there is a latent heat associated with the transformation. On the other hand there is no latent heat associated with a second order transformation but there are discontinuities in specific heat, thermal expansion and bulk modulus at the transition point (see Figures 2.9 and 2.10).

In the Landau (Landau 1937 a, b and Landau and Lifshitz 1959) formalism, the order of the structural transformation is vividly portrayed in terms of the free energy behaviour with the order parameter. The free energy G is expressed as a power series in the order parameter η. That is,

$$G = A\eta^2 + B\eta^3 + C\eta^4 + \text{-----} \qquad (2.21)$$

In Figure 2.11, the free energy G has been plotted as a function of the order parameter η for both the first and second order transformations. In the case of a first order transformation there is a metastable state at $\eta = \eta'$ above the transformation temperature T_c. ΔG, the free energy between metastable and stable states goes to zero as $T \rightarrow T_c$ and there exists the possibility of heterophase fluctuations forming above T_c. From an experimental point of view the metastable state, accounted for in Figure 2.11 by the cubic term in the series expansion of the order parameter η, can often be associated with the two phase region found in Debye-Scherrer powder photographs. In the case of a second order phase transformation there is no metastable phase preceding the transformation, the cubic term in the series expansion of the order parameter is absent and as $T \rightarrow T_c$ the coefficient $A \rightarrow 0$ resulting in large dynamical fluctuations in the order

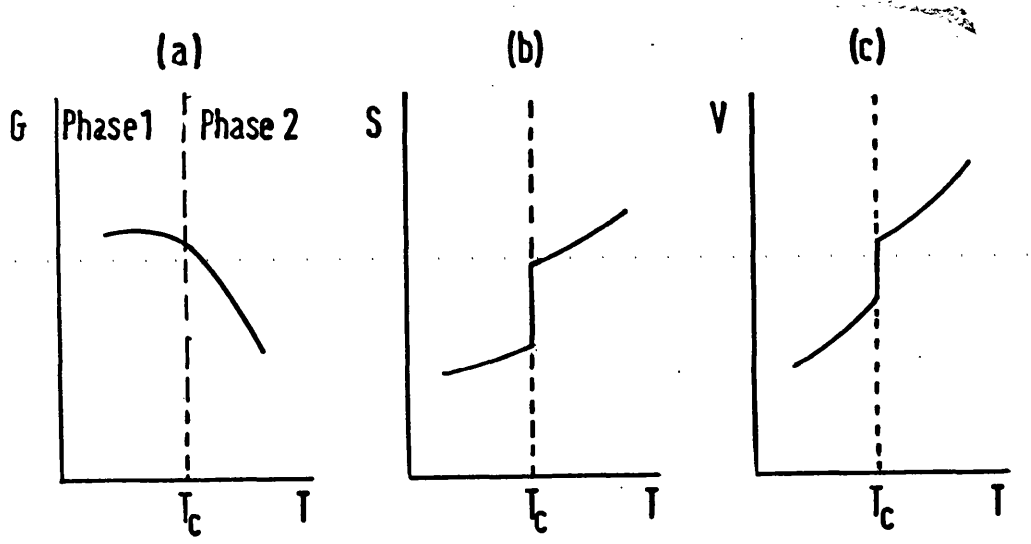

Figure 2.9: Variation of thermodynamic functions at a first order phase change: (a) variation of G (b) variation of $S = -(\partial G/\partial T)_P$ and (c) variation of $V = (\partial G/\partial P)_T$.

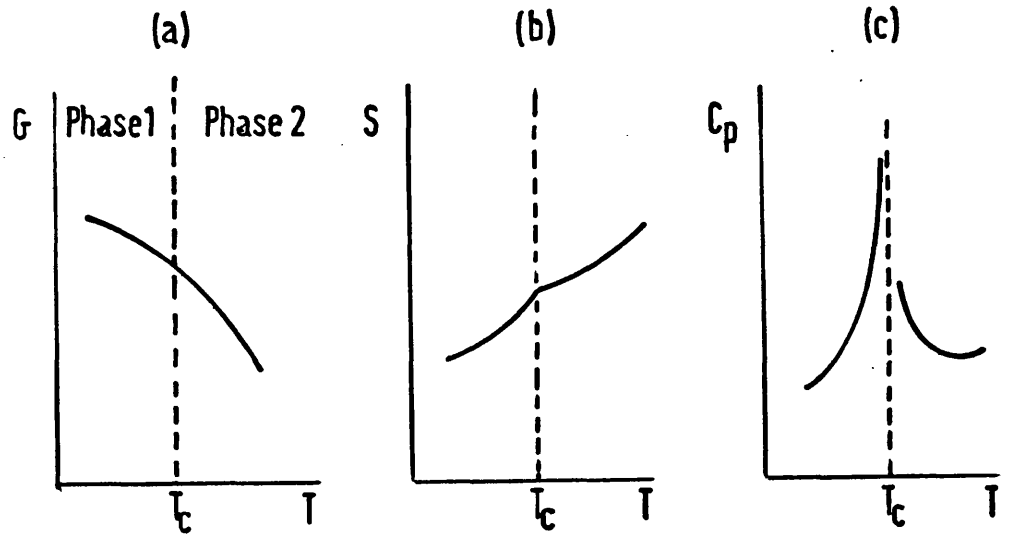

Figure 2.10: Thermodynamic behaviour at a second order phase change: variations of (a) G (b) S and (c) $C_p = -T(\partial^2 G/\partial T^2)_p$.

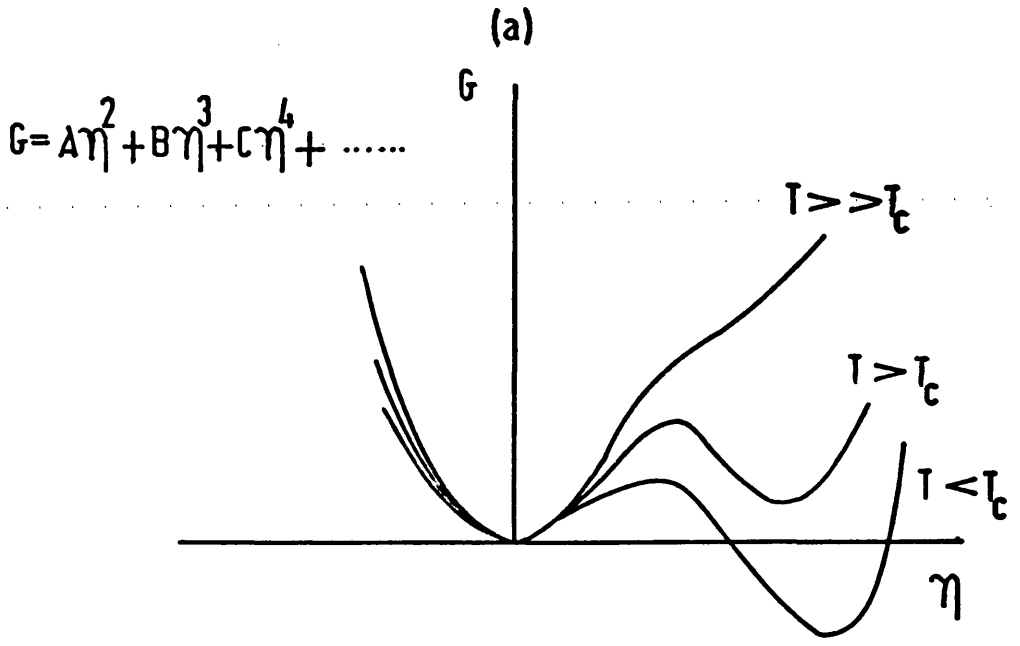

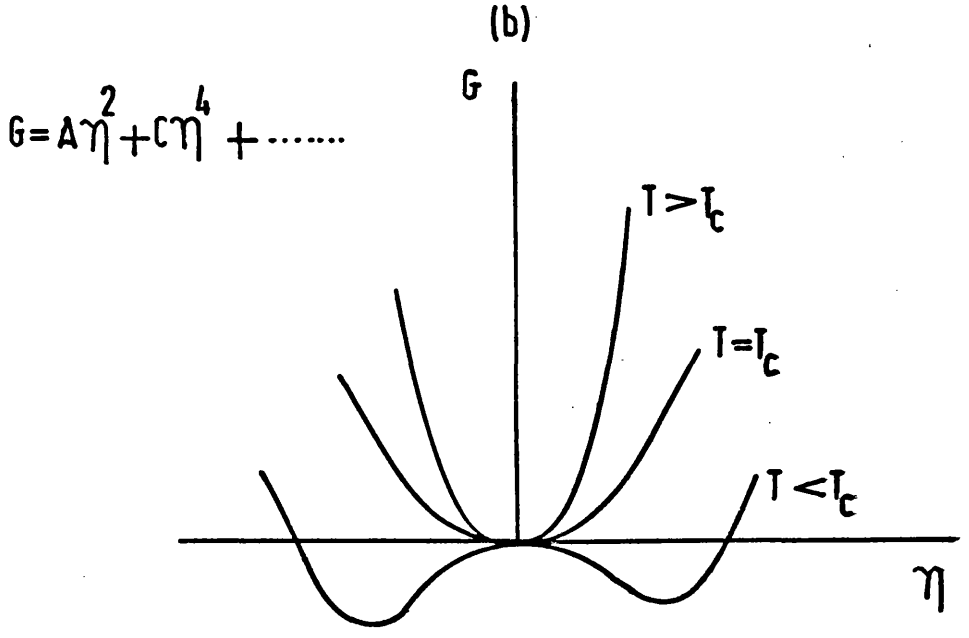

Figure 2.11: Free energy variation with the order parameter in the Landau formalism; (a) First order and (b) Second order phase transformations.

parameter η. So, to summarise, the important difference between the first and second order transformations according to the Landau formalism is in the presence or absence of the cubic invariant in the series expansion of the order parameter. Cowley (1976) and Folk, Iro and Schwabl (1976) have worked this out from a group theoretical point of view for a number of structural transformations. Their analysis will be used in discussing the order of the fcc-fct phase transformation in In-Cd alloys presented in Chapter 6.

2.7 Unique mechanical effects associated with the elastic phase transformations in Indium alloys

The fcc-fct martensitic transformation in In-Tl alloys and the fcc-fct elastic phase transformation in In-Cd alloys both possess unique mechanical properties. The most important and the best studied of these is the shape memory effect (SME). The name SME derives from the fact that after a wire or sheet of these alloys is plastically deformed at a temperature below the transformation temperature, they appear to revert back to their undeformed shape when heated to a temperature higher than the reverse transformation temperature. This rubber-like behaviour was noticed by Burkart and Read (1953) in the case of In-Tl alloys and even earlier by Olander (1932) in Au-Cd alloys. However, the understanding of the SME as a manifestation of the structural and microstructural changes associated with certain displacive phase transformations is of more recent origin. This has been reviewed by Delaey et al (1974). The origins of the SME in terms of the presence of a soft shear mode has been discussed by Nakanishi (1975). Possible application of materials possessing SME, as working 'fluids' in 'heat engines' working on a temperature-stress cycle has also been suggested (Tong and Wayman 1975).

C H A P T E R 3

ULTRASONIC WAVE PROPAGATION IN INDIUM ALLOYS

3.1 Introduction

The propagation characteristics of ultrasonic waves in In alloys having cubic, tetragonal and hexagonal symmetries will be presented in this Chapter. The ultrasonic waves in question are those typically employed in the study of solids by pulse methods (Chapter 5) and have low intensities and wavelengths of about a thousand microns. The strains encountered in the propagating media are small and classical linear elasticity theory is applicable. In addition, as the wavelengths involved are large compared to interatomic distances in the media, the wave propagation is restricted to a continuum regime. The subject of elastic wave propagation in anisotropic solids is now well documented and excellent reviews include those by Auld (1973), Landau and Lifshitz (1975), Musgrave (1970), Nye (1972), Truell, Elbaum and Chick (1969) and Wooster (1973).

3.2 Stress and strain resulting from the passage of an ultrasonic wave

When an ultrasonic wave propagates in a crystal it disturbs the particles of the medium from their equilibrium positions and the internal restoring forces are brought into play. These restoring forces together with the inertia of the particles lead to vibrations of the medium and this gives rise to elastic waves. This excitation of elastic waves in the crystal-which are nothing but time varying deformations - is tantamount to the crystal being acted upon by external forces, with each part of the crystal exerting a force on its neighbouring parts. That is to say the crystal is in a state of stress.

3.3 Tensor formalism of stress and strain

3.3.1 Stress tensor

Stresses within a vibrating medium are defined by regarding the medium to be made up of convenient volume elements with respect to an orthogonal co-ordinate system as depicted in Figure 3.1. Each face of the element is exposed to forces due to the adjoining elements. These forces are proportional to the area of the surface of the element; the force per unit is defined as the stress. Forces are specified by means of the three force components acting on each face of the element. The force per unit area acting on the elemental area facing the +x direction direction in Figure 3.1 is:

$$T_x = \hat{x}\, T_{xx} + \hat{y}\, T_{yx} + \hat{z}\, T_{zx} \qquad (3.1)$$

Similarly, the force per unit area on elemental areas facing the +y and +z directions would be:

$$T_y = \hat{x}\, T_{xy} + \hat{y}\, T_{yy} + \hat{z}\, T_{zy} \qquad (3.2)$$

and

$$T_z = \hat{x}\, T_{xz} + \hat{y}\, T_{yz} + \hat{z}\, T_{zz} \qquad (3.3)$$

The components T_{ij} (where i, j = x, y, z) are the stress components. In a vibrating medium these are always functions of spatial position. For defining the stress at the point r, therefore, the limit δx, δy, $\delta z = 0$, must be taken in order to use the equations (3.1), (3.2) and (3.3). Accordingly, $T_{ij}(r,t)$ is the i^{th} component of stress acting on the +j face of an infinitesimal volume element at position r. $T_{ij}(r,t)$ relates two vectors T_i and r_j in a linear fashion and is hence a second rank tensor. In the absence of body torques, $T_{ij} = T_{ji}$ (Nye 1972), thus the stress tensor is symmetric.

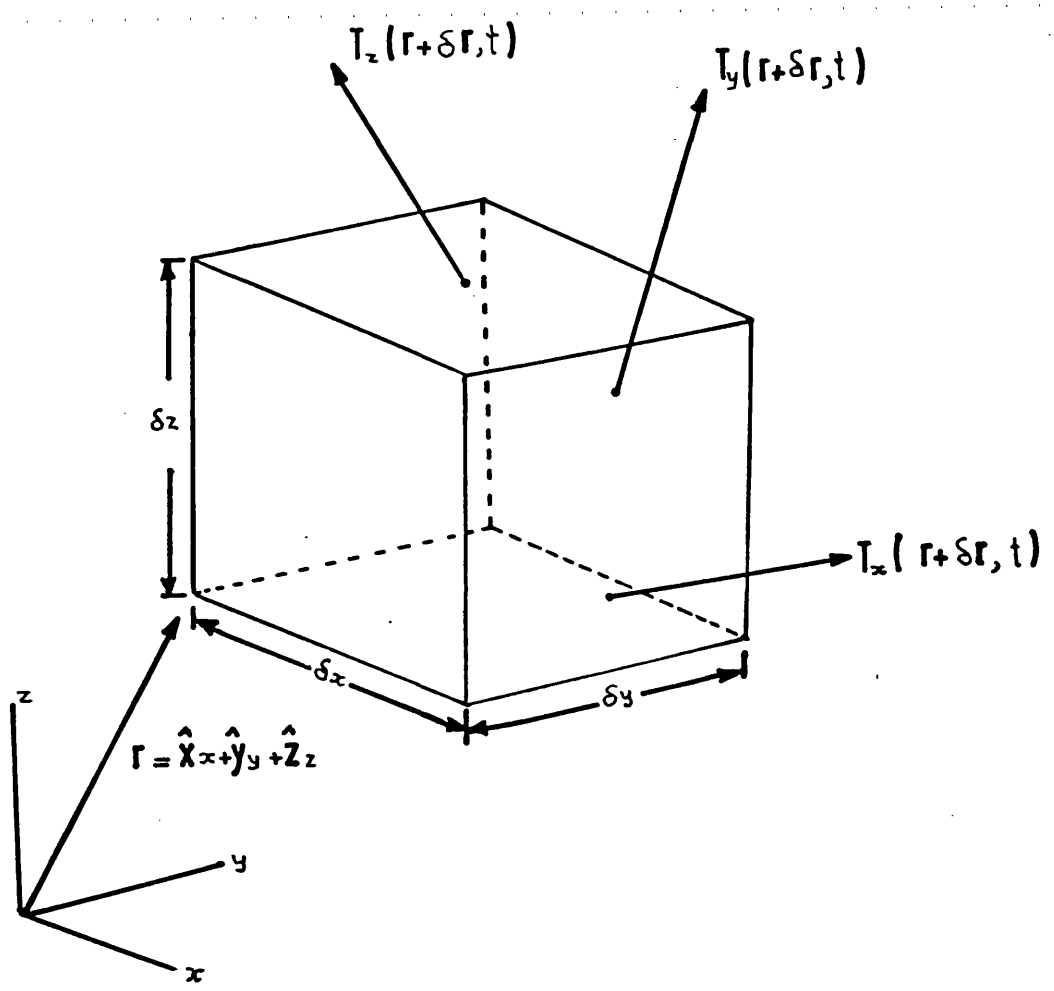

Figure 3.1: Volume element of a vibrating medium.

3.3.2 Strain tensor

Strain specifies the state of deformation of a body. The term deformation is applicable only when particles of the body are displaced relative to each other (Figure 3.2). There is no deformation when all the particles of the body maintain their relative positions as in rigid translation and rotation (Figure 3.3). With reference to Figure 3.1, the particle displacement field **u** which describes the vibrational motion of all particles within a medium can be expressed in terms of a time varying displaced position vector $\ell(L, t)$ and a reference position vector **L** as:

$$u(L, t) = \ell(L, t) - L \tag{3.4}$$

But **u** cannot be used to specify deformation because it remains non-zero for rigid motions as well. To overcome this, a scalar quantity $\Delta = d\ell(L, t) - dL$ is introduced. For rigid motions Δ is always zero while for deformation it is non-zero, as can be seen from Figures 3.2 and 3.3. Therefore Δ is a true measure of deformations. However, it is customary to define $\Delta' = d\ell^2(L, t) - (dL)^2$ as deformation, which meets the same requirements. In rectangular Cartesian co-ordinates the deformation measure Δ' is computed from $u(L, t)$, using relations:

$$d\ell_x = dL_x + du_x = dL_x + \frac{\partial u_x}{\partial L_x} dL_x + \frac{\partial u_x}{\partial L_y} dL_y + \frac{\partial u_x}{\partial L_z} dL_z \tag{3.5}$$

etc.,

This results in:

$$\Delta'(L, t) = 2\, \varepsilon_{ij}(L, t)\, dL_i\, dL_j \tag{3.6}$$

where, $$\varepsilon_{ij}(L, t) = \tfrac{1}{2}\left(\frac{\partial u_i}{\partial L_j} + \frac{\partial u_j}{\partial L_i} + \frac{\partial u_k}{\partial L_i}\,\frac{\partial u_k}{\partial L_j}\right) \tag{3.7}$$

$i, j, k = x, y, z$

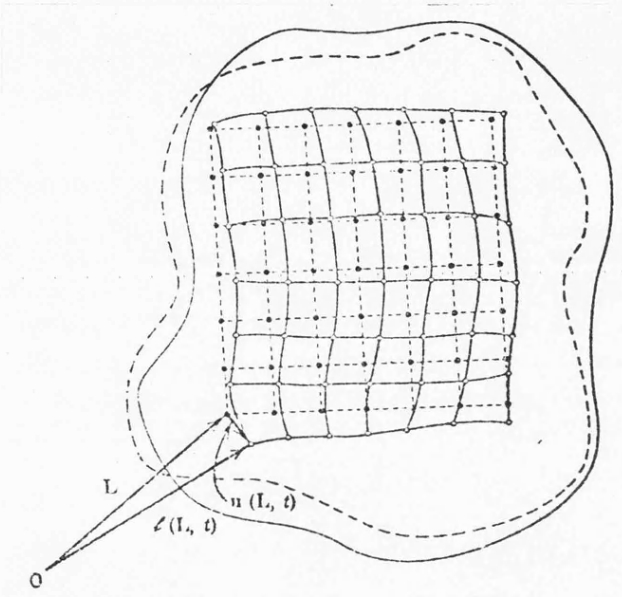

Figure 3.2: Deformation of a solid body (Auld 1973).

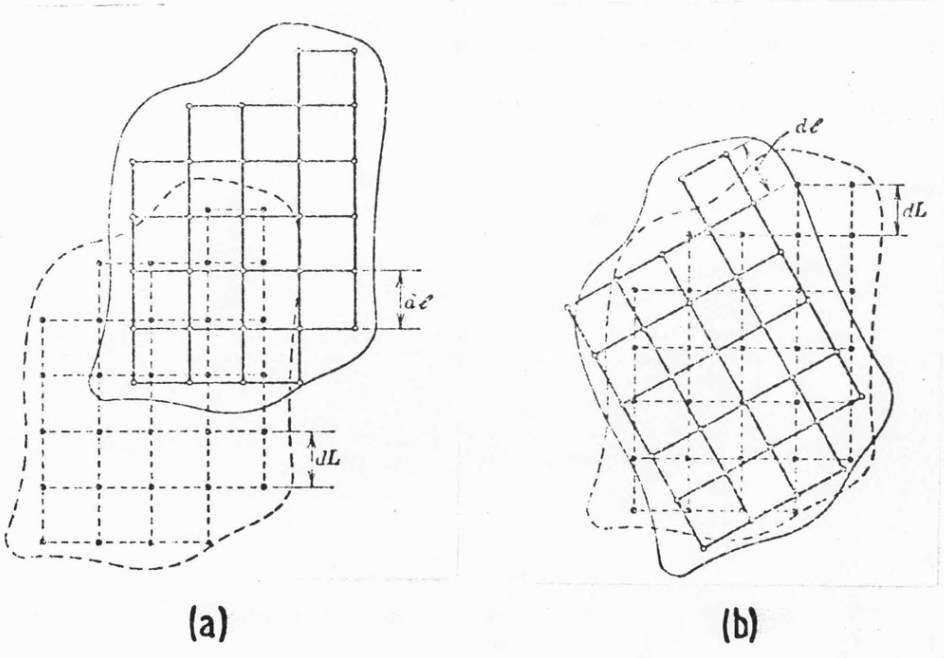

Figure 3.3: Rigid motions of a solid body (Auld 1973); (a) Translation (b) Rotation.

ε_{ij} (L, t) are termed components of the strain field. The strain field thus determines the deformation $\Delta' = (d\ell)^2 - (dL)^2$ in terms of the particle displacement field u(L, t) and reduces to zero for all rigid motions.

In the treatment based on linear elasticity theory, for small strains, the quadratic terms in equation (3.7) are very small and neglecting these terms:

$$\varepsilon_{ij}\ (\mathbf{L},\ t) \quad = \quad \tfrac{1}{2}\left(\frac{\partial u_i (\mathbf{L},\ t)}{\partial L_j} + \frac{\partial u_j (\mathbf{L},\ t)}{\partial L_i} \right) \tag{3.8}$$

$$i,j \quad = \quad x,\ y,\ x$$

Since $dL_j = d\ell_j - du_j$, the partial derivative of u_i with respect to L_j in (3.8) differs from $\frac{\partial u_i}{\partial \ell_j}$ only by quadratic and higher order terms

$$\frac{\partial u_i}{\partial L_j} \quad = \quad \frac{\partial u_i}{\partial \ell_j} \left(1 - \frac{\partial u_j}{\partial \ell_j} \right)^{-1}$$

For a linearised theory there is therefore no need to distinguish between components of the deformed position vector $\boldsymbol{\ell}$ and those of equilibrium position vector **L**. That is:

$$\mathbf{L} \quad \simeq \quad \boldsymbol{\ell} \quad = \quad \hat{x}x + \hat{y}y + \hat{z}z \quad = \quad \mathbf{r} \tag{3.9}$$

in rectangular Cartesian co-ordinates. Therefore the linearised strain-displacement relation takes the form:

$$\varepsilon_{ij}\ (\mathbf{r},t) \quad = \quad \tfrac{1}{2}\left(\frac{\partial u_i}{\partial r_j} + \frac{\partial u_j}{\partial r_i} \right) \tag{3.10}$$

$$i,j \quad = \quad x,y,z$$

ε_{ij}, again, relate two vector quantities in exact analogy with T_{ij}, and form a second rank tensor. Since a second rank tensor can always be expressed as the sum of a symmetrical and an anti-symmetrical

tensor, it is possible to treat the strain tensor as symmetrical with the anti-symmetrical tensor assigned to rotation (Nye 1972).

In conclusion it must be noted that unlike many crystal properties such as permittivity which can be represented by second rank tensors, the orientation of the stress and strain tensors within a crystal is not restricted and thus they do not represent any crystal property. Stress and strain tensors are 'field tensors'.

3.4 Stress-strain relationship for an elastic solid

It is an experimental fact that for small deformations, the strain in the deformed solid is linearly proportional to the applied stress. This is Hooke's law. As the deformations increase, the stress-strain relationship becomes more and more non-linear (Figure 3.4). However, it is the linear stress-strain relationship that is relevant here (see Section 3.1).

Hooke's law states that the strain is linearly proportional to the stress, or conversely, that the stress is linearly proportional to the strain. The latter form is stated mathematically by writing each component of stress as a general linear function of all the strain components:

$$\begin{aligned} T_{xx} = {} & C_{xxxx}\varepsilon_{xx} + C_{xxxy}\varepsilon_{xy} + C_{xxxz}\varepsilon_{xz} \\ & + C_{xxyx}\varepsilon_{yx} + C_{xxyy}\varepsilon_{yy} + C_{xxyz}\varepsilon_{yz} \\ & + C_{xxzx}\varepsilon_{zx} + C_{xxzy}\varepsilon_{zy} + C_{xxzz}\varepsilon_{zz} \end{aligned} \qquad (3.11)$$

In general,

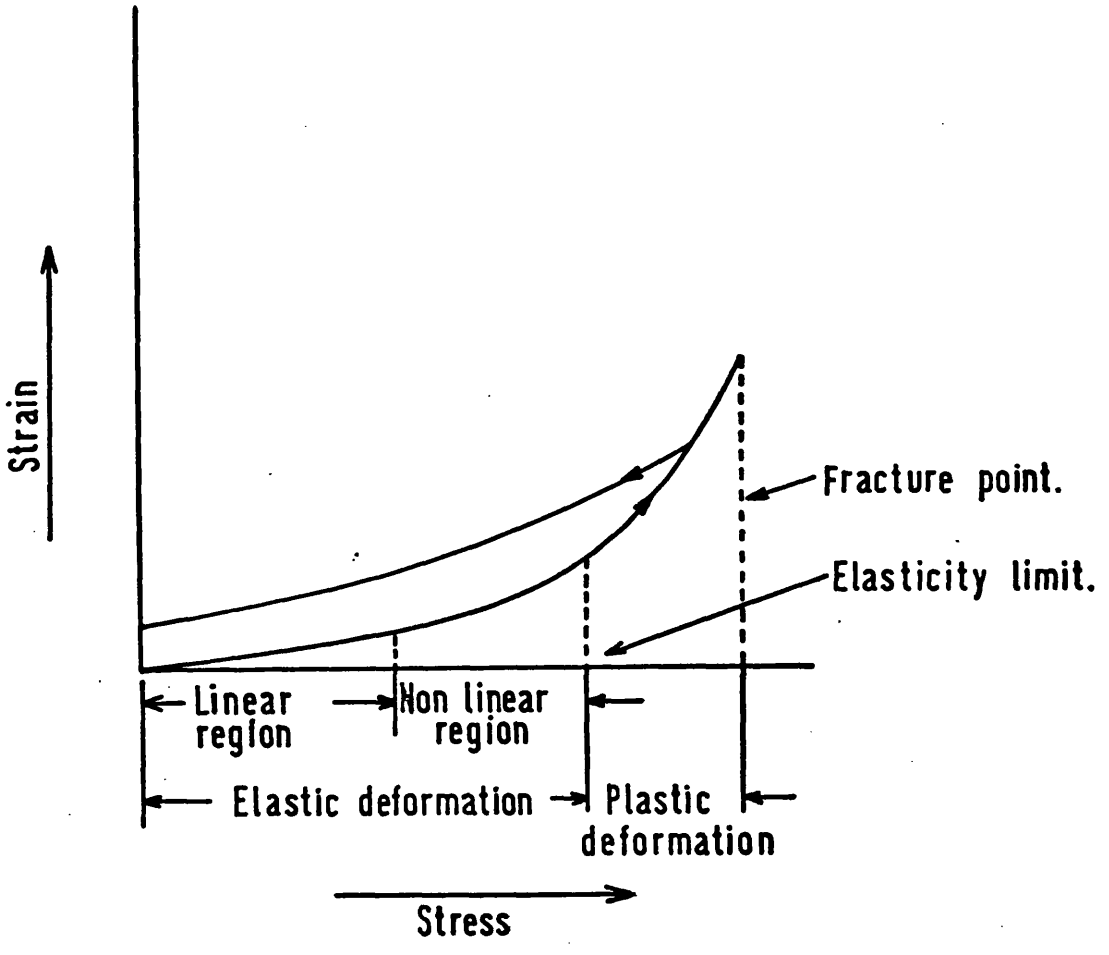

Figure 3.4: Stress-strain relationship for an elastic solid.

$$T_{ij} = C_{ijkl}\,\varepsilon_{kl} \qquad (3.12)$$
$$i,j,k,l = x,y,z$$

with the summation implied over the repeated subscripts k and l. The C_{ijkl} are called the elastic stiffness constants and have small values for easily deformed materials and large values for very rigid materials. Since (3.12) contains nine equations corresponding to all possible combinations of subscripts 'ij' and each equation contains nine strain variables, there are 81 elastic stiffness constants.

Alternatively, the strains may be expressed as a general linear function of all the stresses:

$$\varepsilon_{ij} = S_{ijkl}\,T_{kl} \qquad (3.13)$$
$$i,j,k,l = x,y,z$$

with summation over the repeated subscripts k and l. S_{ijkl} are called elastic compliance constants and are measures of deformability and have large values for easily deformed materials and small values for rigid materials. It is again evident that as with stiffness constants, there are 81 compliance constants.

Both C_{ijkl} and S_{ijkl} form fourth rank tensors since they relate two second rank tensor properties by relations of the form $P_{ij} = Q_{ijkl}\,R_{kl}$ (Nye 1972) where P_{ij} and R_{kl} are second rank tensors.

In Section 3.3 it was noted that both T_{ij} and ε_{ij} form symmetric second rank tensors with $T_{ij} = T_{ji}$ and $\varepsilon_{ij} = \varepsilon_{ji}$. Therefore terms such as $C_{xyxy}\,\varepsilon_{xy}$ and $C_{yxxy}\,\varepsilon_{xy}$ in equation (3.12)

are always equal. Therefore,

$$C_{ijkl} = C_{jikl} \tag{3.14}$$

Furthermore, since $\varepsilon_{ij} = \varepsilon_{ji}$ there is no way to distinguish experimentally between terms such as $C_{xyxy}\,\varepsilon_{xy}$ and $C_{xyyx}\,\varepsilon_{yx}$ and hence no purpose is served by the distinction between C_{ijkl} and C_{ijlk}. Thus,

$$C_{ijkl} = C_{ijlk} \tag{3.15}$$

Similar arguments can be extended to show that:

$$S_{ijkl} = S_{jikl} \tag{3.16}$$

and $$S_{ijkl} = S_{ijlk} \tag{3.17}$$

An additional tensor property:

$$C_{ijkl} = C_{klij} \tag{3.18}$$

and $$S_{ijkl} = S_{klij} \tag{3.19}$$

arises from the fact that in order that the propagating medium be elastic, the strain energy must be a function of state of the body (Nye 1972).

These constraints reduce the number of stiffness and compliance constants from 81 to 21. Also, with these constraints the four subscripts used to denote the compliance and stiffness components are redundant and only two subscripts need be used:

I	ij
1	xx
2	yy
3	zz
4	yz,zy
5	xz,zx
and 6	xy,yx

(3.20)

3.5 Effect of crystal symmetry on the elastic constants

In studying the effect of crystal symmetry on the elastic constants, it is convenient to regard the 21 elastic constants that a general anisotropic solid has as being elements of a 6 x 6 matrix. The basis for symmetry arguments is very simple; namely that if two particular directions in a medium are symmetrically equivalent, then identical stresses along these two directions must give rise to the same amount of strain. Extension of this leads to a more powerful argument: if the medium itself is symmetric with respect to a particular transformation of co-ordinates, then the stiffness and compliance matrices must themselves be unchanged by the same transformation. The point symmetry transformations are sufficient to deal with symmetry properties of compliance and stiffness constants since these constants relate stress and strain at the same point in a crystal. An elegant matrix method has been developed by Bond (1943). The Bond stress $[M]$ and strain $[N]$ transformation matrices are constructed from the general stress and strain transformation laws:

$$T'_{ij} = a_{ik}\, a_{jl}\, T_{kl} \qquad (3.21)$$

$$i,j,k,l = x,y,z$$

and $\quad \varepsilon'_{ij} = a_{ik}\, a_{jl}\, \varepsilon_{kl}$ (3.22)

respectively. Thus:

$$[M] = \left[\begin{array}{ccc|ccc} a_{xx}^2 & a_{xy}^2 & a_{xz}^2 & a_{yx}a_{zx} & a_{yy}a_{zy} & a_{yz}a_{zz} \\ a_{yx}^2 & a_{yy}^2 & a_{yz}^2 & a_{zx}a_{xx} & a_{zy}a_{xy} & a_{zz}a_{xz} \\ a_{zx}^2 & a_{zy}^2 & a_{zz}^2 & a_{xx}a_{yx} & a_{xy}a_{yy} & a_{xz}a_{yz} \\ \hline 2a_{xx}a_{xy} & 2a_{xy}a_{xz} & 2a_{xz}a_{xx} & a_{xy}a_{zz} + a_{yz}a_{zy} & a_{yx}a_{zz} + a_{yz}a_{zx} & a_{yx}a_{zy} + a_{yy}a_{zx} \\ 2a_{yx}a_{yy} & 2a_{yy}a_{yz} & 2a_{yz}a_{yx} & a_{xy}a_{zz} + a_{xz}a_{zy} & a_{xx}a_{zz} + a_{xz}a_{zx} & a_{xx}a_{zy} + a_{xy}a_{zx} \\ 2a_{zx}a_{zy} & 2a_{zy}a_{zz} & 2a_{zz}a_{zx} & a_{xy}a_{yz} + a_{xz}a_{yy} & a_{xz}a_{yx} + a_{xx}a_{yz} & a_{xx}a_{yy} + a_{xy}a_{yx} \end{array}\right] \quad (3.23)$$

and

$$[N] = \left[\begin{array}{ccc|ccc} a_{xx}^2 & a_{xy}^2 & a_{xz}^2 & a_{yx}a_{zx} & a_{yy}a_{zy} & a_{yz}a_{zz} \\ a_{yx}^2 & a_{yy}^2 & a_{yz}^2 & a_{zx}a_{xx} & a_{zy}a_{xy} & a_{zz}a_{xz} \\ a_{zx}^2 & a_{zy}^2 & a_{zz}^2 & a_{xx}a_{yx} & a_{xy}a_{yy} & a_{xz}a_{yz} \\ \hline 2a_{xx}a_{xy} & 2a_{xy}a_{xz} & 2a_{xz}a_{xx} & a_{xy}a_{zz} + a_{yz}a_{zy} & a_{yx}a_{zz} + a_{yz}a_{zx} & a_{yx}a_{zy} + a_{yy}a_{zx} \\ 2a_{yx}a_{yy} & 2a_{yy}a_{yz} & 2a_{yz}a_{yx} & a_{xy}a_{zz} + a_{xz}a_{zy} & a_{xx}a_{zz} + a_{xz}a_{zx} & a_{xx}a_{zy} + a_{xy}a_{zx} \\ 2a_{zx}a_{zy} & 2a_{zy}a_{zz} & 2a_{zz}a_{zx} & a_{xy}a_{yz} + a_{xz}a_{yy} & a_{xz}a_{yx} + a_{xx}a_{yz} & a_{xx}a_{yy} + a_{xy}a_{yx} \end{array}\right] \quad (3.24)$$

Hooke's law in matrix notation can be expressed as:

$$[T] = [C][\varepsilon] \quad (3.25)$$

Application of the Bond stress transformation matrix (3.23) to (3.25) leads to:

$$[T'] = [M][C][\varepsilon] \tag{3.26}$$

The inverse of (3.22) is

$$[\varepsilon] = [N]^{-1}[\varepsilon']$$

where $[N]$ is the Bond strain transformation matrix (3.24) and substitution for $[\varepsilon]$ in (3.26) gives

$$[T'] = [M][C][N]^{-1}[\varepsilon']$$

Comparison with (3.25) now shows that the transformed stiffness matrix is simply

$$[C'] = [M][C][N]^{-1} \tag{3.27}$$

Similarly it follows that

$$[S'] = [N][S][M]^{-1} \tag{3.28}$$

from the compliance formalism of Hooke's law.

The most general anisotropic crystal belongs to the triclinic system with point groups 1 and $\bar{1}$. These crystals have all the 21 stiffness and compliance constants:

$$[C] = \begin{bmatrix} C_{11} & C_{12} & C_{13} & C_{14} & C_{15} & C_{16} \\ C_{12} & C_{22} & C_{23} & C_{24} & C_{25} & C_{26} \\ C_{13} & C_{23} & C_{33} & C_{34} & C_{35} & C_{36} \\ C_{14} & C_{24} & C_{34} & C_{44} & C_{45} & C_{46} \\ C_{15} & C_{25} & C_{35} & C_{45} & C_{55} & C_{56} \\ C_{16} & C_{26} & C_{36} & C_{46} & C_{56} & C_{66} \end{bmatrix} \tag{3.29}$$

$$[S] = \begin{bmatrix} S_{11} & S_{12} & S_{13} & S_{14} & S_{15} & S_{16} \\ S_{12} & S_{22} & S_{23} & S_{24} & S_{25} & S_{26} \\ S_{13} & S_{23} & S_{33} & S_{34} & S_{35} & S_{36} \\ S_{14} & S_{24} & S_{34} & S_{44} & S_{45} & S_{46} \\ S_{15} & S_{25} & S_{35} & S_{45} & S_{55} & S_{56} \\ S_{16} & S_{26} & S_{36} & S_{46} & S_{56} & S_{66} \end{bmatrix} \qquad (3.30)$$

In equations (3.27) and (3.28),

$$[C'] = [C] \qquad (3.31)$$

and $$[S'] = [S]$$

if the transformation co-ordinate is a symmetry operation. The effect of the higher symmetries of tetragonal, cubic and hexagonal crystals on the elements of the general elastic constant matrices (3.29) and (3.30) can hence be studied by appropriate symmetry-based co-ordinate transformations.

3.5.1 Tetragonal crystals

Indium and its tetragonal alloys with Cd, Tl and Pb, point group 4/mmm, belong to the TI Laue group to which the foregoing treatment will now be restricted to. There is another class of tetragonal crystals belonging to the TII Laue group; these have an additional element in the elastic constant matrix. Calcium tungstate, for example, belongs to this category and has been discussed by Farley and Saunders (1972).

Point group : 4/mmm

Generator matrices $[a_{ij}]$:

$$4 \rightarrow \begin{bmatrix} 0 & 1 & 0 \\ -1 & 0 & 0 \\ 0 & 0 & 1 \end{bmatrix} \tag{3.32}$$

$$m \rightarrow \begin{bmatrix} 1 & 0 & 0 \\ 0 & 1 & 0 \\ 0 & 0 & -1 \end{bmatrix} \tag{3.33}$$

and

$$m \rightarrow \begin{bmatrix} 1 & 0 & 0 \\ 0 & -1 & 0 \\ 0 & 0 & 1 \end{bmatrix} \tag{3.34}$$

The Bond stress and strain transformation matrices $[M]$ and $[N]$ from (3.23) and (3.24) respectively for the generator matrix (3.32) would be:

$$[M^{(4)}] = [N^{(4)}] = \left[\begin{array}{ccc:ccc} 0 & 1 & 0 & 0 & 0 & 0 \\ 1 & 0 & 0 & 0 & 0 & 0 \\ 0 & 0 & 1 & 0 & 0 & 0 \\ \hdashline 0 & 0 & 0 & 0 & -1 & 0 \\ 0 & 0 & 0 & 1 & 0 & 0 \\ 0 & 0 & 0 & 0 & 0 & -1 \end{array}\right] \tag{3.35}$$

with,

$$a_{xx} = 0, \quad a_{xy} = 1, \quad a_{xz} = 0$$

$$a_{yx} = -1, \quad a_{yy} = 0, \quad a_{yz} = 0$$

and

$$a_{zx} = 0, \quad a_{zy} = 0, \quad a_{zz} = 1$$

Because $[M^{(4)}]$ and $[N^{(4)}]$ are symmetry based transformations, it follows that:

$$[C][N^{(4)}] = [M^{(4)}][C] \tag{3.36}$$

and

$$[S][M^{(4)}] = [N^{(4)}][S] \tag{3.37}$$

where $[C]$ and $[S]$ are given by (3.29) and (3.30) respectively.

Using the $[C]$ value of (3.29) in (3.36) leads to:

$$\left[\begin{array}{ccc:ccc} C_{11} & C_{12} & C_{13} & C_{14} & C_{15} & C_{16} \\ C_{12} & C_{22} & C_{23} & C_{24} & C_{25} & C_{26} \\ C_{13} & C_{23} & C_{33} & C_{34} & C_{35} & C_{36} \\ \hdashline C_{14} & C_{24} & C_{34} & C_{44} & C_{45} & C_{46} \\ C_{15} & C_{25} & C_{35} & C_{45} & C_{55} & C_{56} \\ C_{16} & C_{26} & C_{36} & C_{46} & C_{56} & C_{66} \end{array}\right] \left[\begin{array}{ccc:ccc} 0 & 1 & 0 & 0 & 0 & 0 \\ 1 & 0 & 0 & 0 & 0 & 0 \\ 0 & 0 & 1 & 0 & 0 & 0 \\ \hdashline 0 & 0 & 0 & 0 & -1 & 0 \\ 0 & 0 & 0 & 1 & 0 & 0 \\ 0 & 0 & 0 & 0 & 0 & -1 \end{array}\right] =$$

$$\left[\begin{array}{ccc:ccc} 0 & 1 & 0 & 0 & 0 & 0 \\ 1 & 0 & 0 & 0 & 0 & 0 \\ 0 & 0 & 1 & 0 & 0 & 0 \\ \hdashline 0 & 0 & 0 & 0 & -1 & 0 \\ 0 & 0 & 0 & 1 & 0 & 0 \\ 0 & 0 & 0 & 0 & 0 & -1 \end{array}\right] \left[\begin{array}{ccc:ccc} C_{11} & C_{12} & C_{13} & C_{14} & C_{15} & C_{16} \\ C_{12} & C_{22} & C_{23} & C_{24} & C_{25} & C_{26} \\ C_{13} & C_{23} & C_{33} & C_{34} & C_{35} & C_{36} \\ \hdashline C_{14} & C_{24} & C_{34} & C_{44} & C_{45} & C_{46} \\ C_{15} & C_{25} & C_{35} & C_{45} & C_{55} & C_{56} \\ C_{16} & C_{26} & C_{36} & C_{46} & C_{56} & C_{66} \end{array}\right] \tag{3.38}$$

When the matrix multiplications are carried out according to:

$$\left[\begin{array}{c:c} A & B \\ \hdashline C & D \end{array}\right] \left[\begin{array}{c:c} E & F \\ \hdashline G & H \end{array}\right] = \left[\begin{array}{cc} [A][E] + [B][G] & [A][F] + [B][H] \\ [C][E] + [D][G] & [C][F] + [D][H] \end{array}\right] \tag{3.39}$$

(3.38) reduces to:

$$\left[\begin{array}{cccccc} C_{12} & C_{11} & C_{13} & C_{15} & -C_{14} & -C_{16} \\ C_{22} & C_{12} & C_{23} & C_{25} & -C_{24} & -C_{26} \\ C_{23} & C_{13} & C_{33} & C_{35} & -C_{34} & -C_{36} \\ C_{24} & C_{14} & C_{34} & C_{45} & -C_{44} & -C_{46} \\ C_{25} & C_{15} & C_{35} & C_{55} & -C_{45} & -C_{56} \\ C_{26} & C_{16} & C_{36} & C_{56} & -C_{46} & -C_{66} \end{array}\right] = \left[\begin{array}{cccccc} C_{12} & C_{22} & C_{23} & C_{24} & C_{25} & C_{26} \\ C_{11} & C_{12} & C_{13} & C_{14} & C_{15} & C_{16} \\ C_{13} & C_{23} & C_{33} & C_{34} & C_{35} & C_{36} \\ -C_{15} & -C_{25} & -C_{35} & -C_{45} & -C_{55} & -C_{56} \\ C_{14} & C_{24} & C_{34} & C_{44} & C_{45} & C_{46} \\ -C_{16} & -C_{26} & -C_{36} & -C_{46} & -C_{56} & -C_{66} \end{array}\right] \tag{3.40}$$

Comparison, element by element of (3.40) gives:

$$C_{11} = C_{22} \qquad C_{33} \text{ - no condition}$$

$$C_{13} = C_{23} \qquad C_{66} \text{ - no condition}$$

$$C_{44} = C_{55} \qquad C_{12} \text{ - no condition}$$

$$C_{16} = -C_{26}$$

and $C_{15} = C_{14} = C_{25} = C_{24} = C_{35} = C_{34} = C_{36} = C_{45} = C_{46} = C_{56} = 0$

from conditions such as $C_{14} = -C_{25}$, $C_{25} = C_{14}$ (3.41)

The Bond transformation for generator matrix (3.33) leads to the same restrictions as found in (3.41), but with the generator matrix (3.34), an additional set of restrictions can be found:

$$m \rightarrow \begin{bmatrix} 1 & 0 & 0 \\ 0 & -1 & 0 \\ 0 & 0 & 1 \end{bmatrix} \tag{3.34}$$

$$[M^{(m)}] = [N^{(m)}] = \left[\begin{array}{ccc:ccc} 1 & 0 & 0 & 0 & 0 & 0 \\ 0 & 1 & 0 & 0 & 0 & 0 \\ 0 & 0 & 1 & 0 & 0 & 0 \\ \hdashline 0 & 0 & 0 & -1 & 0 & 0 \\ 0 & 0 & 0 & 0 & 1 & 0 \\ 0 & 0 & 0 & 0 & 0 & -1 \end{array}\right] \tag{3.42}$$

and equating $[C][N^{(m)}] = [M^{(m)}][C]$ (3.43)

gives

$$\begin{bmatrix} C_{11} & C_{12} & C_{13} & -C_{14} & C_{15} & -C_{16} \\ C_{12} & C_{22} & C_{23} & -C_{24} & C_{25} & -C_{26} \\ C_{13} & C_{23} & C_{33} & -C_{34} & C_{35} & -C_{36} \\ C_{14} & C_{24} & C_{34} & -C_{44} & C_{45} & -C_{46} \\ C_{15} & C_{25} & C_{35} & -C_{45} & C_{55} & -C_{56} \\ C_{16} & C_{26} & C_{36} & -C_{46} & C_{56} & -C_{66} \end{bmatrix} = \begin{bmatrix} C_{11} & C_{12} & C_{13} & C_{14} & C_{15} & C_{16} \\ C_{12} & C_{22} & C_{23} & C_{24} & C_{25} & C_{26} \\ C_{13} & C_{23} & C_{33} & C_{34} & C_{35} & C_{36} \\ -C_{14} & -C_{24} & -C_{34} & -C_{44} & -C_{45} & -C_{46} \\ C_{15} & C_{25} & C_{35} & C_{45} & C_{55} & C_{56} \\ -C_{16} & -C_{26} & -C_{36} & -C_{46} & -C_{56} & -C_{66} \end{bmatrix} \tag{3.44}$$

The additional set of restrictions imposed by the above relation (3.44) are:

$$C_{16} = -C_{16} \text{ and } C_{26} = -C_{26} \tag{3.45}$$

i.e., $$C_{16} = C_{26} = 0 \tag{3.46}$$

The restrictions of (3.41) and (3.46) mean that for tetragonal (TI) crystals the general stiffness matrix (3.29) takes the form:

$$\begin{bmatrix} C_{11} & C_{12} & C_{13} & 0 & 0 & 0 \\ C_{12} & C_{11} & C_{13} & 0 & 0 & 0 \\ C_{13} & C_{13} & C_{33} & 0 & 0 & 0 \\ 0 & 0 & 0 & C_{44} & 0 & 0 \\ 0 & 0 & 0 & 0 & C_{44} & 0 \\ 0 & 0 & 0 & 0 & 0 & C_{66} \end{bmatrix} \tag{3.47}$$

A similar procedure, starting with the general compliance matrix (3.30) leads to an identical form for the compliance matrix of tetragonal (TI) crystals:

$$\begin{bmatrix} S_{11} & S_{12} & S_{13} & 0 & 0 & 0 \\ S_{12} & S_{11} & S_{13} & 0 & 0 & 0 \\ S_{13} & S_{13} & S_{33} & 0 & 0 & 0 \\ 0 & 0 & 0 & S_{44} & 0 & 0 \\ 0 & 0 & 0 & 0 & S_{44} & 0 \\ 0 & 0 & 0 & 0 & 0 & S_{66} \end{bmatrix} \tag{3.48}$$

3.5.2 Cubic crystals

Cubic crystals of all the classes have the same elastic constant matrix. Consider the case of fcc In alloys encountered in the present study:

Point group : m3m

Generator matrices $[a_{ij}]$:

$$4 \rightarrow \begin{bmatrix} 0 & 1 & 0 \\ -1 & 0 & 0 \\ 0 & 0 & 1 \end{bmatrix}$$

$$2 \rightarrow \begin{bmatrix} -1 & 0 & 0 \\ 0 & 0 & 1 \\ 0 & 1 & 0 \end{bmatrix}$$

and

$$m \rightarrow \begin{bmatrix} 1 & 0 & 0 \\ 0 & 1 & 0 \\ 0 & 0 & -1 \end{bmatrix} \qquad (3.49)$$

Carrying out the Bond transformation based on these generator matrices in exactly the same manner as was done for the tetragonal case leads to the stiffness and compliance matrices for the cubic crystals as:

$$\begin{bmatrix} C_{11} & C_{12} & C_{12} & 0 & 0 & 0 \\ C_{12} & C_{11} & C_{12} & 0 & 0 & 0 \\ C_{12} & C_{12} & C_{11} & 0 & 0 & 0 \\ 0 & 0 & 0 & C_{44} & 0 & 0 \\ 0 & 0 & 0 & 0 & C_{44} & 0 \\ 0 & 0 & 0 & 0 & 0 & C_{44} \end{bmatrix} \qquad (3.50)$$

and

$$\begin{bmatrix} S_{11} & S_{12} & S_{12} & 0 & 0 & 0 \\ S_{12} & S_{11} & S_{12} & 0 & 0 & 0 \\ S_{12} & S_{12} & S_{11} & 0 & 0 & 0 \\ 0 & 0 & 0 & S_{44} & 0 & 0 \\ 0 & 0 & 0 & 0 & S_{44} & 0 \\ 0 & 0 & 0 & 0 & 0 & S_{44} \end{bmatrix} \qquad (3.51)$$

respectively.

3.5.3 Hexagonal Crystals

The hexagonal form of Tl and Tl-rich alloys with In have:

Point group : 6/mmm

Generator matrices $[a_{ij}]$:

$$6 \rightarrow \begin{bmatrix} \frac{1}{2} & \frac{\sqrt{3}}{2} & 0 \\ -\frac{\sqrt{3}}{2} & \frac{1}{2} & 0 \\ 0 & 0 & 1 \end{bmatrix}$$

$$m \rightarrow \begin{bmatrix} 1 & 0 & 0 \\ 0 & 1 & 0 \\ 0 & 0 & -1 \end{bmatrix}$$

and

$$m \rightarrow \begin{bmatrix} 1 & 0 & 0 \\ 0 & -1 & 0 \\ 0 & 0 & 1 \end{bmatrix} \qquad (3.52)$$

Bond transformation with these generator matrices results in the stiffness and compliance matrices respectively as:

$$\begin{bmatrix} C_{11} & C_{12} & C_{13} & 0 & 0 & 0 \\ C_{12} & C_{11} & C_{13} & 0 & 0 & 0 \\ C_{13} & C_{13} & C_{33} & 0 & 0 & 0 \\ 0 & 0 & 0 & C_{44} & 0 & 0 \\ 0 & 0 & 0 & 0 & C_{44} & 0 \\ 0 & 0 & 0 & 0 & 0 & \tfrac{1}{2}(C_{11} - C_{12}) \end{bmatrix} \qquad (3.53)$$

with $C_{66} = \tfrac{1}{2}(C_{11} - C_{12})$

and

$$\begin{bmatrix} S_{11} & S_{12} & S_{13} & 0 & 0 & 0 \\ S_{12} & S_{11} & S_{13} & 0 & 0 & 0 \\ S_{13} & S_{13} & S_{33} & 0 & 0 & 0 \\ 0 & 0 & 0 & S_{44} & 0 & 0 \\ 0 & 0 & 0 & 0 & S_{44} & 0 \\ 0 & 0 & 0 & 0 & 0 & 2(S_{11} - S_{12}) \end{bmatrix} \qquad (3.54)$$

The relationships between stiffness and compliance constants (Schmid and Boas 1968) for tetragonal, cubic and hexagonal crystals are collected in Table 3.1.

3.6 Elastic wave propagation and the Christoffel equation

The first step in obtaining the components of elastic constant matrices of a crystal from ultrasonic wave propagation studies is to establish the general equation governing the wave propagation in an elastic medium.

Consider the motion of a volume element (as in Figure 3.1) in the medium. Let ρ denote the density of the medium. Using Newton's second law of motion, in the absence of body forces and

Table 3.1

Relationships between stiffness and compliance constants

Tetragonal crystals (TI Laue group)

$(C_{11} + C_{12}) = S_{33}/S$, $(C_{11} - C_{12}) = 1/(S_{11} - S_{12})$

$C_{13} = -S_{13}/S$, $C_{33} = (S_{11} + S_{12})/S$, $C_{44} = 1/S_{44}$, $C_{66} = 1/S_{66}$

where $S = S_{33}(S_{11} + S_{12}) - 2S_{13}^2$

Cubic crystals

$$C_{11} = (S_{11} + S_{12})/(S_{11} - S_{12})(S_{11} + 2S_{12})$$

$$C_{12} = -S_{12}/(S_{11} - S_{12})(S_{11} + 2S_{12})$$

$$C_{44} = 1/S_{44}$$

Hexagonal crystals

$(C_{11} + C_{12}) = S_{33}/S$, $(C_{11} - C_{12}) = 1/(S_{11} - S_{12})$

$C_{13} = -S_{13}/S$, $C_{33} = (S_{11} + S_{12})/S$, $C_{44} = 1/S_{44}$

where $S = S_{33}(S_{11} + S_{12}) - 2S_{13}^2$

torques, the net force acting on the volume element can be equated to the acceleration components:

$$\frac{\partial T_{ij}}{\partial r_j} = \rho \left(\frac{\partial^2 u_i}{\partial t^2} \right) \quad i, j = x, y, z \tag{3.55}$$

or

$$\nabla . \mathbf{T} = \rho \left(\frac{\partial \mathbf{v}}{\partial t} \right) \tag{3.56}$$

where $\mathbf{v} = \frac{\partial \mathbf{u}}{\partial t}$ is the particle velocity field (3.57)

and

$$\nabla . \rightarrow \begin{bmatrix} \frac{\partial}{\partial x} & 0 & 0 & 0 & \frac{\partial}{\partial z} & \frac{\partial}{\partial y} \\ 0 & \frac{\partial}{\partial y} & 0 & \frac{\partial}{\partial z} & 0 & \frac{\partial}{\partial x} \\ 0 & 0 & \frac{\partial}{\partial z} & \frac{\partial}{\partial y} & \frac{\partial}{\partial x} & 0 \end{bmatrix} \tag{3.58}$$

Strain and hence stress is related to the particle displacement field $\mathbf{u}$:

$$\boldsymbol{\varepsilon} = \nabla_s \mathbf{u} \tag{3.59}$$

i.e., $$\nabla_s \mathbf{v} = \frac{\partial \boldsymbol{\varepsilon}}{\partial t} \tag{3.60}$$

Hooke's law of (3.13) with 'double dot' notation can be written as

$$\boldsymbol{\varepsilon} = \mathbf{S} : \mathbf{T} \tag{3.61}$$

Using the above value of ε (3.61) in (3.60) gives:

$$\nabla_s \mathbf{v} = \mathbf{S} : \frac{\partial \mathbf{T}}{\partial t} \tag{3.62}$$

where,

$$\nabla_s \rightarrow \begin{bmatrix} \frac{\partial}{\partial x} & 0 & 0 \\ 0 & \frac{\partial}{\partial y} & 0 \\ 0 & 0 & \frac{\partial}{\partial z} \\ 0 & \frac{\partial}{\partial z} & \frac{\partial}{\partial y} \\ \frac{\partial}{\partial z} & 0 & \frac{\partial}{\partial x} \\ \frac{\partial}{\partial y} & \frac{\partial}{\partial x} & 0 \end{bmatrix} \tag{3.63}$$

Differentiation of (3.56) with respect to t yields:

$$\nabla . \quad \frac{\partial T}{\partial t} = \rho \left(\frac{\partial^2 v}{\partial t^2} \right) \tag{3.64}$$

Multiplication of (3.62) by the stiffness constant gives

$$\mathbf{C} : \nabla_s v = \frac{\partial T}{\partial t} \tag{3.65}$$

Substituting this value for $\frac{\partial T}{\partial t}$ (3.65) in (3.64) results in:

$$\nabla . \mathbf{C} : \nabla_s v = \rho \left(\frac{\partial^2 v}{\partial t^2} \right) \tag{3.66}$$

which is the equation governing the elastic wave propagation. In matrix form with abbreviated subscripts the wave equation of (3.66) will be

$$\nabla_{iK} \; C_{KL} \; \nabla_{Lj} \; v_j = \rho \left(\frac{\partial^2 v_i}{\partial t^2} \right) \tag{3.67}$$

where $\nabla_{iK} = \nabla .$ and $\nabla_{Lj} = \nabla_s$ have already been defined.

The ultrasonic waves introduced into crystals in pulse echo techniques (Chapter 5) are essentially bulk, uniform plane waves and the solutions of the wave equation (3.67) will be restricted to this case.

A uniform plane wave propagating with a wave vector $\mathbf{k}$ defined by the unit vector:

$$\mathbf{l} = \hat{x} l_x + \hat{y} l_y + \hat{z} l_z \tag{3.68}$$

where $l_x = \frac{k_x}{k}$, $l_y = \frac{k_y}{k}$ and $l_z = \frac{k_z}{k}$ (3.69)

are the direction cosines of the propagation direction, has its particle displacement fields proportional to

$$e^{i(\omega t - k\mathbf{l}.\mathbf{r})} \tag{3.70}$$

where ω is the angular frequency: $\left(\frac{\omega}{v}\right) = k$ (3.71)

Under these circumstances the operators ∇_{iK} and ∇_{Lj} in (3.67) can be replaced by matrices:

$$-ik \begin{bmatrix} l_x & 0 & 0 & 0 & l_z & l_y \\ 0 & l_y & 0 & l_z & 0 & l_x \\ 0 & 0 & l_z & l_y & l_x & 0 \end{bmatrix} \tag{3.72}$$

and

$$-ik \begin{bmatrix} l_x & & 0 & & 0 \\ 0 & & l_y & & 0 \\ 0 & & 0 & & l_z \\ 0 & & l_z & & l_y \\ l_z & & 0 & & l_x \\ l_y & & l_x & & 0 \end{bmatrix} \tag{3.73}$$

respectively.

The wave equation (3.67) then becomes:

$$k^2 \Gamma_{ij} v_j = \rho \omega^2 v_i \tag{3.74}$$

This is the celebrated Christoffel equation. Γ_{ij} form a matrix called the Christoffel matrix and its elements are functions only of the

plane wave propagation direction and the elastic constants of the medium.

The Christoffel matrix is diagonally symmetric and when expanded gives a cubic expression involving powers up to the third of ρv^2. Since this matrix is in real cases equal to zero, there are three roots of the equation which correspond to ρv^2 for any particular crystallographic direction. Out of these three solutions, two usually bear similarity to transverse waves with particle displacements normal to the direction of propagation and the other to a longitudinal or compressional wave with particle displacement along the direction of propagation.

3.7 Christoffel equation solutions for ultrasonic wave propagation in In alloys

The ultrasonic wave propagation along high symmetry, low index directions in In alloys will now be studied and the solutions of the Christoffel equation will be worked out to yield all the elements of the stiffness matrices established in (3.47), (3.50) and (3.53).

Substitution of the general stiffness matrix (3.29) of the triclinic crystals in (3.74) will result in the Christoffel equation for a general anisotropic solid in the form:

$$k^2 \begin{bmatrix} \Gamma_{11} & \Gamma_{12} & \Gamma_{13} \\ \Gamma_{12} & \Gamma_{22} & \Gamma_{23} \\ \Gamma_{13} & \Gamma_{23} & \Gamma_{33} \end{bmatrix} \begin{bmatrix} v_x \\ v_y \\ v_z \end{bmatrix} = \rho\omega^2 \begin{bmatrix} v_x \\ v_y \\ v_z \end{bmatrix} \qquad (3.75)$$

where,

$$\Gamma_{11} = C_{11}l_x^2 + C_{66}l_y^2 + C_{55}l_z^2 + 2C_{56}l_yl_z + 2C_{15}l_zl_x + 2C_{16}l_xl_y$$

$$\Gamma_{22} = C_{66}l_x^2 + C_{22}l_y^2 + C_{44}l_z^2 + 2C_{24}l_yl_z + 2C_{46}l_zl_x + 2C_{26}l_xl_y$$

$$\Gamma_{33} = C_{55}l_x^2 + C_{44}l_y^2 + C_{33}l_z^2 + 2C_{34}l_yl_z + 2C_{35}l_zl_x + 2C_{45}l_xl_y$$

$$\Gamma_{12} = C_{16}l_x^2 + C_{26}l_y^2 + C_{45}l_z^2 + (C_{46} + C_{25})l_yl_z + (C_{14} + C_{56})l_zl_x + (C_{12} + C_{66})l_xl_y$$

$$\Gamma_{13} = C_{15}l_x^2 + C_{46}l_y^2 + C_{35}l_z^2 + (C_{45} + C_{36})l_yl_z + (C_{13} + C_{55})l_zl_x + (C_{14} + C_{56})l_xl_y$$

and

$$\Gamma_{23} = C_{56}l_x^2 + C_{24}l_y^2 + C_{34}l_z^2 + (C_{44} + C_{23})l_yl_z + (C_{36} + C_{45})l_zl_x + (C_{25} + C_{46})l_xl_y \quad (3.76)$$

and $l_x = \frac{k_x}{k}$, $l_y = \frac{k_y}{k}$, and $l_z = \frac{k_z}{k}$ are the direction cosines of the ultrasonic wave propagation direction.

3.7.1 Tetragonal (TI Laue group) alloys

After the stiffness constraints of (3.41) and (3.46) are substituted in (3.76), the Christoffel equation for the tetragonal case becomes:

$$\begin{bmatrix} (C_{11}l_x^2+C_{66}l_y^2+C_{44}l_z^2) & (C_{12}+C_{66})l_xl_y & (C_{13}+C_{44})l_xl_z \\ (C_{12}+C_{66})l_xl_y & (C_{66}l_x^2+C_{11}l_y^2+C_{44}l_z^2) & (C_{13}+C_{44})l_yl_z \\ (C_{13}+C_{44})l_xl_z & (C_{13}+C_{44})l_yl_z & (C_{44}l_x^2+C_{44}l_y^2+C_{33}l_z^2) \end{bmatrix} = [\Gamma_{ij}]$$

$$k^2[\Gamma_{ij}] \begin{bmatrix} v_x \\ v_y \\ v_z \end{bmatrix} = \rho\omega^2 \begin{bmatrix} v_x \\ v_y \\ v_z \end{bmatrix} \qquad (3.77)$$

Solutions of (3.77) for high symmetry directions yielding all the elements of the stiffness matrix are presented in Table 3.2.

3.7.2 Cubic alloys

The stiffness constraints of cubic crystals are contained in the results of Section 3.5.2. When these constraints are used in (3.76) the Christoffel equation becomes:

$$\begin{bmatrix} C_{11}l_x+C_{44}(1-l_x^2) & (C_{12}+C_{44})l_xl_y & (C_{12}+C_{44})l_xl_z \\ (C_{12}+C_{44})l_xl_y & C_{11}l_y^2+C_{44}(1-l_y^2) & (C_{14}+C_{44})l_yl_z \\ (C_{12}+C_{44})l_xl_z & (C_{12}+C_{44})l_yl_z & C_{11}l_z^2+C_{44}(1-l_z^2) \end{bmatrix} = [\Gamma_{ij}]$$

$$k^2[\Gamma_{ij}] \begin{bmatrix} v_x \\ v_y \\ v_z \end{bmatrix} = \rho\omega^2 \begin{bmatrix} v_x \\ v_y \\ v_z \end{bmatrix} \qquad (3.78)$$

Solutions of (3.78) for ultrasonic wave propagation along appropriate crystallographic directions are collected in Table 3.3.

Table 3.2

Solutions of the Christoffel equation for tetragonal crystals of TI Laue group

Propagation direction	Particle displacement direction	Christoffel equation solutions ρv^2, in terms of the elements of the stiffness matrix
[100]	[100]	C_{11}
[100]	[010]	C_{66}
[100]	[001]	C_{44}
[001]	[001]	C_{33}
[001]	in (001) plane	C_{44}
[110]	[110]	$\frac{1}{2}(C_{11} + C_{12} + 2C_{66})$
[110]	$[1\bar{1}0]$	$\frac{1}{2}(C_{11} - C_{12})$
[110]	[001]	C_{44}
[011]	[100]	$\frac{1}{2}(C_{44} + C_{66})$
[011]	ϕ	$\frac{1}{2}(A+\{A^2 - B + C^2\}^{\frac{1}{2}})$
[011]	$\phi + \frac{\pi}{2}$	$\frac{1}{2}(A-\{A^2 - B + C^2\}^{\frac{1}{2}})$

ϕ is an angle which depends upon the values of the elastic stiffness matrix elements and is measured from [001] in the (100) plane.

$A = C_{44} + \frac{1}{2}(C_{11} + C_{33})$, $B = (C_{11} + C_{44})(C_{33} + C_{44})$ and $C = C_{13} + C_{44}$

Table 3.3

Solutions of the Christoffel equation for cubic crystals

Propagation direction	Particle displacement direction	Christoffel equation solutions ρv^2, in terms of the elements of the stiffness matrix
[100]	[100]	C_{11}
[100]	in (100) plane	C_{44}
[110]	[110]	$\frac{1}{2}(C_{11} + C_{12} + 2C_{44})$
[110]	[001]	C_{44}
[110]	$[1\bar{1}0]$	$\frac{1}{2}(C_{11} - C_{12})$
[111]	[111]	$\frac{1}{3}(C_{11} + 2C_{12} + 4C_{44})$
[111]	in (111) plane	$\frac{1}{3}(C_{11} - C_{12} + C_{44})$

3.7.3 Hexagonal alloys

The Christoffel equation - starting with the results of Section 3.5.3 - is the same as for the tetragonal case (3.77) except that for the hexagonal crystals C_{66} is not arbitrary but is related to C_{11} and C_{12}:

$$C_{66} = \tfrac{1}{2}(C_{11} - C_{12}) \qquad (3.79)$$

Solutions of the Christoffel equation are given in Table 3.4.

3.8 Significance of the choice of ultrasonic wave propagation directions

The solutions of Christoffel equations given in Tables 3.2, 3.3 and 3.4 have been obtained for ultrasonic wave propagation along directions that have simple direction cosines, yielding clements of the stiffness matrix in a convenient fashion. In addition, most of these directions have high symmetries and ultrasonic samples aligned in these directions can be easily obtained by the Laue back reflection technique (Chapter 4). Furthermore, there is the advantage that many of these directions are pure mode directions and the deviation of the energy flux associated with the ultrasonic wave in these propagation directions is a minimum so that the chances of the wave impinging on the sides of the ultrasonic specimen, giving rise to mode conversion and the ensuing errors in the velocity measurements are reduced. Farley (1973) has discussed all these aspects in great detail.

3.9 Pure mode directions

In general, in an anisotropic crystal, ultrasonic waves do not have particle displacement either parallel or normal to the

Table 3.4

Solutions of the Christoffel equation for hexagonal crystals

Propagation direction	Particle displacement direction	Christoffel equation solutions ρv^2, in terms of the elements of the stiffness matrix
[001]	[001]	C_{33}
[001]	in (001) plane	C_{44}
[100]	[100]	C_{11}
[100]	[001]	C_{44}
[100]	[010]	$\frac{1}{2}(C_{11} - C_{12}) = C_{66}$
[101]	*ϕ	$\frac{1}{4}(C_{11} + C_{33} + 2C_{44}) + \left[\{\frac{1}{2}(C_{11} - C_{33})\}^2 + (C_{13} + C_{44})^2\right]^{\frac{1}{2}}$

* This is quasi-longitudinal mode and ϕ, an angle measured from [001] in (010) plane depends upon the values of the elastic stiffness matrix elements.

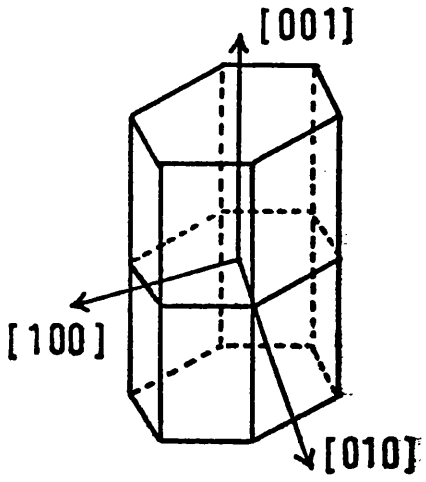

Orthorgonal co-ordinate system for hexagonal crystals

propagation direction. However, there are certain symmetry and non-symmetry directions - the pure mode directions-for which the particle displacement is either parallel or normal to the propagation direction. The non-symmetry directions have been explained by Brugger (1965). The symmetry directions are as follows:

(i) Propagation in a symmetry plane - one pure shear mode, polarised normal to the plane

(ii) Propagation normal to a two-fold, four-fold or six-fold axis - one pure shear mode, polarised parallel to the axis

(iii) Propagation along a two-fold axis - all the modes are pure

and (iv) Propagation along a three-fold, four-fold or six-fold axis - all the modes are pure, shear modes are degenerate.

C H A P T E R 4

CRYSTAL GROWTH AND CHARACTERISATION

4.1 Introduction

Large, homogeneous single crystals are required for the study of anisotropic elastic properties of solids by ultrasonic pulse techniques. The growth and characterisation of crystals of a number of In alloys forms the subject matter of this Chapter.

Both the repeated pass horizontal zone levelling method and a modified Bridgman method have been successfully used to grow large (30-70 gm) single crystals of In alloys with Cd (3.4, 4.4 and 6.5 at% Cd), Tl (30, 31, 76.5 and 81.5 at% Tl) and Pb (5, 17 and 75 at% Pb). Previously, Verkin and Svechkarev (1965) have grown small (∿ 60 mg) spherical shaped single crystals of In-Cd alloys in the range 0 - 5 at% Cd. Growth of large single crystals of In-Tl alloys while extensively reported (Pace 1970, Gunton 1973 and Murtha, Jensen and Burnet 1973) has however been restricted to the fct and fcc phases extending over the composition range 0 - 40 at% Tl (Figure 2.3). As regards In-Pb alloys, Volotskaya and Fogel (1970) report the growth of cylindrical single crystals (∿ 1mm diameter) over a wide range of composition covering both In-and Pb-rich regions of the phase diagram (Figure 2.4). van der Planken, Greiner and Smith (1971) have measured the elastic constants of Bridgman-grown Pb-rich (80 - 100 at% Pb) alloys.

4.2 Crystal growth from the melt

4.2.1 General considerations

The methods in vogue for the growth of metal and alloy single crystals by the controlled solidification of a melt or of part of a melt are based on the simple principle of extraction of latent heat generated by the solidification process without allowing the

melt to supercool sufficiently to permit nucleation of new crystals. Problems that arise in practice are a consequence of the fact that it is often necessary to control certain characteristics of the crystals to be grown such as, shape, size, composition and homogeneity.

4.2.2 Constitutional supercooling

Consider, for example, the In-rich portion of the In-Cd phase diagram described in Chapter 2. For the purposes of present discussion, this may be schematically represented as in Figure 4.1. Let K denote the distribution coefficient - defined as the ratio of the concentration of solute (Cd) in the solid to the concentration of solute in the liquid with which it is in equilibrium. When liquid of composition C_o (Figure 4.1) is lowered in temperature to the liquidus, solidification can start. The first solid to form will have a solute concentration of KC_o. In the case illustrated here, K is less than unity and the solid which forms will contain less solute than the liquid adjacent to the solid-liquid interface. As freezing proceeds, this will result in the formation of a liquid layer of high solute concentration adjacent to the advancing interface. This enrichment of the liquid layer will continue until a steady state value of C_o/K is reached. Solute rejection at the advancing interface is then balanced by diffusion of the rejected solute away from the interface into the liquid. This process is schematically illustrated in Figure 4.2. The solute concentration decreases into the liquid according to the equation (Rutter and Chalmers 1953, Rutter 1958):

$$C_L/C_o = 1 + (q/K) \exp\{-(R/D)x\} \qquad (4.1)$$

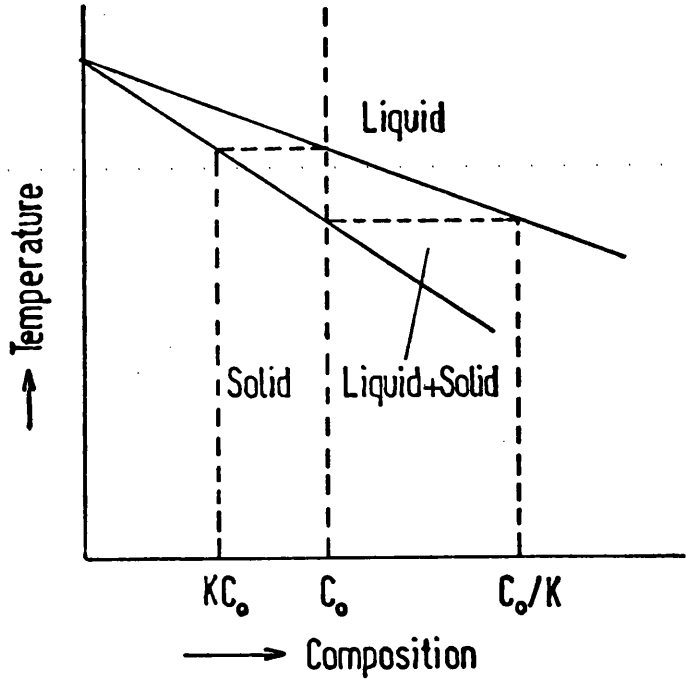

Figure 4.1: Schematic representation of In-rich portion of the In-Cd phase diagram.

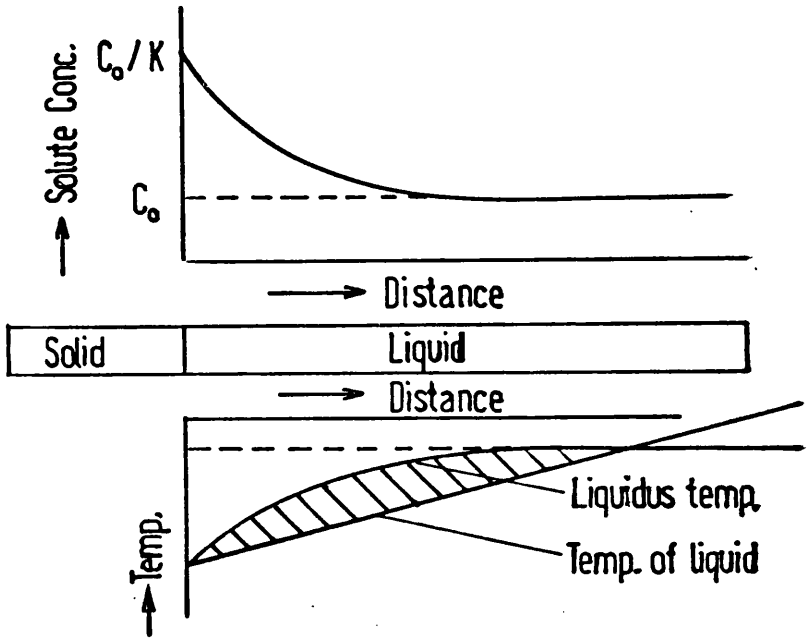

Figure 4.2: Development of constitutional supercooling.

where

C_L = Solute concentration in the liquid

C_o = Starting solute concentration in the melt

q = $1 - K$

R = Speed of freezing

D = Diffusion coefficient of the solute in the liquid

X = Distance measured from the interface into the liquid

Corresponding to this variation of composition in the liquid there will be a variation of liquidus temperature in accord with the phase diagram. This liquidus temperature variation is shown in Figure 4.2. Assuming that the solidus and liquidus lines are straight, liquidus temperature variation with distance is given by:

$$T_L = T_m - MC_o\left\{1 + (q/K)\exp\left(-(R/D)X\right)\right\} \qquad (4.2)$$

where

T_L = Liquidus temperature

T_m = Melting point of pure metal (solvent)

M = Slope of the liquidus line

Because of the variation of liquidus temperature in the neighbourhood of the interface, the actual temperature of the liquid- as imposed by the established conditions of freezing- may be below the liquidus temperature in a limited region, as shown in Figure 4.2. The liquid represented by the shaded area in Figure 4.2 is below its liquidus temperature and is therefore supercooled. Supercooling which arises in this way- because of composition changes which occur in the liquid during freezing- is termed constitutional supercooling.

4.2.3 Growth parameters and the suppression of constitutional supercooling

As explained in the last Section, the presence of supercooling in the liquid adjacent to the interface – other than the supercooling necessary for the propagation of the liquid-solid transformation at a finite rate – constitutes an instability in the solidifying alloy. If some point on the growth interface proceeds ahead of neighbouring points, it gets into a region of greater supercooling and, therefore, can grow more rapidly. The interface will then be covered with an array of projections. The tip of the projections tend to grow out ahead of the layer of high solute concentration in the liquid. Thus, solute diffusion from the tip of the projections would be enhanced by the addition of a component of diffusion parallel to the growth interface. This lateral solute diffusion gives rise to segregation of solute so that the solute concentration is enriched in the projection boundaries and depleted in the projection centres. In short, constitutional supercooling gives rise to alloy inhomogeneities. The effect of constitutional supercooling must therefore be reduced to a minimum. This can be tackled by controlling the growth parameters. Following the solute redistribution theory of Chalmers and co-workers (Rutter and Chalmers 1953, Tiller et al 1953), Dismukes and Ekstrom (1965) have shown that constitutional supercooling can be 'suppressed' if:

$$\frac{R}{G} \leq \frac{D}{M(C_S - C_L)} \qquad (4.3)$$

where

R = Growth rate in $cm.sec^{-1}$

G = Temperature gradient at the growth interface in $^{o}C.cm^{-1}$

D = Diffusion coefficient of the solute in the melt in $cm^{2}.sec^{-1}$

C_S, C_L = Solute concentrations at the interface in solid and liquid respectively in (at%)

and M = Slope of the liquidus line in $^{o}C.(at\%)^{-1}$

An estimate of $\frac{R}{G}$ based on this criterion has been made for the In alloys studied here (Table 4.1).

Equation (4.3) indicates that constitutional supercooling is best 'avoided' by using slow growth rates and large temperature gradients. The In alloys of the present study have low melting points (140-300^{o}C) and large temperature gradients are not easy to attain. This has to be compensated for by a choice of smaller growth rates. It follows from Table 4.1, that for each In alloy system, for a given temperature gradient, slower growth rates are required for alloys with larger solute concentrations. These factors have been taken into account in the choice of the growth method for the different alloy compositions. Although the repeated pass horizontal zone levelling technique - which has been likened by Pfann (1959) to a soil-levelling drag - appears to be the ideal method for the growth of homogeneous alloy crystals, the effectiveness of this method will be impaired if the growth parameters do not conform to the criterion set by equation (4.3). A modified Bridgman technique, wherein the apparatus allowed larger temperature gradients and slower growth rates than possible with the available zone-leveller has therefore been used

Table 4.1

R/G estimates based on the constitutional supercooling criterion

Indium alloy composition	R/G ($\times 10^{-5}$ $cm^2/^oC/sec$)	Remarks
3.4 at% Cd	0.7	M, C_S and C_L from Figure 2.2.D from Kaiser and Shuck (1970)
4.4 at% Cd	0.6	"
6.5 at% Cd	0.4	"
30 at% Tl	1.8	M, C_S and C_L from Figure 2.3.D from Eckert and Drickamer (1952)
31 at% Tl	1.8	"
76.5 at% Tl	0.07	"
81.5 at. Tl	0.1	"
5 at% Pb	1.2	M, C_S and C_L from Figure 2.4.D from Campbell, Tu and Robinson (1976) and Smithells (1976)
17 at% Pb	0.3	"
75 at% Pb	0.1	"

to grow those alloys of rather higher solute concentrations.

4.3 Zone levelling technique

In zone levelling, the motion of a molten zone along the sample produces a large region of uniform composition as distinct from zone refining, in which the composition varies continuously from one end of the sample to the other. The problem is usually to produce a uniform distribution of a solute in a solvent. The way in which this is achieved in the zone levelling method will now be explained. Figure 4.3 illustrates a zone levelling process. For example, let the ingot being zone levelled be that of an In-Cd alloy belonging to the phase diagram schematically shown in Figure 4.1. Let C_o denote the constant mean concentration of the alloy ingot. Now consider the first passage of a molten zone along the ingot. As the zone advances, material of concentration C_o enters the zone at the leading or melting interface, and solid of concentration KC_L where C_L is the concentration in the zone, leaves the zone at the trailing or freezing interface. In the example illustrated, $K < 1$ and the zone accumulates solute as it travels until a concentration C_o/K is reached in the liquid. From there onwards a uniform concentration is frozen out as shown in Figure 4.3 because the same concentration leaves and enters the zone. When the front of the zone comes to the end of the ingot a normal freezing process begins and the freezing of the last zone generates a normal freezing distribution. The solute distribution achieved in this way is often not satisfactory because- as indicated in Figure 4.3- there is an initial transition region which might occupy a major portion of the alloy ingot. A more uniform solute distribution (Figure 4.4) can be achieved by using the terminal transient which has a high solute concentration as the excess starting

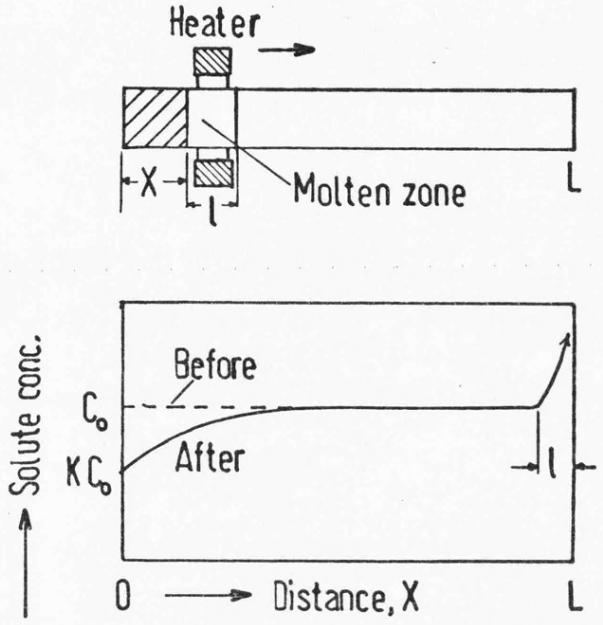

Figure 4.3: Approximate solute concentration after passage of one molten zone through a charge of uniform mean concentration C_o (Pfann 1959).

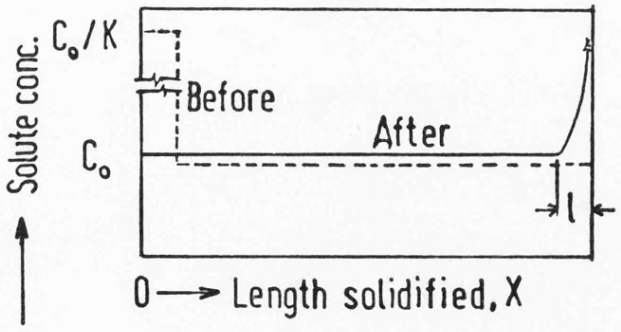

Figure 4.4: Elimination of initial transition region (Pfann 1959).

charge for the second zone pass. In practice, at least six zone passes in alternating directions were required for growing homogeneous single crystals.

4.3.1 The horizontal zone leveller

The horizontal zone leveller used for growing single crystals of In-Cd (3.4 and 4.4 at% Cd), In-Tl (30 and 31 at% Tl) and In-Pb (5 and 17 at% Pb) alloys is illustrated in Figure 4.5. This equipment consisted of a horizontal travelling furnace capable of uniform traverse. The furnace itself was made up by winding Kanthal wire (17Ω/yd) toroidally on to an asbestos bobbin. A copper-constantan thermocouple with one junction embedded in the heater wire was used to monitor the temperature. The heater assembly was cased in an aluminium block through which passed two steel guide rods, the ends of which were clamped to a massive rectangular bed of welded angle-iron. A central lead-screw passing through the aluminium block and housed in a frictionless bearing at the bed-support could be driven by an electric motor through a slip-free precision gear mechanism and enabled the heater assembly to travel uniformly across the guide rods. The speed of traverse could be varied by a choice of gear ratios. The motor circuit included a reversing switch which set the direction of travel of the heater assembly, while two micro-switches limited the length of travel. Power to the furnace was fed through a variac. An ammeter in the circuit indicated the current passing through the heater wire. The temperature gradient at the growth interface could be altered with the help of water-cooled copper coils arranged on either side of the furnace. The zone-leveller was placed on a foundation of three layers of thick concrete slabs separated from each other and the laboratory floor by rubber

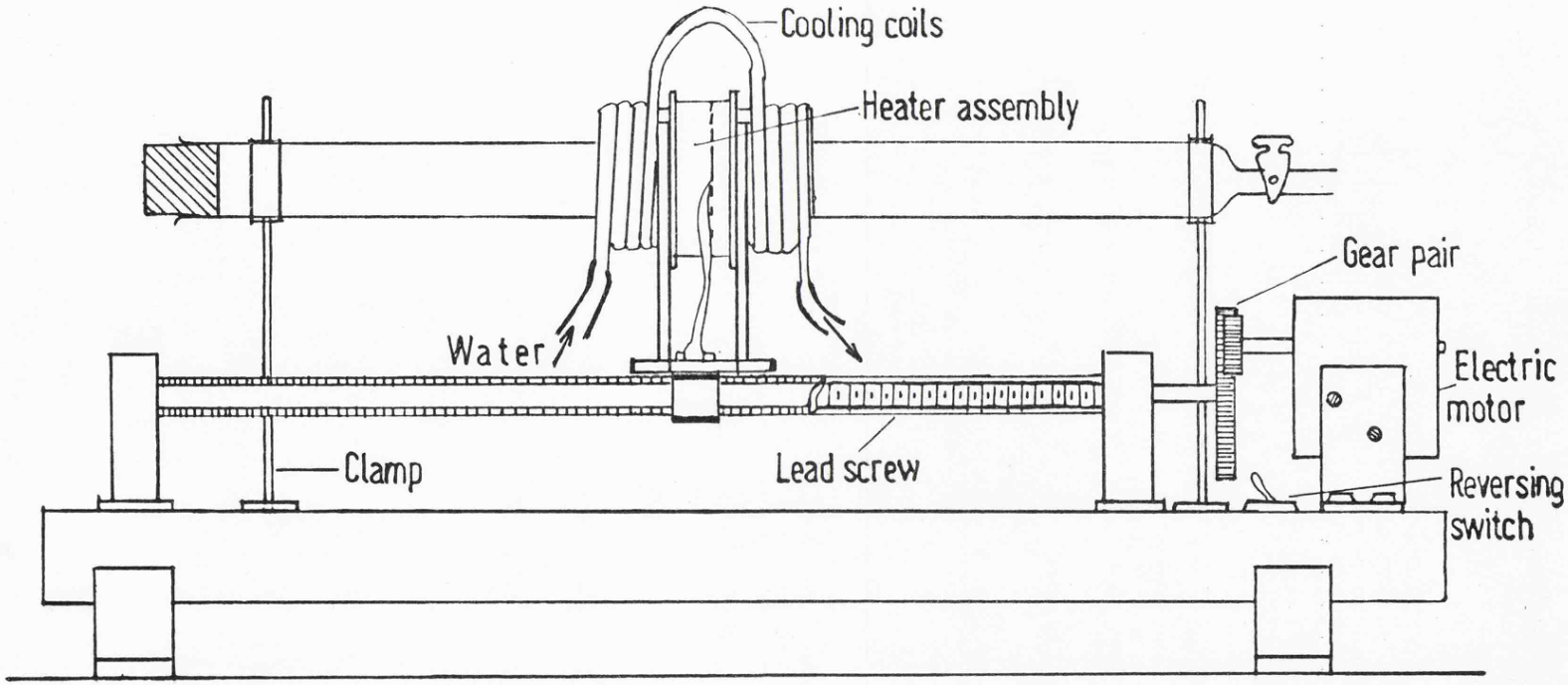

Figure 4.5: The horizontal zone leveller (not to scale)

bungs to dampen mechanical vibrations. The entire set up was housed in a cubicle with constant ambient temperature.

4.3.2 Growth procedure

The feed materials - 99.999% pure In, Cd, Tl and Pb ingots- were cut into small bits (∿ 0.2 cc), etched (etchants are listed in Table 4.3), washed in distilled water and thoroughly dried. Appropriate amounts in the ratios required to give the desired compositions were then weighed to an accuracy of ±0.001 gm and contained in pre-cleaned, baked quartz growth boats designed with pointed ends to promote seeding and a smooth inside surface to reduce nucleation centres. The boat with the contents was then placed inside a clean quartz tube with vacuum connections (Figure 4.5) and was first evacuated to better than 10^{-5} torr and then filled with oxygen-free nitrogen to about 0.5 atmosphere. After this procedure, the tube was transferred to the zone leveller with its heater current set to give the desired temperature profile (Figure 4.6). The growth process accomplished with typical growth rates of 2.5 mm/hr and temperature gradients of 20°C/cm at the growth interface lasted several weeks.

4.4 Bridgman method

The Bridgman method of crystal growth is based on the liquid-solid transition as a result of controlled cooling from the liquid phase. Since the pioneering efforts of Bridgman (1925b)- who grew several metal crystals by slowly lowering a pointed mould containing the liquid metal through a temperature gradient- many improvements have been made in the growth techniques. With the electronic control of melting point isotherm commonly used

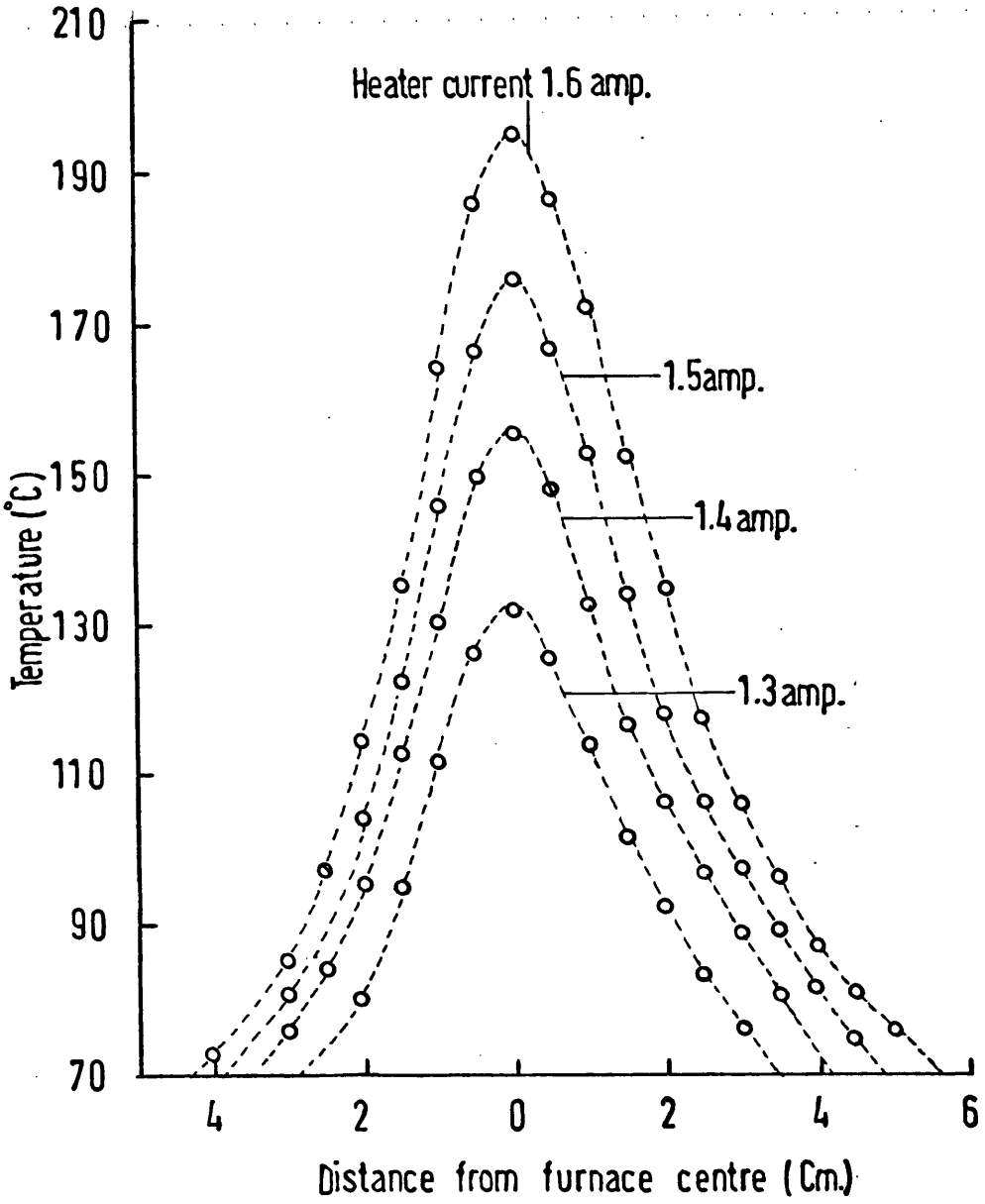

Figure 4.6: Zone leveller temperature profiles.

now-a-days,it is possible to reach very small growth rates - as low as 1 mm/10^4 min (Goss 1963)- a factor which has helped in the successful use of this method for growing homogeneous alloy crystals.

4.4.1 Description of the growth apparatus

The vertical growth furnace used here was originally designed for the growth of HgTe and some of its pseudo-binary alloys and has been described by Seddon (1972). The furnace (Figure 4.7) was made by winding Kanthal wire on a ceramic tube in three sections with the ratio of current in each section being adjusted by means of ballast resistors. The furnace tube was housed in an asbestos box and only the top half of the intervening space was insulated by packing with vermiculite. This feature helped in increasing the temperature gradient at the growth interface. The temperature control and the 'temperature profile lowering' were accomplished by a potentiometric proportional temperature controller and a ramp generator programmer- both of Eurotherm Industrial Control Equipments Ltd. The temperature controller worked on standard feed-back principles with an error voltage developed between a monitoring thermocouple embedded in the furnace wiring and a reference setting on the controller, controlling the load output power. The control circuitry ensured fast enough response to be able to override temperature fluctuations. The ramp generator programmer allowed the furnace temperature profile to be lowered in a linear fashion at a programmable rate, variable between about 0.5^{o}C/hr and 9^{o}C/hr.

4.4.2 Growth procedure

The charge preparation prior to the growth process is

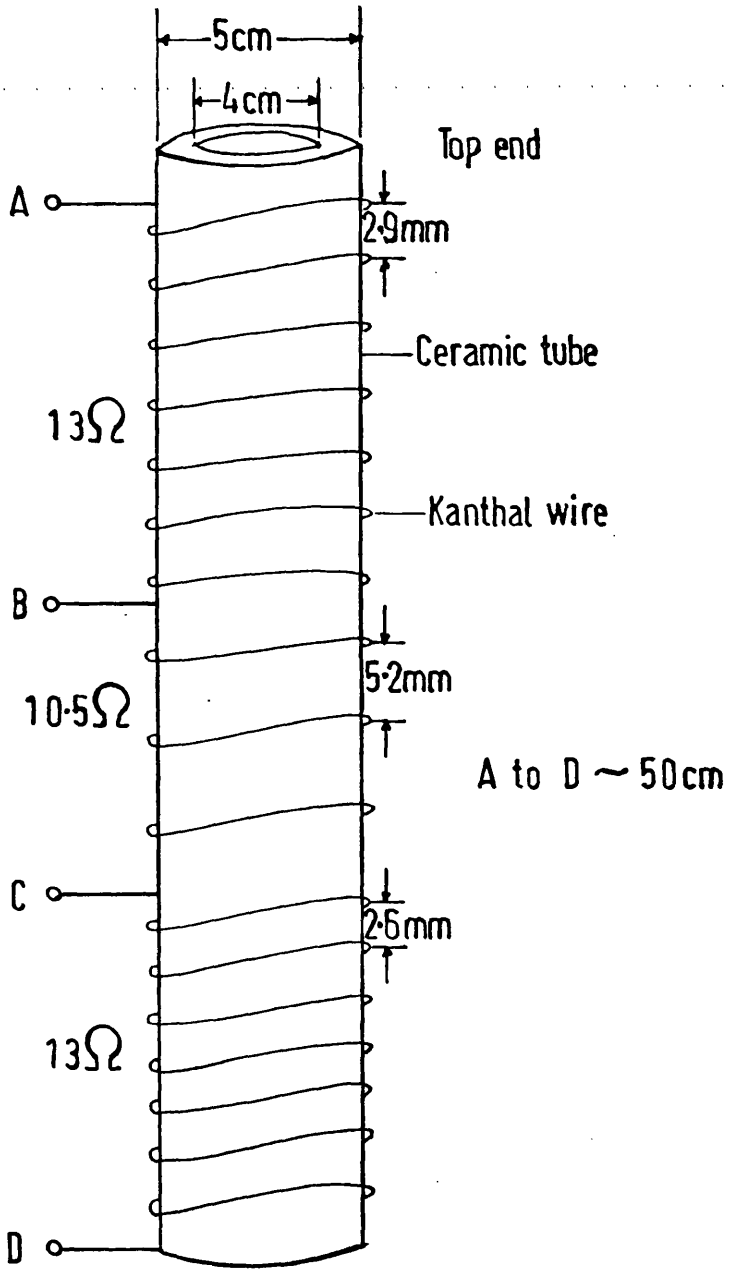

Figure 4.7: The vertical Bridgman furnace.

similar to that described for the zone levelling method in Section 4.3.2 except that the mixing of the constituents in the liquid state is much more important as there is no 'levelling' inherent in the freezing procedure employed. For this reason, the charge contained in a vacuum sealed (better than 10^{-5} torr) carbon-coated quartz growth tube (Figure 4.8) was left in the molten state for 10 to 12 hours in a vertical rotary furnace to ensure thorough mixing. After this procedure, the growth tube was fixed inside the Bridgman furnace so as to site the charge appropriately with respect to the temperature profile (Figure 4.9) which gave the requisite temperature gradient ($\sim 30^{\circ}$C/cm) at the growth interface. The temperature profile was then lowered by programming the ramp generator and with slow growth rates ($\sim$ 0.5cm/day) the growth process lasted several weeks.

4.5 Crystal characterisation

After the growth process, the crystal boules could be easily removed, there being little tendency to stick to the mould. Each boule was then examined for crystallinity, homogeneity and perfection by various methods described in the following Sections.

4.5.1 Etching characteristics

The requirements of an etchant here are: (i) it should be capable of revealing grain boundaries, if any, enabling the isolation of the part of the boule which is single (ii) remove oxide layers and any surface defects occurring during the growth process so that these do not influence the form of the back reflection Laue spots which can then be used to assess the crystal quality.

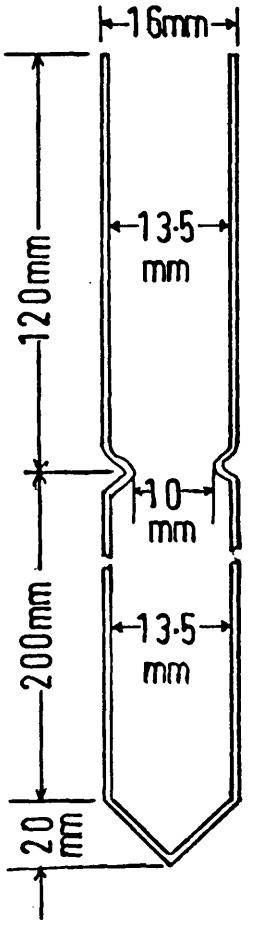

Figure 4.8: Quartz growth tube (Bridgman method).

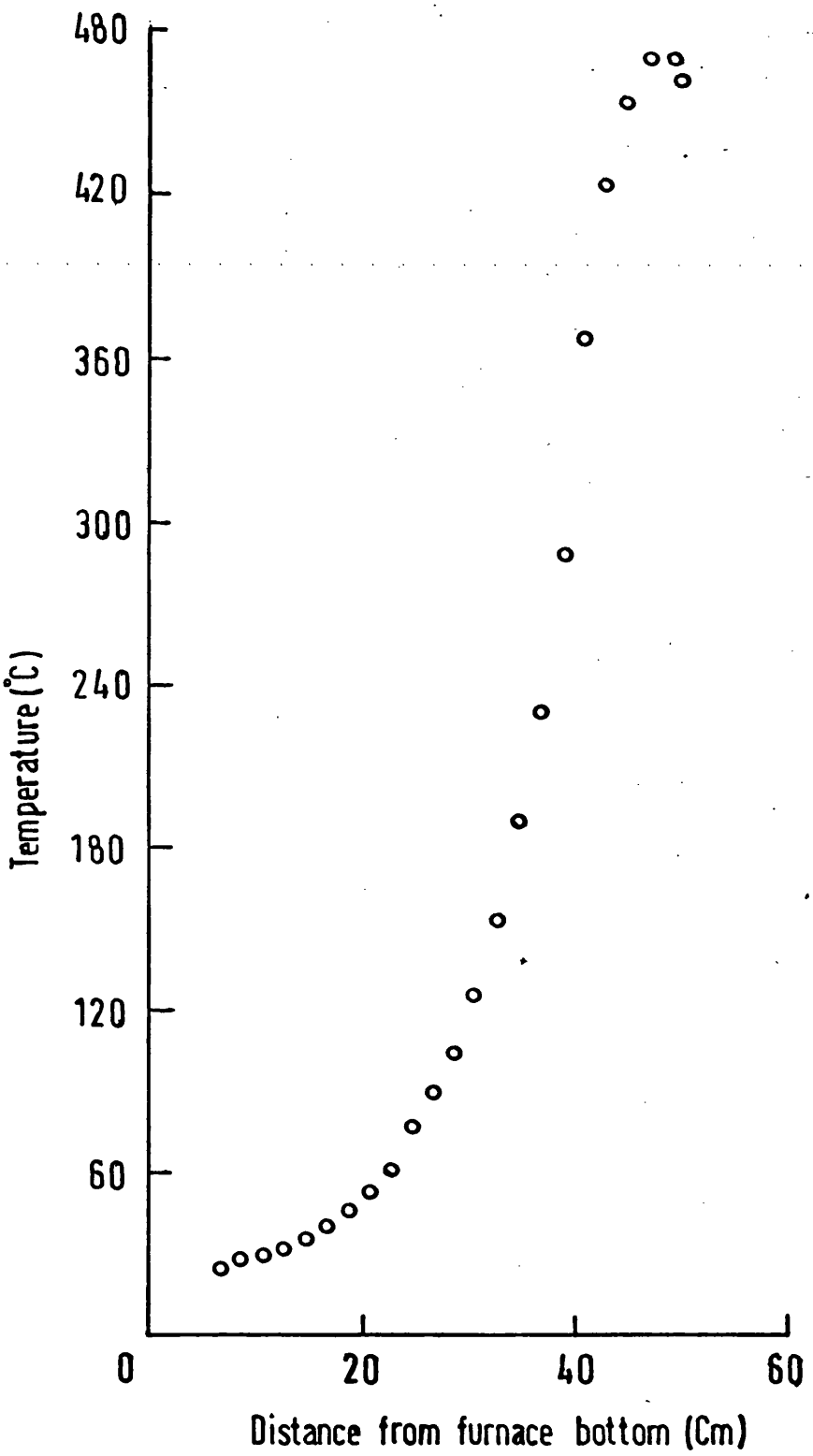

Figure 4.9: A typical temperature profile of the Bridgman furnace.

A number of chemical etchants are available for In and its alloys (Table 4.2). Many of these etchants are used in conjunction with conventional metallographic polishing techniques. Indium and its alloys with Cd, Tl and Pb are all very soft and any mechanical polishing is best avoided, especially with single crystal specimens. The etchants that yielded best results are listed in Table 4.3. Etching was accomplished by immersing the boule in the freshly prepared etchant contained in a Petri dish and slightly agitating to ensure that fresh etchant is in contact with the boule all the time. During the etching process, the metallic lustre is lost to some extent indicating that etching is in progress. In practice, it was possible to ascertain from the degree of dullness of the surface when etching should be stopped. After the completion of etching, the boules were rinsed in warm running water and dried in a stream of warm air. Etched boules when examined under light revealed any grain boundaries present; usually the boules were either entirely single or contained large grains from which suitable samples for ultrasonic experiments could be obtained.

4.5.2 Electropolishing of In-Pb alloys

It must be mentioned that for Pb-rich alloys like the In - 75 at% Pb alloy boule, chemical etching procedure outlined in the previous Section, alone was not sufficient in the preparation and maintenance of an oriented crystal because of smearing and tarnishing during etching. Best results - as evidenced by the disappearance of rings due to the surface structure and sharpening of Laue spots on back-reflection X-ray photographs (Figure 4.26) - were obtained by electropolishing the boule in an electrolyte made up of 1 volume of perchloric acid (sp.gr. 1.58) and 4 volumes of

Table 4.2

List of etchants reported for In alloys with Cd, Tl and Pb

Etchant	Remarks	Reference
Hydrogen peroxide + Glacial acetic acid	Used on In-Cd alloys	Wilson and Wick (1937)
20ml Hydrochloric acid + 4gm Picric acid + 400ml Ethylalcohol	In and In-rich alloys	Carapella and Peretti (1949)
Nitric acid (1: 1 W/W)	In-Tl alloys 0 - 30 at% Tl	Gunton (1973)
95% - 5% solution of Methanol and Nitric acid	In-12 and In-24 at% Pb	Volotskaya and Fogel (1970)

Table 4.3

Etchants used in the present work

Metal or alloy	Etchant	Remarks
In	1 Vol. Conc. HNO_3 + 3 Vol. H_2O	
Cd	1 Vol. Conc. Hcl + 1 Vol. H_2O	
Tl	3 Vol. Conc. HNO_3 + 2 Vol. H_2O	
Pb	4 Vol. Glycerol + 1 Vol. Glacial Acetic acid + 1 Vol. Conc NHO_3	
In - 3.4, 4.4 and 6.5 at% Cd	Conc. HCl + $KClO_3$ (to generate sufficient chlorine)	Previously reported by Goss and Vernon (1952) for pure In
In - 30, 31 at % Tl	1 Vol. Conc. HNO_3 + 1 Vol. H_2O	
In - 76.5, 81.5 at% Tl	2 Vol. Conc. HNO_3 + 1 Vol. H_2O	
In - 5, 17 at % Pb	3 Vol. Methanol + 2 Vol. Conc. HNO_3	
In - 75 at% Pb	5 Vol. Conc. HNO_3 + 1 Vol. Methanol	See Section 4.5.2 for electropolishing

acetic anhydride (Hofman 1970) and using a current density of 0.2 amp. cm^{-2} at 50V. Because of the explosive nature of the electrolyte used, the bath temperature was maintained well below the critical temperature ($\sim 3^{o}C$) with the help of a suitable cooling arrangement (Figure 4.10).

4.5.3 Lattice parameter measurements

The many and varied information that can be obtained from a knowledge of lattice spacing relationships in binary alloys have been discussed in standard texts (Hume-Rothery and Raynor 1962, Massalski 1970). Important to this work are the homogeneity of the alloy boules and the formation and composition limits of the alloy phases. Considerable attention has therefore been paid to the accurate determination of the lattice parameters.

The lattice parameters were obtained from Debye-Scherrer powder photography using a Phillips cylindrical type camera of circumference 360mm. With this camera, reflections over the whole range of Bragg angles can be recorded. The powder specimens of the In alloys were produced by filing under carbon tetra chloride and afterwards annealed *in vacuo* at a temperature of about $0.5T_m$ where T_m is the melting point. After the strain-relieving anneal, the specimens were allowed to cool to room temperature and left for a few days before being sieved (75μ mesh) and filled into a 0.5mm diameter Lindeman glass tube which was later heat sealed. The powder specimen tube was then located along the axis of the powder camera around which was located a single length of film with the X-ray beam entering through holes punched in the film. A small electric motor was then used to rotate the specimen ($\sim$ 1rpm) in a Ni filtered X-ray

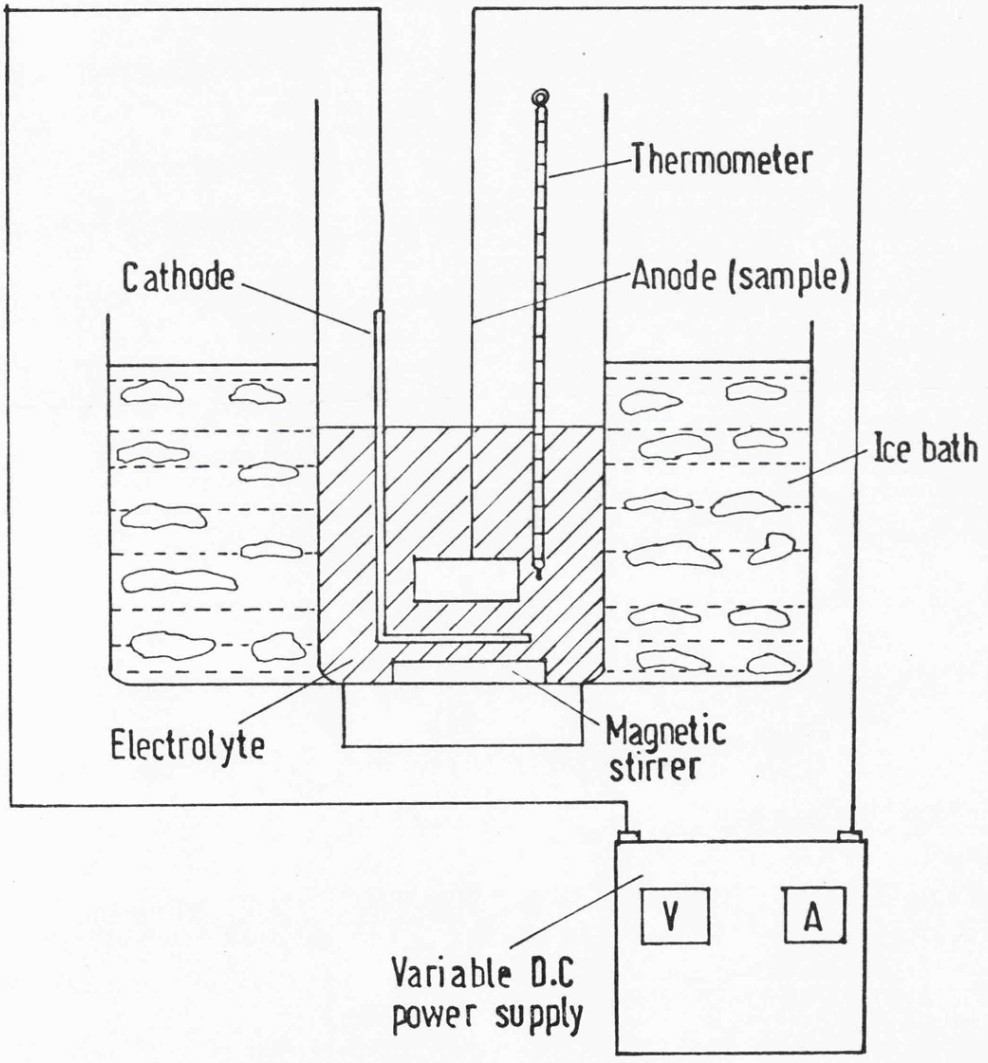

Figure 4.10: The electropolishing unit.

beam excited from a Cu target. The exposure time was adjusted to give the best results namely uniform low angle lines and well resolved high angle lines from which measurements could be accurately carried out.

In order to derive accurate lattice parameters from powder photographs obtained from cylindrical cameras it is necessary to take account of the systematic errors due to absorption in the specimen, eccentricity of the specimen in the camera, divergence of the X-ray beam and refraction. Accurate centring of the specimen reduces the eccentricity errors and absorption and beam divergence errors are minimised by the use of thin specimens and finely collimated X-ray beams. However, as absorption, eccentricity and beam divergence errors all tend to zero as the Bragg angle θ approaches 90°, further refinement is possible by extrapolating out the errors by graphical or analytical means. This refinement of the lattice parameter data has been made for cubic alloys using the Nelson-Riley extrapolation procedure (Nelson and Riley 1945) and for tetragonal alloys a modification of this procedure (King and Massalski 1962) has been adopted.

This procedure of measuring lattice parameters gave consistently reproducible results for the same powder specimen and for specimens from different portions of an alloy boule indicating good homogeneity.

4.5.4 Indexing of the Debye-Scherrer powder photographs

Room temperature ($295^{\circ}K$) Debye-Scherrer powder photographs of In alloys have been reproduced in Figures 4.11 - 4.15. In addition,

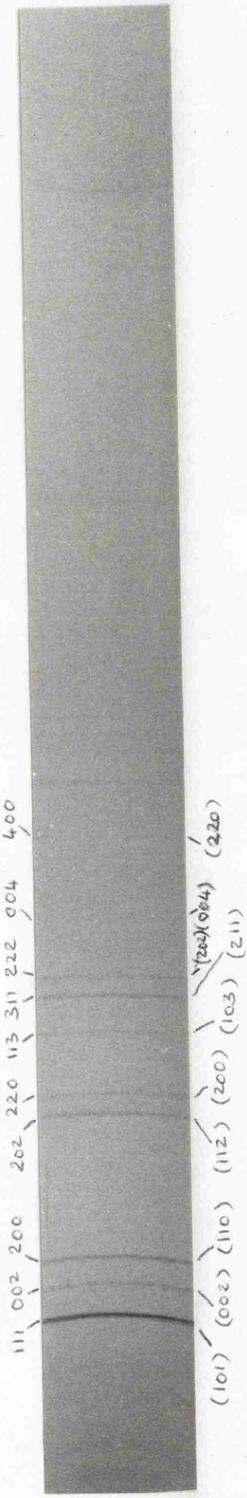

Figure 4.11: Room temperature Debye-Scherrer powder photograph of In. Indexing has been done on the basis of both face-centred and body-centred (shown in parentheses) unit cells.

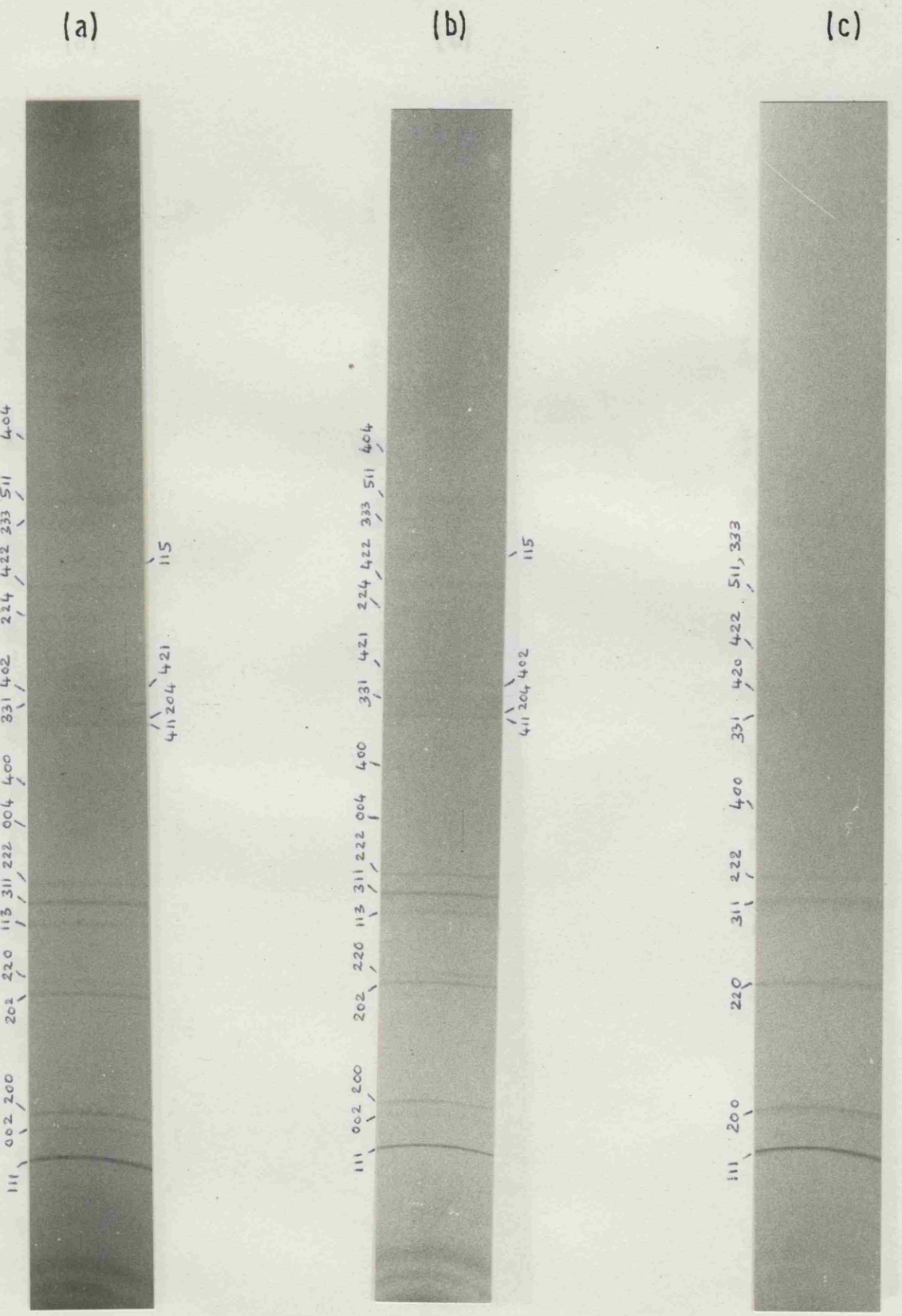

Figure 4.12: Room temperature powder photographs of In-Cd alloys - (a) 3.4 at% Cd, fct (b) 4.4 at% Cd, fct and (c) 6.5 at% Cd, fcc.

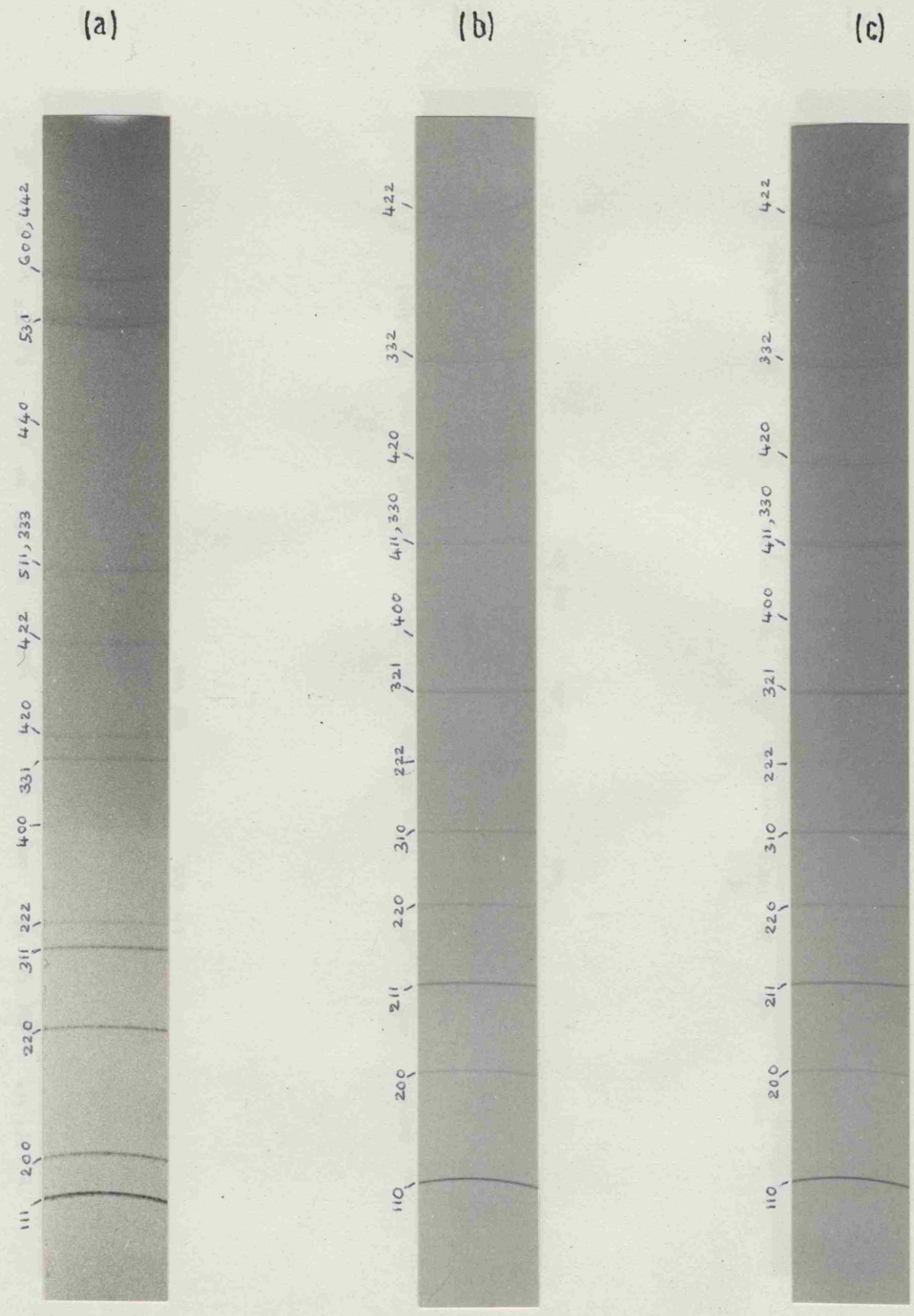

Figure 4.13: Room temperature powder photographs of In-Tl alloys - (a) 30 at% Tl, fcc (b) 76.5 at% Tl, bcc and (c) 81.5 at% Tl, bcc.

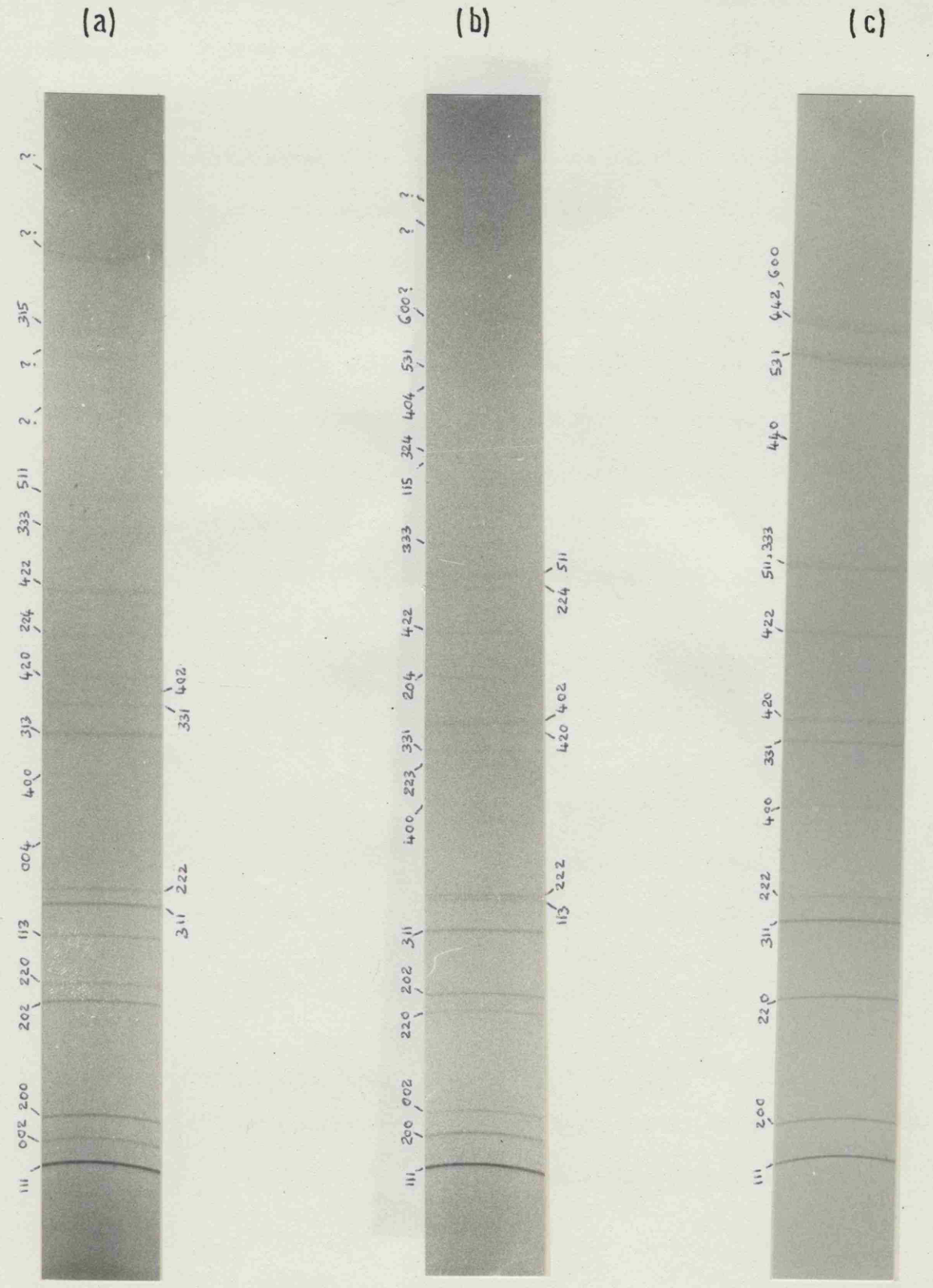

Figure 4.14: Room temperature powder photographs of In-Pb alloys - (a) 5 at% Pb, fct (c/a > 1) (b) 17 at% Pb, fct (c/a < 1) and (c) 75 at% Pb, fcc.

Figure 4.15: Room temperature powder photograph of In - 13.2 at% Pb. The diffraction pattern indicates the presence of a two-phase region prior to the fct (c/a > 1) - fct (c/a < 1) transformation.

interplanar spacings and indexed reflections have also been tabulated (Tables 4.4 - 4.12). All the powder photographs were indexed using a Bunn chart (Bunn 1961), the cubic alloys being treated as tetragonal with $\frac{c}{a} = 1$. Because of the loss in the diffracted intensity, some of the high θ lines could not be indexed with certainty and have therefore been left unindexed. All the indices labelled on the powder photographs conform to the reflection conditions set by the unit cell (see Table 4.13). In this connection it must be mentioned that In and its tetragonal alloys are often indexed on the basis of a body centred cell (D_{4h}^{17} - I 4/mmm). Conversion of these indices to the face centred cell (D_{4h}^{17} - F 4/mmm) used here, and vice-versa, can easily be done using the transformation matrices (Henry and Lonsdale 1965):

$$\begin{matrix} & \text{F} & & \\ \begin{bmatrix} \frac{1}{2} & -\frac{1}{2} & 0 \\ \frac{1}{2} & \frac{1}{2} & 0 \\ 0 & 0 & 1 \end{bmatrix} & , & \begin{matrix} & \text{I} & \\ \begin{bmatrix} 1 & 1 & 0 \\ \bar{1} & 1 & 0 \\ 0 & 0 & 1 \end{bmatrix} & & \end{matrix} \end{matrix} \qquad (4.4)$$

To illustrate this, the powder photograph of In (Figure 4.11) has been indexed on the basis of both body-centred and face-centred unit cells.

4.5.5 Lattice parameter results

Lattice parameter results of the present study will now be elucidated in conjunction with the previously published results.

4.5.5.1 In-Cd alloys

In principle, the upper limit of Cd concentration at which homogeneous alloy single crystals could be grown is the solid solubility limit of Cd in In. Although this is known to increase

Table 4.4

fct In - 3.4 at% Cd
- Interplanar spacings and indexed reflections

Line No	d spacing Å	h, k, ℓ
1	2.6968	111
2	2.4282	002
3	2.3026	200
4	1.6706	202
5	1.6295	220
6	1.4493	113
7	1.3973	311
8	1.3538	222
9	?	004
10	1.1547	400
11	1.0839	411
12	?	204
13	1.0604	331
14	1.0425	402
15	1.0307	421
16	0.9719	224
17	0.9495	422
18	0.9314	115
19	0.9031	333
20	0.8905	511
21	?	404

Table 4.5

fct In - 4.4 at% Cd
- Interplanar spacings and indexed reflections

Line No	d spacing Å	h, k, ℓ
1	2.6889	111
2	2.3983	002
3	2.3094	200
4	1.6653	202
5	1.6353	220
6	1.4371	113
7	1.3971	311
8	1.3533	222
9	1.1984	004
10	1.1569	400
11	1.0806	411
12	?	204
13	1.0643	331
14	1.0450	402
15	1.0327	421
16	0.9702	224
17	0.9529	422
18	0.9256	115
19	0.9039	333
20	0.8929	511
21	0.8361	404

Table 4.6

fcc In - 6.5 at% Cd
- Interplanar spacings and indexed reflections

Line No	d spacing Å	h, k, ℓ
1	2.6851	111
2	2.3255	200
3	1.6455	220
4	1.4037	311
5	1.3468	222
6	1.1666	400
7	1.0713	331
8	1.0443	420
9	0.9569	422
10	0.9026	511,333

Table 4.7

fcc In - 30 at% Tl
- Interplanar spacings and indexed reflections

Line No	d spacing Å	h, k, ℓ
1	2.7143	111
2	2.3470	200
3	1.6681	220
4	1.4231	311
5	1.3636	222
6	1.1798	400
7	1.0878	331
8	1.0588	420
9	0.9672	422
10	0.9130	511,333
11	0.8400	440
12	0.8037	531
13	0.7925	600,442

Table 4.8

bcc In - 76.5 at% Tl
- Interplanar spacings and indexed reflections

Line No	d spacing Å	h, k, ℓ
1	2.6786	110
2	1.8899	200
3	1.5452	211
4	1.3976	220
5	1.2025	310
6	1.0985	222
7	1.0184	321
8	0.9544	400
9	0.8998	411,330
10	0.8548	420
11	0.8154	332
12	0.7818	422

Table 4.9

bcc In - 81.5 at% Tl
- Interplanar spacings and indexed reflections

Line No	d spacing Å	h, k, ℓ
1	2.6889	110
2	1.9067	200
3	1.5583	211
4	1.3513	220
5	1.2091	310
6	1.0967	222
7	1.0235	321
8	0.9581	400
9	0.9031	411,330
10	0.8567	420
11	0.8172	332
12	0.7827	422

Table 4.10

fct ($\frac{c}{a}$>1) In - 5 at% Pb -

Interplanar spacings and indexed reflections

Line No	d spacing Å	h, k, ℓ
1	2.7023	111
2	2.4764	002
3	2.2869	200
4	1.6836	202
5	1.6208	220
6	1.4744	113
7	1.3930	311
8	1.3576	222
9	1.2411	004
10	1.1463	400
11	1.0789	313
12	1.0595	331
13	1.0435	402
14	1.0279	420
15	0.9873	224
16	0.9508	422
17	0.9084	333
18	0.8883	511
19	0.8450	?
20	0.8224	?
21	0.8136	315
22	0.7931	?
23	0.7794	?

Table 4.11

fct ($\frac{c}{a}$<1) In - 17 at% Pb

- Interplanar spacings and indexed reflections

Line No	d spacing Å	h, k, ℓ
1	2.7324	111
2	2.4279	200
3	2.2553	002
4	1.7217	220
5	1.6570	202
6	1.4583	311
7	1.3822	113
8	1.3715	222
9	1.2200	400
10	1.1301	223
11	1.1150	331
12	1.0904	420
13	1.0760	402
14	1.0273	204
15	0.9832	422
16	0.9484	224
17	0.9377	511
18	0.9162	333
19	0.8763	115
20	0.8639	324
21	0.8308	404
22	0.8242	531
23	0.8095	600?
24	0.7871	?
25	0.7824	?

Table 4.12

fcc In - 75 at% Pb
- Interplanar spacings and indexed reflections

Line No	d spacings Å	h, k, ℓ
1	2.8139	111
2	2.4407	200
3	1.7285	220
4	1.4749	311
5	1.4116	222
6	1.2246	400
7	1.1237	331
8	1.0963	420
9	1.0001	422
10	0.9431	511,333
11	0.8666	440
12	0.8288	531
13	0.8170	600,442

Table 4.13

General Conditions limiting possible X-ray reflections

Structure	Reflection conditions	Remarks
I 4/mmm D_{4h}^{17}	hkℓ: h + k + ℓ = 2n hko: (h + k = 2n) okℓ: (k + ℓ = 2n) hhℓ: (ℓ = 2n)	See equation (4.4) for conversion to F4/mmm
Fm3m O_h^5	hkℓ: (h+k), (k+ℓ), (ℓ+h) = 2n hhℓ: (ℓ + h = 2n) okℓ: (k, ℓ = 2n)	
Im3m O_h^9	hkℓ: h + k + ℓ = 2n hhℓ: (ℓ = 2n) okℓ: (k + ℓ = 2n)	

with the temperature, its actual value has been subject to some disagreement. The X-ray values (at 20°C) - 4.5 ± 0.5 at% Cd (Betteridge 1938), 5.8 at% Cd (Heumann and Predel 1962)-are quite different from the metallographically evaluated limit of ∿15 at% Cd (Wilson and Wick 1937). More recently, the disagreement has been resolved in favour of the higher limit: Straumanis, Rao and James (1971) found no evidence of Cd lines on X-ray powder photographs of alloys containing up to about 12 at% Cd, while alloys with 14 and 16 at% Cd showed very weak Cd lines.

Lattice parameters obtained from Debye-Scherrer powder photographs (Table 4.14) are in good agreement with those of Straumanis, Rao and James (1971). These results illustrate the progressive reduction of the $\frac{c}{a}$ ratio from the value of 1.08 for In itself with increasing Cd content in the alloys (Figure 4.16). Powder photographs of the alloy with the highest Cd concentration (6.5 at% Cd) showed no trace of Cd lines even after storage at room temperature for several months. Furthermore, this alloy showed only fcc lines (Figure 4.12); Straumanis, Rao and James (1971) found that a 6.225 at% Cd alloy was wholly cubic; however, they did observe barely visible fct lines for a 5.945 at% Cd alloy indicating the presence of a two phase region preceding the fct-fcc transformation.

Heumann and Predel (1959b) measured floatation densities of In-Cd alloys which were significantly greater than those calculated from X-ray lattice parameter measurements and concluded that under equilibrium conditions these alloys contain abnormally large concentrations of interstitial In atoms. However, Ridley (1965, 1968)

Table 4.14

Room temperature density and lattice parameters of In-Cd alloys. Data for In are from Straumanis, Rao and James (1971)

Composition (at% Cd)	Lattice parameters (Å)			Floatation density (gm. cm^{-3})	X-ray density $\rho_x = nM/a^2CN$ (gm. cm^{-3})
	a	c	c/a		
0	4.5993	4.9507	1.076	7.2833	7.2824
3.4	4.6253 ± 0.0088	4.8526 ± 0.0128	1.049 ± 0.004	7.316 ± 0.001	7.339 ± 0.048
4.4	4.6297 ± 0.0057	4.8226 ± 0.0087	1.042 ± 0.003	7.338 ± 0.002	7.369 ± 0.032
6.5	4.6910 ± 0.0042	-	1	7.376 ± 0.002	7.376 ± 0.020

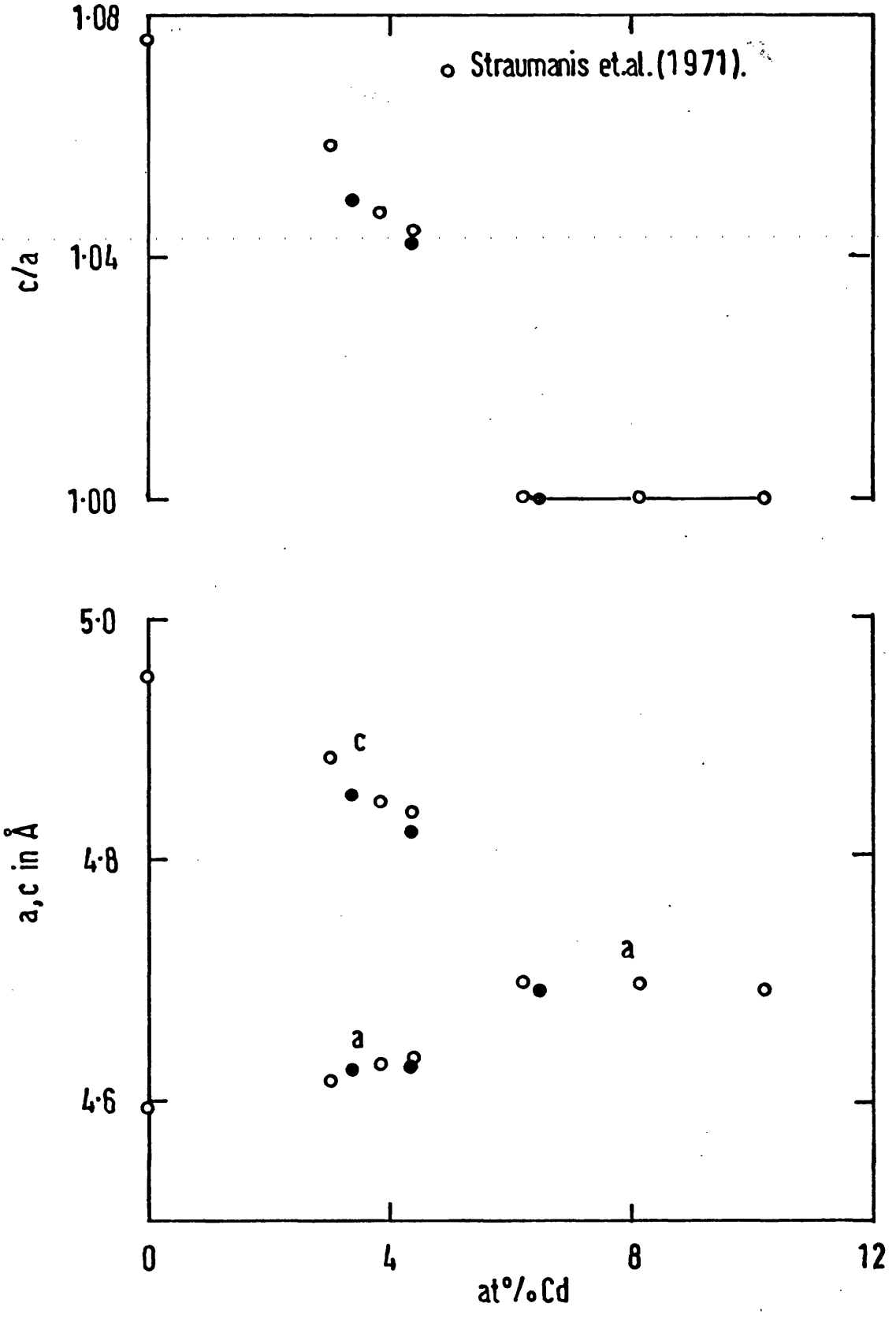

Figure 4.16: Room temperature lattice parameters of In-Cd alloys

and Straumanis, Rao and James (1971) found no significant discrepancies between the measured and calculated densities of polycrystalline materials and they stressed the true substitutional nature of the solid solutions. A high density of interstitials would influence both the mechanical properties of the alloys and the phase transformation itself. Since the single crystal growth procedures adopted here were quite different in kind from those used by previous workers to prepare their polycrystalline samples, it was necessary to find out whether the single crystals themselves did or did not contain a large number of interstitial atoms. Measured floatation densities ρ of the single crystals are included in Table 4.14; these agree within experimental error with those (ρ_x) computed (using $\rho_x = nm/a^2cN$, where n (= 4) is the number of atoms in the unit cell and M is the mean atomic weight) from the lattice parameters a and c. Thus, these single crystals did not contain significant numbers of interstitial atoms - the work supports the findings of Ridley (1965, 1968). Extensive X-ray powder diffraction studies showed that the crystals were homogeneous and were grown well within the solubility limit. Further confirmation was obtained by scanning electron probe microanalysis on the actual ultrasonic specimens. No segregation of Cd was found. These crystals were homogeneous, substitutional solid solutions.

4.5.5.2 In-Tl alloys

The bcc phase is arrested at the eutectoid (see Section 2.2.2). Strictly speaking it should not be possible to retain a single phase bcc alloy below the eutectoid. However, Luo and Willens (1967) showed that the eutectoid decomposition could be suppressed by fast-quenching. Their X-ray diffraction measurements

also indicated that alloys with a composition between 75 and 83 at% Tl stayed single phase after being kept at room temperature for a day. Somewhat different composition limits for single phase bcc alloys were earlier given by Valentiner (1940) and Guttman (1950). Room temperature Debye-Scherrer powder photographs of the alloys studied here - 76.5 and 81.5 at% Tl-show a single phase bcc structure (Figure 4.13). Lattice parameters obtained from these photographs (Figure 4.17) are in good agreement with those of Luo and Willens (1967). Within the experimental error, X-ray densities agree with the floatation densities (Table 4.15).

Measured lattice parameters of the fcc alloys of this study (30 and 31 at% Tl) are included in Figure 4.17 along with those of a series of fcc and fct In-rich alloys previously measured by Gunton (1973). As pointed out in Section 2.2.2, the fct-fcc transformation in In-Tl alloys is not preceded by a two phase region.

4.5.5.3 In-Pb alloys

Detailed X-ray studies of lattice spacing relationships in In-Pb alloys have been made by Raynor and his collaborators (Tyzack and Raynor 1954a, b and Moore, Graham, Williamson and Raynor 1955). They found three different phase fields in the alloy system: (i) 0-12.7 at% Pb, fct with the axial ratio progressively increasing from a value of 1.08 for In itself to 1.09, (ii) 13.7-31 at% Pb, fct with the $\frac{c}{a}$ ratio progressively decreasing from a value of 0.934 to 0.928, (iii) 32-100 at% Pb, fcc Pb structure. They also found from powder photographs evidence for a two-phase region preceding the fct ($\frac{c}{a} > 1$) - fct ($\frac{c}{a} < 1$) and fct ($\frac{c}{a} < 1$) - fcc transformations.

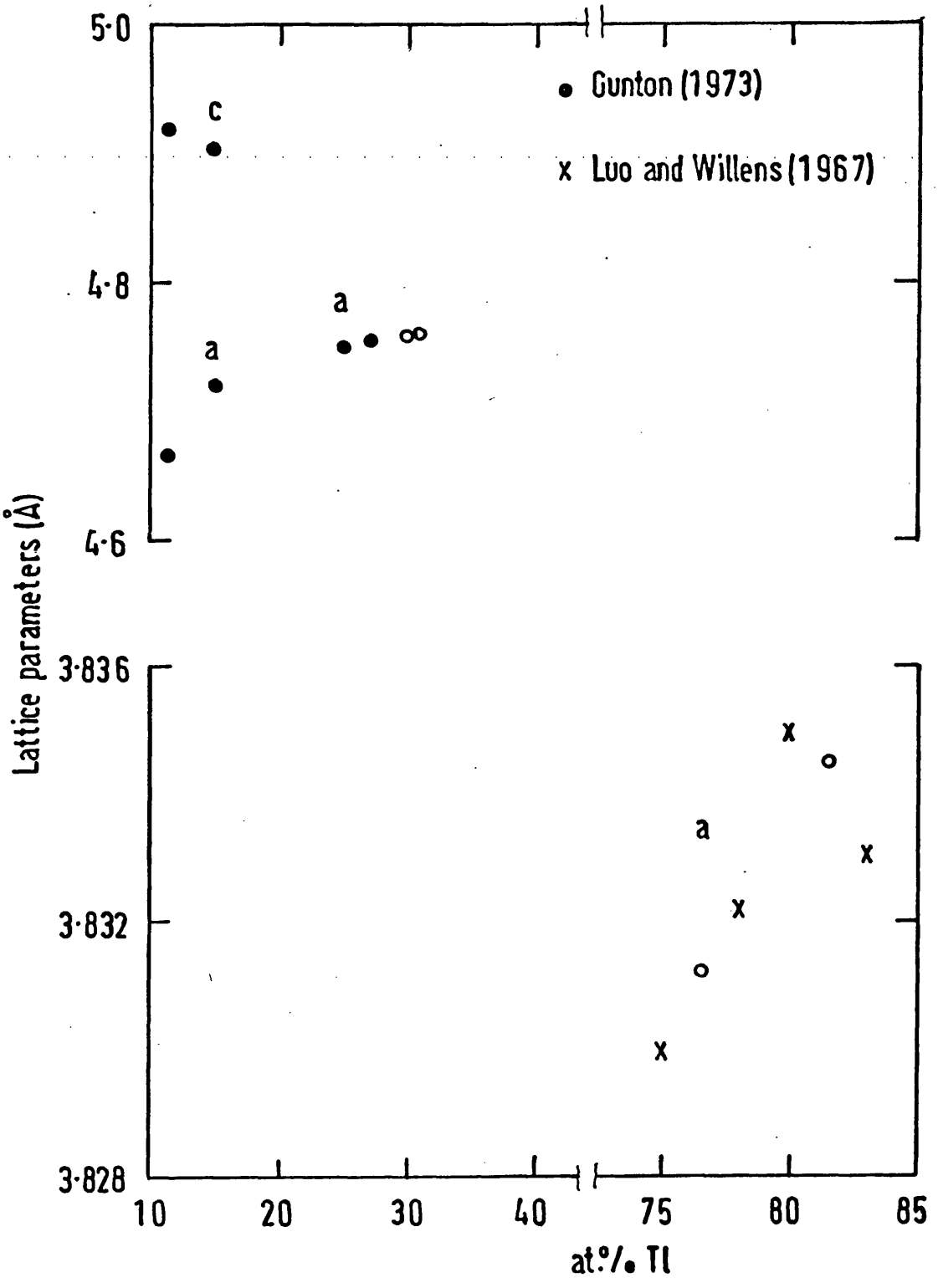

Figure 4.17: Room temperature lattice parameters of In-Tl alloys.

Table 4.15

Room temperature density and lattice parameters of In-Tl alloys

Composition (at% Tl)	Lattice parameter a (Å)	Floatation density ρ (gm. cm^{-3})	X-ray density ρ_x (gm. cm^{-3})
30 } fcc	4.758±0.002	8.72 ± 0.02	8.735 ± 0.011
31 } fcc	4.760±0.002	8.80 ± 0.02	8.779 ± 0.011
76.5 } bcc	3.8312±0.0005	10.80± 0.02	10.824± 0.004
81.5 } bcc	3.8345±0.0005	11.04± 0.02	11.060± 0.004

Debye-Scherrer powder photographs of the alloys investigated here (5, 17 and 75 at% Pb) are reproduced in Figure 4.14. Figure 4.15 shows the diffraction pattern of a 13.2 at% Pb alloy which contains lines due to both the tetragonal phases. The measured lattice spacings are in good agreement with those of Tyzack and Raynor (1954a,b) and are plotted in Figure 4.18. X-ray and floatation densities are listed in Table 4.16 and again there is good agreement between the two.

4.6 Orientation of single crystals

This has been accomplished by back-reflection Laue photography (Barrett and Massalski 1966) to an accuracy of $\pm \frac{1}{2}^{o}$ using a Phillips three-circle goniometer. White X-radiation from a copper or cobalt target and a specimen-to-film distance of 3 cms have been used.

4.6.1 Cubic alloys

Cubic In alloys of this work belong to the point group m3m and possess the following symmetry elements: three tetrad axes, four triad axes, six diad axes, three cubic planes of symmetry and six dodecahedral planes of symmetry (Figure 4.19). Three directions - [100], [110] and [111]- have been chosen for ultrasonic studies (see table 3.3). These directions are part of the equivalent tetrad, diad and triads respectively (Figure 4.19). Laue photographs taken with the X-ray beam along these directions display 4-, 2- and 3-fold spot symmetries respectively. This leads to a straightforward orientation procedure.

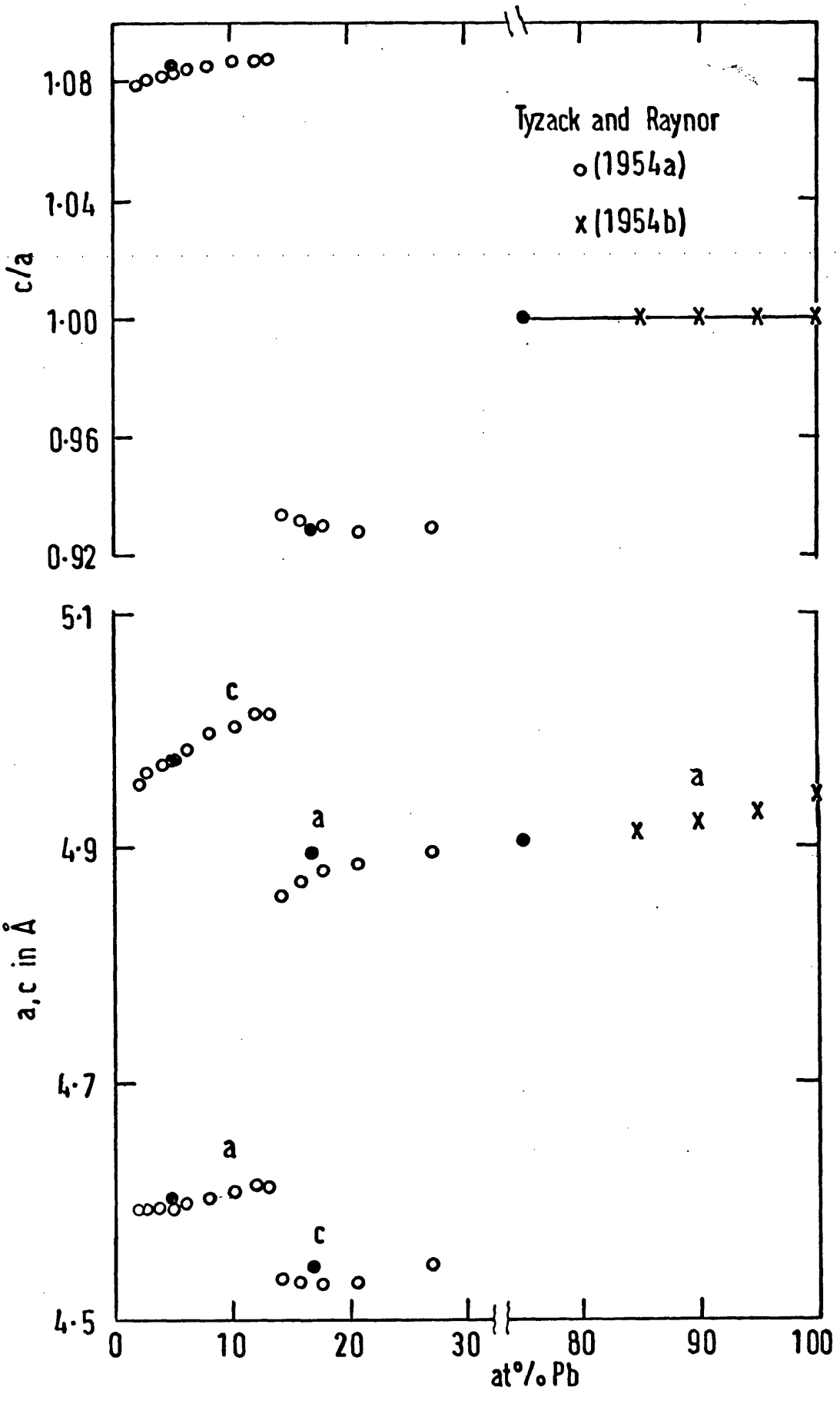

Figure 4.18: Room temperature lattice parameters of In-Pb alloys.

Table 4.16

Room temperature density and lattice parameters of In-Pb alloys

Composition (at% Pb)	Lattice parameters (Å)			Floatation density ρ ($gm.cm^{-3}$)	X-ray density ρ_x ($gm.\ cm^{-3}$)
	a	c	c/a		
5	4.6004 ± 0.0005	4.9748 ± 0.0005	1.081	7.54±0.02	7.535 ± 0.003
17	4.8924 ± 0.0005	4.5413 ± 0.0005	0.928	7.98±0.02	7.975 ± 0.003
75	4.9044 ± 0.0005	-	1	10.35±0.02	10.366 ± 0.003

4.6.2 Tetragonal alloys

Tetragonal In alloys studied here retain the In structure - point group 4/mmm. The symmetry elements of this class are: a tetrad axis at the intersection of two pairs of planes of symmetry, two pairs of horizontal diad axes normal to these planes and a plane of symmetry normal to the tetrad (Figure 4.20). Four directions - [001], [100], [110] and [011] - have been used for elastic constant measurements (see Table 3.2). Figure 4.20 shows that [100] and [110] are both diad directions - Laue photographs taken with the X-ray beam along either of these directions will result in a spot pattern of mm symmetry. These two diad directions have been distinguished by making use of the pseudo 3-fold symmetry displayed by the [111] direction in these nearly cubic ($\frac{c}{a} \sim 0.928 - 1.08$) tetragonal alloys. The orientation procedure consisted in locating the tetrad - [001] - and the two different axes showing mm symmetries. If a rotation from an axis of mm symmetry towards the tetrad passed through a pseudo 3-fold axis, then that axis of mm symmetry was designated as [110] and on the other hand if the rotation passed through an axis of m symmetry - [011] - then the axis of mm symmetry in question was [100].

4.6.3 In - 4.4 at% Cd alloy

Sharp and well defined Laue spots on the back-reflection photographs (Figures 4.21 - 4.26) are characteristic of good strain-free single crystals except in the case of In - 4.4 at% Cd alloy wherein the spots are split (Figure 4.22) - the paired diffraction spots correspond to a banded twin lamellar fct structure similar to that of the well-studied In-Tl banded twin fct structure (Bowles, Barrett and Guttman 1950, Burkart and Read 1953 and Basinski and

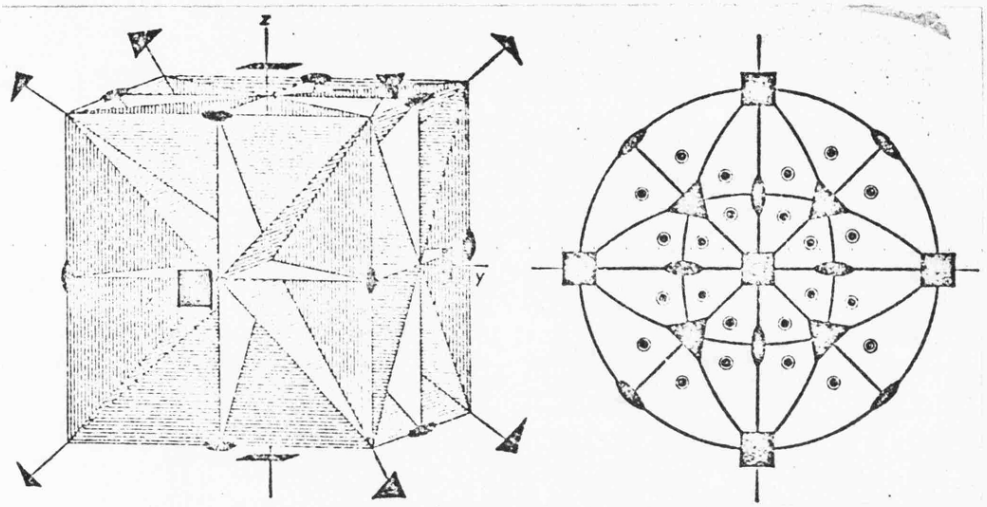

Figure 4.19: Symmetry elements of cubic crystals belonging to the m3m class.

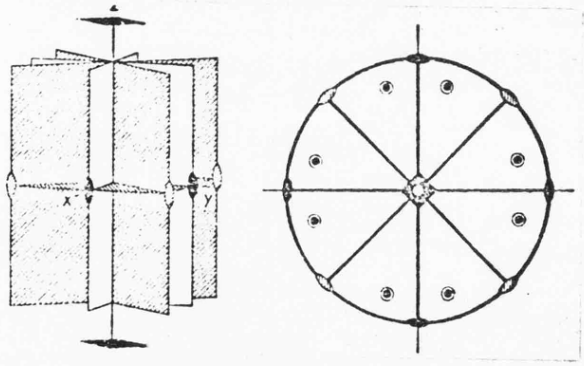

Figure 4.20: Symmetry elements of tetragonal crystals belonging to the 4/mmm class.

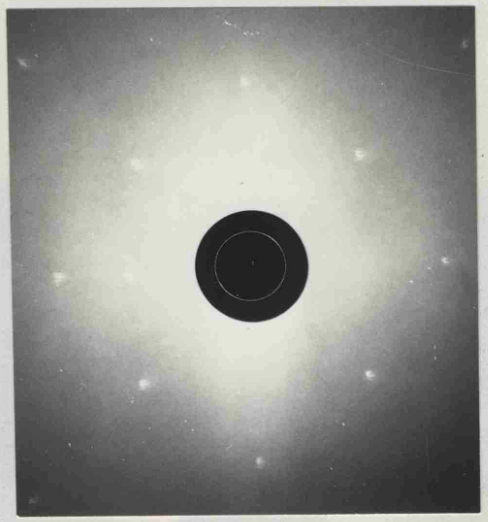

(a)

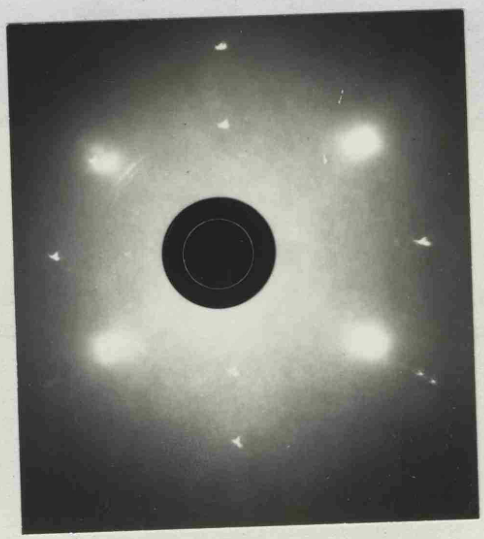

(b)

Figure 4.21: Back-reflection Laue photographs of fct In - 3.4 at% Cd alloy taken with the X-ray beam incident in (a) [001] and (b) [110] directions.

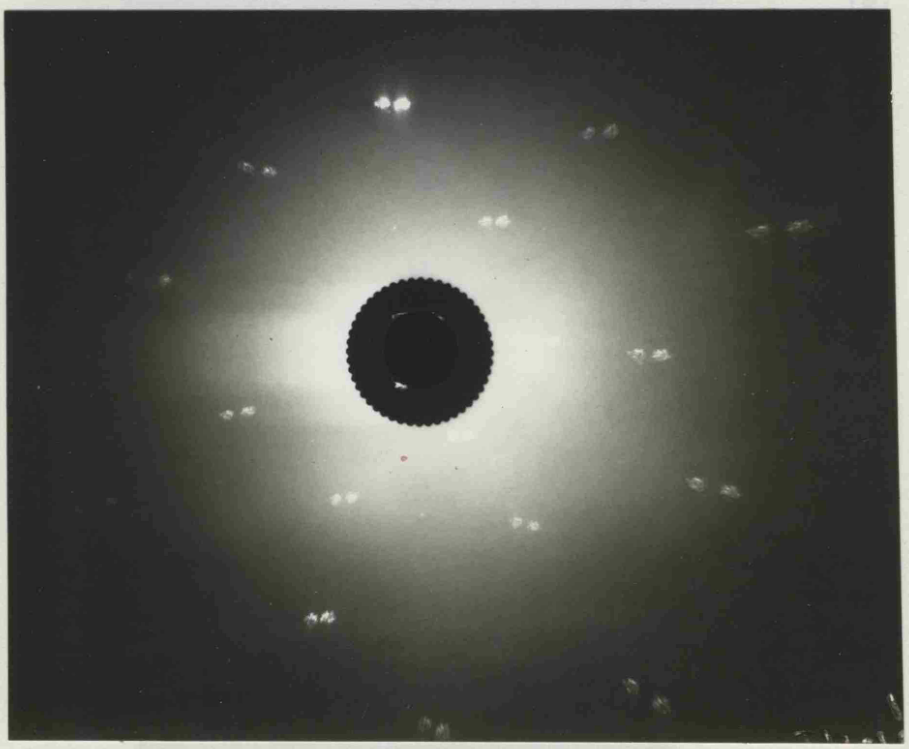

Figure 4.22: Laue photograph of In - 4.4 at% Cd alloy. The paired diffraction spots correspond to a banded twin lamellar fct structure.

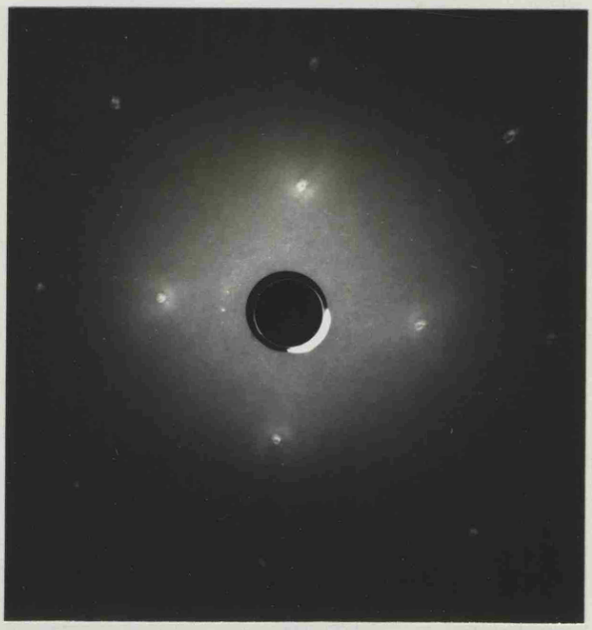

(a)

(b)

Figure 4.23: Laue photographs of fcc In - 6.5 at% Cd alloy with the X-ray beam incident in (a) [001] and (b) [110] directions.

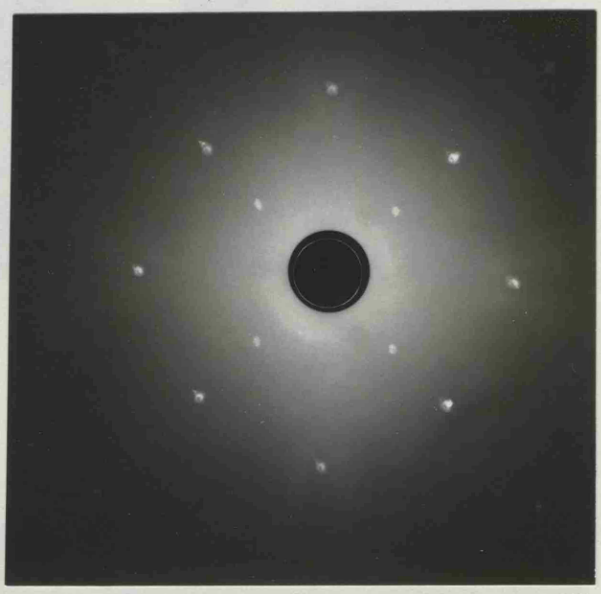

Figure 4.24: Back-reflection X-ray photograph of bcc In - 76.5 at% Tl alloy with the X-ray beam parallel to [001] direction.

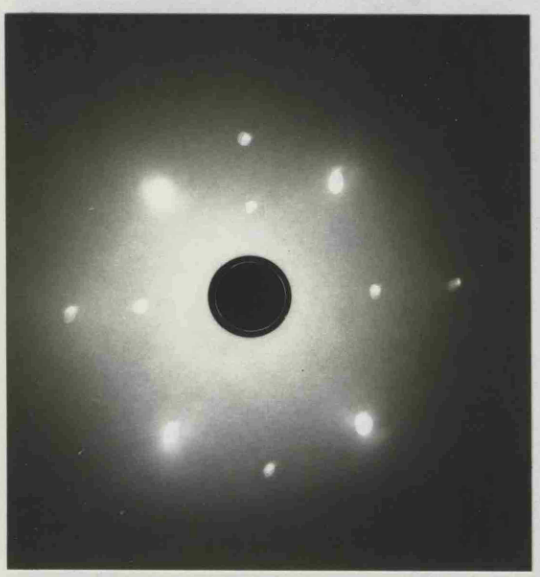

(a)

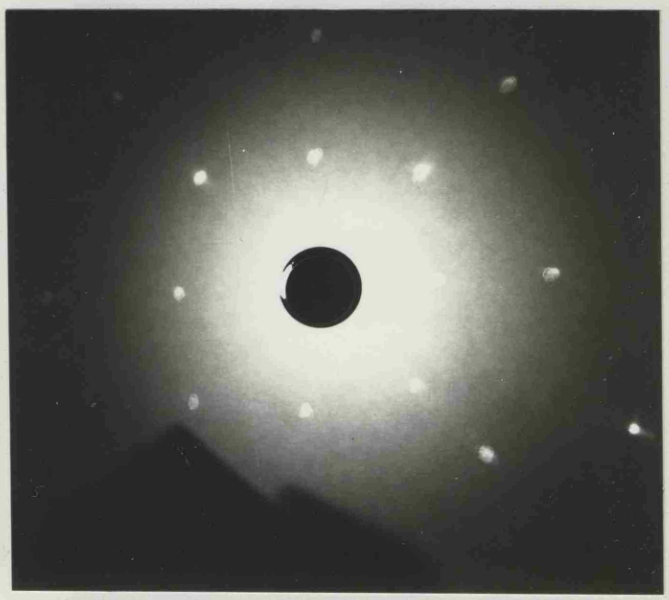

(b)

Figure 4.25: Laue photographs of In-Pb alloys - (a) 5 at% Pb (fct, c/a > 1), X-ray beam incident in [110] direction (b) 17 at% Pb (fct, c/a < 1), X-ray beam incident in [001] direction.

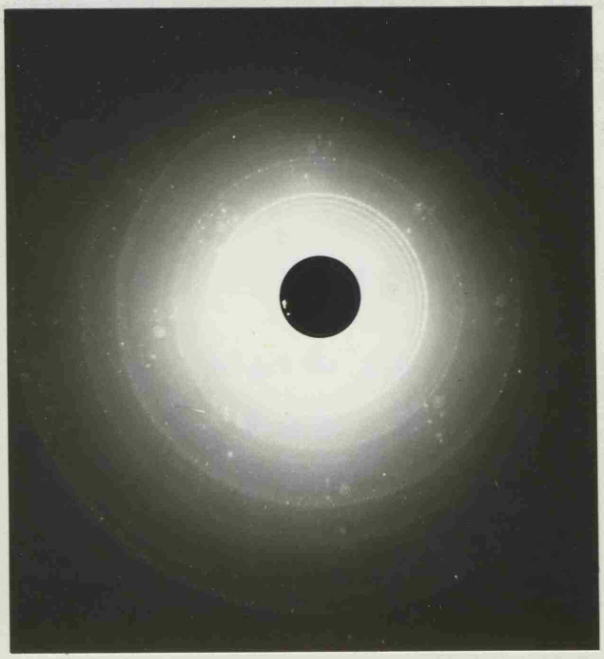

(a)

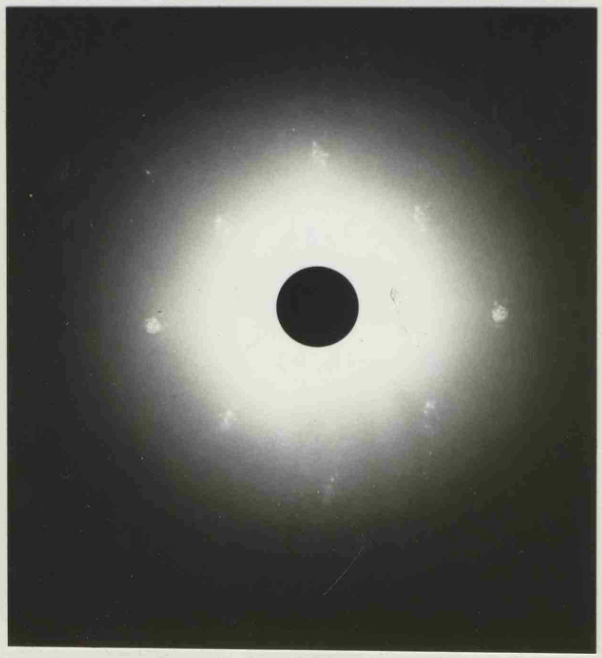

(b)

Figure 4.26: Laue photographs of fcc In - 75 at% Pb alloy with the X-ray beam incident in [001] direction - (a) before and (b) after electropolishing (see Section 4.5.2).

Christian 1954). Also, identical Laue photographs were obtained at different points along the alloy sample suggesting that the transformation had ensued by passage of a single interface. As regards the crystal orientation, the twinned fct alloy was treated just like the other fct alloys.

CHAPTER 5

ULTRASONIC EXPERIMENTATION

5.1 Introduction

Ultrasonic wave velocity and attenuation in In alloys have been measured as a function of temperature with particular emphasis on their behaviour in the vicinity of structural phase transformations. In this Chapter, the operating principles and the instrumentation of the ultrasonic pulse techniques used for measuring these wave propagation parameters will be described. Errors and uncertainties in the ultrasonic measurements will also be discussed.

5.2 Pulse ultrasonic measuring techniques

5.2.1 The pulse echo method

The pulse echo method has mainly been used here for attenuation measurements. It also forms the basis of the pulse superposition technique described in Section 5.2.2.

5.2.1.1 Principle of the single ended technique

An ultrasonic wave of the requisite frequency and polarisation is propagated into the bulk of a specimen with plane parallel end faces by exciting an appropriate piezoelectric transducer acoustically bonded to one of the specimen end faces (Figure 5.1). The r·f oscillations used for driving the transducer may be tuned either to the transducer resonant frequency or an odd harmonic of this. Reflection of the ultrasonic wave occurs at the lower end face of the specimen because of the high acoustic impedance mismatch and returns to the transducer-specimen interface where some of the acoustic energy is converted into electrical impulses and with the help of suitable electronic circuitry can be displayed in a detected form on an oscilloscope. Meanwhile the rest of the acoustic energy - other than that converted into electrical form-is reflected at the

transducer-specimen interface and proceeds towards the lower end face of the specimen where it again suffers reflection and is picked by the transducer as before. What one observes on the oscilloscope is therefore a series of equally spaced decaying echoes (Figure 5.2). The time interval t between the successive echoes is the time taken by the ultrasonic wave for a round trip in the specimen and if ℓ is the wave path length – being the distance of separation between the specimen end faces – then the ultrasonic wave velocity v is given by

$$v = \frac{2\ell}{t} \qquad (5.1)$$

The extent of the decay of the echoes depends on the ultrasonic wave absorbing mechanisms of the specimen. If V_1 and V_2 are the peak amplitudes of the successive echoes, then

$$\alpha \text{ (dB/cm)} = \frac{20}{2\ell} \log_{10} \frac{V_1}{V_2} \qquad (5.2)$$

is a measure of the attenuation of the ultrasonic wave.

5.2.1.2 Instrumentation and operation

A block diagram of the single ended pulse echo system is given in Figure 5.3. The pulse modulator-receiver set up in conjunction with the plug-in provides a r·f pulse source up to 1Kw with the total receiver gain at about 110 dB. The use of push-pull circuitry using ceramic tetrodes confers excellent modulation flexibility upon this unit. R·f pulse output from the plug-in, having a carrier frequency of between 10 and 20 MHz, a pulse duration of about 1μs and peak-to-peak voltage of about 1 Kv was used to drive X-cut longitudinal and Y-cut shear gold plated quartz transducers every milli second. High attenuation in the In alloy specimens meant that use of higher harmonics to drive the 10-20 MHz

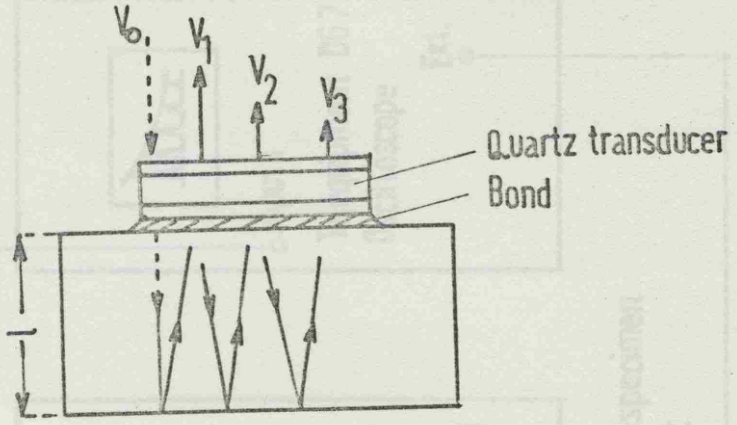

Figure 5.1: An ultrasonic specimen arrangement.

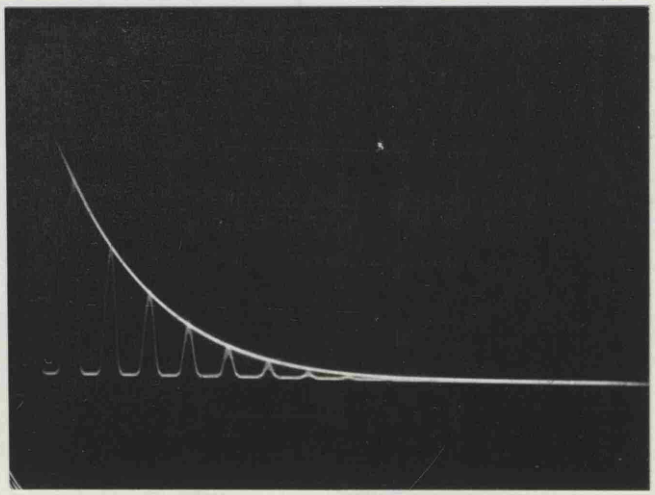

Figure 5.2: A typical pulse echo display.

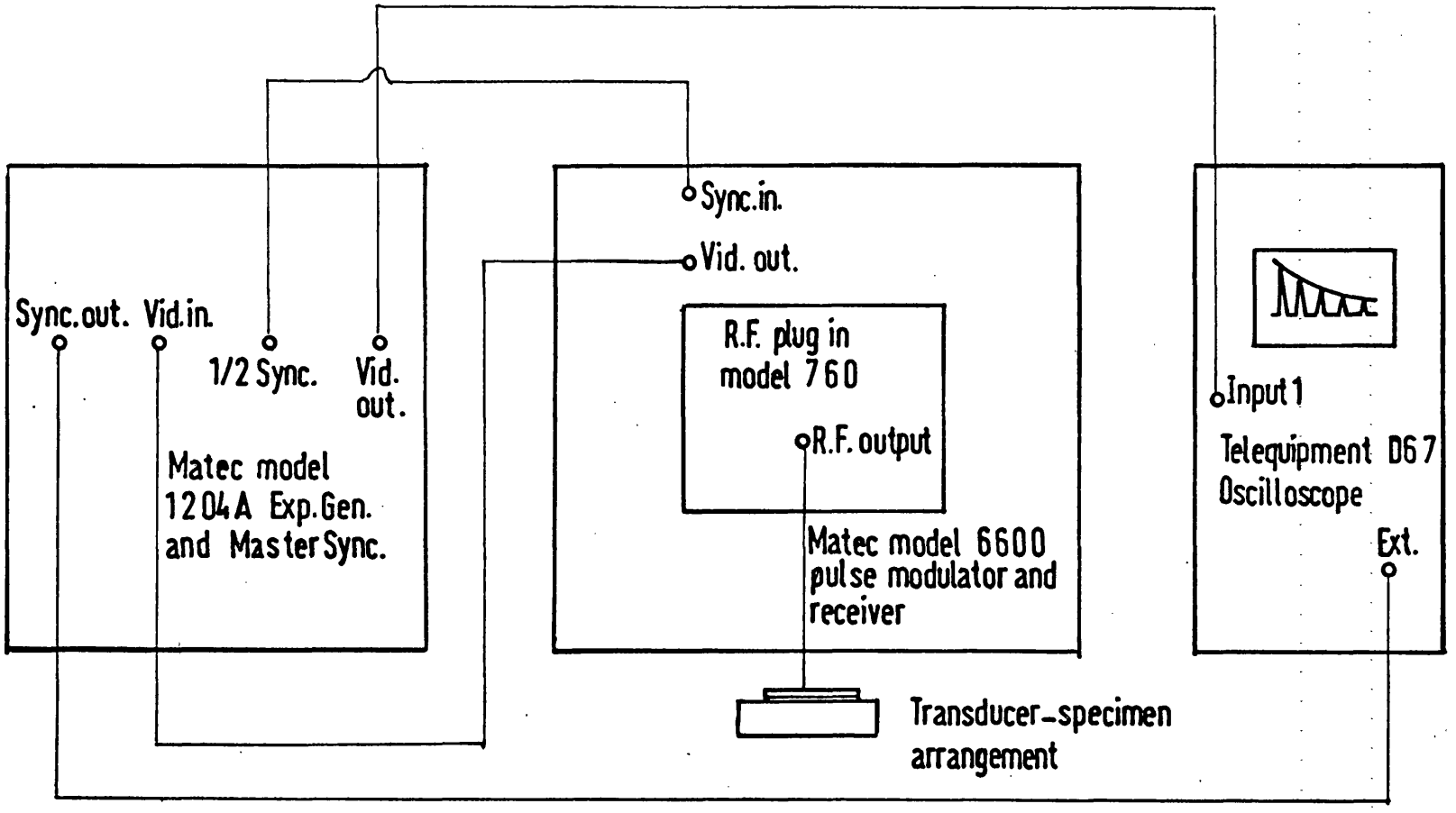

Figure 5.3: Block diagram of the pulse echo system.

resonant quartz transducers was not always rewarding. The reflected ultrasonic wave picked up by the transducer as a series of decaying echoes was then amplified by the r·f pre-amplifier included in the plug-in unit and the pre-amplified signals were then converted to an intermediate frequency (I·F) of 60 MHz for further amplification by the I·F amplifier located in the main frame of the pulse modulator-receiver unit. At the I·F amplifier output, the echoes were amplitude detected and filtered. The buffering of the resulting video envelope of the echoes with a compound emitter follower meant that the output impedance was sufficiently low to allow the use of a co-axial cable for coupling the echoes to the Master synchroniser/ Exponential generator unit (used for attenuation measurements). This unit generates synchronising and timing pulses and a calibrated exponentially decaying waveform with variable decay rate. The Master synchroniser/Exponential generator unit was operated from its internal synchronous source together with an oscilloscope with the synchronous source triggering the oscilloscope time-base. This mode of operation enabled the decaying ultrasonic pulse echo train to be simultaneously displayed with the delay generator operated, calibrated exponential waveform. This waveform could be fitted to the pulse echo train envelope by suitable potentiometric dial controls. In this way, attenuation α of up to 4.2 dB/μsec could be measured. Using the leading edge of the exponential waveform traversed with a potentiometric control with the head calibrated in μsecs (up to 1000 μsecs) it was also possible to make velocity measurements within the following limitations: (i) absolute velocity measurements to an accuracy of $\pm$1% and (ii) velocity changes of about 1 part in 10.

5.2.2 The pulse superposition method

Better sensitivities and accuracies are required for ultrasonic wave velocity measurements as a function of temperature or through a structural phase transformation; for instance, velocity change with a temperature change of $10^{o}K$ for most solids is less than a few parts in thousand. The pulse superposition technique was developed by McSkimin (1961) to meet these requirements and in the version used here, sensitivities of 1 part in 10^{5} can be achieved in low attenuation solids. Versions with better sensitivities have also been reported (McSkimin and Andreatch 1967, Holder 1970 and Ishizaki, Spain and Bolsaitis 1976).

5.2.2.1 Principle of the method

The application of a short duration r·f pulse to the transducer-specimen arrangement shown in Figure 5.1 will result in a series of echoes V_1, V_2, V_3 etc. If now an identical sequence of pulses is generated after every T seconds where T is approximately equal to an integral multiple p of the round trip delay in the specimen, then for example for p = 2, this will result in all odd numbered echoes to appear in the same time 'compartment' and these echoes tend to interfere with each other. In the pulse superposition method, the repetition frequency of the r·f pulses (T^{-1}) is critically adjusted so that the echoes tending to interfere do so constructively, i.e., the echoes arrive at the transducer in phase so that a maximum signal is obtained for detected overlapping echoes. This sequence is illustrated in Figure 5.4. When critically adjusted for pulse superposition, the pulse repetition frequency T^{-1} is related to the echo time interval t (and hence the ultrasonic wave velocity $v = \frac{2\ell}{t}$):

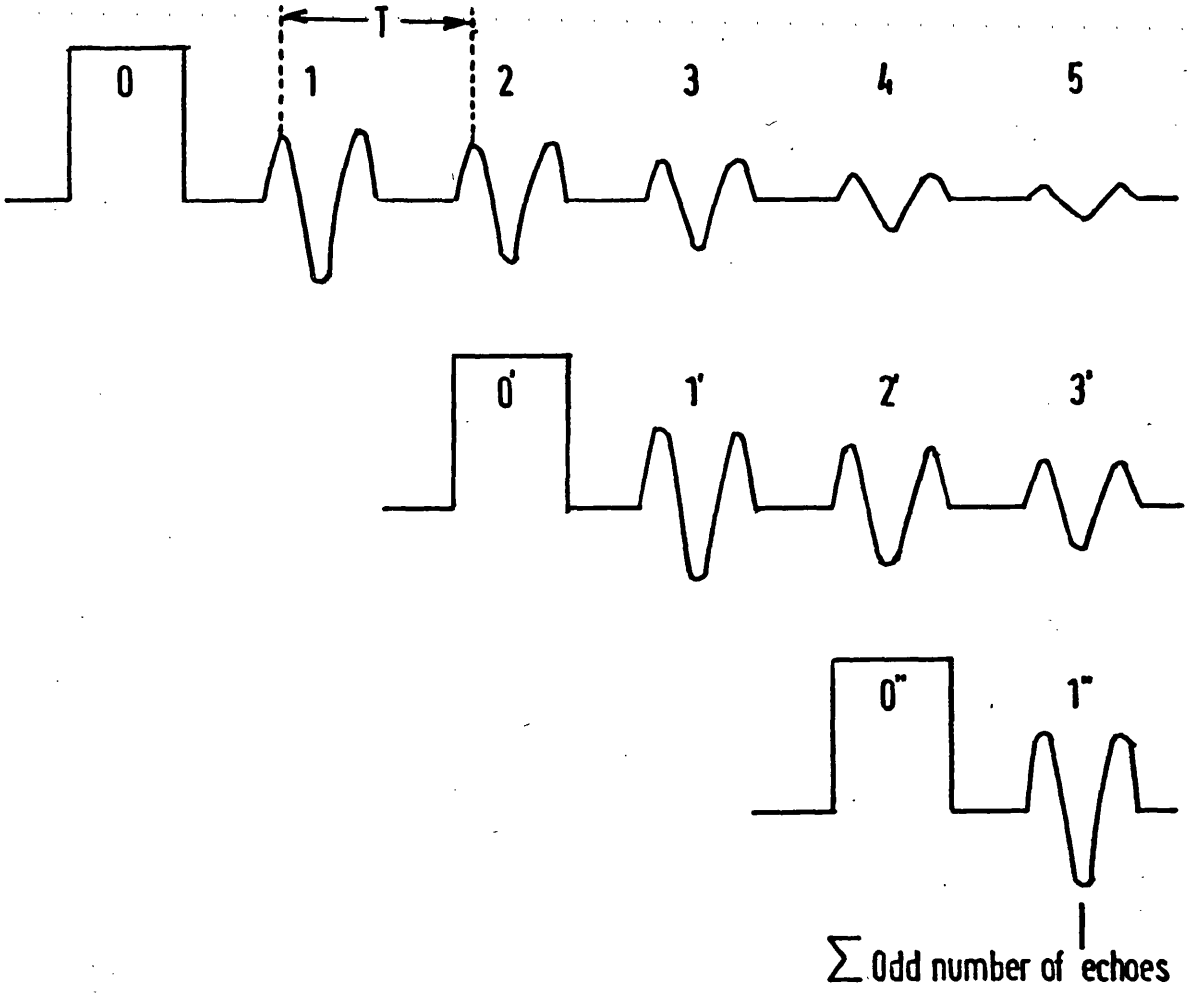

Figure 5.4: Pulse superposition for p = 2.

$$T = pt - \frac{p\phi}{360f} + \frac{n}{f} \qquad (5.3)$$

where ϕ is the phase angle between the incident and reflected waves at the transducer coupling interface, f is the frequency of the r·f oscillations used for driving the transducer and n is a number which can have positive or negative integral values or zero. Since the pulse repetition frequency T^{-1} – governing the velocity measurement – can be set by high stability precision frequency synthesisers, very small velocity changes can be measured.

5.2.2.2 Instrumentation

The pulse superposition system used in the present work was constructed by C. A. Maynell (1972), J. M. Farley (1973) and R. I. Cottam (1973). A block diagram of the system is shown in Figure 5.5. The r.f pulses of frequency f used for exciting the resonant quartz transducer are generated by the pulse oscillator which has a range of 5 - 84 MHz set by 7 standard r·f coils and an adjustable peak-to-peak voltage of 0-500v. The pulse oscillator is operated in the externally modulated mode and the pulse width and the pulse repetition frequency T^{-1} are controlled by the unit pulse generator. The triggering source for the unit pulse generator is the frequency synthesiser which gives a sine wave output of up to 8v peak-to-peak amplitude over a frequency range 0.1 Hz to 2 MHz with an eight digit frequency selection in steps of 0.1 Hz. The frequency synthesiser in effect sets the pulse repetition frequency T^{-1}. The manufacturer's specification for the synthesiser frequency stability is: 1 part in 10^7 in 5 min., 2 parts in 10^8 per day and 5 parts in 10^9 after three months' uninterrupted operation. The ultrasonic echoes generated in the specimen in a manner similar to that described in Section 5.2.1.1

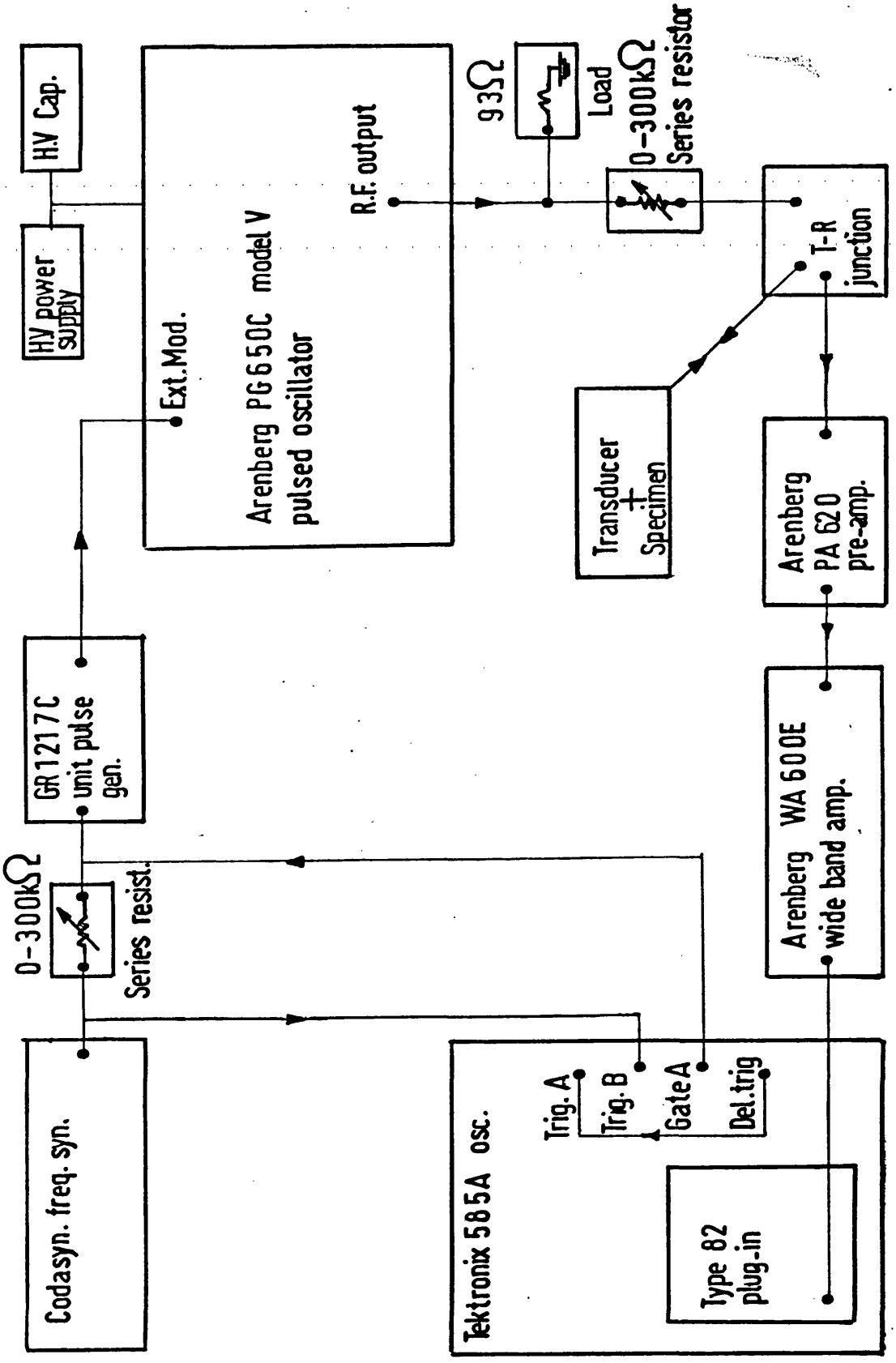

Figure 5.5: Block diagram of the pulse superposition system.

for the single ended pulse echo system are first amplified by a pre-amplifier tunable over a frequency range of 5 - 60 MHz and then by a wide band amplifier which has a gain of 70 dB between 5 and 60 MHz. The wide band amplifier is also the demodulating unit and the detected echoes are displayed on the Tektronix oscilloscope. The pulse superposition condition is illustrated in Figure 5.4 for the case of p = 2 wherein all the even numbered echoes are obscured by the r·f pulses and the odd numbered echoes appear in the gaps between the pulses being superimposed. If p = 1, then clearly, all the echoes will be obscured by the r·f pulses themselves which means for this case the superposition of the echoes can be observed only if the sequence of the input pulses is interrupted to allow for the observation of the echoes from the earlier pulses. This situation is tackled with the help of facilities available on the Tektronix oscilloscope and will be explained in the next Section.

5.2.2.3 Operation

For low repetition frequencies T^{-1} ($\sim$ 1 KHz), the pulse superposition system of Figure 5.5 is analogous to the pulse echo system described in Section 5.2.1 and an approximate value of the echo time separation t can be obtained. From this, an approximate value of the pulse repetition frequency T^{-1} can be found. The generator synthesiser is set to read this value and the wide-band amplifier detected echo output is displayed on the oscilloscope using the B timebase. Using the A timebase and the'B intensified by A' display mode, some of the r·f pulses which are to be removed from the input sequence are intensified on the oscilloscope screen. The oscilloscope gate A output is a 50v pulse in synchronism with the timing and duration of the intensifying A timebase and application of

this gate output to the trigger input of the unit pulse generator causes the sine wave input from the frequency synthesiser to rise by 50v above the ground level for the duration of the gating pulse which means that over this duration, the unit pulse generator is not triggered and hence over the duration represented by the intensified part of the oscilloscope display, the r·f pulses are discarded from the input sequence. This enables the display of the superposed echoes from the preceding r·f pulses. The 'A delayed by B' mode facility of the oscilloscope allows the display of the intensified region of the trace on its own. The pulse repetition frequency is then critically adjusted digit by digit on the frequency synthesiser until the exact pulse superposition as evidenced by the maximisation in the amplitude of the superposed echo pattern on the oscilloscope display is obtained. The sequence of operations leading to the pulse superposition is sketched in Figure 5.6. The uncertainties involved in obtaining the correct pulse superposition condition will be discussed in Section 5.3.3.

5.3 Errors and uncertainties in the ultrasonic measurements

5.3.1 Errors in transit time and velocity measurements

The principal errors are due to: (i) phase changes at the transducer coupling interface, (ii) transducer thickness effects, (iii) diffraction caused by beam divergence, (iv) ultrasonic wave path length determination and (v) specimen non-parallelism.

5.3.1.1 Phase changes at the transducer coupling interface

The reflection phase shift at the free end of the specimen is zero because the acoustic impedance mismatch between the specimen and air is effectively infinite. But at the transducer end there

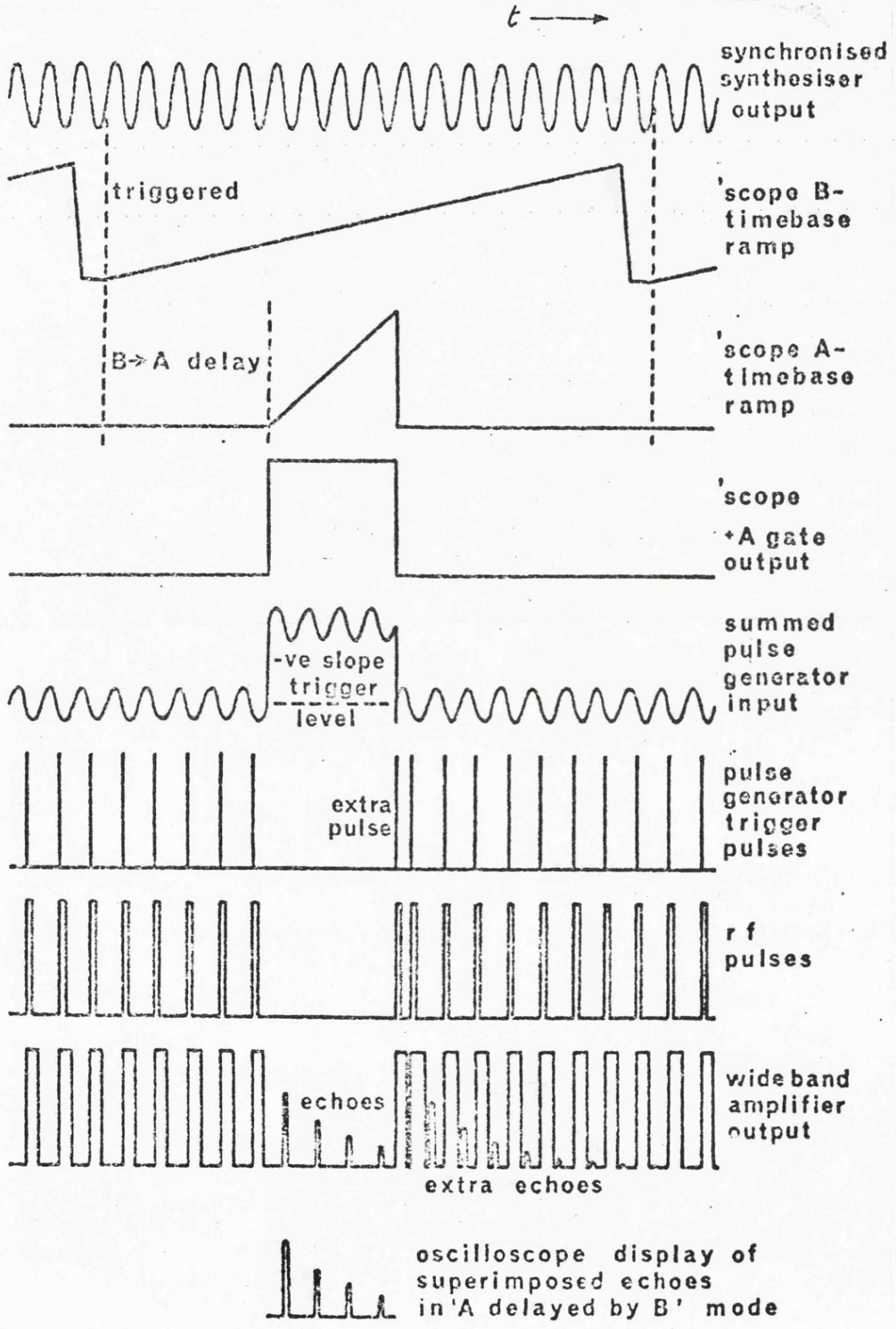

Figure 5.6: Operation of the pulse superposition system.

is an angle ϕ between the incident and reflected ultrasonic waves and a knowledge of this is necessary (see equation 5.3) for velocity measurements. For the quartz transducers and bonding agents - 'Nonaq' stopcock grease and 'Bedacryl 122X' (ICI compound)-used in this work, Maynell (1972) has estimated the delay due to the phase change at the transducer coupling interface as up to 0.03% of the measured transit time values.

5.3.1.2 Transducer thickness effects

The electronically measured ultrasonic wave transit time in a non-dispersive medium is a linear function of the transducer thickness under similar bonding conditions; with the thinner and hence higher resonant frequency transducers giving smaller transit times. This behaviour has been attributed to the transducer loading effects - the finite transducer thickness introduces a perturbation (Kammer 1964, Lichnowski 1975). To obtain the unperturbed transit time, measurements have been made using transducers of different thicknesses between 0.14 and 0.60 mm and the extrapolated value of the transit time corresponding to a transducer of zero thickness has been taken as the unperturbed value. Typically for a 10 MHz transducer, the unperturbed transit time was less than the measured value by about 0.3%.

5.3.1.3 Beam divergence

In general, an ultrasonic wave propagating in a specimen from an excited, finite area, circular disc transducer will not be confined to a collimated cylindrical column underneath but will spread as shown schematically in Figure 5.7. Papadakis (1966) has computed the phase advance for a pure longitudinal wave in various anisotropic media as a function of the distance of the echoes from the transducer

into the elastic half-space. The pulse superposition effectively adds many echoes of different phase advances weighted by the attenuation in the sample. In the case of low attenuation materials, this effect leads to different echoes in the train maximising at slightly different pulse repetition frequencies. In the case of the In alloys studied here, the attenuation was high and the maximisation of the echoes in the train was restricted to a single pulse repetition frequency.

5.3.1.4 Ultrasonic wave path length measurement

The determination of the ultrasonic wave velocity v given by equation 5.1 requires the measurement of the specimen thickness ℓ (Figure 5.1). This has been accomplished at room temperature with the aid of a dial gauge as well as a micrometer; an average of a number of thickness measurements made at various positions over the area subsequently covered by the transducer has been taken as the ultrasonic wave path length. A typical specimen thickness measurement was 0.2808 cm, standard deviation 0.0002 cm or 0.07%. The specimen thickness changes with the temperature and the extent of this change depends on the thermal expansion coefficients α_{ij}. So, in computing the temperature dependences of ultrasonic wave velocities, where available, the thermal expansion data has been used for correcting the path length changes. Further discussion pertaining to the thermal expansion corrections will be given in Chapters 6, 7 and 8. It will suffice here to add that existing thermal expansion data for a number of In alloys (Smith and Schneider 1964, Gunton 1973) indicate that the path length corrections are of the order of 0.25% per $100^{o}K$ change from room temperature.

5.3.1.5 Specimen non-parallelism

Specimens for ultrasonic measurements should have plane parallel end faces (Figure 5.1). Because of the soft nature of the In alloys, ultrasonic specimens have been prepared using a spark machine. Spark cut and planed specimen end faces had a parallelism of better than 3×10^{-4} radians. With such specimens – at typical transducer frequencies of 10 MHz – velocity errors due to non-parallelism effects are insignificant compared to other sources of error.

5.3.2 Errors in attenuation measurements

The attenuation measurements presented in this work are fairly limited in scope. This is mainly because of the high attenuation values encountered - an attenuation α, greater than 4.2 dB/μsec could not be measured with the equipment used here (Section 5.2.1.2). The measured α value is composed of the physically significant intrinsic losses and the apparent losses arising from errors, whose main cources are: (i) diffraction effects, (ii) non-parallelism and wedging effects and (iii) coupling losses. Using the analysis presented by Truell, Elbaum and Chick (1969), α_{error} in In alloy specimens due to the first two sources of error have been estimated as about 0.05 dB/μsec. Maynell (1972) has estimated the coupling loss errors as about 0.02 dB/μsec. The apparent loss part of the attenuation is therefore less than 0.1 dB/μsec. This is much smaller than the measured attenuation values of between 1.5 and 4.2 dB/μsec. The attenuation losses arising from measuring techniques are therefore insignificant compared to the intrinsic losses.

5.3.3 Uncertainty in the identification of the pulse superposition maxima

In the pulse superposition method, a series of superposition maxima are possible. This is explicit in equation (5.3). Here, the integer n represents the number of cycles of mismatch - when n = 0, there is no mismatch. Incorrect assignment of the n value to the observed superposition maxima will therefore lead to an error in the velocities calculated from equation (5.3) even after the necessary phase change correction has been made. McSkimin (1961) and McSkimin and Andreatch (1962) provide a method - the 'McSkimin ΔT criterion'- for identifying the n = 0 superposition maximum. However, this method has not been found very effective in cases where 'Nonaq' is the bonding agent (Maynell 1972, Farley 1973). For the majority of the present measurements, 'Nonaq' has been used for acoustic bonding and therefore a different identification procedure has been followed. The summed amplitudes of the echoes in the train at superposition maxima vary in a manner similar to that shown schematically in Figure 5.8 and the maximum amplitude corresponds to the n = 0 echo train (Cottam 1973). Use of this behaviour has been made here for identifying the n = 0 superposition maximum.

5.4 Measurement of the temperature dependences of the ultrasonic attenuation and wave velocities

From the equipment consideration, the temperature range (4.2 - 450^{o}K) of the ultrasonic measurements presented in Chapters 6, 7 and 8 fall into two categories: (i) 300 - 4.2^{o}K - the low temperature measurements have been carried out in a glass dewar system with pumping facilities using liquid nitrogen and helium as refrigerants

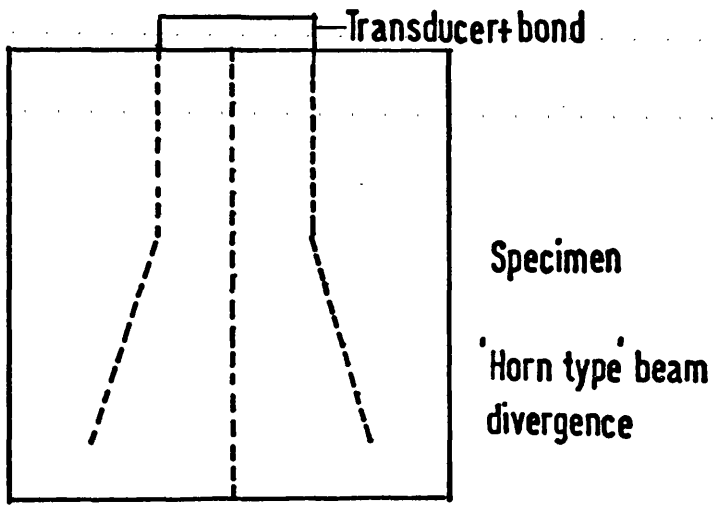

Figure 5.7: Schematic representation of beam divergence due to diffraction.

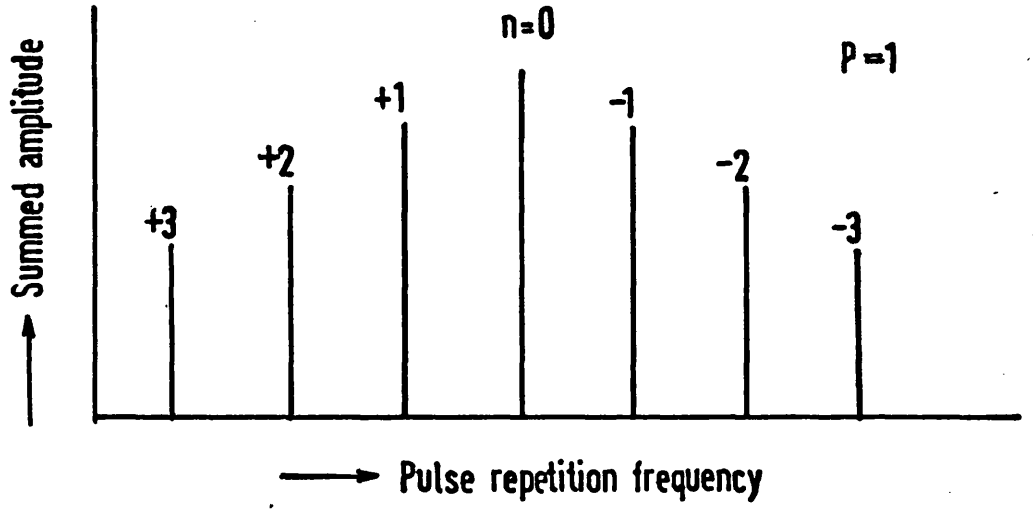

Figure 5.8: Summed amplitudes of the echo trains at superposition maxima (schematic).

and (ii) 300 - 450°K - the high temperature measurements have been accomplished in a thermostatically controlled oil bath.

5.4.1 The glass cryostat

The cryostat and the pumping arrangement is schematically shown in Figure 5.9. The system consists of a dewar pair - a hermetically sealed outer dewar exposed to the atmosphere and a loosely fitting inner dewar with a vacuum tight demountable top carrying the ultrasonic sample holder of a design similar to that used for room temperature and high temperature measurements (Figure 5.10) but with a thin walled stainless steel tubing framework to reduce heat leaks. Provision exists for evacuating the inter and inner spaces of the inner dewar. To carry out ultrasonic measurements as a function of temperature down to 77°K, the procedure consisted in positioning the sample holder completely inside the inner dewar and after securing an inter-space vacuum of better than 0.05 torr, liquid nitrogen flow to the outer dewar was regulated resulting in a drift assisted cooling of the sample. Typically a liquid nitrogen run lasted 4-5 hours. Cooling between 77 and 4.2°K was accomplished in steps. First of all, by controlled pumping of liquid nitrogen into the inner dewar, temperatures down to 45°K could be attained. Below this and down to 4.2°K cooling was achieved with helium gas and liquid helium syphoned into the inner dewar. The liquid helium flow could be regulated by adjusting the syphoning head. For this reason, the helium can was placed on a suitable fork lift.

The temperature measurements were made using a sensitive (± 0.01°K) 'Harwell' temperature controller (Oxford Instruments,

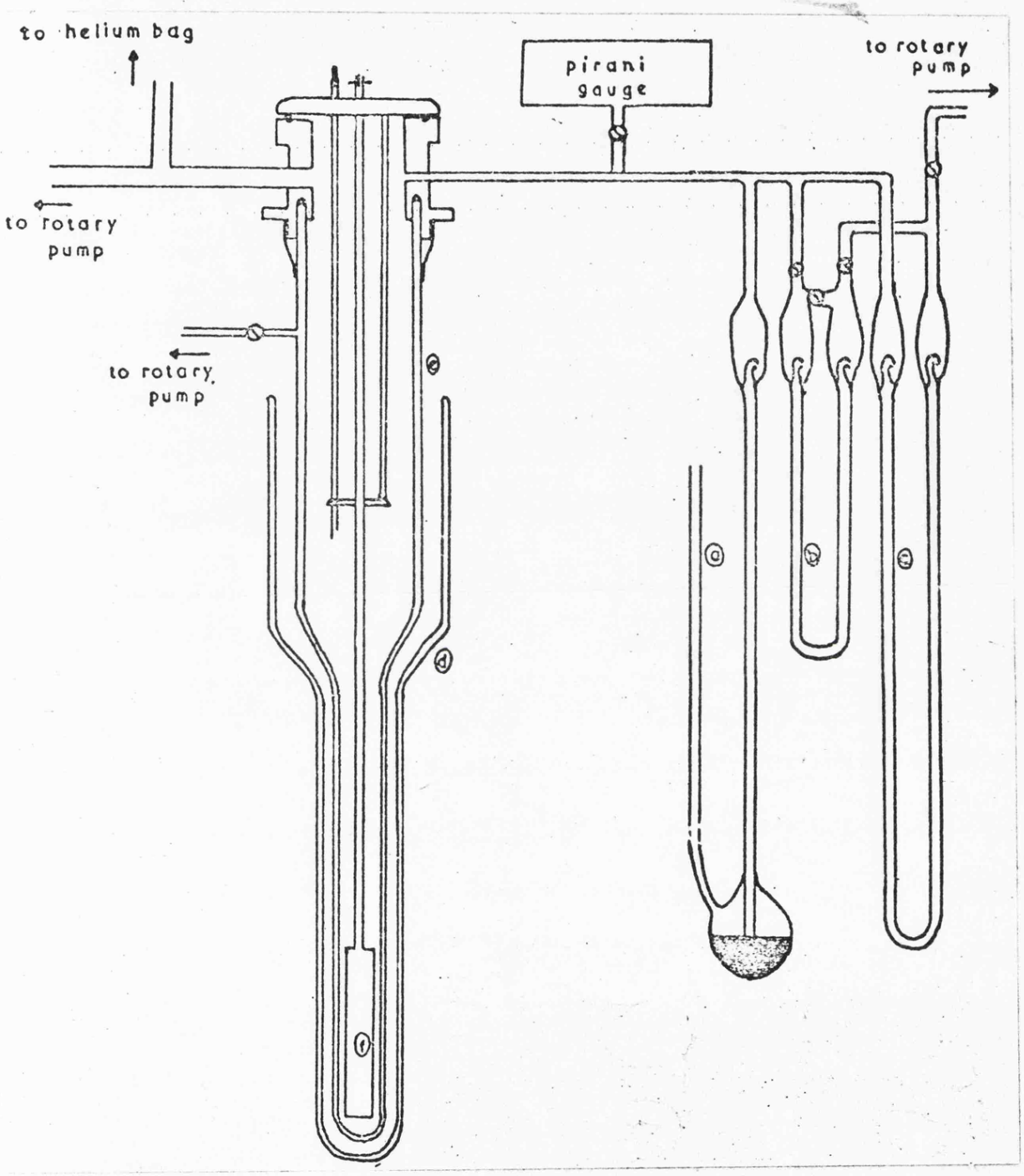

Figure 5.9: The glass cryostat - (a) Hg protection valve (b) oil manometer (c) Hg manometer (d) outer dewar (e) inner dewar (f) sample holder.

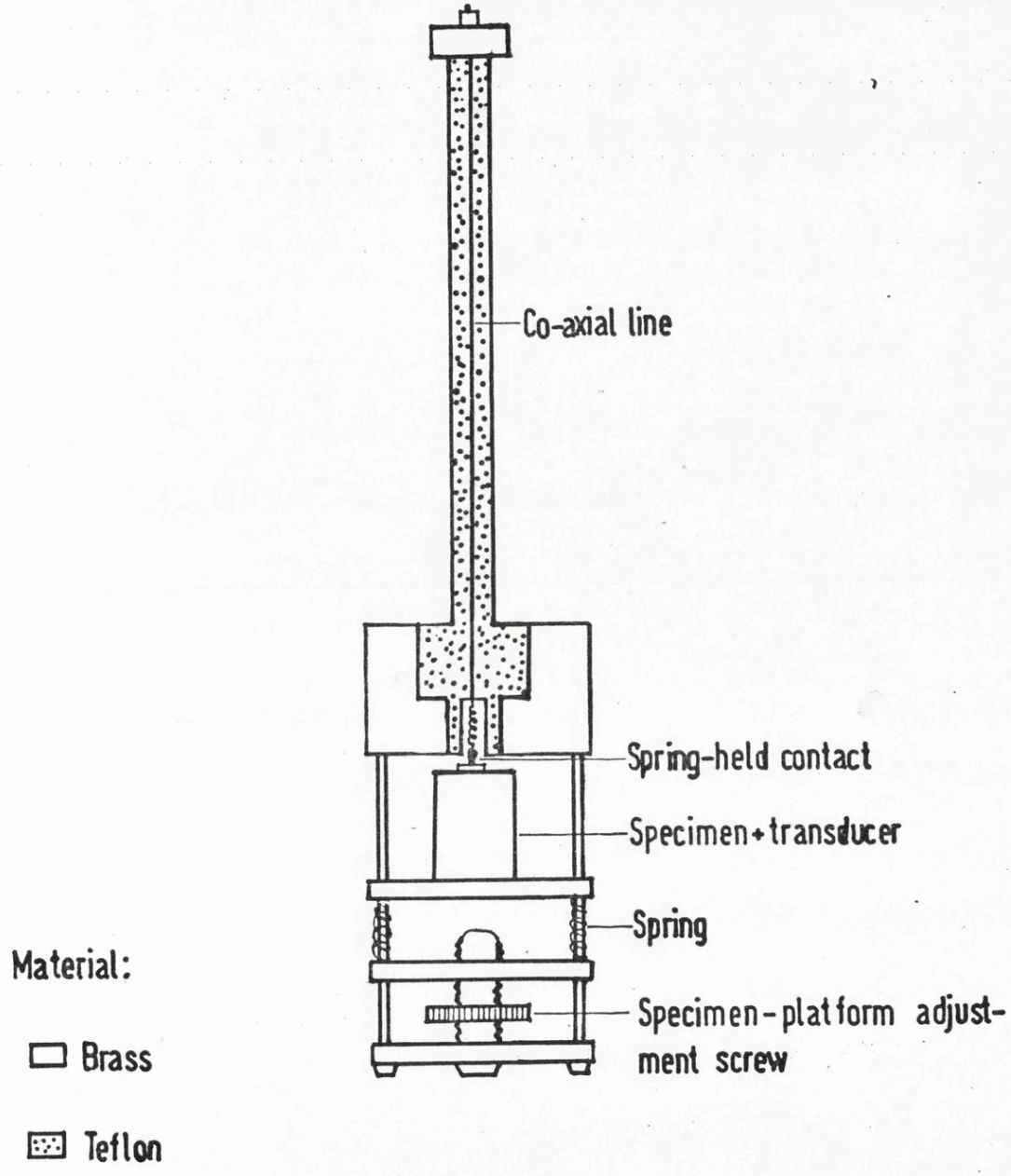

Figure 5.10: Ultrasonic specimen holder used for room temperature and high temperature measurements (not to scale).

model SO 974) with a calibrated copper-constantan thermocouple. With this instrument, temperatures are read on a manually operated potentiometric dial whose setting for null deflection on the instrument panel meter gives the temperature in terms of the thermocouple e.m.f. Down to 5°K the 'thermocouple output' selector can be used and below this, readings were taken with the 'Carbon resistance' selector. Temperatures below 4.2°K could also be measured from the helium vapour pressure readings monitored by the manometers (Figure 5.9). A digital temperature meter (Thor cryogenics, model 7010) was also used in addition to the 'Harwell' temperature controller. This meter, working on a gold-iron/Chromel sensor, with a read-out resolution of ±1°K largely served the purpose of providing a convenient visual aid for regulating the cooling rates especially in the vicinity of a phase transformation.

5.4.2 The oil bath

The high temperature measurements (300 - 450°K) were made in an oil bath. A motor-driven stirrer constantly stirred the heated oil and thus helped in minimising the temperature gradient across the sample. A thermostat arrangement controlled the power input to the oil bath. The sample temperature was measured with a mercury-in-glass thermometer with ½°C graduations.

CHAPTER 6

ACOUSTIC PHONON MODE SOFTENING AND THE STRUCTURAL TRANSFORMATION IN In-Cd ALLOYS

6.1 Introduction

Indium-rich, In-Cd alloys undergo an fcc to fct structural phase transformation. Ultrasonic wave velocity and attenuation measurements have been made in single crystals of both the fcc and fct phases, emphasis being placed on behaviour near the phase transformation.

6.2 Choice of the alloy composition

Three compositions - 3.4, 4.4 and 6.5 at% Cd-have been chosen for ultrasonic measurements. The significance of these compositions becomes clear on reference to the phase diagram (Figure 2.2). The 3.4 at% Cd alloy is a primary solid solution of In and crystallises in the fct In structure (point group 4/mmm) at room temperature. This alloy retains the fct structure right up to the melting point; however, near the melting point it is very close to the phase boundary. The 4.4 at% Cd alloy transforms during cooling from the melt to room temperature and at room temperature it has a twinned tetragonal structure. The transformation above room temperature (T_c = 380 ± 2°K) in this alloy has been studied. To assess the extent of acoustic phonon mode softening at the phase transformation, it is necessary to measure the temperature dependence of ultrasonic wave velocities in an fcc crystal which transforms below room temperature. Extrapolation of the transformation temperature versus alloy composition line on the previously published phase diagram suggested that a 6.5 at% Cd alloy - which crystallises in the fcc (point group m3m) phase at room temperature - should transform below room temperature. It does - at 232±2°K on cooling and this value of T_c obtained from the present ultrasonic

measurements is in good agreement with the extrapolated phase boundary (Figure 2.2). To sum up, the three alloy compositions chosen enable the phase transformation to be followed from both the fcc and fct phases.

6.3 Thermal expansion correction

Ultrasonic wave path length and sample density changes with temperature have been taken into account in computing the temperature dependences of the ultrasonic wave velocities and the elastic constants from the pulse superposition measured transit times. The necessary thermal expansion corrections have been made using the available data for the thermal expansion coefficients α_{ij}. α_{ij} is a symmetric second rank tensor and symmetry requirements reduce the number of principal coefficients to two (α_a and α_c : measured perpendicular and parallel to the c-axis respectively) in the case of fct crystals and to just one ($\alpha = \alpha_a = \alpha_c$) for fcc crystals. The thermal expansion coefficient α_ℓ in any arbitrary direction making an angle θ with the c-axis can then be expressed in terms of α_a and α_c as $\alpha_\ell = \alpha_a \sin^2\theta + \alpha_c \cos^2\theta$. α_{ij} values at 300°K have been obtained from Straumanis, Rao and James (1971) and their temperature dependences (Figure 6.1) away from T_c have been computed from

$$\begin{aligned} \alpha_a &= 0.0015T + 0.0004T^2 + C_1 \\ \alpha_c &= 0.0005T - 0.0004T^2 + C_2 \end{aligned} \qquad (6.1)$$

where T is the temperature in °K and the values of C_1 and C_2 - constants for any particular alloy composition-can be obtained by substituting the α_{ij} (300°K) values. The expressions in (6.1) have

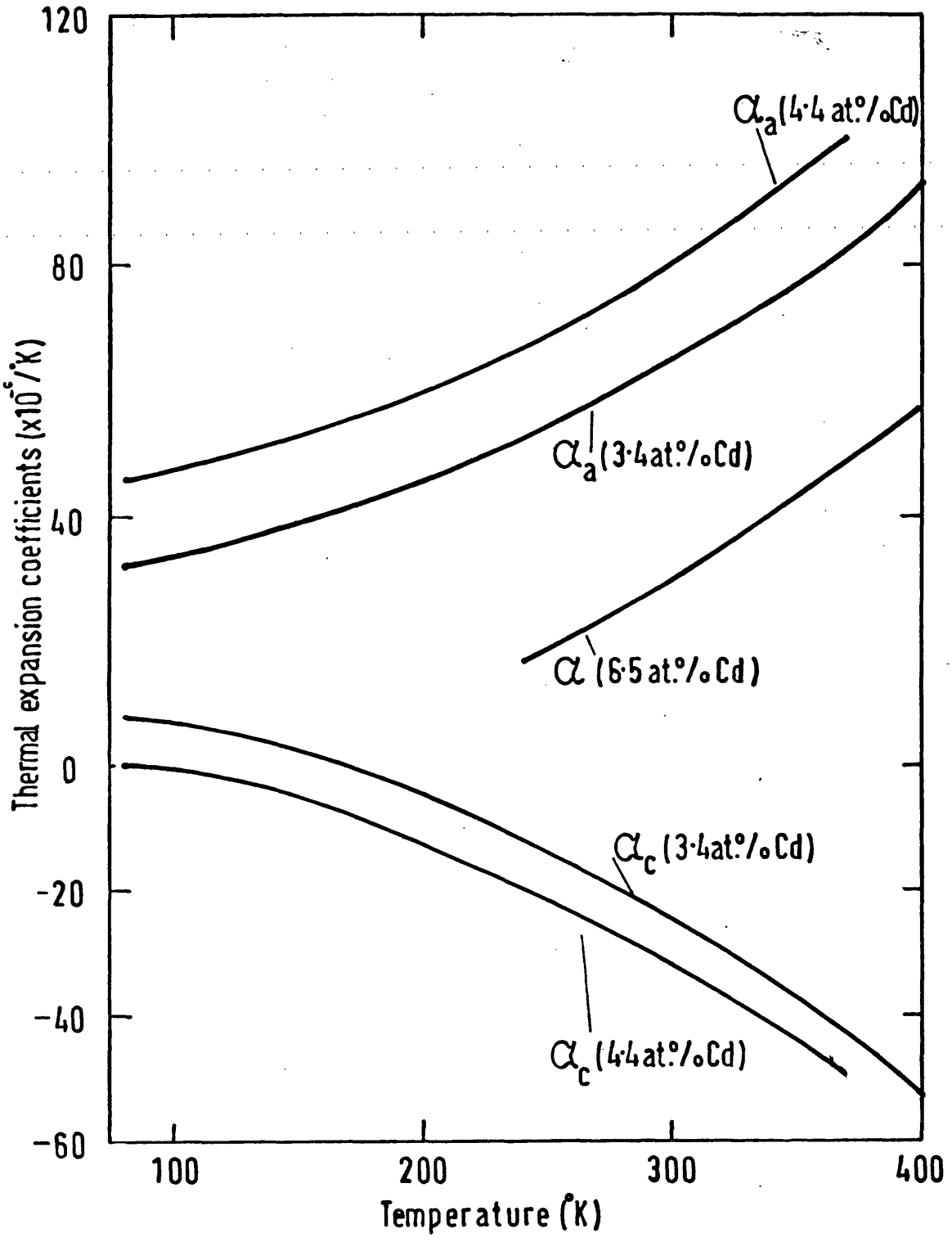

Figure 6.1: Estimated temperature dependences of the thermal expansion coefficients of In-Cd alloys.

been formulated making use of the thermal expansion measurements of Smith and Schneider (1964). The volume expansion coefficient $\beta = 2\alpha_a + \alpha_c$ has been used for correcting sample volume changes with temperature.

6.4 Ultrasonic wave velocities and the elastic constants

6.4.1 In - 3.4 at% Cd alloy

As noted earlier, this alloy retains the fct structure right up to the melting point ($T_m = 423 \pm 1.5^{\circ}K$) but near the melting point it is very close to the phase boundary. Therefore, the ultrasonic measurements made near T_m on this particular composition are of interest for two reasons: (i) is there any mode softening in the fct modification due to the incipient structural transformation (ii) are there any premelting effects? A number of ultrasonic wave velocity measurements in the vicinity of T_m are presented in Figure 6.2 - the propagation and polarisation directions have been labelled therein. These results have a bearing on the nature of the melting process. Lattice instability is often invoked in theories of melting. The inability of a liquid to support shear forces prompted Born (1939) to suggest that the velocity of shear waves should tend to zero as the melting point is approached. More recently, Ida (1969, 1971) based a theory of melting on critical behaviour of a vibrational elongation and Ishizaki, Bolsaitis and Spain (1973) have shown that Ida's approach leads to the requirement that either $v \to 0$ or $\left(\frac{\partial v}{\partial T}\right)_P \to -\infty$ as $T \to T_m$. The validity of these conditions has since been examined by measurements near T_m of ultrasonic wave velocities in In and its alloys with Tl (Chung, Gunton and Saunders 1976) and also in solid argon (Ishizaki, Bolsaitis and Spain 1976). Thus, Ida's theory has been put to the experimental test in both metallic

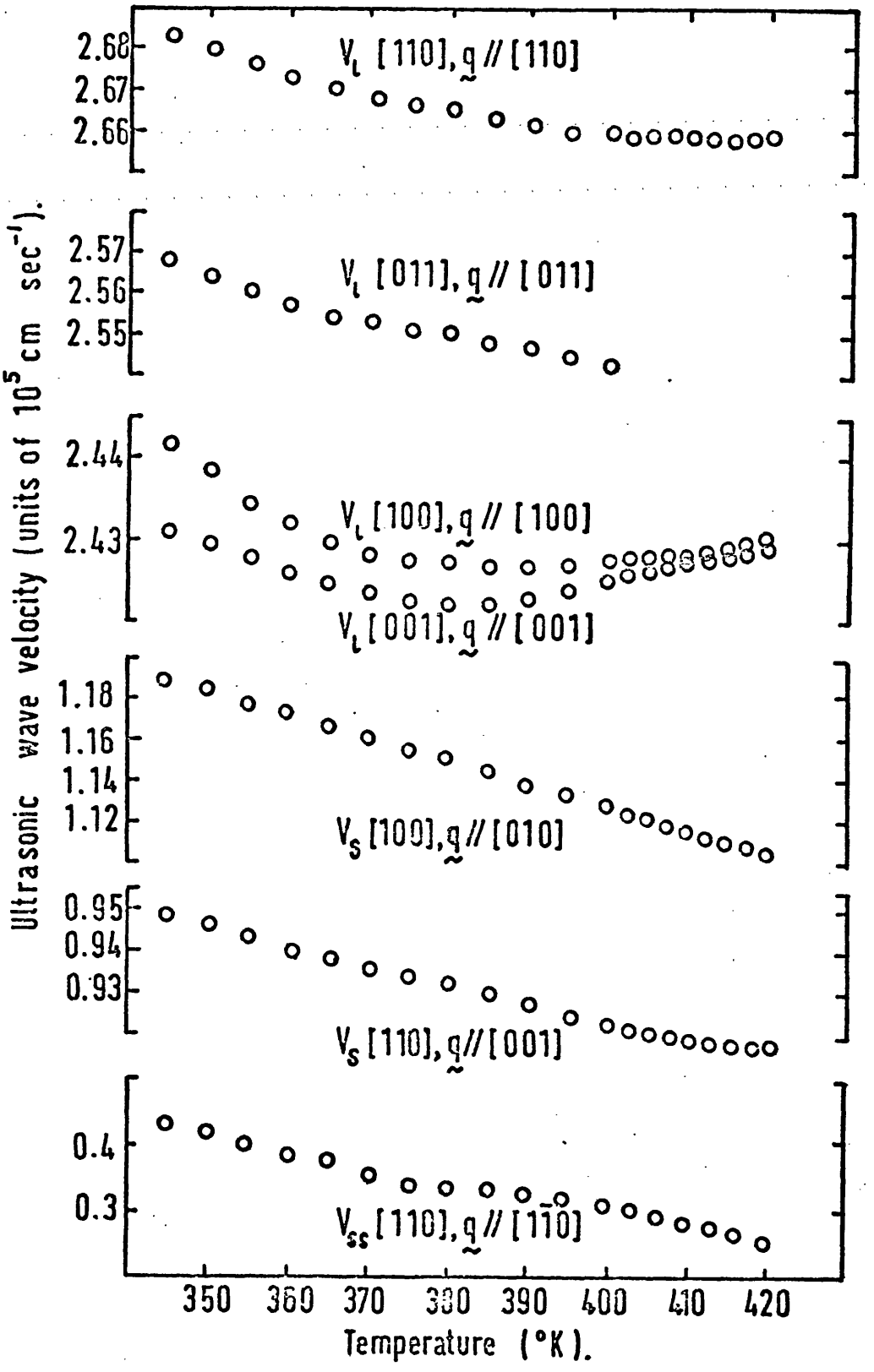

Figure 6.2: Ultrasonic wave velocities in the fct In - 3.4 at% Cd alloy between 340°K and the melting point T_m (423 ± 1.5°K).

crystals and in a van der Waals's bound solid. In neither type of material did the shear or longitudinal velocities tend to zero or their derivatives $\left(\frac{\partial v}{\partial T}\right)_P$ tend to $-\infty$ as $T \to T_m$. A further test of the Ida theory and of the possibility that melting is accompanied by mode softening is afforded by ultrasonic wave velocity measurements near the melting of In - 3.4 at% Cd alloy (Figure 6.2). The velocity of the $[110]$, $\underline{q} \,//\, [1\bar{1}0]$ mode in this fct alloy does decrease rapidly as the temperature rises and reaches a small value near T_m but (as Chung, Gunton and Saunders (1976) have shown for In-Tl alloys) this softening is due rather to the incipient phase transformation than to melting. No tendency is observed for $\left(\frac{\partial v}{\partial T}\right)_P \to -\infty$ as $T \to T_m$. In fact, the longitudinal wave velocities begin to increase somewhat below the melting point and have a positive $\left(\frac{\partial v}{\partial T}\right)_P$ at T_m - certain elastic constants stiffen rather than soften as the melting point is approached (Figure 6.3). In neither the metallic In alloys nor in the van der Waals's solid argon does acoustic mode softening (in the sense of that found in the displacive phase transformations) accompany melting.

The elastic constants have been computed from the ultrasonic wave velocity measurements using the solutions of the Christoffel equation (3.74) collected in Table 3.2. All the elastic stiffness tensor components of the 3.4 at% Cd alloy have been plotted as a function of temperature between 80 and 420°K in Figure 6.3. C_{13} appears in the expressions (Table 3.2) in such a way that mathematically two values are possible; however, one of these violates both of the Born stability criteria $C_{33}(C_{11} + C_{12}) > 2C_{13}^2$ and $C_{11}C_{33} > C_{13}^2$ and so is physically unreal and has been rejected. An interesting feature of the temperature dependence of

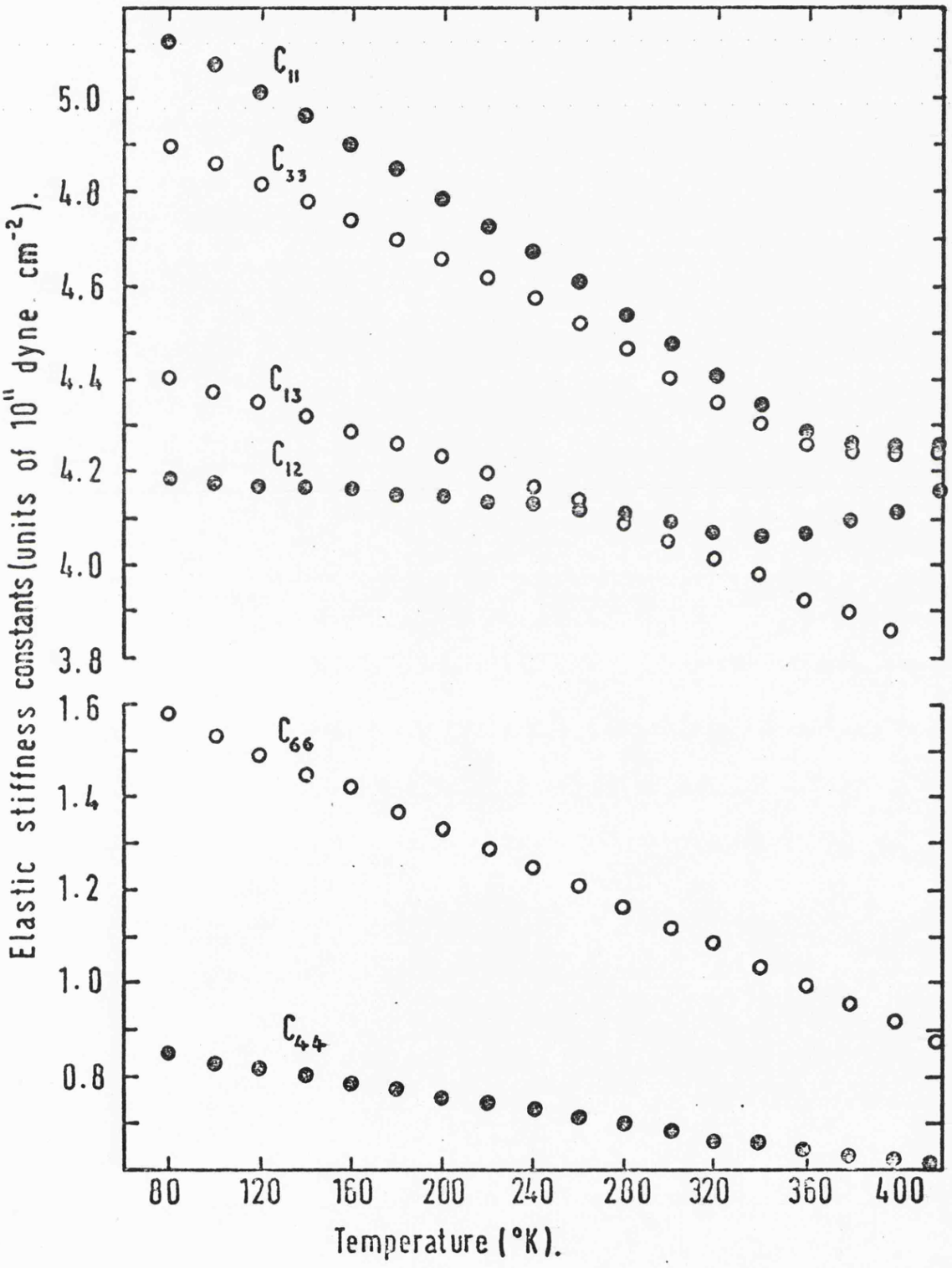

Figure 6.3: Temperature dependences of the elastic stiffness constants of In - 3.4 at% Cd alloy.

the elastic constants is that they converge in the pairs C_{33} with C_{11} and C_{66} with C_{44} (Figure 6.3); the additional symmetry elements for cubic crystals require that $C_{33} = C_{11}$, $C_{66} = C_{44}$ and $C_{13} = C_{12}$ (see matrices 3.47 and 3.50). The value of C_{13} is subject to a much greater error than the other moduli because differences in velocity squared are involved in its determination; thus no definite conclusion can be drawn as to whether C_{13} does converge on C_{12}. Another feature of the elastic constant results is the temperature dependence of the shear modulus $\frac{1}{2}(C_{11} - C_{12})$. This has been plotted in Figure 6.4 and has been obtained from the ultrasonic wave velocity of the [110], $\underline{q}$ // [1$\bar{1}$0] mode and as mentioned earlier this decreases rapidly as the temperature rises and reaches a small value near T_m.

6.4.2 In - 6.5 at% Cd alloy

The velocities of the three ultrasonic modes which can be propagated down the [110] direction have been measured as a function of temperature in this fcc alloy from room temperature down to 160°K. For these modes

$$\begin{aligned} \rho v_{\ell}^2 &= \tfrac{1}{2}(C_{11}+C_{12}+2C_{44}) = C_{\ell};\ \underline{q} \text{ along } [110] \\ \rho v_{fs}^2 &= C_{44};\ \underline{q} \text{ along } [001] \\ \rho v_{ss}^2 &= \tfrac{1}{2}(C_{11} - C_{12}) = C';\ \underline{q} \text{ along } [1\bar{1}0] \end{aligned} \qquad (6.2)$$

These three elastic constants, C_{ℓ}, C_{44} and C' have direct physical significance and are plotted in Figure 6.5. The temperature range covered includes the phase transformation temperature T_c(232 ± 2°K). Experimental results obtained on [100] cut crystals agree within experimental error with the data obtained on [110] samples. Down to

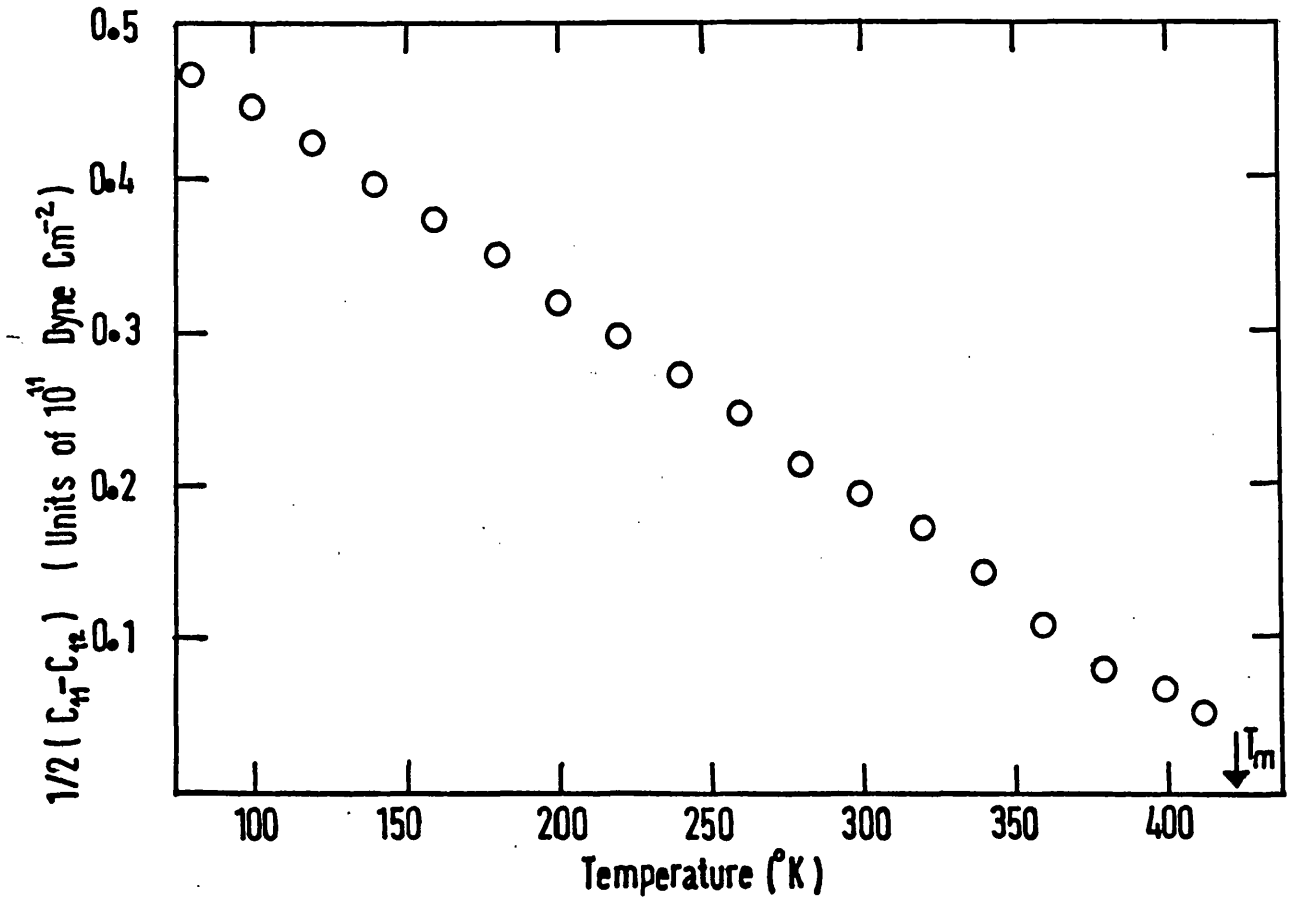

Figure 6.4: The shear modulus $C' = \frac{1}{2}(C_{11} - C_{12})$ of In - 3.4 at% Cd alloy as a function of temperature.

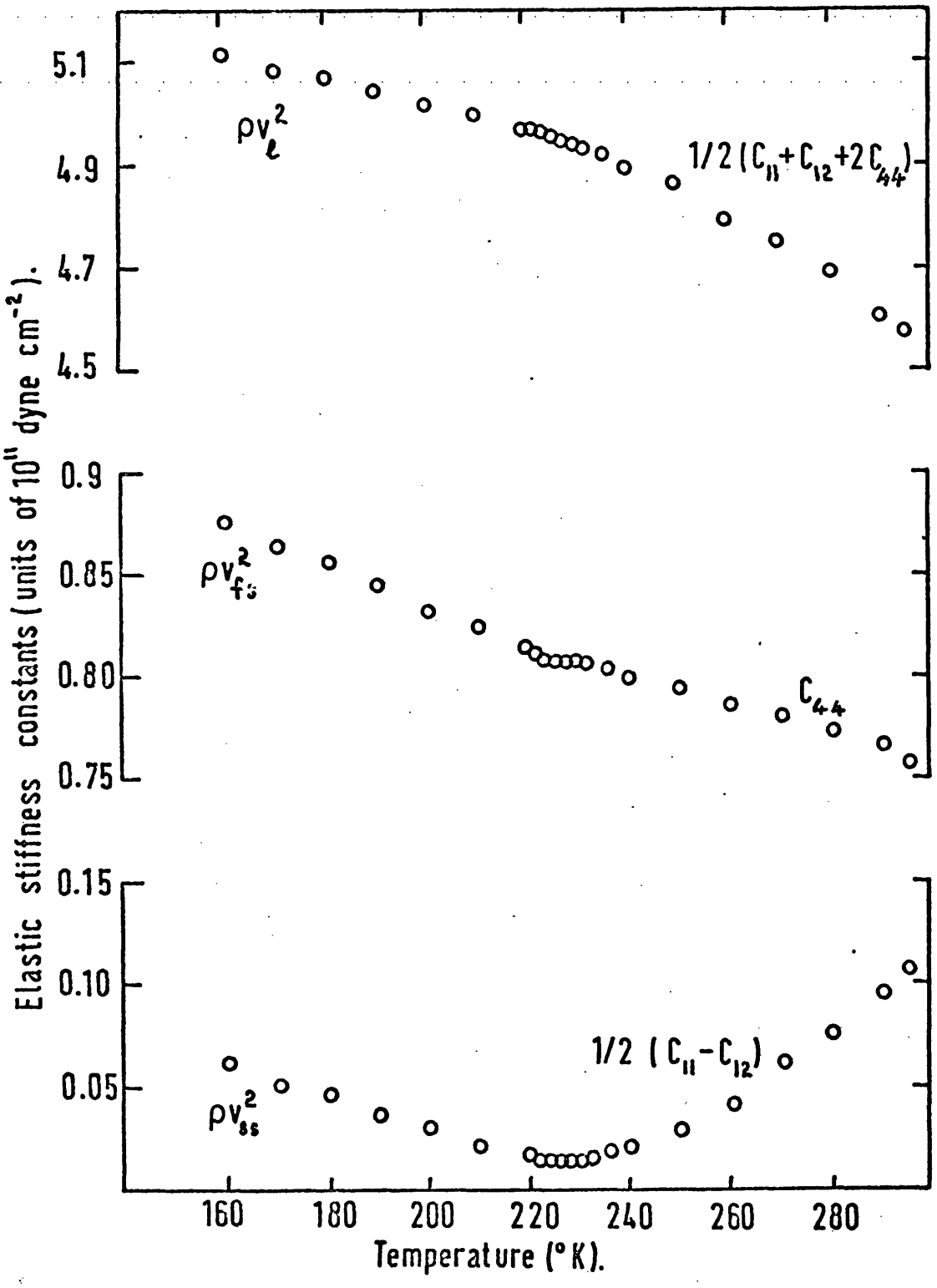

Figure 6.5: Temperature dependences measured on cooling of the elastic stiffness constants of In - 6.5 at% Cd alloy.

T_c the results presented in Figure 6.5 are the single crystal elastic constants. What do the results below T_c correspond to? When the transformation occurs, a banded twin lamellar entity is formed of domains with their c-axes almost along what were the three equivalent cubic axes; the domain boundaries are comprised of {110} planes. Now in the banded twin structure the velocity of a slow shear wave propagating normally to a (110) habit plane polarised in the $[1\bar{1}0]$ direction is

$$\rho v_{s'}^2 = \tfrac{1}{2}(C_{11} - C_{12}) \qquad (6.3)$$

for domains with c-axis in the original [001] direction and

$$\rho v_{s''}^2 = \{\tfrac{1}{2}(C_{11} + C_{33}) - C_{13}\}/2 \qquad (6.4)$$

for domains with c-axes corresponding to the original [010] and [100] directions. Now the average slow shear wave velocity v_{ss} through the banded twin can be written

$$\langle v_{ss} \rangle = \left\{ \left(\frac{(1/3)}{v_{s'}} \right) + \left(\frac{(2/3)}{v_{s''}} \right) \right\}^{-1} \qquad (6.5)$$

Therefore

$$\frac{1}{\langle v_{ss} \rangle} = \frac{1}{3}\left(\frac{2\rho}{C_{11}-C_{12}} \right)^{\frac{1}{2}} + \frac{2}{3}\left(\frac{2\rho}{\frac{1}{2}(C_{11}+C_{33})-C_{13}} \right)^{\frac{1}{2}} \qquad (6.6)$$

The elastic constant data obtained on the fct 3.4 at% Cd alloy (Figure 6.3) indicated that $C_{33} \rightarrow C_{11}$ and $C_{13} \rightarrow C_{12}$ as $T \rightarrow T_c$. Writing C_{11} for C_{33} and C_{12} for C_{13} in equation (6.6), leads in the limit to

$$\frac{1}{\langle v_{ss} \rangle}\Bigg|_{T \to T_c} \longrightarrow \left(\frac{2\rho}{C_{11}-C_{12}}\right)^{\frac{1}{2}} \qquad (6.7)$$

Thus, it can be concluded that the data given below T_c in Figure 6.5 for ρv_{ss}^2 does give $\frac{1}{2}(C_{11}-C_{12})$ to a reasonable approximation, especially close to T_c. This result is significant because it provides evidence for the behaviour of $\frac{1}{2}(C_{11}-C_{12})$ in the fct phase near T_c, which the single crystal fct data presented in Figures 6.2 and 6.3 cannot do.

The reasoning used for $\langle v_{ss} \rangle$ is put on to a firmer experimental footing by extending the argument to the other two waves which can be propagated normal to the (110) habit plane in the twinned material. It can be shown that the reciprocal of the mean velocity of the longitudinal wave can be written (assuming that $C_{66} \to C_{44}$) (see Figure 6.3) as

$$\frac{1}{\langle v_\ell \rangle} = \frac{1}{3}\left\{\frac{2\rho}{\frac{2}{3}(C_{11}+2C_{12})+2C_{44}+\frac{1}{3}(C_{11}-C_{12})}\right\}^{\frac{1}{2}} + \frac{2}{3}\left\{\frac{2\rho}{\frac{2}{3}\left(\frac{3}{4}C_{11}+\frac{1}{4}C_{33}+2C_{13}\right)+2C_{44}+\frac{1}{3}(C_{33}-C_{13})}\right\}^{\frac{1}{2}} \qquad (6.8)$$

As $T \to T_c$, $C_{33} \to C_{11}$ and $C_{13} \to C_{12}$ and this expression tends to

$$\frac{1}{\langle v_\ell \rangle}\Bigg|_{T \to T_c} \longrightarrow \left(\frac{2\rho}{C_{11}+C_{12}+2C_{44}}\right) \qquad (6.9)$$

which is the velocity down the [110] direction in the cubic phase (above 232 ± 2°K). Thus, a direct test of the approximation is that as $T \to T_c$ from either above or below the transition the longitudinal wave velocities in the fcc or fct phases should approach the same

value: which they do (Figure 6.5). There is a measurable difference of temperature dependence of the longitudinal wave velocity in the two phases. Similar arguments and confirmation come from the fast shear mode elastic constant ρv_{fs}^2; thus $1/\langle v_{fs} \rangle$ in the twinned phase reduces to $(\rho/C_{44})^{\frac{1}{2}}$ at the transformation temperature and the velocities of this mode in the two phases approach the same value at T_c (Figure 6.5)

6.4.3 In - 4.4 at% Cd alloy

The behaviour of the twinned fct crystal has been studied further through ultrasonic measurements on a 4.4 at% Cd alloy which was twinned fct at room temperature and transformed to an fcc sample at T_c ($380 \pm 2^{\circ}K$) on warming. The twin plane is effectively a (110) plane of the cubic phase. The velocities of the three ultrasonic modes propagated normal to the habit plane are presented in the form ρv_i^2 in Figure 6.6. Below T_c the effective elastic constants which correspond to ρv_ℓ^2 and ρv_{ss}^2 are given by equations (6.8) and (6.6) respectively.

6.5 Ultrasonic attenuation measurements

In the vicinity of the phase transformation, ultrasonic wave attenuation was high and signal quality poor. This was especially true for the $[110]$, $\underline{q} \,//\, [1\bar{1}0]$ mode, for which, even away from T_c, attenuation was considerable and near T_c only two echoes could be observed. Therefore it has not been possible to follow the attenuation peaks at T_c for all the ultrasonic modes. Some of the propagation modes for which attenuation peaks at T_c could be measured are presented in Figures 6.7 and 6.8. Each alloy shows hysteresis of the transformation temperature on warming and cooling

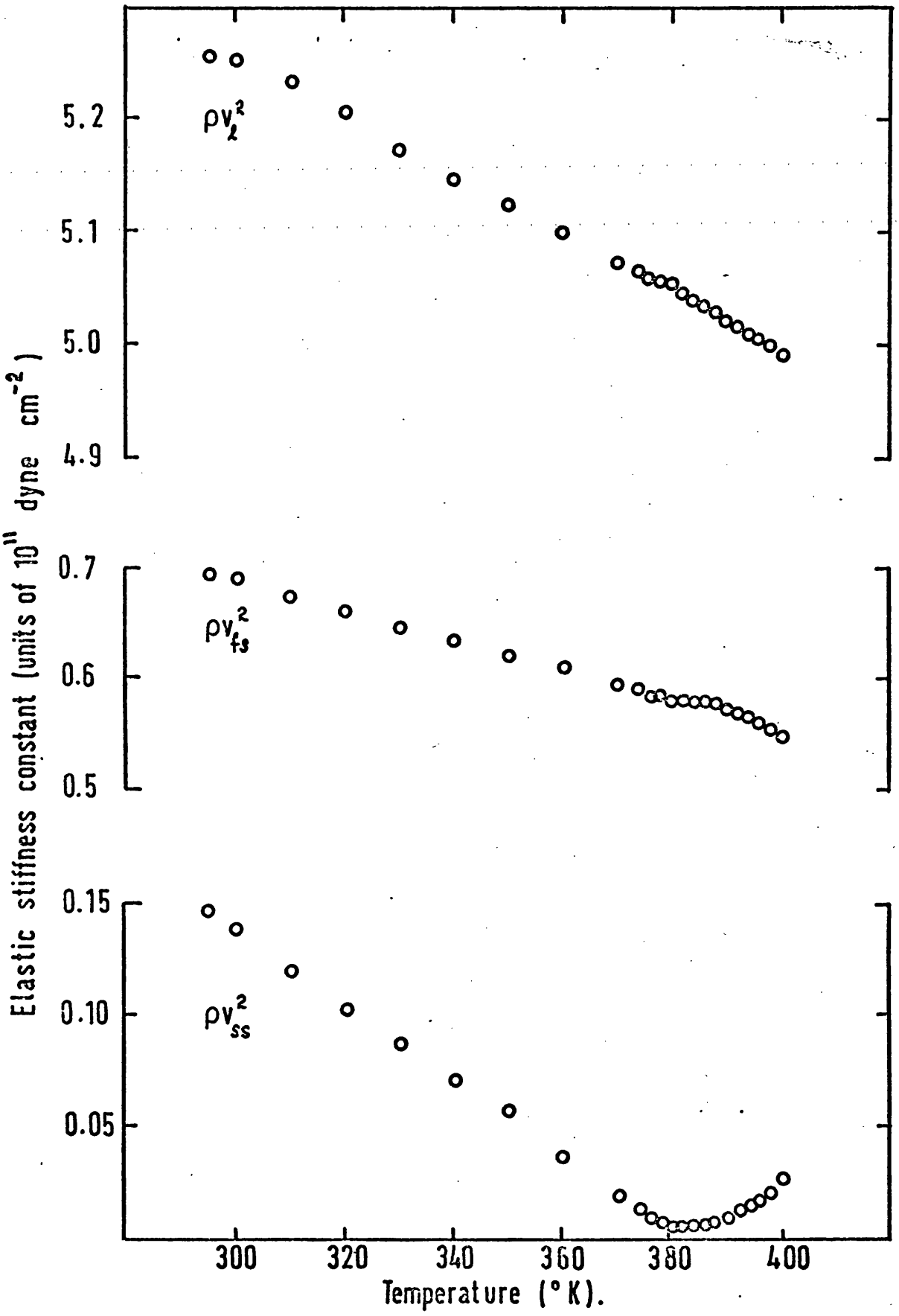

Figure 6.6: The elastic stiffness constants (ρv_i^2) of In - 4.4 at% Cd alloy "[110]" sample.

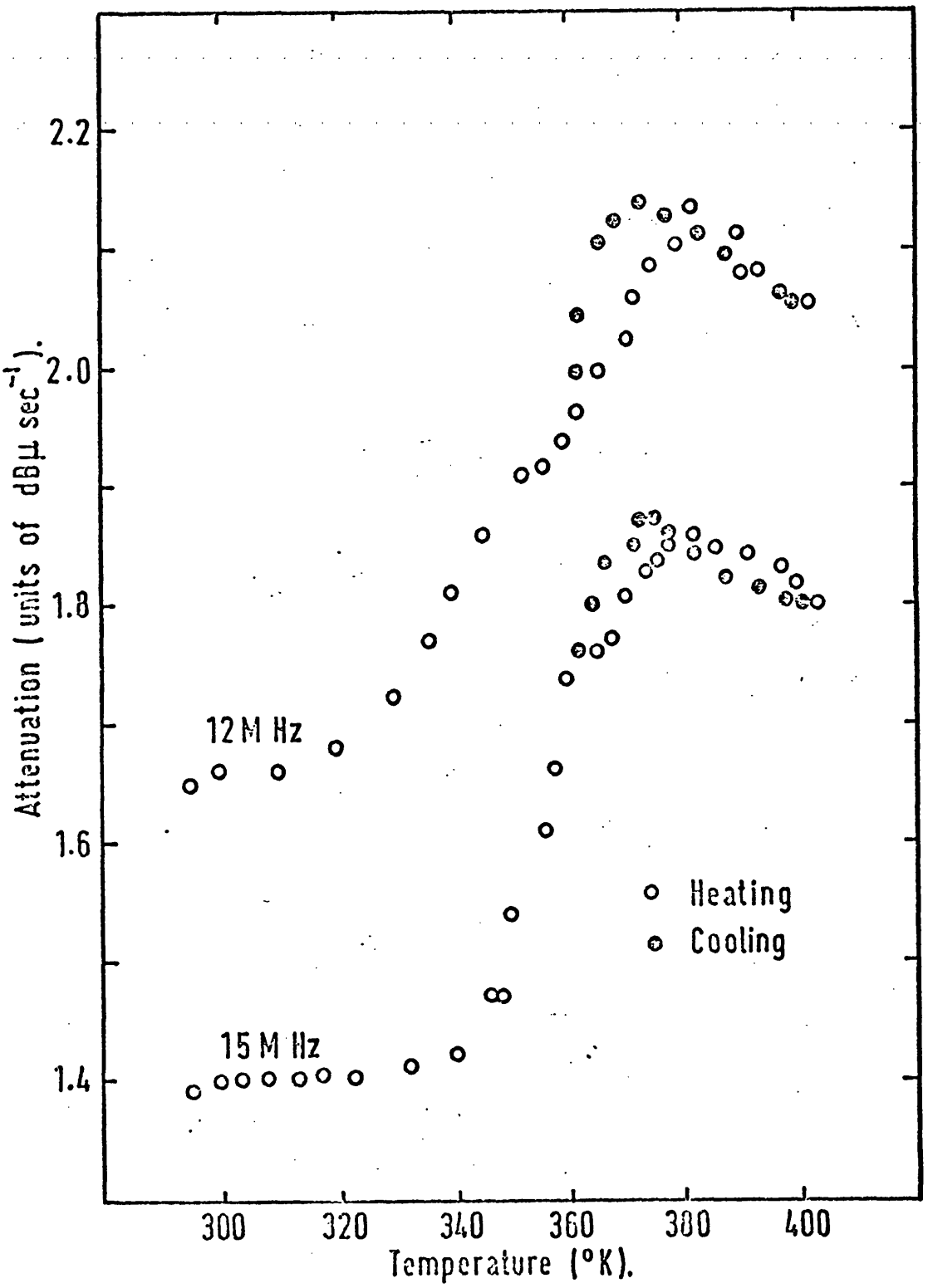

Figure 6.7: Attenuation of ultrasonic waves along the "[110]" direction in In - 4.4 at% Cd alloy. 12 MHz - shear wave corresponding to ρv_{fs}^2 and 15 MHz - longitudinal wave corresponding to ρv_{ℓ}^2

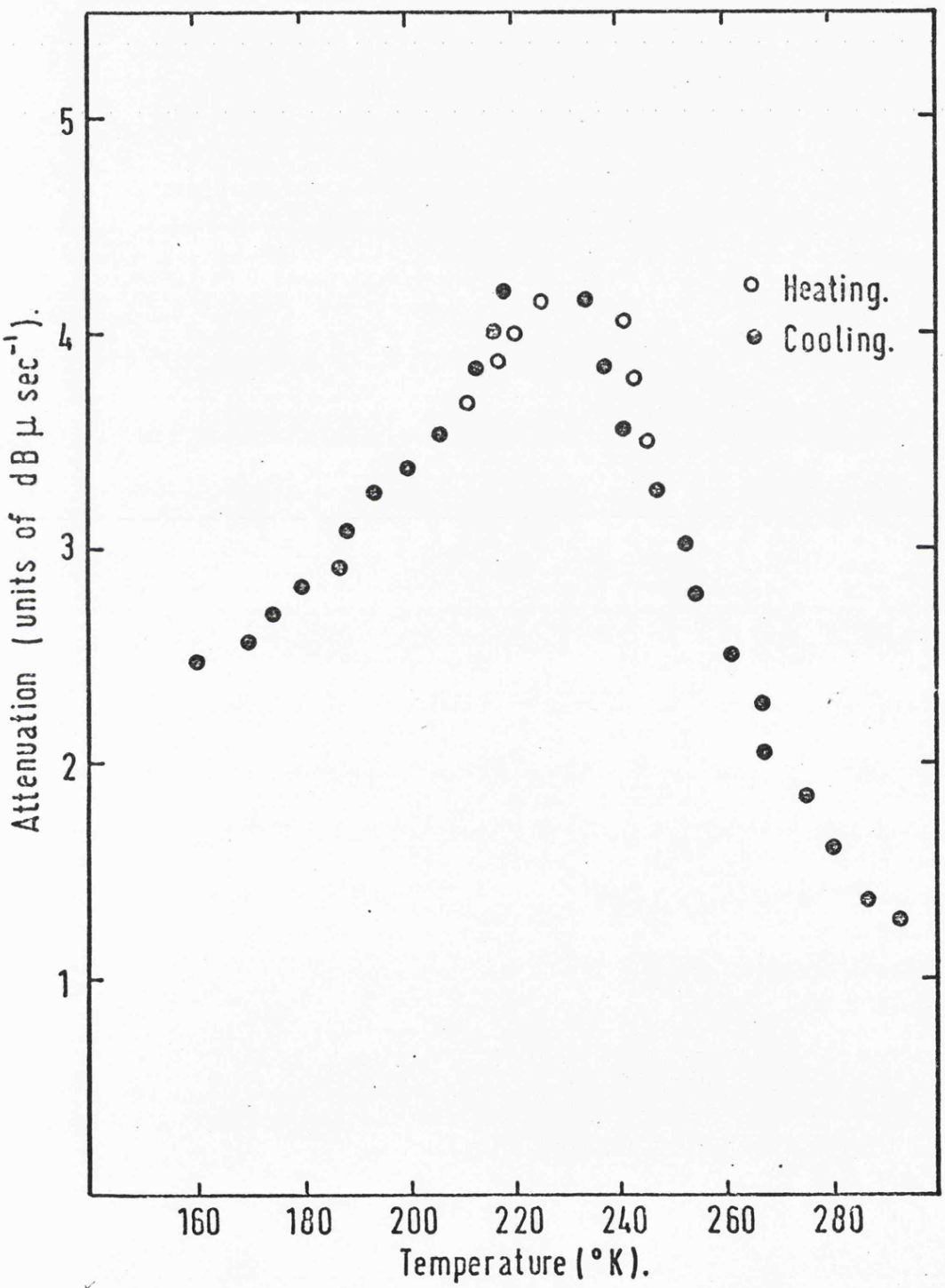

Figure 6.8: Attenuation of the fast shear wave (corresponding to C_{44}) along the [001] direction in In - 6.5 at% Cd alloy.

cycles. In Figures 6.7 and 6.8, the hysteresis can be clearly seen as a shift of the attentuation peak which accompanies the phase transformation. For the 4.4 at% Cd alloy the attenuation peak occurs at 380 ± 2°K on heating but at 370 ± 2°K on cooling and for the 6.5 at% Cd alloy at 240±2°K on heating and 232±2°K on cooling. Hysteresis evidences the first order character of the phase transformation.

6.6 Acoustic phonon mode softening

Under this heading the elastic constant results and their implications will be discussed.

From the elastic constant data in Figures 6.3 - 6.6 and in Table 6.1, it can be seen that the behaviour of the elastic constant $C' = \frac{1}{2}(C_{11} - C_{12})$ is unusual in two respects:

(i) It is small in In itself and becomes even smaller in the fct alloys with Cd. It is also very small in the fcc alloy.

(ii) As the phase transformation is approached from either the fct or the fcc side, $\frac{1}{2}(C_{11} - C_{12})$ decreases to even smaller values and reaches a minimum but finite value at the transformation itself.

$\frac{1}{2}(C_{11} - C_{12})$ varies much more strongly with temperature than any of the other moduli. For example, at 300°K for the fct 3.4 at% Cd alloy $\left(\{C_{ij}(280^{\circ}K) - C_{ij}(320^{\circ}K)\} / C_{ij}(300^{\circ}K)\right)$ has normal values for the other elastic constants (0.028 for C_{11}, 0.025 for C_{33}, 0.048 for C_{44}, 0.069 for C_{66}) but is large (0.21) for $\frac{1}{2}(C_{11} - C_{12})$.

Table 6.1

Elastic constants and related parameters of In-Cd alloys. Data for In are from Chandrasekhar and Rayne (1961)

Composition (at. % Cd)	0	3·4			6·5		
Temperature (K)	300	400	295	80	300	260	232
Elastic stiffness constants (in units of 10^{11} dyne cm^{-2})							
C_{11}	4·54	$4·26_2$	$4·48_5$	$5·12_0$	$3·92_6$	$4·06_0$	$4·14_6$
C_{12}	4·01	$4·12_7$	$4·10_0$	$4·19_1$	$3·71_4$	$3·95_3$	$4·12_2$
C_{13}	4·15	$3·86_3$	$4·05_4$	$4·40_8$			
C_{33}	4·51	$4·25_3$	$4·41_1$	$4·90_0$			
C_{44}	0·651	0·616	0·686	0·85	0·756	0·785	0·806
C_{66}	1·21	0·921	1·125	1·579			
$C'=\frac{1}{2}(C_{11}-C_{12})$	0·26	$0·06_7$	$0·19_3$	$0·46_5$	$0·10_6$	$0·05_3$	$0·01_3$
Debye temperature (K):							
$\bar{\theta}_D$	87·1	77·9	88·2	106·3	76·2	67·2	51·3
θ_1	261·4	253·3	259·7	275·7	245·3	250·6	254·2
θ_2	98·1	91·6	98·1	113·4	92	92·6	92·9
θ_3	66·3	58·5	67·5	82·8	56·9	48·9	36·3
Mean square atomic displacement $\langle u^2\rangle$ in (Å)^2					0·19	0·22	0·33
Anistropy factor $A=C_{44}/C'$					7·132	14·811	67·167
Elastic compliance constants (in units of 10^{-10} cm^2 dyne^{-1})							
S_{11}	0·150	0·407	0·174	0·090	0·317	0·626	2·78
S_{12}	−0·039	−0·334	−0·086	−0·018	−0·154	−0·309	−1·39
S_{13}	−0·101	−0·066	−0·081	−0·065			
S_{33}	0·208	0·144	0·172	0·138			
S_{44}	0·154	0·162	0·146	0·118	0·132	0·127	0·124
S_{66}	0·083	0·109	0·089	0·063			
Bulk modulus (in units of 10^{12} dyne cm^{-2})	0·385	0·404	0·417	0·454	0·378	0·399	0·410
Compressibilities (in units of 10^{-12} cm^2 dyne^{-1})							
βv (volume)	2·36	2·47	2·38	2·19	2·64	2·51	2·44
βz (linear)	0·583	1·14	0·954	0·732	0·881	0·836	0·811
βx (linear)	0·888	0·669	0·714	0·727	0·881	0·836	0·811

This temperature dependence $\Delta C_{ij}/\Delta T$ reflects the anharmonicity of the interatomic binding forces corresponding to the mode of vibration; the large $\Delta C_{ij}/\Delta T$ found for $\frac{1}{2}(C_{11} - C_{12})$ suggests that the atomic displacements associated with the $[110]$, $\underline{q} \,//\, [1\bar{1}0]$ mode are particularly subject to anharmonicity. In the fcc alloy $\frac{1}{2}(C_{11} - C_{12})$ is unusual in that it increases with temperature - as the crystal recedes from the phase transformation, this modulus stiffens. Alloying In with Cd has comparatively little effect on the other elastic constants. In particular, the bulk modulus which is $1/\{3(S_{11}+2S_{12})\}$ for fcc crystals and $1/\{2(S_{11}+S_{12}+2S_{13}) + S_{33}\}$ for fct crystals behaves normally even near T_c.

For a crystal to be stable, the strain energy density

$$U_s = \frac{1}{2} \sum_{ijkl} C_{ijkl}\, \varepsilon_{ij}\, \varepsilon_{kl} \qquad (6.10)$$

or in Voigt notation

$$= \frac{1}{2} \sum_{ij} C_{ij}\, \varepsilon_i\, \varepsilon_j \qquad (6.11)$$

must be a positive definite quantity. An elastic body is stable only when work has to be done to create a state of strain from the equilibrium state. For the matrices in equation (6.10) to be positive definite, their eigenvalues must be positive definite. The eigenvalues of the stiffness matrix for cubic crystals are $\mu_1 = C_{11} + 2C_{12}$; $\mu_2 = \mu_3 = \frac{1}{2}(C_{11} - C_{12})$; $\mu_4 = \mu_5 = \mu_6 = C_{44}$. Therefore, stability of a cubic crystal requires that $(C_{11} + 2C_{12}) > 0$, $(C_{11} - C_{12}) > 0$, $C_{44} > 0$. For the eigenvalues of the stiffness matrix for a tetragonal (Laue group 4/mmm) crystal to be positive definite

requires $C_{11} > 0$, $C_{33} > 0$, $C_{44} > 0$, $C_{66} > 0$, $C_{11}C_{33} > C_{13}^2$, $(C_{11} - C_{12}) > 0$, $C_{33}(C_{11} + C_{12}) > 2C_{13}^2$. Thus, stability of both cubic and tetragonal crystals requires that $(C_{11} - C_{12}) > 0$. If one of the eigenvalues of the stiffness matrix tends towards zero, the structure may distort continuously to a new structure whose symmetry is determined by the eigenvector of that eigenvalue. The displacive transformation in In-Cd alloys is accompanied by softening of $\frac{1}{2}(C_{11} - C_{12})$. The acoustic phonon mode which softens is that polarised $[1\bar{1}0]$ for a wave vector along $[110]$. The elastic modulus $\frac{1}{2}(C_{11} - C_{12})$ provides a measure of the resistance to deformation when shear stress is applied across a (110) plane in a $[1\bar{1}0]$ direction; when $\frac{1}{2}(C_{11} - C_{12})$ has become very small near T_c, then a small shear stress can produce the change of shape which corresponds to that known to occur during the martensitic transformation in In-Tl alloys (Guttman 1950, Bowles, Barrett and Guttman 1950, Burkart and Read 1953, Basinski and Christian 1954). The mode softening behaviour in the In alloys with Cd resembles that of those with Tl except in one particular : $\frac{1}{2}(C_{11} - C_{12})$ does not approach zero at T_c nearly so closely as it does in Tl alloys.

Folk, Iro and Schwabl (1976) have proposed the following classification of elastic phase transformations : softening may occur

A. in a finite number of one-dimensional sectors in space,

B. in a set of two-dimensional sectors, or

C. in a combination of one and two dimensional sectors.

For cubic crystals, types A and B are possible. When $\frac{1}{2}(C_{11} - C_{12})$ softens the velocity which decreases as the phase transformation is approached is that determined by the eigenvalue when the wave vector is directed along <110> directions. This is a one dimensional (type A) manifold (Cowley (1976) denotes this case as type I). The transverse acoustic modes of the fcc In-Cd alloys which soften are those with $\underline{k} = \frac{1}{\sqrt{2}}$ (k, ±k, o) and polarisation vector $\underline{q} = \frac{1}{\sqrt{2}}$ (1, ±1, o): there are six (s = 6) equivalent directions and therefore six (s = 6, m = 1) soft sectors. The symmetry restoring mode is the symmetry destroying mode. For the fct alloys the soft wave vector is $\underline{k}$ which is again $\frac{1}{\sqrt{2}}$ (k, ±k, o) and $\underline{q}$ is $\frac{1}{\sqrt{2}}$ (1, ±1, o); there are two soft mode directions below the transformation - these are along the diagonals of the basal plane.

6.6.1 Velocity surfaces

For one dimensional manifolds in the neighbourhood of the <110> directions, mode softening should evidence itself as cone-like sectors in $\underline{k}$-space. Previously, Pace and Saunders (1972) used velocity space to illustrate this sectorial softening. Using anisotropic continuum acoustics, the velocity of long-wavelength acoustic phonons in the In-Cd alloys has been calculated by computation of the eigenvalues of the Christoffel equation (3.74). The (110) and (001) plane cross-sections of the wave velocity surfaces of In - 6.5 at% Cd alloy are plotted in Figures 6.9 - 6.12 at two temperatures: 300°K and T_c (232°K). The marked sectorial softening down the <110> type directions at the phase transformation temperature T_c can be seen by comparison between the set of results at 300°K and T_c.

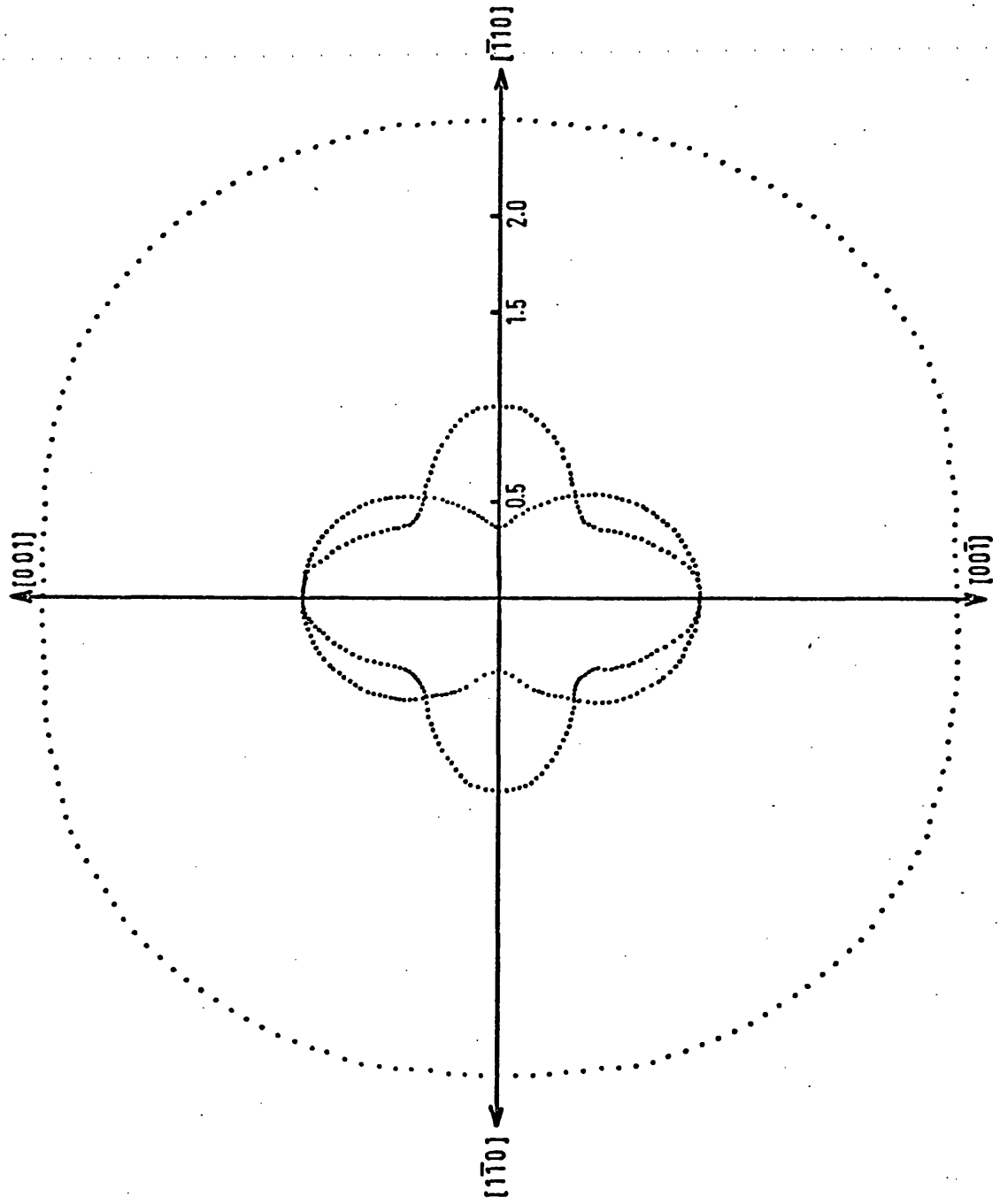

Figure 6.9: The (110) plane cross-sections of the velocity surface of In - 6.5 at% Cd at 300°K. Units; 10^5 cm/sec.

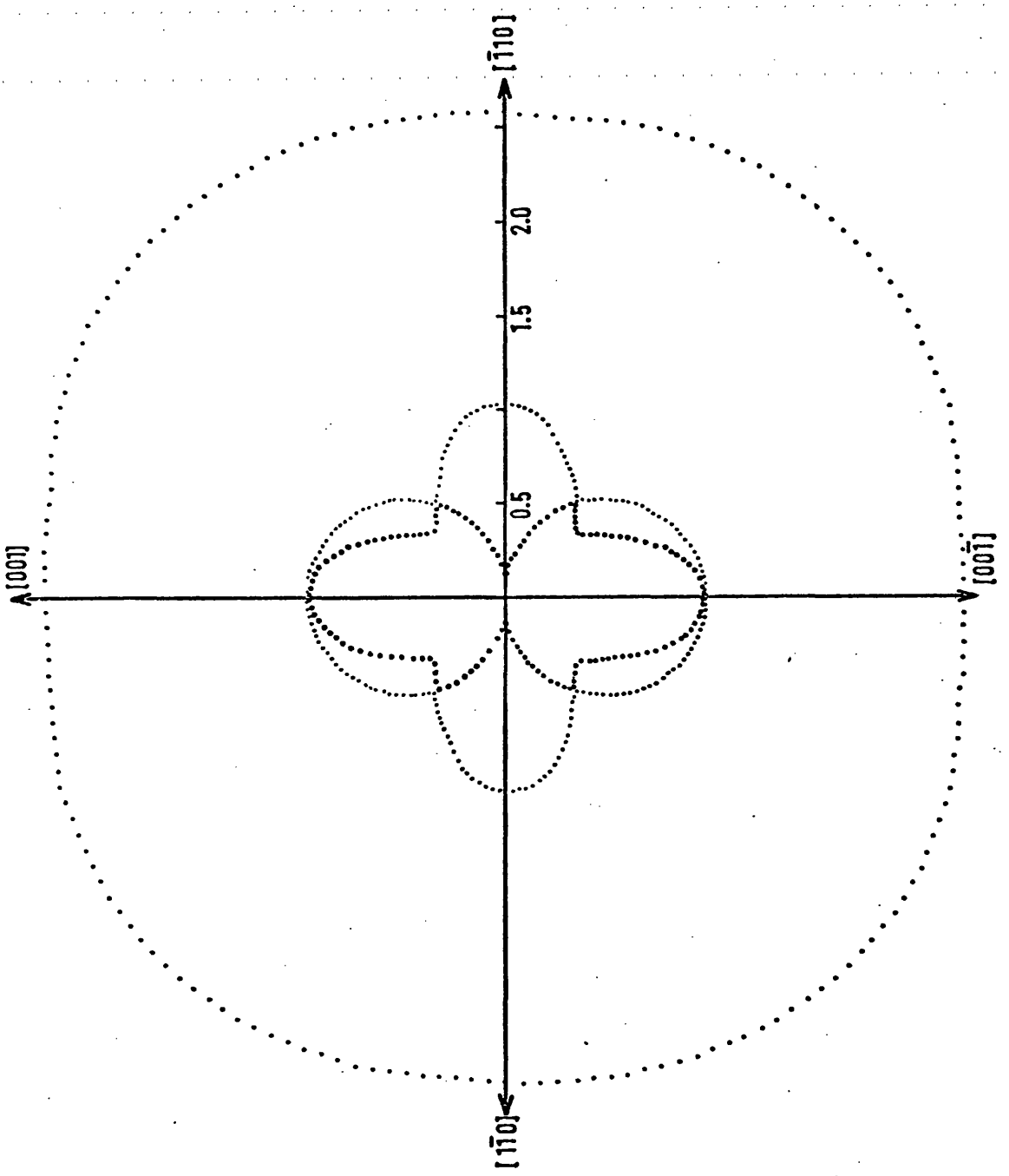

Figure 6.10: The (110) plane cross-sections of the velocity surface of In - 6.5 at% Cd at T_c (232 ± 2°K). Units: 10^5 cm/sec.

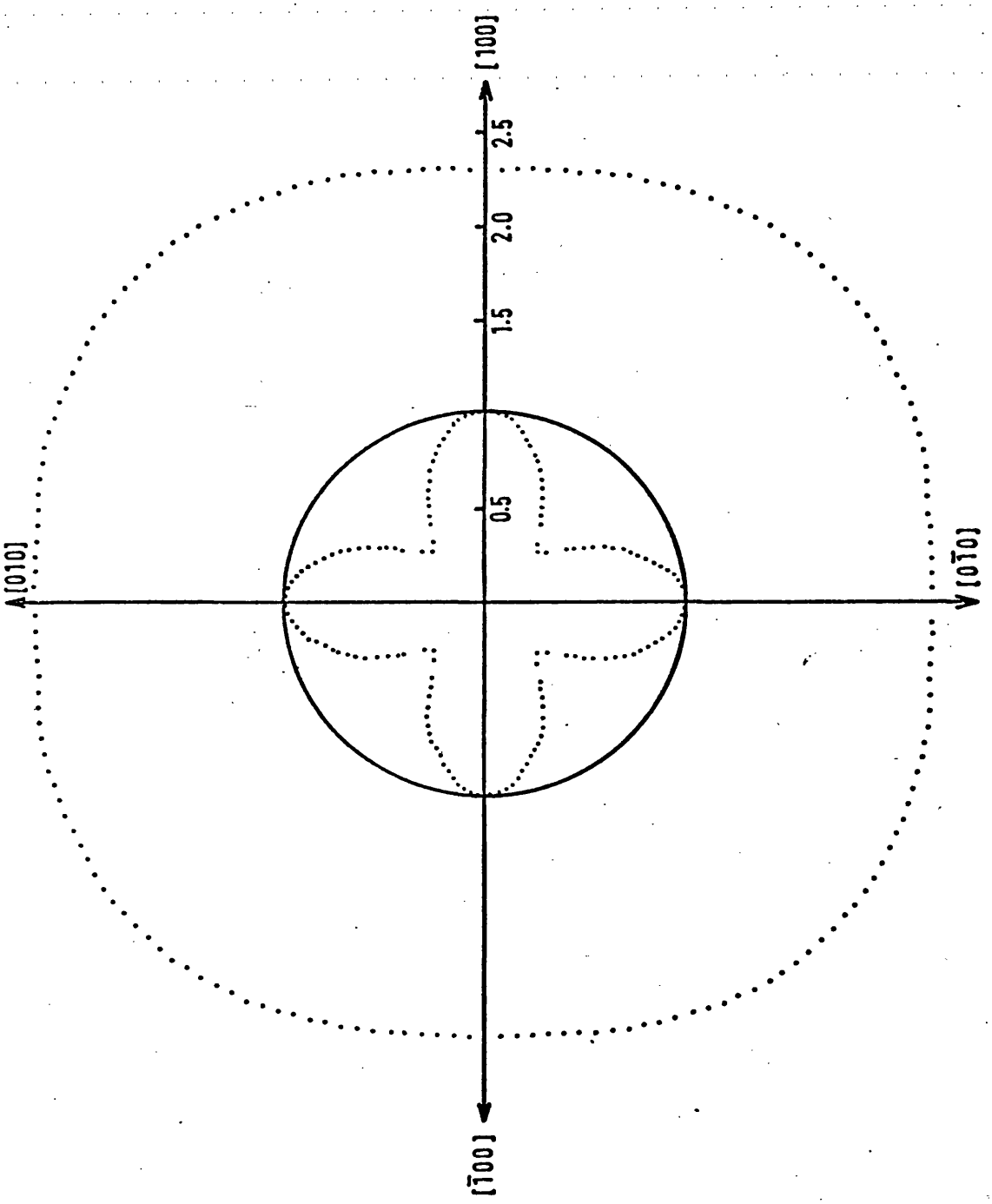

Figure 6.11: The (001) plane cross-sections of the velocity surface of In - 6.5 at% Cd at 300°K. Units: 10^5 cm/sec.

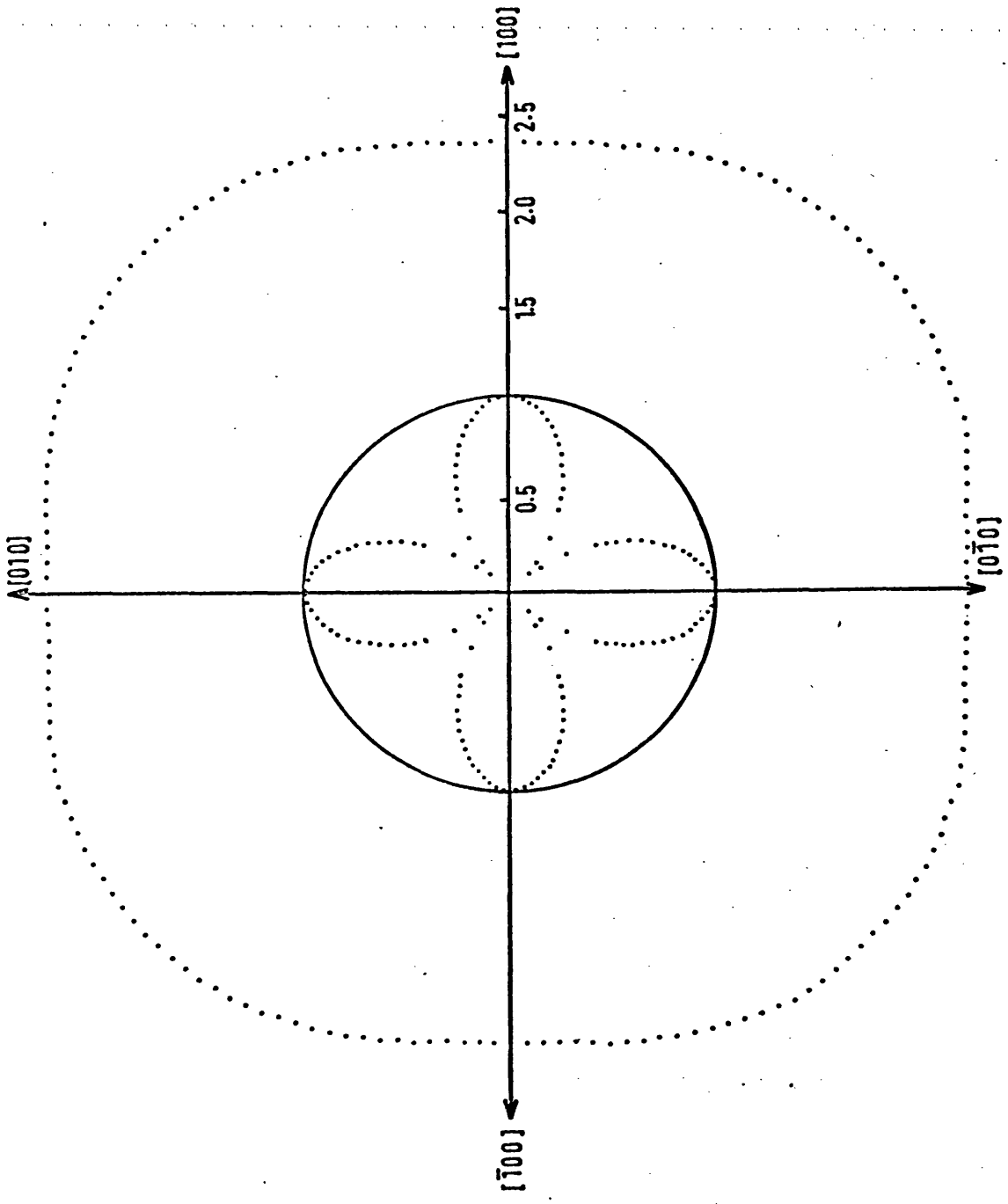

Figure 6.12: The (001) plane cross-sections of the velocity surface of In - 6.5 at% Cd at T_c (232 ± 2°K). Units; 10^5 cm/sec.

6.6.2 Elastic anisotropy and Young's modulus surface

For a cubic crystal, the degree of elastic anisotropy is usually expressed by the anisotropy factor $A = \frac{2C_{44}}{C_{11}-C_{12}}$. For an elastically isotropic crystal, A would be unity. Now in the case of the fcc 6.5 at% Cd alloy, as the phase transformation is approached, $\frac{1}{2}(C_{11} - C_{12})$ decreases rapidly while C_{44} remains essentially unaltered (Figure 6.5): the anisotropy factor increases to a very large number (Table 6.1) and the elastic anisotropy becomes extreme. This is a ramification of the directional dependence of the interatomic cohesion. It is interesting to note in passing that the delta, fcc form of plutonium which exists between 592 and 724^{o}K has been prepared in single crystal form at room temperature by stabilising with 1 wt% gallium by Ledbetter and Moment (1976); the elastic constants $\frac{1}{2}(C_{11} - C_{12}) = 0.478 \pm 0.032 \times 10^{11}$ dynes cm^{-2} and $C_{44} = 3.359 \pm 0.011 \times 10^{11}$ dynes cm^{-2} give an elastic anisotropy A of 7.03, which Ledbetter and Moment state to be much larger than that known for any other fcc metal. Alloys of In-Cd can have much larger values of A than this, especially close to the phase transformation (Table 6.1).

A useful visual illustration of the anisotropy of the elastic behaviour of a crystal is provided by the familiar technical parameter - Young's modulus (the ratio of the longitudinal stress to the resulting longitudinal strain), which is a single valued function of the direction cosines ℓ_1, ℓ_2, ℓ_3 of the applied stress and the elastic moduli. For a cubic crystal stressed in a <100> direction, Young's modulus E is just $(S_{11})^{-1}$ and in any other direction it is $(S'_{11})^{-1}$ or

$$\frac{1}{E} = S_{11} - 2\left\{(S_{11} - S_{12}) - \tfrac{1}{2}S_{44}\right\}(\ell_1^2\ell_2^2 + \ell_2^2\ell_3^2 + \ell_3^2\ell_1^2) \qquad (6.12)$$

For a tetragonal crystal belonging to one of the point groups 422, 4mm, $\bar{4}$2m, 4/mmm, Young's modulus is given by

$$\frac{1}{E} = (\ell_1^4+\ell_2^4)S_{11} + \ell_3^4 S_{33} + \ell_1^2\ell_2^2 (2S_{12} + S_{66}) + \ell_3^2(1-\ell_3^2)(2S_{13} + S_{44}) \qquad (6.13)$$

Young's modulus can be represented by a surface; cross-sections of this surface have been computed for each alloy composition at selected temperatures. The (110) cross-section of the fcc 6.5 at% Cd crystal at 300 and 232°K illustrate directly the influence on Young's modulus of increasing mode softening as the transformation temperature is approached. In a cubic crystal, equation (6.12) shows that the directional dependence of Young's modulus depends upon the product of (i) a directional quantity $(\ell_1^2\ell_2^2 + \ell_2^2\ell_3^2 + \ell_3^2\ell_1^2)$ and (ii) $\left\{(S_{11} - S_{12}) - \tfrac{1}{2}S_{44}\right\}$. Now $(\ell_1^2\ell_2^2 + \ell_2^2\ell_3^2 + \ell_3^2\ell_1^2)$ is zero for <100> directions, $\frac{1}{4}$ for <110> directions and takes its maximum value of $\frac{1}{3}$ for <111> directions. Thus if $\left\{(S_{11} - S_{12}) - \tfrac{1}{2}S_{44}\right\}$ is positive - as it is for the In-Cd alloys - the Young's modulus surface has its maxima in <111> and its minima in <100> directions (Boas and Mackenzie 1950). Now the quantity $\left\{(S_{11} - S_{12}) - \tfrac{1}{2}S_{44}\right\}$ reflects directly any influence of shear mode softening on the Young's modulus ($(S_{11} - S_{12})$ is $(C_{11} - C_{12})^{-1}$ and S_{44} is $(C_{44})^{-1}$ - see Table 3.1). As $\tfrac{1}{2}(C_{11} - C_{12})$ decreases as the transformation temperature is approached the value of $\left\{(S_{11} - S_{12}) - \tfrac{1}{2}(S_{44})\right\}$ becomes very large; for example for the 6.5 at% Cd alloy it is 4.05×10^{-11} dyne^{-1}cm^2 at 300°K, 8.71×10^{-11} dyne^{-1}cm^2 at 260°K and 41.1×10^{-11} dyne^{-1}cm^2 at the transformation temperature 232°K. The dominating influence of the mode softening on the Young's modulus of this cubic

alloy as the phase transformation is approached is shown in Figure 6.13. Similar effects which are not quite so easy to see physically, also occur in the Young's modulus of the tetragonal alloys (Figure 6.14)

6.6.3 Debye temperatures

According to the Debye theory of solids, the lattice frequencies take a continuous range of values up to the cut-off frequency ν_D - there are 3N lattice modes for a solid containing N atoms. This situation is expressed as

$$\int_0^{\nu_D} N(\nu)\, d\nu = 3N \qquad (6.14)$$

where $N(\nu)$ is the density of states function. The Debye temperature θ_D corresponding to the cut-off frequency ν_D ($\theta_D = h\nu_D/k$, h is Planck's constant and k is Boltzmann's constant) can be obtained from the ultrasonic wave velocities:

$$\theta_D = \frac{h}{k}\left(\frac{9N}{4\pi V}\right)^{\frac{1}{3}} \Bigg/ \left\{\int\left(\frac{1}{v_1^3} + \frac{1}{v_2^3} + \frac{1}{v_3^3}\right)\frac{d\Omega}{4\pi}\right\}^{\frac{1}{3}} \qquad (6.15)$$

where V is the crystal volume and v_i are the velocities which are the eigenvalues of the Christoffel equation (3.74) and the integration is performed over the entire solid angle Ω. Also, three mode Debye temperatures can be calculated:

$$\theta_i = \frac{h}{k}\left(\frac{3N}{4\pi V}\right)^{\frac{1}{3}} \Bigg/ \left\{\int \frac{1}{v_i^3}\,\frac{d\Omega}{4\pi}\right\}^{\frac{1}{3}} \qquad (6.16)$$

The total ($\bar{\theta}_D$) and the mode Debye temperatures (θ_1, θ_2 and θ_3) of the In-Cd alloys have been calculated as a function of temperature

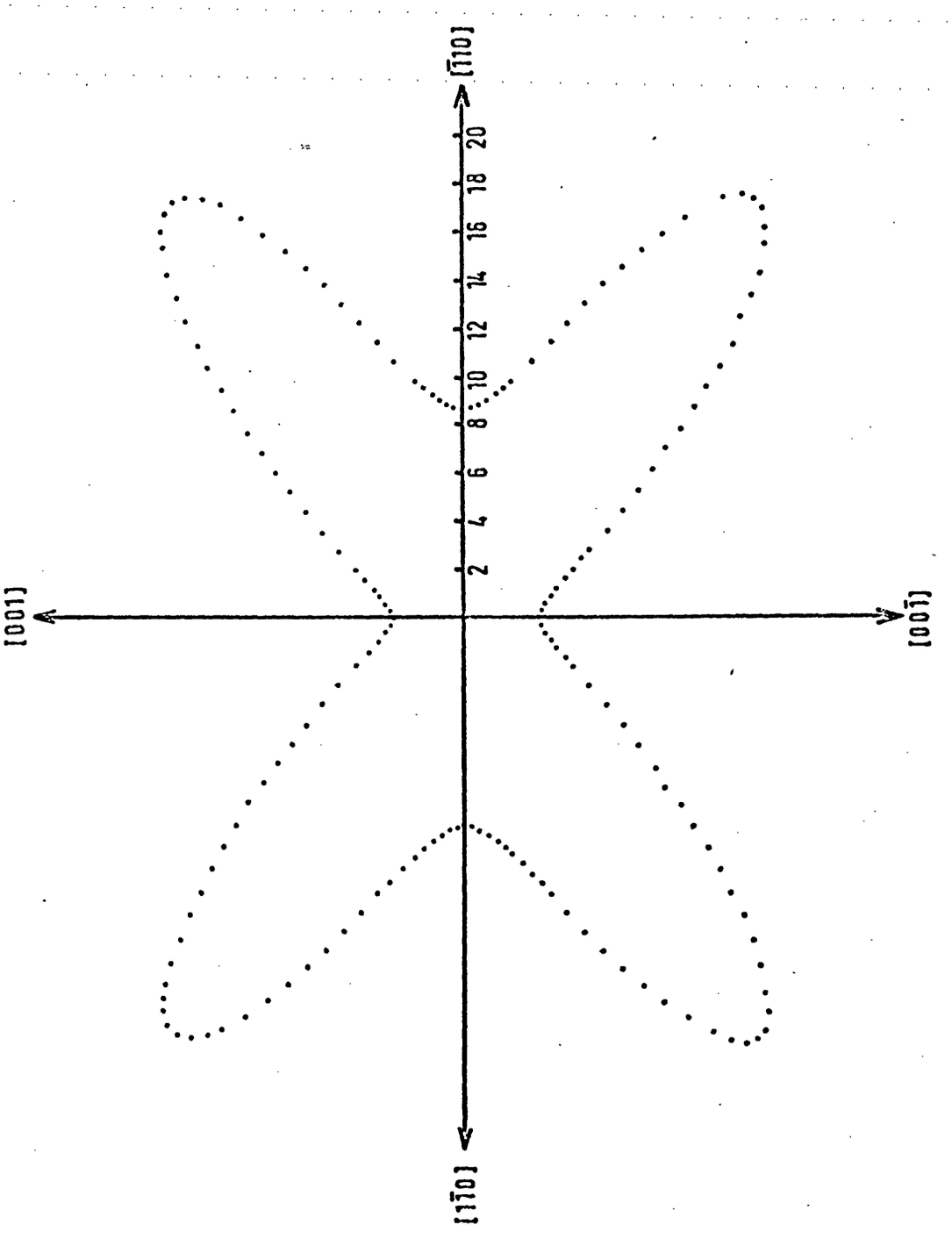

Figure 6.13 (a): The (110) plane cross-section of the Young's modulus surface of the fcc In - 6.5 at% Cd alloy at 300°K. Units: 10^{10} dyne/cm^2.

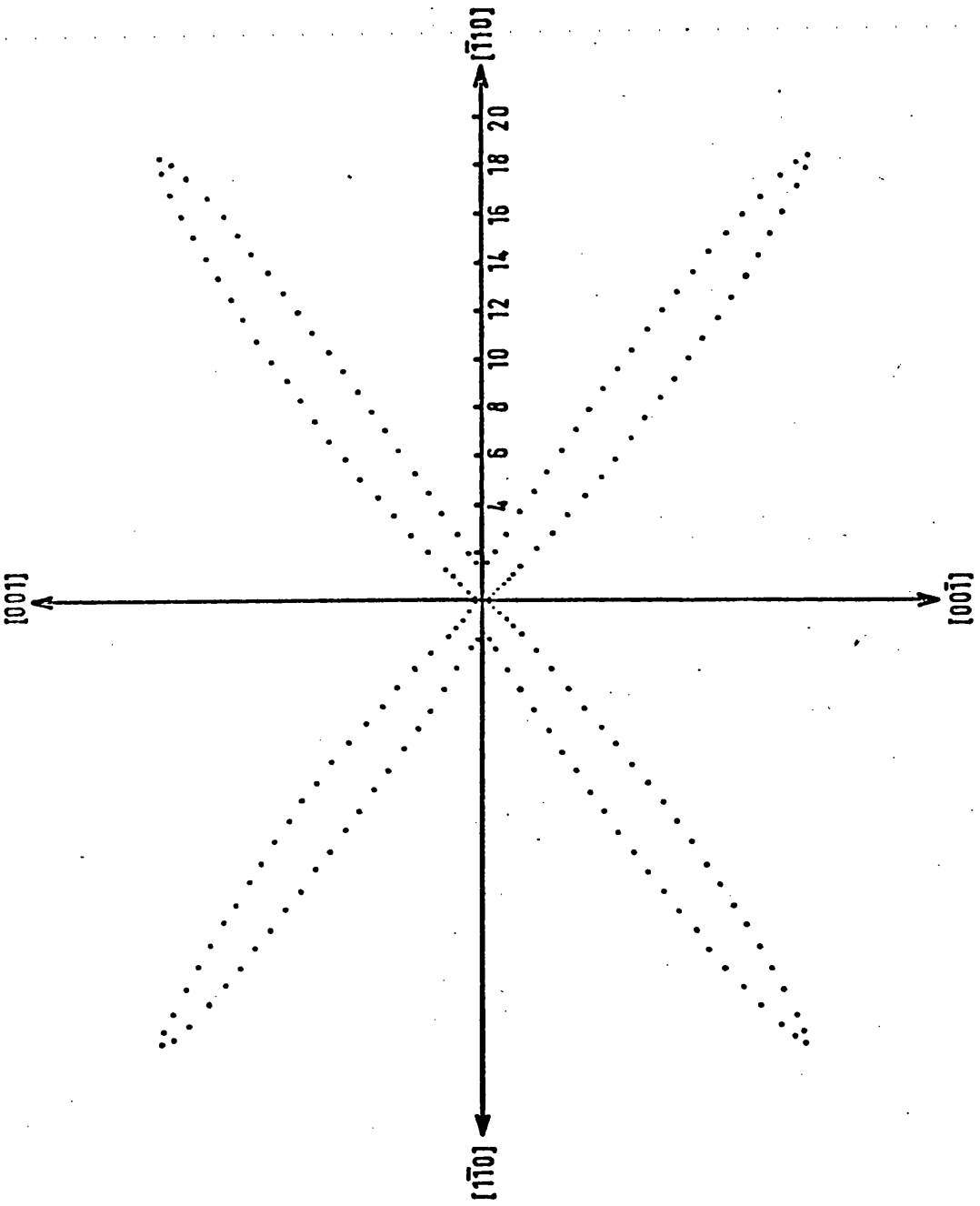

Figure 6.13 (b): The (110) plane cross-section of the Young's modulus surface of the fcc In - 6.5 at% Cd alloy at T_c (232 ± 2°K). Units: 10^{10} dyne/cm^2.

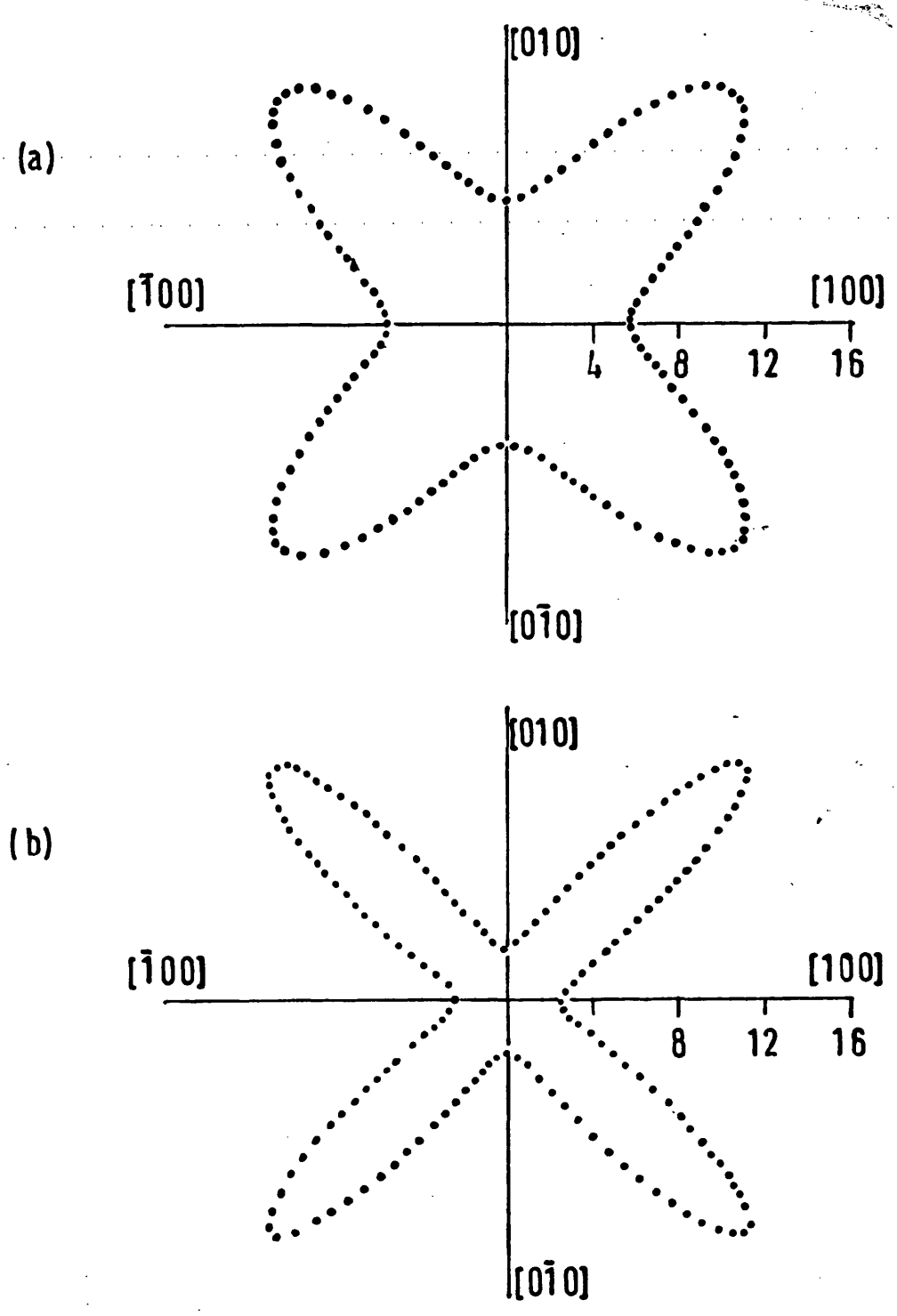

Figure 6.14: The (001) plane cross-section of the Young's modulus surface of the fct In ~ 3.4 at% Cd alloy at (a) 300°K and (b) 400°K. Units: 10^{10} dyne/cm^2.

and are included in Table 6.1. In computing these temperatures from the elastic constant data, integral over the solid angle Ω (equations 6.15 and 6.16) has been approximated by a sum taken at 10288 points each subtending an equal solid angle $\Delta\Omega$ (= 1.218×10^{-3} steradians). This method - as opposed to the simpler methods reviewed by Alers (1965) - has been found necessary because of the sectorial softening in the velocity space of In-Cd alloys. The θ_D values at 300°K for the fcc 3.4 at% Cd and fcc 6.5 at% Cd alloys are lower than that for In and decrease even further as the transformation temperature is approached (Table 6.1). This decrease is very pronounced for θ_3 of the slow shear branch reflecting the enhanced acoustic mode softening at T_c. The Debye temperatures of the longitudinal (θ_1) and fast shear (θ_2) branches remain essentially unaltered (Figure 6.15).

6.6.4 Mean square atomic displacement

The mean square atomic displacement $\langle u^2 \rangle$ can be calculated on the basis of the Debye model from the Debye-Waller factor exponent 2M. The Debye-Waller exponential factor e^{-2M} accounts for the weakening in the scattered amplitude of elastic waves from scatterers such as thermal vibrations. If λ is the wavelength of the incident elastic wave and θ is the Bragg angle, then the following relations for M of a Debye solid with cubic symmetry can be worked out (James 1962):

$$3\lambda^2 M = 8\pi^2 \sin^2\theta \langle u^2 \rangle \qquad (6.17)$$

and

$$2M = \frac{48\pi^2 \hbar^2}{mk\theta_m} \left(\frac{\Phi(x)}{x} + \frac{1}{4} \right) \left(\frac{\sin\theta}{\lambda} \right)^2 \qquad (6.18)$$

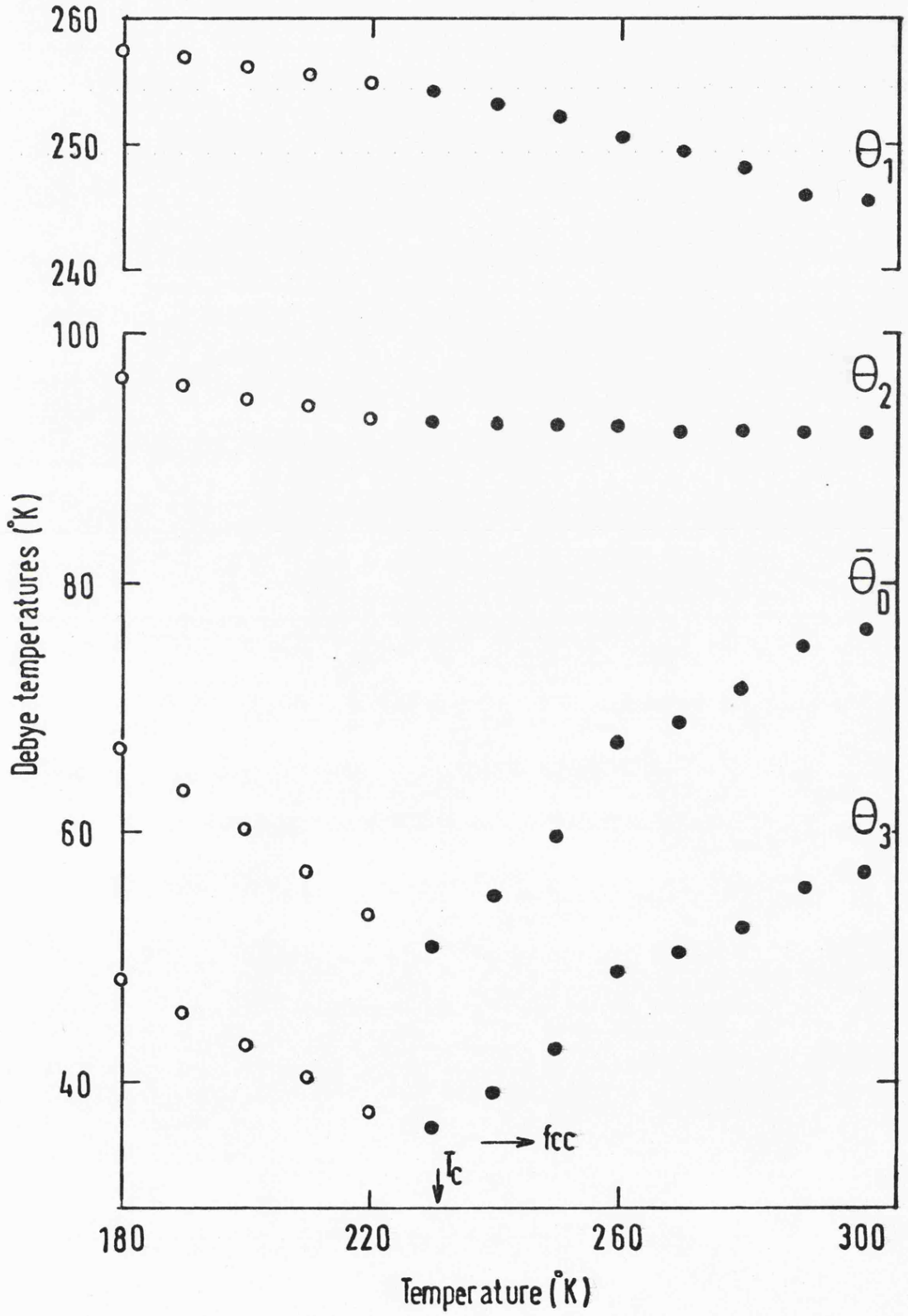

Figure 6.15: Temperature dependences of the Debye temperatures of the fcc In - 6.5 at% Cd alloy.

From equations (6.17) and (6.18) it follows that

$$\langle u^2 \rangle = \frac{9\hbar^2}{mk\theta_M} \left(\frac{\Phi(x)}{x} + \frac{1}{4} \right) \qquad (6.19)$$

where m is the mean atomic weight, θ_M is the characteristic Debye temperature, $x = \frac{\theta_M}{T}$ and $\Phi(x) = \frac{1}{x}\int_0^x \frac{\xi}{e^{\xi}-1}\, d\xi$ is the Debye integral. A tabulation of this integral for various x values can be found in Debye's original paper (Debye 1914).

The mean square atomic displacement $\langle u^2 \rangle$ has been calculated as a function of temperature T for the fcc 6.5 at% Cd alloy (Figure 6.16 and Table 6.1). In this calculation the elastic constant Debye temperature θ_D which is slightly larger than θ_M (James 1962) has been used. From Figure 6.16 it is clearly seen that as the temperature decreases towards T_c, $\langle u^2 \rangle$ rapidly increases and reaches its peak value at T_c. This behaviour reflects the diminishing value of the force constant as a result of the acoustic mode softening.

6.7 Order of the elastic phase transformation in In-Cd alloys

Many displacive phase transformations are accompanied by a symmetry reduction such that the symmetry group F of the low temperature phase is a sub-group G of the high temperature phase. Landau (1937 a,b) has shown that all continuous phase changes are driven by an order parameter which transforms according to an irreducible representation of G. In an elastic phase transformation, this parameter can be identified with the soft mode normal co-ordinate of the high symmetry phase. The Landau theory predicts

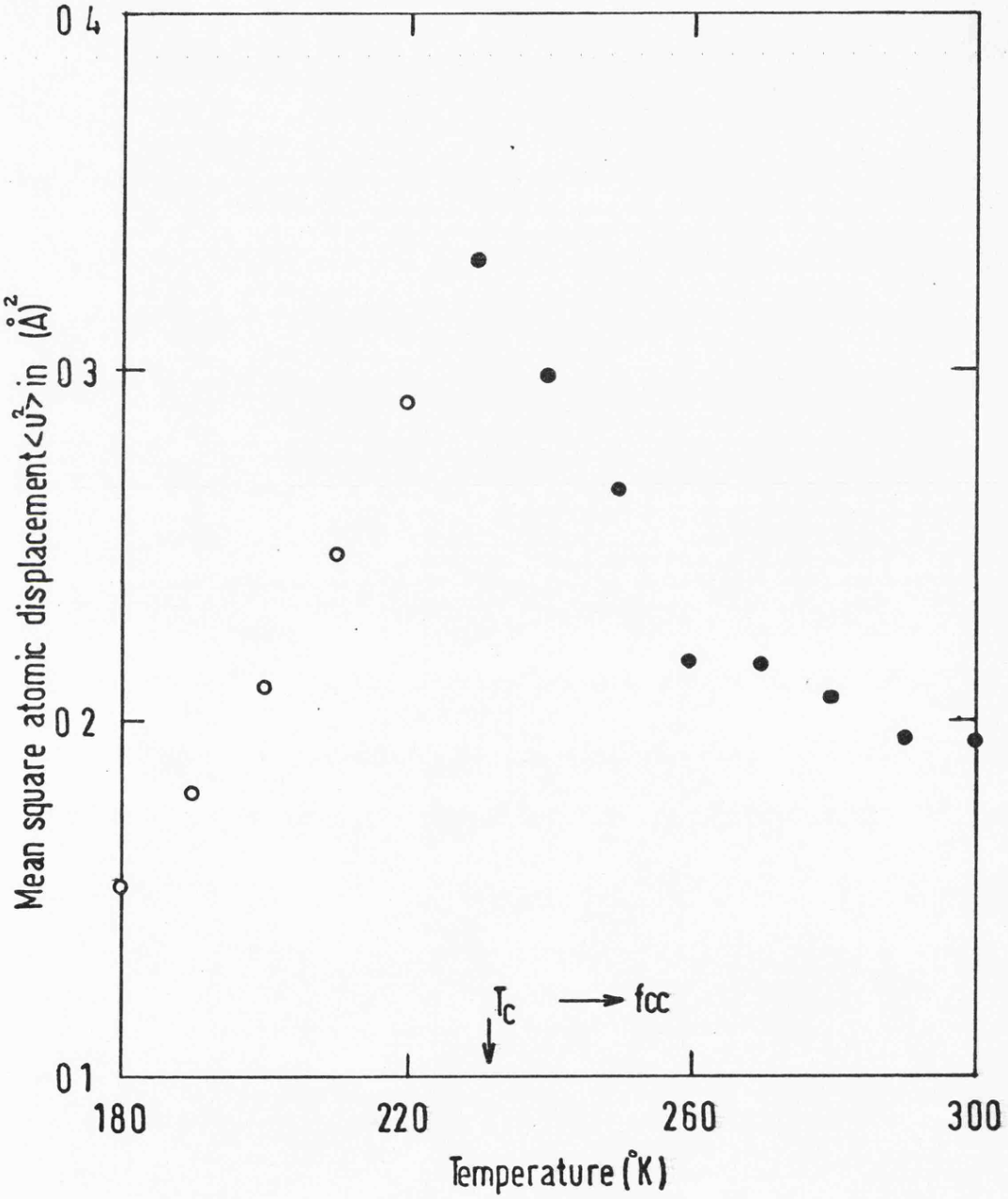

Figure 6.16: Mean square atomic displacement $\langle u^2 \rangle$ of the fcc In - 6.5 at% Cd alloy as a function of temperature.

that a phase transformation is first order if there is a cubic invariant in the expansion of the free energy as a power series in the order parameter (Figure 2.11). Cowley (1976) and Folk, Iro and Schwabl (1976) have tested for presence of cubic invariants using the symmetry of the irreducible representation of the elastic constant matrix and have found that there is such an invariant for an elastic phase transformation from the fcc to fct structure. Thus the transformations of the In-Tl and In-Cd alloys should be first order.

For the In alloys, the tetragonal distortion and the heat capacity effects at T_c are small: it is quite difficult to establish experimentally the order of the phase transformation. At a second order transformation not only the thermodynamic potentials of the two phases but also their first derivatives are equal - the phases are indistinguishable, there is no latent heat or a change in volume (Figure 2.10). Schwartz and Gerstein (1971) could not detect by adiabatic calorimeter specific heat measurements in In - 28.9 at% Tl any latent heat of transformation. Volume changes at the transformation lie within the experimental errors of dilatometric or X-ray methods (Heumann and Predel 1962, Moore et al 1955). Polovov and Ponyatovskii (1973) obtained a value of $(8.6 \pm 0.7) \times 10^{-3}$ cal/gm for ΔH and $dT_c/dP = (7 \pm 0.7)$ deg/Kbar for an In - 4.85 at% Cd alloy and estimated the change in volume at T_c as $\Delta V/V = (0.5 \pm 0.1)$ %. These parameters are much larger than those obtained for an In - 20 at% Tl alloy: $\Delta H = (4.3 \pm 0.5) \times 10^{-3}$ cal/gm, $dT_c/dP = (0 \pm 0.5)$ deg/Kbar and $\Delta V/V = (0 \pm 0.03)$ %. The phase transformation in In-Tl alloys is so weakly first order, that its character has been difficult to establish. This is not so for In-Cd

alloys. The fcc - fct transformation in In-Cd alloys is much more recognisably first order than that of the In-Tl alloys. Further experimental confirmation that this is so comes from the observation of Straumanis, Rao and James (1971) of the presence of both fcc and fct phases in a 5.945 at% Cd alloy: the simultaneous presence of both phases indicates that the phase transformation involves a two phase region - behaviour characteristic of a first order transformation. Guttman (1950) found no evidence for a two phase region in the In-Tl alloys containing up to 30 at% Tl. The major difference found between the elastic moduli of the two alloy systems corresponds to this variation between their thermodynamic behaviours at the transformation. The elastic constant $\frac{1}{2}(C_{11} - C_{12})$ in the In-Cd alloys does not go to zero at T_c (Figures 6.5 and 6.6). Yet that of the 25 at% and 27 at% Tl alloys did so within experimental error (Gunton and Saunders 1974). The presence of the cubic invariant in the Hamiltonian should render the fcc - fct transformation first order (Cowley 1976); as a result $\frac{1}{2}(C_{11} - C_{12})$ should have a finite value at T_c - the magnitude of the cubic invariant must be substantially smaller in the In-Tl alloys than in the In-Cd alloys.

C H A P T E R 7

ELASTIC CONSTANTS OF In-Tl ALLOYS AND THE POLYMORPHIC TRANSFORMATION IN Tl

7.1 Introduction

The bcc In-Tl alloys (phase diagram, Figure 2.3) correspond to solid solutions of In in the bcc polymorph of Tl. Ultrasonic wave velocities have been measured in single crystals of two compositions - 76.5 and 81.5 at% Tl. A linear extrapolation of the computed elastic constants of the alloys to the pure Tl limit has been used to provide the first estimate of the elastic constants of bcc Tl. These results have been used to examine Zener's proposals (Zener 1947, 1948, 1967) regarding the stability of bcc metals and alloys. In addition, low temperature elastic constants of fcc In-Tl alloys (30 and 31 at% Tl)-to complement previously published data (Gunton and Saunders 1974)-will also be given.

7.2 Elastic behaviour of bcc In-Tl alloys

Alloys in the In-Tl system (Figure 2.3) crystallise in the fct, fcc, bcc, and hcp structures. Previously, elastic constant measurements have been made on alloys belonging to the fct and fcc phases in the composition range 0 to 39 at% Tl (Novotny and Smith 1965, Pace and Saunders 1972 and Gunton and Saunders 1974) and it has been shown that the fcc-fct martensitic phase transformation is accompanied by softening of the $[110]$, $\underline{q}$ // $[1\bar{1}0]$acoustic phonon mode close to the Brillouin zone centre (Gunton and Saunders 1973). The present work on the bcc alloys completes knowledge of the elastic constants of the In-Tl alloys by providing single crystal data for the previously unstudied phase.

7.2.1 Elastic constants

The temperature dependences of $C_\ell = \frac{1}{2}(C_{11} + C_{12} + 2C_{44})$, C_{44} and $C' = \frac{1}{2}(C_{11} - C_{12})$ of the 76.5 and 81.5 at% Tl alloys

obtained from ultrasonic wave velocity measurements in [110] oriented samples have been plotted in Figures 7.1 and 7.2 respectively. In computing the temperature dependences of the elastic constants, corrections for sample length and density changes have been made using the thermal expansion coefficient α of 29 x $10^{-6}/^{o}K$ for bcc In-Tl alloys between 77 and 300^{o}K (Luo and Willens 1967). Table 7.1 lists the ultrasonic wave velocities at 300^{o}K measured in [110] and [100] oriented samples and provide a useful cross-check. All the elastic constants show normal behaviour with temperature: the temperature dependences of C_{ij} designated by the ratio $\Delta C_{ij}/C_{ij}$ = $C_{ij}(280^{o}K) - C_{ij}(320^{o}K)/C_{ij}(300^{o}K)$ are all positive, the values for the two alloys being (i) In - 76.5 at% Tl: $\Delta C_{\ell}/C_{\ell}$ = 0.014, $\Delta C_{44}/C_{44}$ = 0.043 and $\Delta C'/C'$ = 0.058 (ii) In - 81.5 at% Tl: $\Delta C_{\ell}/C_{\ell}$ = 0.019, $\Delta C_{44}/C_{44}$ = 0.041 and $\Delta C'/C'$ = 0.06. The temperature variations of the elastic constants are remarkably linear and there are no discontinuities which would have arisen if the eutectoid reaction (see also Chapters 2 and 4) was taking place as the temperature was lowered. Irrespective of the rate of cooling ($\sim$ 0.75 to 2^{o}K/min), the ultrasonic wave velocities were all reproducible to three significant figures after a temperature run. Further evidence that the crystals did not change phase even after cooling down to as low as 80^{o}K was obtained from X-ray studies (Chapter 4) before and after each temperature run: Laue photographs established that after each cycle the single crystals had not altered and Debye-Scherrer powder photographs showed that the alloys retained the single phase bcc structure. Apparently, there was no eutectoidal decomposition in these alloys at the rates of cooling employed. There is every reason to believe that the elastic

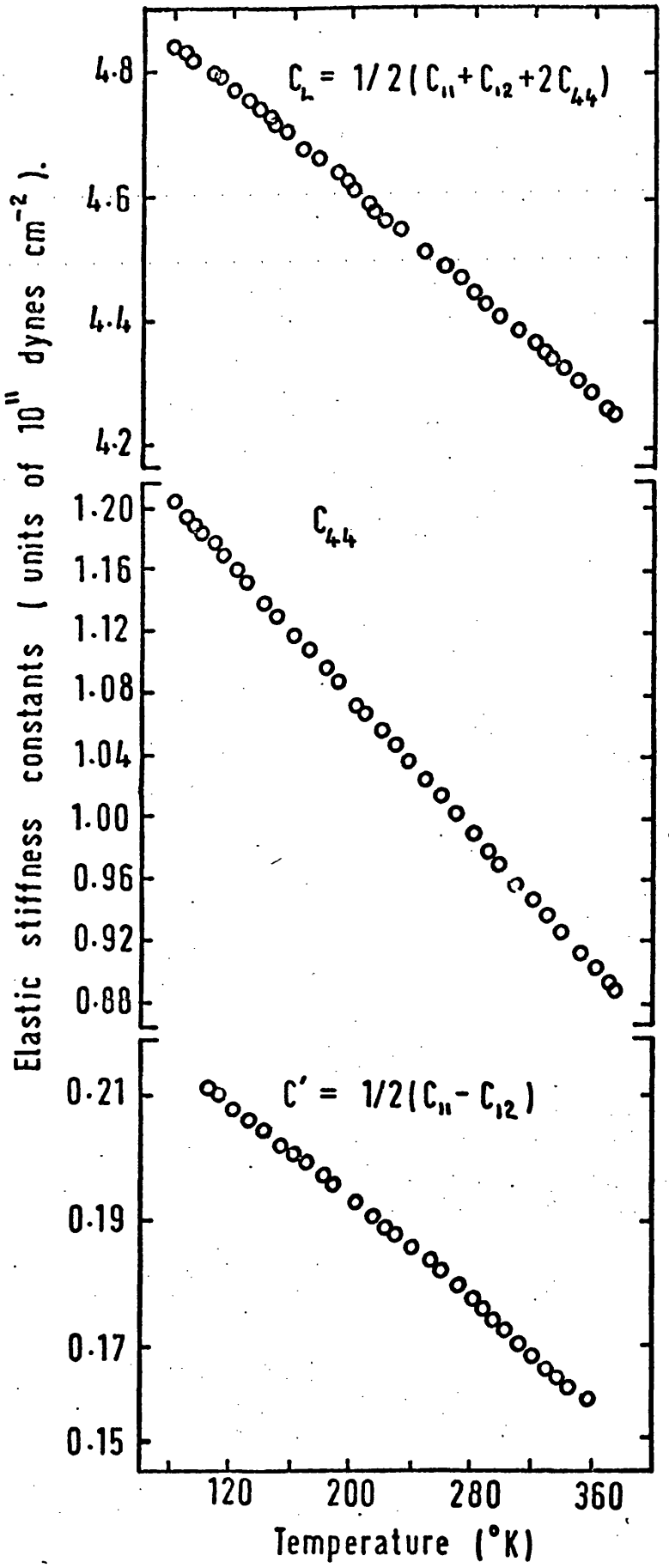

Figure 7.1: Temperature dependences of the elastic stiffness constants of In - 76.5 at% Tl alloy.

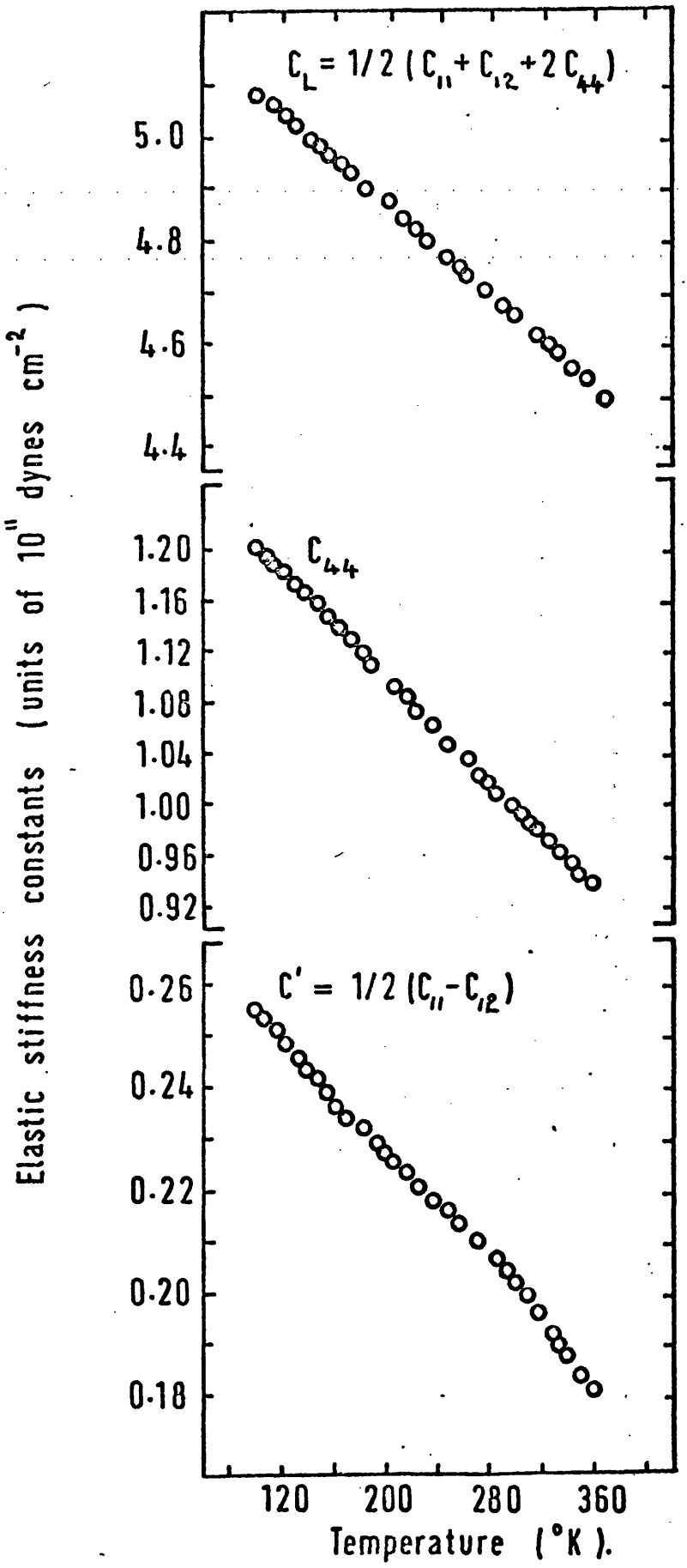

Figure 7.2: Temperature dependences of the elastic stiffness constants of In - 81.5 at% Tl alloy.

Table 7.1

Relationships between measured ultrasonic wave velocities and elastic stiffness constants

Propagation direction	Polarisation direction	Elastic Constant relationships	Ultrasonic wave velocities 'v' at 300°K (units: 10^5 cm.sec^{-1})	
			In-76.5 at% Tl	In-81.5 at% Tl
[100]	[100]	$\rho v_1^2 = C_{11}$	1.834	1.878
[100]	in (001) plane	$\rho v_2^2 = C_{44}$	0.947	0.957
[110]	[110]	$\rho v_3^2 = C_L = (C_{11}+C_{12}+2C_{44})/2$	2.02	2.051
[110]	[001]	$\rho v_4^2 = C_{44}$	0.946	0.952
[110]	$[1\bar{1}0]$	$\rho v_5^2 = C' = \frac{1}{2}(C_{11}-C_{12})$	0.399	0.434

constant data given in Figures 7.1 and 7.2 correspond to those of single phase bcc alloy crystals right down to 80°K.

The elastic stiffness constants C_{11}, C_{12} and C_{44} and the compliance constants S_{11}, S_{12} and S_{44} of the alloys calculated from the experimental results plotted in Figures 7.1 and 7.2 are given in Table 7.2 at selected temperatures. Each elastic constant C_{ij} of the 81.5 at% Tl alloy is stiffer at all the temperatures than the corresponding constant of the 76.5 at% Tl alloy. This compositional dependence affects the value of C' much more than the other elastic constants. For example, at 300°K, C' for the 81.5 at% Tl alloy is 21% stiffer than that of the 76.5 at% Tl alloy; whereas for C_{44} this difference is only 3.5%. Despite this increased stiffening, C' remains small compared to the other principal shear modulus C_{44}.

7.2.2 Volume compressibility

The elastic constant results have been used to calculate the adiabatic compressibility $\beta_S (= -V^{-1}(\partial V/\partial P)_S = 3/(C_{11} + 2C_{12}))$; the values obtained are given in Table 7.2 at selected temperatures. β_S values at 300°K for alloys belonging to the different phase fields in the In-Tl system have been plotted as a function of the alloy composition in Figure 7.3. Included in this plot are the isothermal compressibilities β_T $(= -V^{-1}(\partial V/\partial P)_T)$ for bcc alloys of comparable composition to those of the present study calculated from Bridgman's high pressure data (Bridgman 1955); the difference $(\beta_T - \beta_S)$ is $TV\alpha^2/C_p$ and is approximately 0.7% only. Thus the present results for the compressibility of bcc alloys are in reasonable agreement with those of Bridgman (Figure 7.3). The variation of the compressibility

Table 7.2

The elastic properties of bcc In-Tl alloys

Composition (at% Tl)	76.5			81.5		
Temperature (^{o}K)	100	300	350	100	300	350
Elastic stiffness Constants (in units of 10^{11} dyne cm^{-2})						
C_{11}	3.836	3.611	3.555	4.147	3.853	3.786
C_{12}	3.414	3.267	3.231	3.625	3.437	3.408
C_{44}	1.184	0.967	0.914	1.206	1.001	0.948
$C' = \frac{1}{2}(C_{11} - C_{12})$	0.211	0.172	0.162	0.261	0.208	0.189
Debye temperature (^{o}K)						
θ_D	79.6	72.2	70.2	82.9	75.3	72.5
θ_ℓ	200.7	192.5	190.5	204.5	195.8	193.5
θ_{fs}	93.0	84.0	81.7	93.3	85.3	82.5
θ_{ss}	60.2	54.6	53.1	63.4	57.4	55.1
Mean Square atomic displacement $\langle u^2 \rangle$ in $(\text{Å})^2$	0.038	0.135	0.168	0.034	0.121	0.153
Anisotropy factor $A = C_{44}/C'$	5.611	5.622	5.642	4.621	4.812	5.016
Elastic Compliance Constants (in units of 10^{-10} cm^2 $dyne^{-1}$)						
S_{11}	0.161	0.197	0.209	0.131	0.163	0.179
S_{12}	-0.076	-0.094	-0.099	-0.061	-0.077	-0.085
S_{44}	0.084	0.103	0.109	0.083	0.099	0.105
Bulk modulus B (in units of 10^{12} dyne cm^{-2}) $\left(= \frac{1}{3}\{C_{11}+2C_{12}\}\right)$	0.355	0.338	0.334	0.380	0.357	0.353
Compressibility β_S (in units of 10^{-12} cm^2 $dyne^{-1}$) $(= B^{-1})$	2.81	2.96	2.99	2.63	2.80	2.83

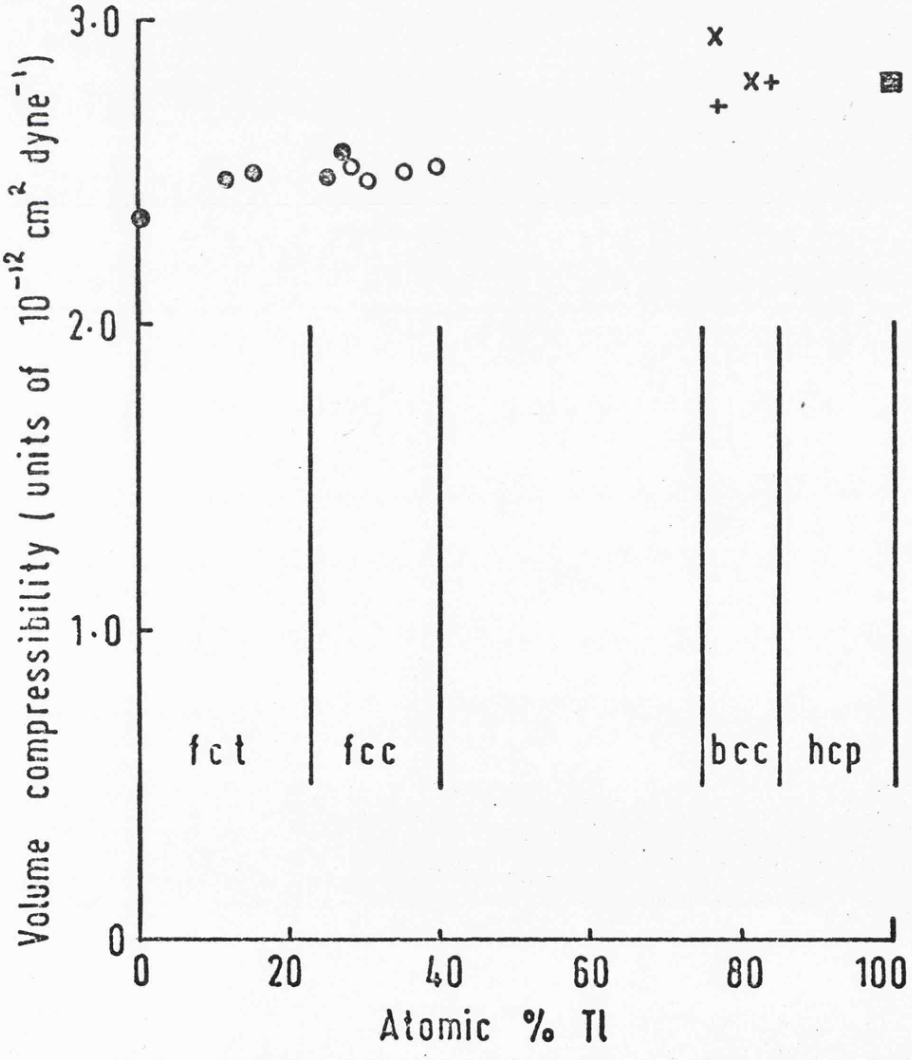

Figure 7.3: Volume compressibilities of In-Tl alloys.
● Gunton and Saunders (1974), o Novotny and Smith (1965),
+ Bridgman (1955) and ■ Ferris et al (1963).

over the whole composition range from pure fct In through the fcc and bcc alloys to hcp Tl is surprisingly small: alloying between these two group IIIB metals has only a small effect on the cohesive energy throughout the alloy system.

7.2.3 Anisotropy ratio and stability

Resistance to shear of a cubic crystal is best characterised by the two moduli $C' = \frac{1}{2}(C_{11} - C_{12})$ and C_{44} (Figure 7.4). In the bcc In-Tl alloys, the former is much smaller than the latter and also exhibits stronger temperature dependence (Figures 7.1 and 7.2). Therefore, the anisotropy factor $A(= C_{44}/C')$ has large values and is sensitive to temperature and composition. Since the magnitude of C' in metallic bcc crystals relates to the occurrence of displacive phase transformations, the anisotropy factor A is a useful guide to the relative stability of these materials. The elastic behaviour can be displayed with advantage on a plot of the reduced elastic stiffnesses C_{12}/C_{11} against C_{44}/C_{11}; here A can be represented by a fan of lines originating at the point ($C_{12}/C_{11} = 1$, $C_{44}/C_{11} = 0$) and the Cauchy relation $C_{12} = C_{44}$ for central force crystals is a diagonal. The data for bcc metals and alloys plotted in this way (Figure 7.5) can be compared with those for fcc materials collected together by Ledbetter and Moment (1976) in Figure 6 of their paper. The bcc metals and alloys separate into two distinct groups the members of which cluster into two different areas on this reduced elastic stiffness diagram (Figure 7.5): the marked difference between stability of crystals in these two groups can be understood qualitatively on the basis of elastic anisotropy of the shear moduli. (i) The bcc transition metals V, Cr, Nb, Mo, Ta and W, which tend to be elastically isotropic are rendered stable

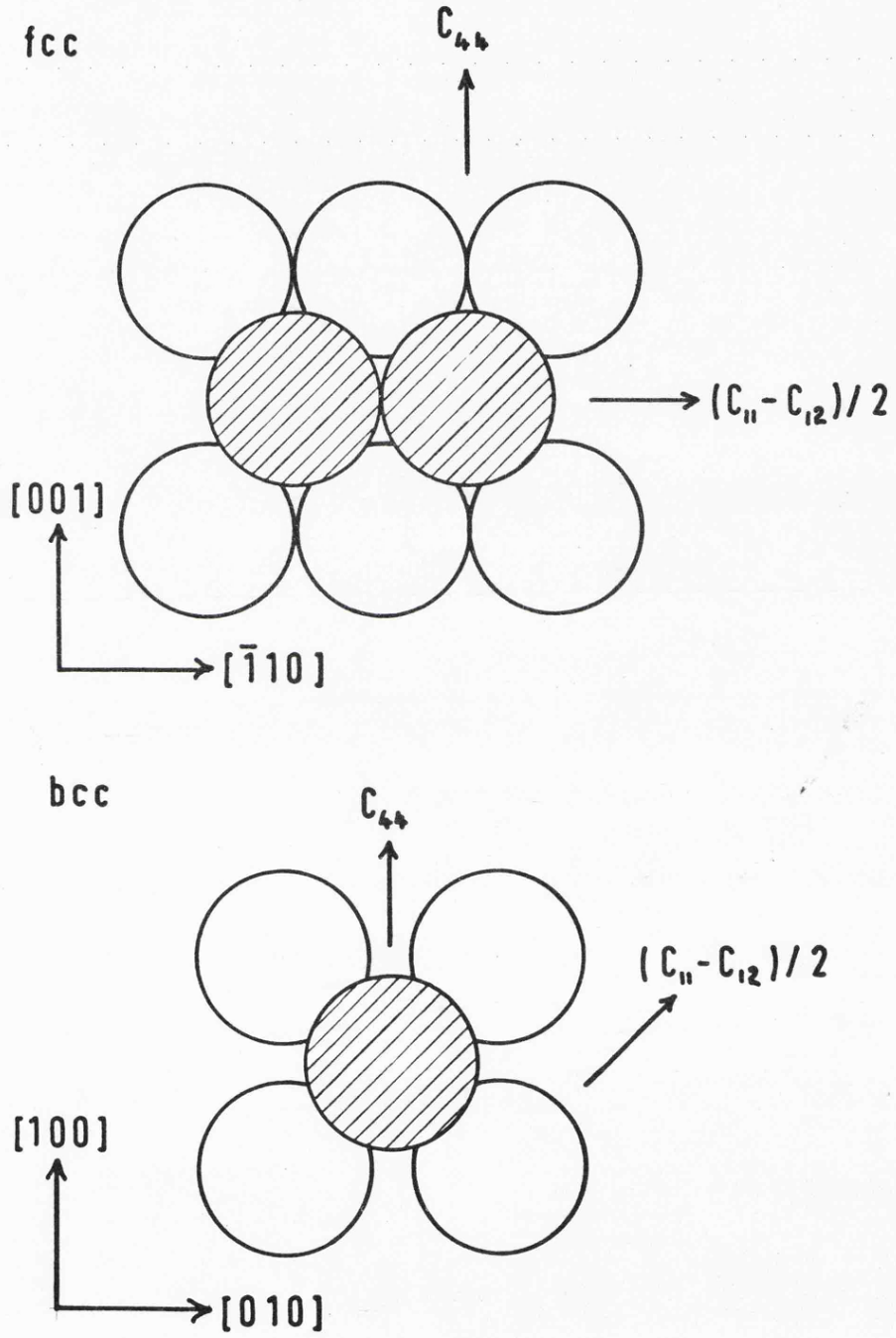

Figure 7.4: Shear moduli of cubic crystals.

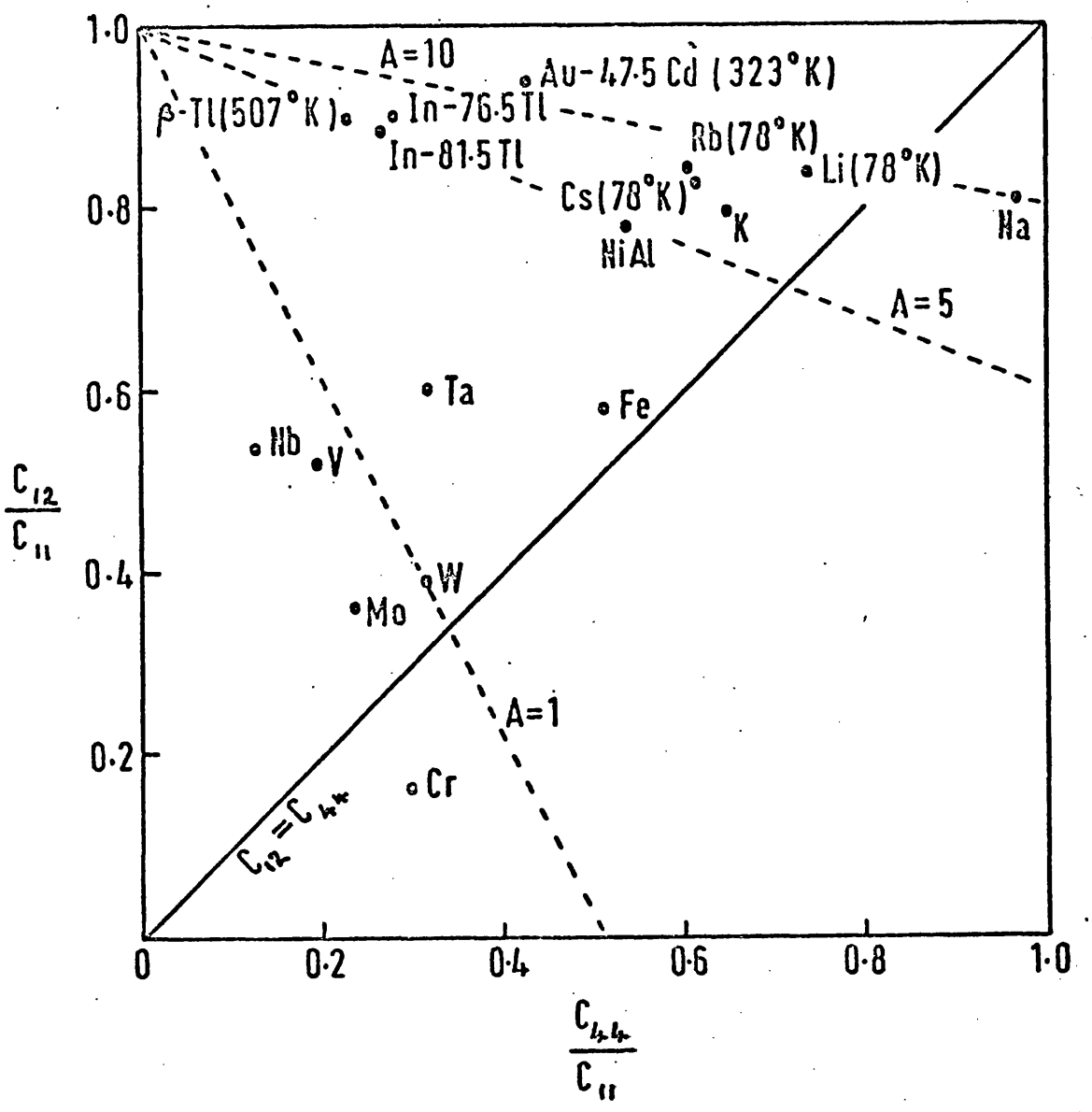

Figure 7.5: Anisotropy factor A(= C_{44}/C') of bcc metals and alloys. Unless otherwise indicated the results are at 300°K. Elastic constant data have been obtained from Gutman and Trivisonno (1967) for Rb, Kollarits and Trivisonno (1968) for Cs and France et al (1967) for all the others.

at all temperatures by long range interactions between the electrons in the unfilled d-shells: the comparatively large magnitude of C' in these elements is related to the number of electrons per atom in the unfilled d-bands (Fisher and Dever 1970). (ii) The second group is comprised of those metals and alloys which crystallise in the bcc structure but transform to a close-packed structure on cooling. This latter group into which bcc In-Tl alloys fall, includes the alkali metals and β-brass. Zener (1947, 1948) first pointed out that a bcc crystal comprised of rigid spheres (or of ions containing only closed shells) would show no resistance to a (110), $[1\bar{1}0]$ shear and would tend to shear spontaneously on the (110) plane in a $[1\bar{1}0]$ direction. He concluded that the corresponding shear modulus $\frac{1}{2}(C_{11} - C_{12})$ should be abnormally small in those bcc crystals in which the interatomic repulsive forces are qualitatively similar to those between contacting rigid spheres: such materials would be inherently mechanically unstable. For bcc Tl (ionic radius = 1.05 Å, a = 3.879 Å) like bcc Na (ionic radius = 0.98Å, a = 4.225 Å), the ions are too small to overlap appreciably. The small values of $\frac{1}{2}(C_{11} - C_{12})$ found here for the bcc In-Tl alloys (Table 7.2) conform to Zener's original prediction and establish that these alloys are not far from being mechanically unstable to a (110), $[1\bar{1}0]$ shear. The large deviation from the Cauchy relation ($C_{12} = C_{44}$) in Figure 7.5 indicates appreciable non-central force contributions to the elastic constants.

As explained in Chapter 6 (Section 6.6.2), the anisotropy of elastic behaviour can be illustrated by polar plots of Young's modulus. The (100) and (110) plane cross-sections of the Young's modulus surface shown in Figures 7.6 and 7.7 respectively for the

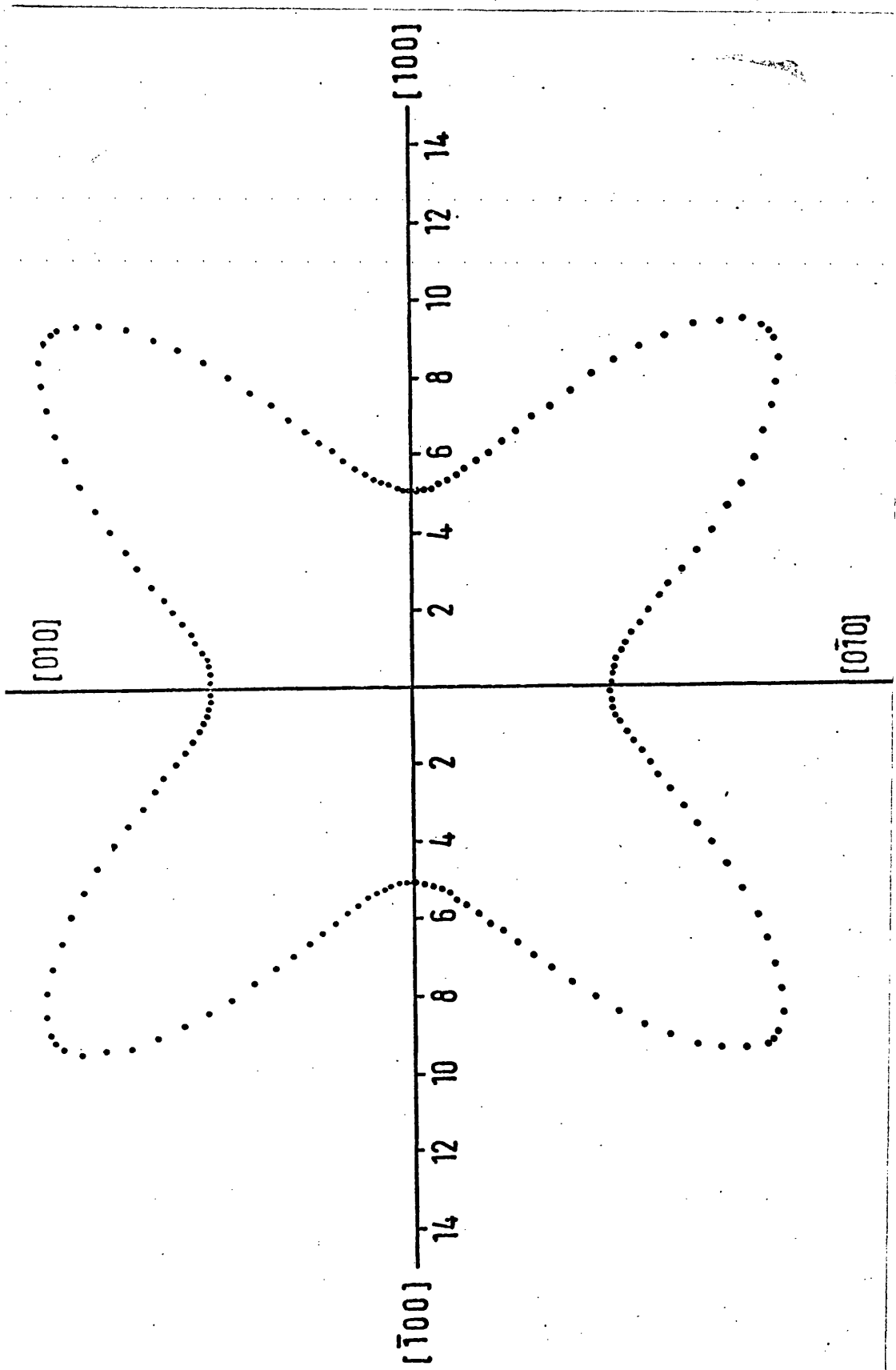

Figure 7.6: The (100) plane cross-section of the Young's modulus surface of In - 76.5 at% Tl alloy at 300°K. Units: 10^{10} dyne/cm^2.

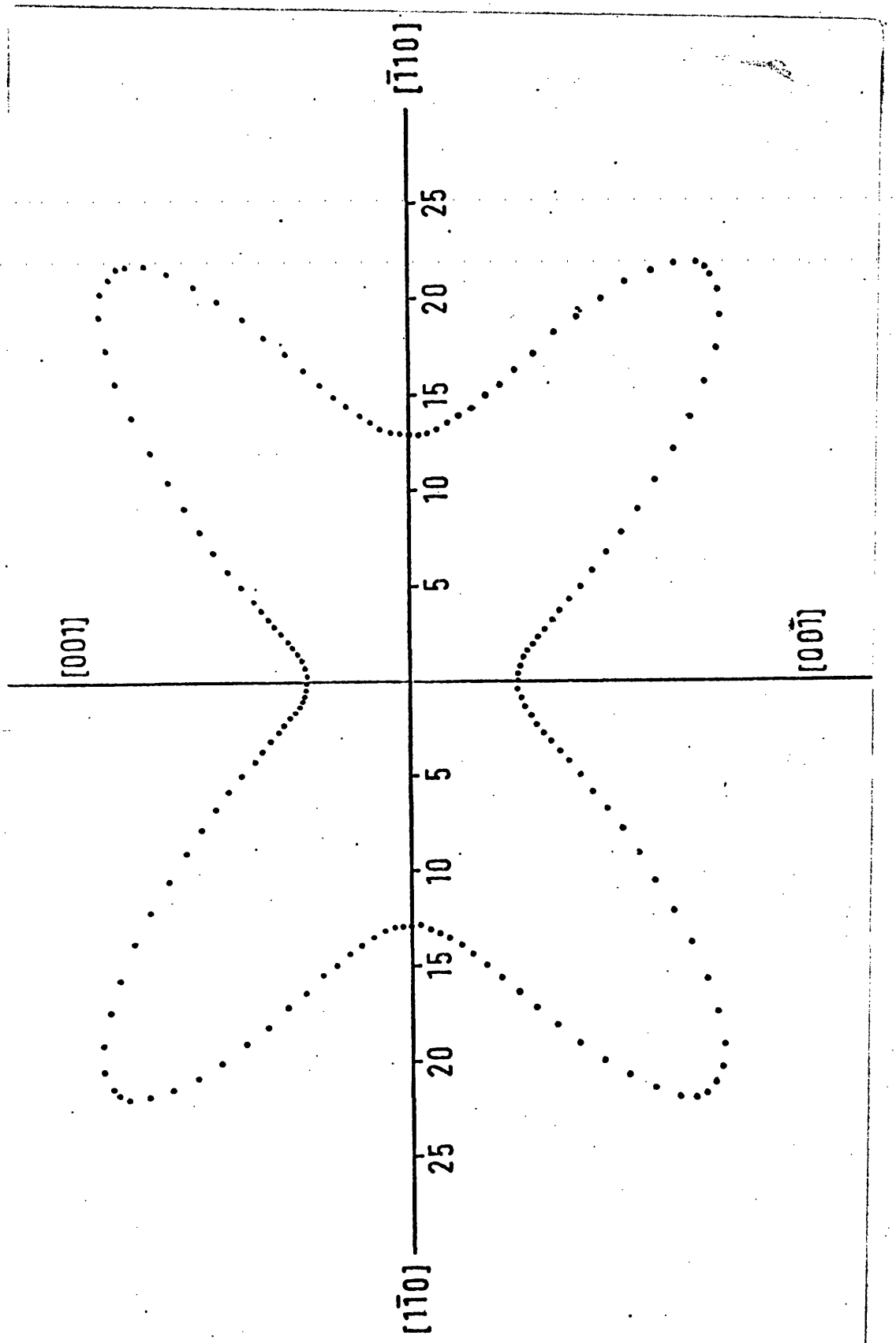

Figure 7.7: The (110) plane cross-section of the Young's modulus surface of In - 76.5 at% Tl alloy at 300°K. Units: 10^{10} dyne/cm^2.

In - 76.5 at% Tl at 300°K emphasise the marked anisotropy of these alloys.

7.2.4 Debye temperature

The Debye temperature θ_D has been calculated from ultrasonic wave velocity measurements using equation 6.15 (see Chapter 6). The marked anisotropy of (100) and (110) plane cross-sections of the velocity surfaces (Figures 7.8 and 7.9) again demonstrates the necessity for using a fine mesh grid of points in velocity space for the solution of the integral in equation 6.15 if an accurate Debye temperature is to be obtained. Using the elastic constant set obtained at a given temperature, one obtains $\theta_D(T)$ as distinct from θ_o the low temperature limit. The calculated Debye temperatures are given in Table 7.2. There is no specific heat data for the bcc In-Tl alloys available at the present for comparison.

7.3 Polymorphic transformation in Tl

7.3.1 The pressure-temperature diagram

Since the classic experiments of Werner (1913) and Bridgman (1935), the pressure-temperature (P-T) diagram of Tl has been the subject of a number of studies. The triple point found by Bridgman (1935) as 153°C and 38 Kbar has been re-measured by thermal analysis (Ponyatovskii 1959, Jayaraman et al 1963) and resistance studies (Adler and Margolin 1964) leading to the value of 110 ± 7°C and 37 ± 0.3 Kbar. The P-T diagram reproduced in Figure 7.10 lists the stability limits of the polymorphs as:

(i) hcp (ε) phase - atmospheric pressure and up to 507°K

(ii) bcc (β) phase - atmospheric pressure and between 507 and the

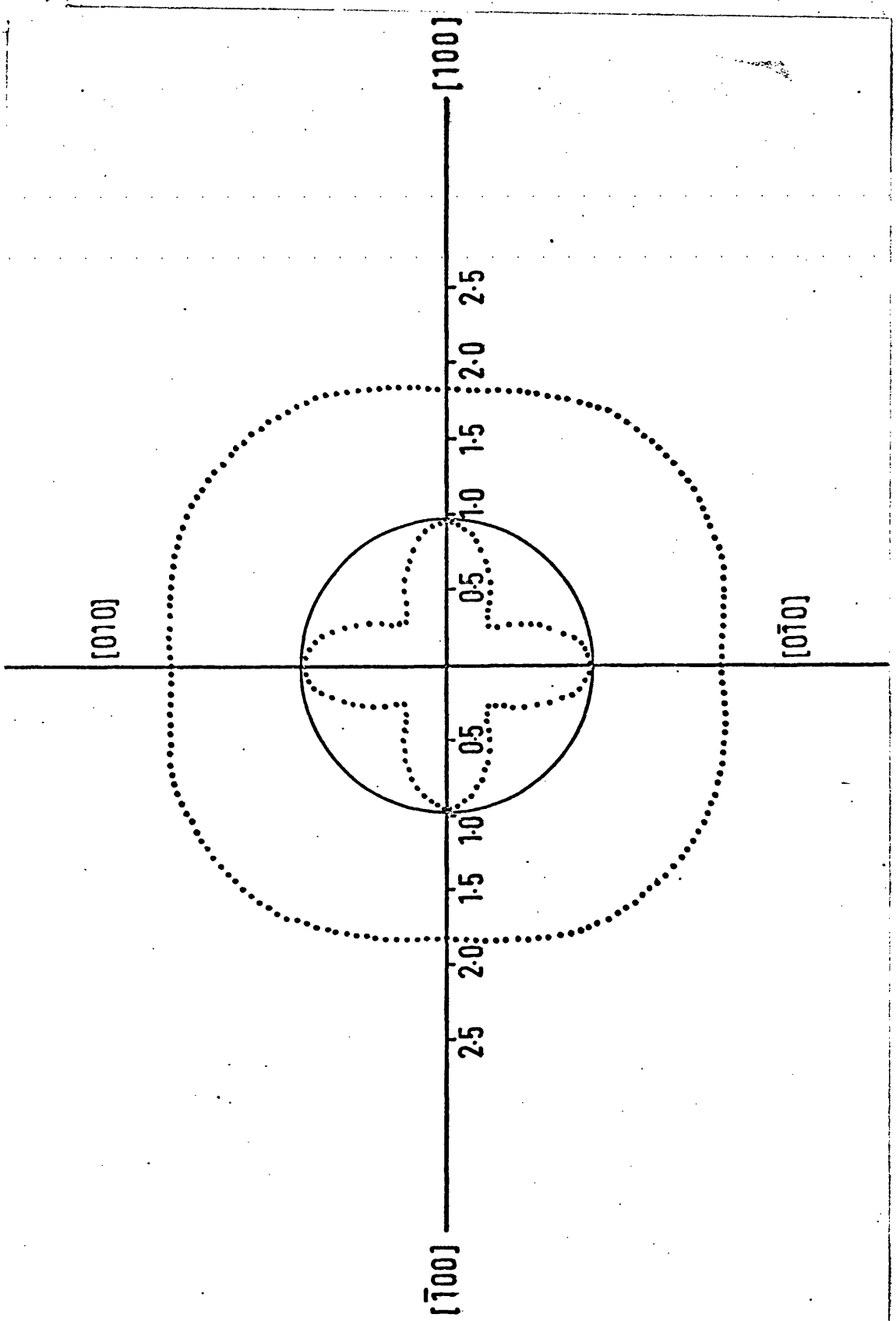

Figure 7.8: The (100) plane cross-sections of the velocity surface of In - 76.5 at% Tl alloy at 300°K. Units: 10^5 cm/sec.

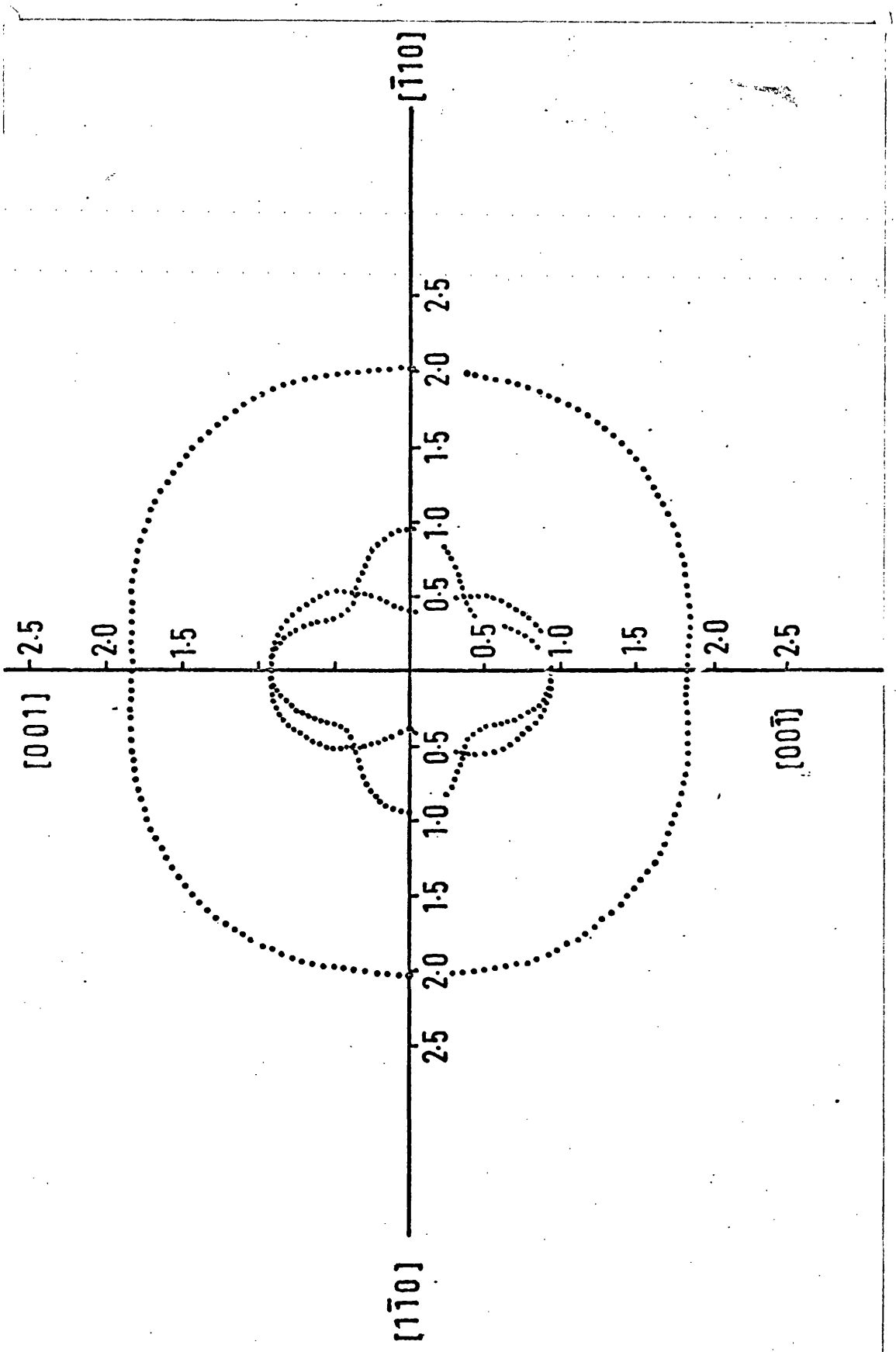

Figure 7.9: The (110) plane cross-sections of the velocity surface of In - 76.5 at% Tl at 300°K. Units: 10^5 cm/sec.

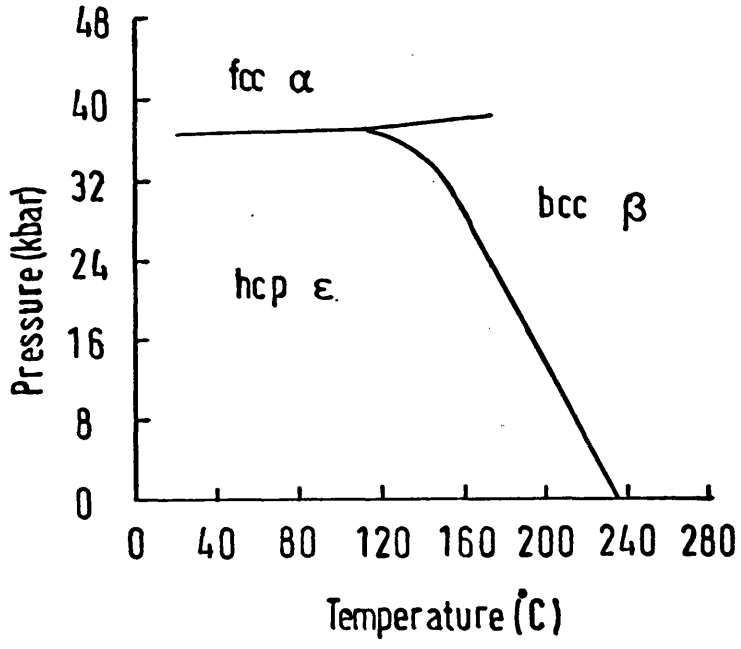

Figure 7.10: The pressure-temperature (P-T) diagram of Tl (Adler and Margolin 1964).

melting point (T_m = 577°K) and (iii) fcc (α) phase - at room temperature and above 37 Kbar.

7.3.2 Elastic constants of bcc Tl

Tl exhibits each of the three most common structures of the elemental metals: hcp, fcc and bcc. Of these the fcc phase is stable only under high pressures. The high temperature bcc phase while stable at atmospheric pressure, cannot be retained at room temperature even with fact quenching techniques (Luo and Willens 1967). Yet comparison between the elastic constants is pre-requisite for assessing the relative stability of each of the three phases. To do this, recourse has to be made to extrapolation of elastic constant data obtained for Tl-rich alloys. Previously, estimates of the elastic constants of fcc Tl have been made by extrapolation of data both for fcc In-Tl alloys (Novotny and Smith 1965) and for fcc Pb-Tl alloys (Shepard and Smith 1967). The elastic constants of the normally occurring hcp form have also been reported (Ferris, Shepard and Smith 1963, Weil 1965).

The elastic constants of bcc Tl have been obtained by linear extrapolation of the bcc alloy data back to the pure Tl limit. Results are presented in Table 7.3. The elastic constants of all the polymorphs of Tl are compared in Table 7.4. The two cubic forms show very similar elastic behaviour.

7.3.3 Debye temperatures of bcc and hcp Tl

$\theta_D(T)$ values for bcc Tl obtained from the ultrasonic wave velocity measurements are included in Table 7.3. For hcp Tl,

Table 7.3

Elastic properties of bcc β polymorph of Tl based on the alloy composition extrapolated elastic stiffnesses of bcc In-Tl alloys.
The elastic constants at 507 and 577°K are the temperature extrapolated values

Temperature (°K)	100	300	350	507	577
Elastic stiffness constants (units: 10^{11} dyne cm^{-2})					
C_{11}	5.3	4.74	4.63	4.21	4.02
C_{12}	4.41	4.05	4.06	3.78	3.67
C_{44}	1.29	1.12	1.07	0.94	0.88
$C' = \frac{1}{2}(C_{11} - C_{12})$	0.44	0.34	0.28	0.21	0.17
Anisotropy ratio $A = C_{44}/C'$	2.93	3.29	3.82	4.48	5.18
Bulk modulus $B = (C_{11} + 2C_{12})/3$ (units: 10^{12} dyne cm^{-2})	0.47	0.43	0.43	0.39	0.38
Compressibility $\beta_S = B^{-1}$ (units: 10^{-12} cm^2 $dyne^{-1}$)	2.1	2.3	2.3	2.5	2.6
Debye temperature θ_D (°K)	91.3	83.2	79.2	71.6	67.3

Table 7.4

The elastic stiffness constants of the Tl polymorphs

Elastic stiffness constants (units: 10^{11} dyne cm^{-2})	ε (hcp)*	α (fcc)**	β (bcc)
C_{11}	4.08	4.08	4.74
C_{12}	3.54	3.40	4.05
C_{13}	2.9	-	-
C_{33}	5.28	-	-
C_{44}	0.726	1.10	1.12
$\frac{1}{2}(C_{11} - C_{12})$	0.270	0.34	0.34

* Ferris, Shepard and Smith (1963)

** Shepard and Smith (1967)

Debye temperatures of 75°K (Ferris, Shepard and Smith 1963) and 83.2°K (Weil 1965) have been obtained from ultrasonic measurements made at 300 and 4.2°K respectively and 85°K from specific heat data at low temperatures (van der Hoeven and Keesom 1964). On the basis of these numbers, it is difficult to establish a precise value for the Debye temperature of hcp Tl. However, 80 ± 3°K would seem to be an acceptable value for $\theta_D(T)$ for $T > \theta_D$.

7.3.4 High temperature stability of bcc Tl

The existence of the bcc to hcp structural transformation in Tl requires that the Gibbs free energy G(T,P) (equal to U + PV - TS) curves for the two phases cross over. Thus the stability of the phases is determined by two factors: (i) the binding energy at absolute zero (ii) the entropy. The internal energy of close-packed structures should be lower than that of the bcc structure and hence the close-packed structure is expected to be stable at low temperatures (Zener 1947, 1948, 1967). However, in general the looser the packing of a structure, the greater will be the entropy of vibration. Due to the abnormally small value of $\frac{1}{2}(C_{11} - C_{12})$, as the temperature is raised, there is a large amplitude of vibration of the (110), $[1\bar{1}0]$ shear strain co-ordinate; this produces a large vibrational entropy contribution and thus a more rapid decrease of free energy with temperature for the bcc than for the close-packed structures. Thus, the bcc structure is thermodynamically favoured at high temperatures. Zener's old argument has recently been examined by detailed analysis by Grimvall and Ebbsjö (1975) who point out that there are no measurements of elastic constants or of neutron or X-ray scattering experiments that can be used to put the idea to a firm experimental test.

The present experimental results can be used to examine the hypothesis that the stability of the bcc structure at high temperatures is due to its larger vibrational entropy. In the first place, the finding that $\frac{1}{2}(C_{11} - C_{12})$ is small provides direct confirmatory evidence. Previously, measurements of the latent heats of phase transformation between the low temperature close-packed and the bcc phases have shown that the excess entropy of the bcc phase is equivalent to a sizable proportion of the entropy of melting (see for example Kubaschewski and Evans 1958). In the harmonic approximation, the free energy of phonons having a frequency spectrum $f(\nu)$ is given by

$$G_{ph} = kT \int \ell n \left(2\sinh(h\nu/2kT) \right) f(\nu) d\nu \qquad (7.1)$$

Grimvall and Ebbsjö (1975) proceed by defining a characteristic temperature that corresponds to a geometrical average of the phonon frequencies and find that at high temperatures where T is greater than θ

$$G_{ph} \sim 3NkT \ell n (\theta/T) \qquad (7.2)$$

where N is the number of atoms.

In general, the difference $\Delta\theta (= (\theta_1 - \theta_2))$ between the characteristic temperatures of the two polymorphs will be small and to a reasonable approximation the phonon spectrum can be replaced either by the Einstein or Debye model. Then the Helmholtz free energy and entropy at a temperature T can be written as:

Einstein model

$$A = \Phi_o + \frac{3}{2}Nk\theta_E + 3NkT\ell n\,(1-e^{-\theta_E/T}) \qquad (7.3)$$

$$S = -\left(\frac{\partial A}{\partial T}\right)_V = 3Nk\left[(\theta_E/T)(e^{\theta_E/T}-1)^{-1} - \ell n(1-e^{-\theta_E/T})\right] \qquad (7.4)$$

Debye model

$$A = \Phi_o + 9N\left\{k\theta_D/8 + kT(T/\theta_D)^3\int_o^{\theta_D/T}\xi^2\ell n(1-e^{-\xi})\,d\xi\right\} \qquad (7.5)$$

$$S = 3kN\left\{-\ell n(1-e^{-\theta_D/T}) + 4(T/\theta_D)^3\int_o^{\theta_D/T}\frac{\xi^3}{(e^{\xi}-1)}\,d\xi\right\} \qquad (7.6)$$

where Φ_o is the static crystal potential and the other notations take their usual significance (Wallace 1972). It can be shown that the excess entropy ΔS of the bcc (β) phase over that of the hcp (ε) phase when $T > \theta$ is given for the Einstein model by

$$\Delta S = S^{\beta} - S^{\varepsilon} = 3Nk\ \ell n(\theta_E^{\varepsilon}\ /\ \theta_E^{\beta}) \qquad (7.7)$$

and for the Debye model of vibration spectrum

$$\Delta S \simeq 3Nk\ \ell n(\theta_D^{\varepsilon}\ /\ \theta_D^{\beta}) \qquad (7.8)$$

From these expressions it is possible to calculate the excess entropy and the difference $-T(S^{\beta} - S^{\varepsilon})$ in the vibrational entropy contribution to the free energy between the two polymorphs once the Debye or the Einstein temperatures are known.

Using 71.6°K (Table 7.3) and 80 ± 3°K for θ_D of bcc and hcp

Tl respectively at the polymorphic transformation temperature of 507°K, the excess entropy of the bcc structure calculated using equation (7.8) will be (0.35 ± 0.15) k per atom. The value obtained from latent heat (TΔS) measurements was (0.18 ± 0.02) k per atom (quoted by Friedel 1974).

Friedel (1974) has suggested that the high temperature stability of the bcc phase may be related to the fact that it is an alternate structure (i.e., a close circuit of interatomic jumps between successive nearest neighbours requires an even number of jumps) while the hcp and fcc structures are not. The expression found by Friedel for the excess entropy of the bcc (β) phase over the hcp (ε) phase written in the same terminology used here is for the Einstein model

$$\Delta S = S^{\beta}-S^{\varepsilon} \simeq 3Nk\left\{ \ell n\ (\omega_E^{\varepsilon}/\omega_E^{\beta}) - \hbar^2/24k^2T^2\left((\omega_E^{\beta})^2 - (\omega_E^{\varepsilon})^2 \right)\right\} \qquad (7.9)$$

(where ω_E is the Einstein frequency).

Or in terms of the number of nearest neighbours p

$$\Delta S \simeq 3Nk\left\{ \tfrac{1}{2}\ell n\,(p^{\varepsilon}/p^{\beta}) - (p^{\beta}-p^{\varepsilon})\,(\hbar\omega_E^{\varepsilon})^2/24p^{\varepsilon}k^2T^2\right\} \qquad (7.10)$$

The Einstein temperature θ_E is approximately 3/4 θ_D (and so is ∿54°K for bcc Tl and ∿60°K for hcp Tl). For $T > \theta_E$ which is true at the polymorphic transformation temperature (507°K), the second term in equation (7.10) is negligible (it is only 0.002% of the first term). The excess entropy of the bcc phase is then

$$\Delta S \simeq 3/2\ Nk\ell n(12/8) = 0.6\ Nk \qquad (7.11)$$

Thus in the case of the bcc to hcp transformation in Tl the excess entropy calculated on the basis of number of nearest neighbours and the consequent reduction in the Einstein frequency of the more open bcc structure is three times greater than that obtained from latent heat measurements and twice that obtained from the elastic constant data. The discrepancy may arise from a strong contribution to the elastic constants from the higher order neighbours which the Friedel model does not take into account.

It can be concluded that in agreement with Zener's predictions (Zener 1947, 1948, 1967): (i) the shear stiffness constant $\frac{1}{2}(C_{11} - C_{12})$ of bcc In-Tl alloys is small and (ii) the stability of the bcc phase at high temperatures is due to the lower Debye temperature and excess vibrational entropy relative to the hcp structure.

7.4 Elastic constants of fcc In-Tl alloys

The fcc (high temperature) to fct (low temperature) martensitic transformation in In-rich, In-Tl alloys occurs at a temperature set by the alloy composition. In alloys containing between 15.5 and 31 at% Tl (Figure 2.3), the transformation temperature T_c varies approximately linearly between $425^{\circ}K$ (just below the melting point) for the 15.5 at% Tl alloy and $\sim 0^{\circ}K$ for the 31 at% Tl alloy (Pollock and King 1968). For alloys falling in this composition range, the following measurements of the temperature dependences of the elastic constants are now available: (i) fct alloys - 18 ($T_c \sim 383^{\circ}K$) and 21 ($T_c \sim 333^{\circ}K$) at% Tl in the temperature range 290 to $390^{\circ}K$ (Pace and Saunders 1972) (ii) fcc alloys - 25 ($T_c = 195^{\circ}K$) and 27 ($T_c = 125^{\circ}K$) at% Tl between 290 and $100^{\circ}K$

(Gunton and Saunders 1974) and (iii) fcc alloys - 28.13 ($T_c \sim 60^oK$) and 30.16 ($T_c \sim 0^oK$) at% Tl between 350 and 200^{o}K (Novotny and Smith 1965). To extend the elastic constant data around T_c in the low temperature limit, temperature variations of the elastic constants of fcc alloys (30 and 31 at% Tl) with T_c in the neighbourhood of 0^{o}K have been measured between 295 and 4.2^{o}K.

7.4.1 Results and discussion

The three independent elastic constants C_{11}, C_{12} and C_{44} of 30 and 31 at% Tl fcc alloys have been obtained from ultrasonic wave velocity measurements made on [100] and [110] oriented samples. C_{11} and C_{44} were determined directly from [100], $\underline{q}$ // [100] and [110], $\underline{q}$ // [001] modes respectively (see also Table 7.1) whereas C_{12} was extracted from the longitudinal modulus $\frac{1}{2}(C_{11} + C_{12} + 2C_{44})$ associated with the [110], $\underline{q}$ // [110] mode. C_{12} could also be determined from the shear modulus $\frac{1}{2}(C_{11} - C_{12})$; but such an evaluation could only be made at room temperature because of the low velocity and high attenuation of the [110], $\underline{q}$ // [1$\bar{1}$0] mode. The room temperature elastic constants are in good agreement with the values previously reported for alloys of comparable compositions (Table 7.5). Figure 7.11 (30 at% Tl) and 7.12 (31 at% Tl) give the temperature variations of C_{11}, C_{12} and C_{44}. In the computation of the temperature dependences of the elastic constants, thermal expansion corrections for sample length and density changes have been made making use of the results of Pahlman and Smith (1968) and Gunton (1973). All the three elastic constants stiffen with decrease in temperature. The difference between C_{11} and C_{12} - already small at room temperature - narrows down further with the lowering of temperature and at 4.2^{o}K (the lowest temperature attained,

Table 7.5

Room temperature elastic stiffness constants of fcc In-Tl alloys

Elastic stiffness constants (units: 10^{11} dyne cm^{-2})	25 at% Tl*	27 at% Tl*	28.13 at% Tl**	30 at% Tl	30.16 at% Tl**	31 at% Tl
C_{11}	4.046	3.94	4.012	3.976	4.085	4.150
C_{12}	4.00	3.875	3.954	3.896	4.009	4.054
C_{44}	0.796	0.838	0.837	0.835	0.858	0.873
$C' = \frac{1}{2}(C_{11}-C_{12})$	0.023	0.027	0.028	0.04	0.038	0.048

* Gunton and Saunders (1974)

** Novotny and Smith (1965)

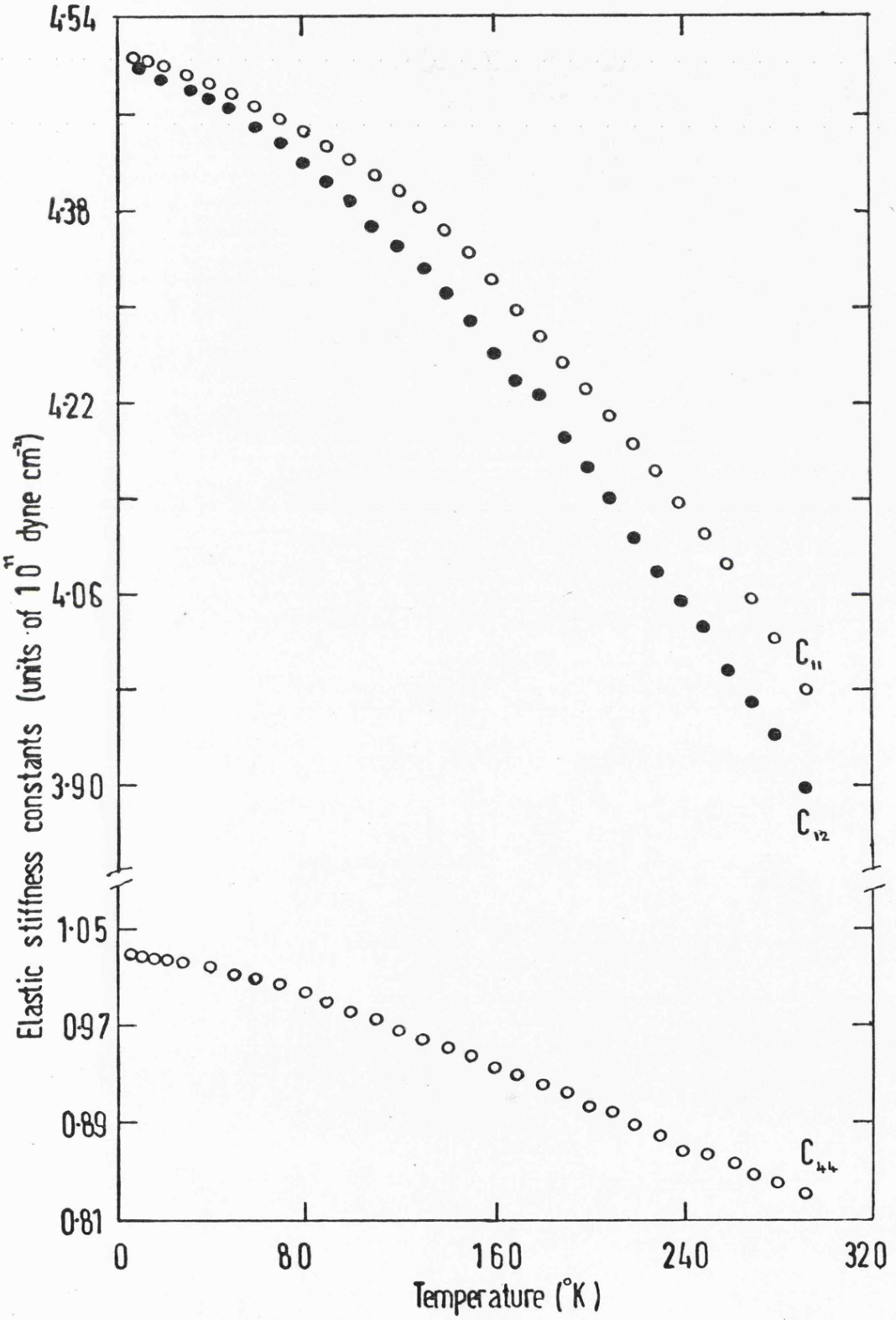

Figure 7.11: Temperature dependences of the elastic stiffness constants of In - 30 at% Tl alloy.

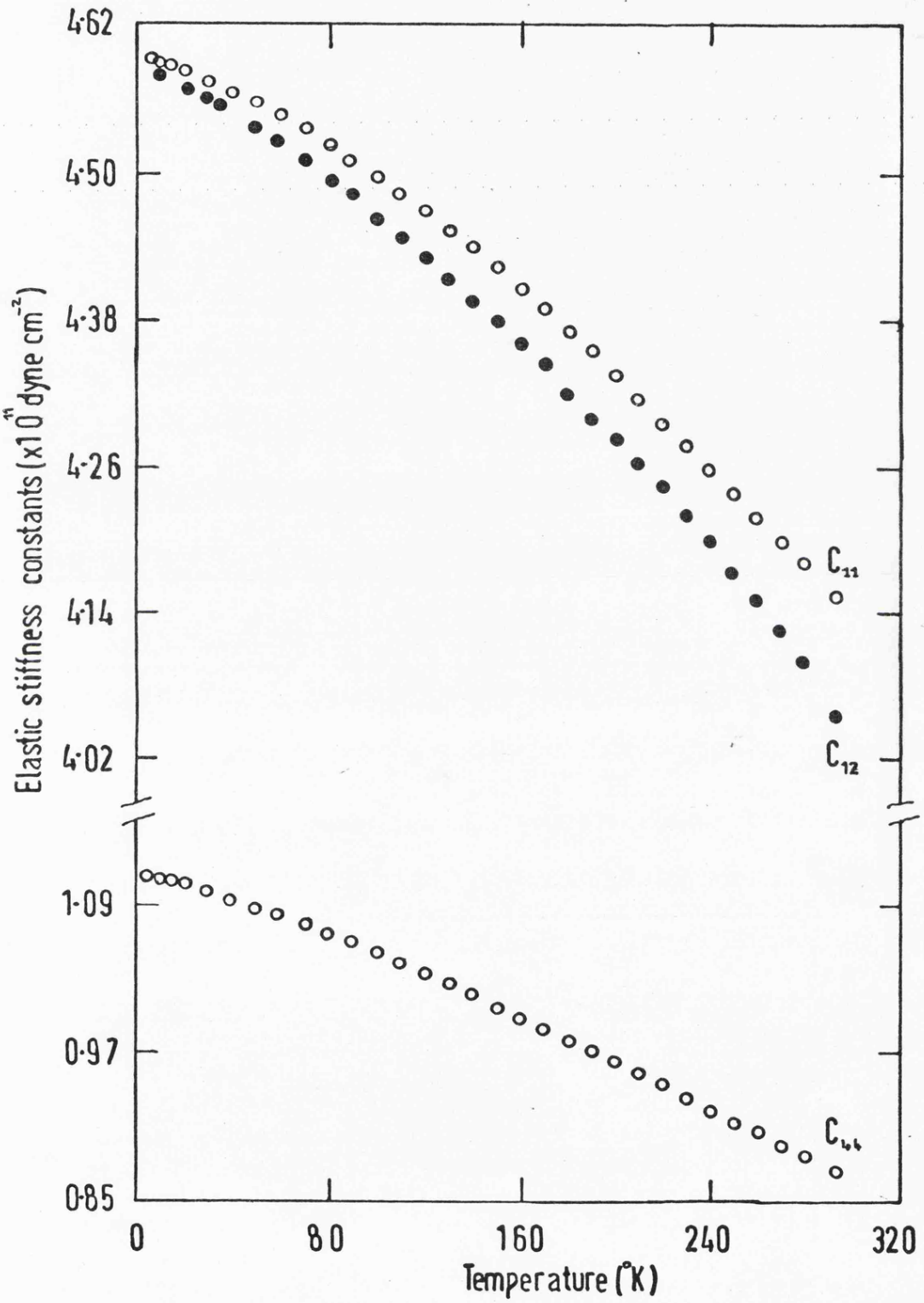

Figure 7.12: Temperature dependences of the elastic stiffness constants of In - 31 at% Tl alloy.

$T_c \sim 0^{\circ}K$) $(C_{11} - C_{12})$ is almost zero for both the alloys and strongly suggest an impending phase transformation. However, even around $4.2^{\circ}K$ the variations of all the elastic constants are smooth. Previously, Pace and Saunders (1972) and Gunton and Saunders (1974) both detected a dip in the variation of C_{44} in the vicinity of T_c. The dip found was larger for alloys with higher T_c values than for those with lower T_c values. The dip in C_{44} found by Gunton and Saunders (1974) for the 27 at% Tl alloy (T_c = $125^{\circ}K$) was barely recognisable. The magnitude of the peak in thermal expansion (Pahlman and Smith 1968) also follow this pattern. These results indicate an increased anharmonic effect for alloys with lower Tl and higher transformation temperatures.

CHAPTER 8

ELASTIC CONSTANTS OF In-Pb ALLOYS

8.1 Introduction

Alloys in the In-Pb system extend over three different phases (Chapter 2): (i) 0-12.7 at% Pb - fct with c/a ratio increasing from 1.08 to 1.09 (ii) 13.7-31 at% Pb - fct with c/a ratio decreasing from 0.934 to 0.928 (iii) above 31 and right up to 100 at% Pb - fcc. To study the elastic behaviour and stability of these phases, elastic stiffness tensor components of three alloy compositions - 5, 17 and 75 at% Pb - have been measured as a function of temperature in the range 80 - 300°K. Of particular interest is the effect of tetravalent Pb addition on the shear modulus $\frac{1}{2}(C_{11} - C_{12})$ of In (valency 3) and the behaviour of this modulus in comparison to that found in In alloys with divalent Cd and trivalent Tl.

8.2 Elastic behaviour of In-Pb alloys

8.2.1 In - 5 at% Pb (fct, c/a > 1)

The six components of the elastic stiffness tensor of this primary solid solution of In (fct, c/a > 1) have been obtained from ultrasonic wave velocity measurements made on samples oriented in the [100], [001], [110] and [011] directions (see also Section 6.4.1). The temperature variations of the elastic constants are plotted in Figure 8.1. The effect of temperature on acoustic path length and sample density have been corrected using the thermal expansion coefficients α_{ij} - obtained from previous X-ray studies (Tyzack and Raynor 1954a, Preece and King 1969) - in a manner similar to that described for In-Cd alloys (Section 6.3).

Referring to Figure 8.1, the elastic constants vary almost linearly with temperature - in the temperature range covered (80 - 300°K) the 5 at% Pb alloy suffers no phase transformation.

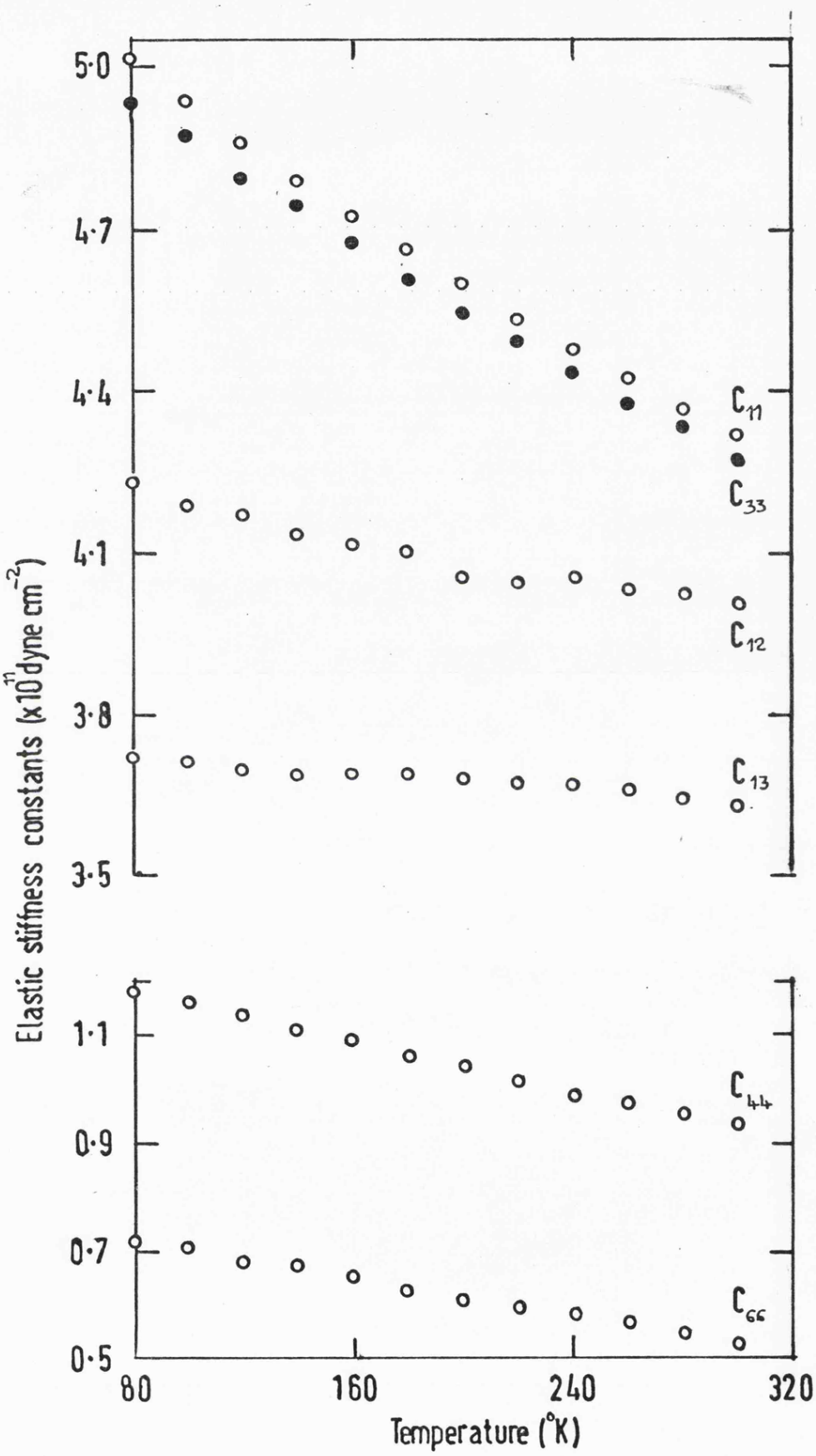

Figure 8.1; Temperature dependences of the elastic stiffness constants of In - 5 at% Pb (fct c/a > 1).

The scatter in C_{12} and C_{13} arises from the fact that these components are not obtained on their own, but are extracted from elastic constant combinations (Table 3.2) and are hence subject to a larger computational error. Turning to the magnitudes of the elastic constants, certain interesting features can be observed (Table 8.1). The changes in the elastic constants of In resulting from alloying with 5 at% Pb are fairly small in the case of the longitudinal moduli C_{11} and C_{33} but substantial for shear constants C_{44}, C_{66} and $C' = \frac{1}{2}(C_{11} - C_{12})$. At 300°K, C_{11} and C_{33} are reduced by 4.8 and 5.1% respectively, whereas C_{44} increases by 43% and C_{66} and C' decrease by 56.8 and 40% respectively. *The softening of C' is similar to that of the In - 3.4 at% Cd primary solid solution (Table 6.1)* but the changes in the other shear moduli are quite different - addition of 3.4 at% Cd to In leaves C_{44} and C_{66} almost unchanged. As already mentioned (Section 6.6.2), the surface showing the Young's modulus variation with orientation is a useful aid for visualising the elastic anisotropy of a crystal. Figure 8.2 shows the (110) plane cross-section of the Young's modulus surface and demonstrates the marked elastic anisotropy of In - 5 at% Pb alloy. From the measured stiffnesses,compliance constants, bulk modulus and volume and linear compressibilities have been calculated and these are included in Table 8.1. Compressibility results indicate that at 300°K under hydrostatic pressure the 5 at% Pb alloy contracts 1.6 times more in the z-direction than in directions in the x-y plane whereas for pure In the contraction is 1.5 times more in directions in the x-y plane than in the z-direction.

8.2.2 In - 17 at% Pb (fct, c/a < 1)

The procedure adopted for obtaining the elastic stiffness

Table 8.1

Elastic Constants and related parameters of fct In-Pb alloys. Data for In are from Chandrasekhar and Rayne (1961)

Composition (at% Pb)	0	5		17	
Temperature (^{o}K)	300	300	80	300	80
Elastic Stiffness Constants (x 10^{11} dyne cm^{-2})					
C_{11}	4.54	4.31_6	5.01_7	4.54_0	5.17_1
C_{12}	4.01	4.00_4	4.23_3	3.00_2	2.85_1
C_{13}	4.15	3.62_4	3.71_3	3.33_1	3.26_2
C_{33}	4.51	4.27_6	4.93_3	4.98_1	5.50_0
C_{44}	0.651	0.931	1.179	0.654	0.801
C_{66}	1.21	0.522	0.714	0.816	0.977
$C' = \frac{1}{2}(C_{11} - C_{12})$	0.26	0.15_6	0.39_2	0.76_9	1.16_0
Debye Temp. (^{o}K)					
$\bar{\theta}_D$	87.1	89.6	113.2	105.3	120.2
θ_1	261.4	248.4	265	237.6	248.5
θ_2	98.1	96.4	112.3	95.1	110.3
θ_3	66.3	69.4	91.4	91	102.9

Continued

Table 8.1
Continued

Elastic Compliance Constants ($\times 10^{-11}$) cm^2 $dyne^{-1}$)					
S_{11}	1.50	1.83	0.77	0.49	0.34
S_{12}	-0.39	-1.37	-0.50	-0.16	-0.09
S_{13}	-1.01	-0.39	-0.21	-0.22	-0.14
S_{33}	2.08	0.89	0.51	0.49	0.35
S_{44}	1.54	1.07	0.85	1.53	1.25
S_{66}	0.83	1.92	1.40	1.23	1.06
Bulk Mod. ($\times 10^{12}$ dyne cm^{-2})	0.385	0.392	0.423	0.368	0.382
Compressibilities ($\times 10^{-12}$ cm^2 $dyne^{-1}$)					
β_v (volume)	2.36	2.55	2.36	2.72	2.62
β_z (linear)	0.583	1.15	1.01	0.57	0.66
β_x (linear)	0.888	0.70	0.68	1.07	0.98

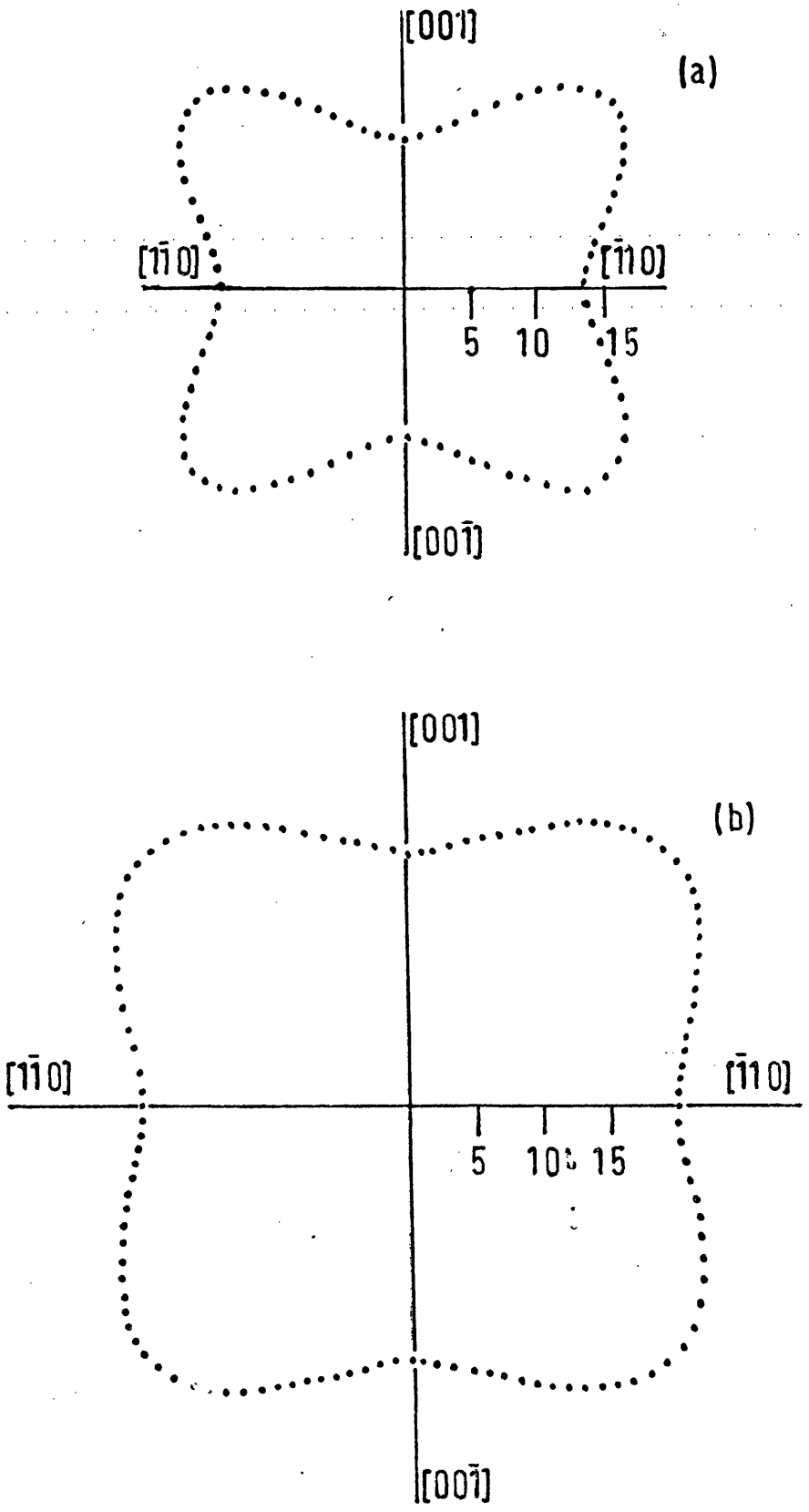

Figure 8.2: The (110) plane cross-section of the Young's modulus surface of In - 5 at% Pb at (a) 300°K and (b) 80°K. Units: 10^{10} dyne/cm^2.

tensor components and their variations with temperature of this fct ($c/a < 1$) alloy is the same as that used for the 5 at% Pb fct ($c/a > 1$) alloy described in the previous Section. Figure 8.3 gives the temperature dependences of the elastic constants. The temperature variations are again smooth and qualitatively similar to that of the 5 at% Pb alloy and the comments made in Section 8.2.1 also hold good. Concerning the alloying effects on the magnitudes of the elastic constants it can be noted from Table 8.1 that the shear modulus C_{44} at $300^{o}K$ is almost identical to that of pure In whereas the shear constants C_{66} and $C' = \frac{1}{2}(C_{11} - C_{12})$ change appreciably - C_{66} softens by a factor of 1.5 and C' is nearly three times stiffer. This leaves C' with a magnitude comparable to those of C_{44} and C_{66} and accounts for the almost isotropic elastic behaviour (Figure 8.4). At this juncture it must be mentioned that it has not been possible to obtain C' directly from the $[110]$, $\underline{q}$ // $[1\bar{1}0]$ mode and hence its value is subject to a larger error than those of C_{44} and C_{66}. Of the longitudinal moduli, C_{11} remains unchanged and C_{33} stiffens by about 10%. Coming to the compressibilities (Table 8.1), the 17 at% Pb alloy shows a response under hydrostatic pressure similar to that of In.

To summarise, the elastic behaviour of the fct ($c/a < 1$) phase is altogether different in kind from that of the fct ($c/a > 1$) phase. In particular, C' does not soften in the way it does in the fct ($c/a > 1$) phase.

8.2.3 In - 75 at% Pb (fcc)

The elastic constants $C_{\ell} = \frac{1}{2}(C_{11} + C_{12} + 2C_{44})$, C_{44} and $C' =$

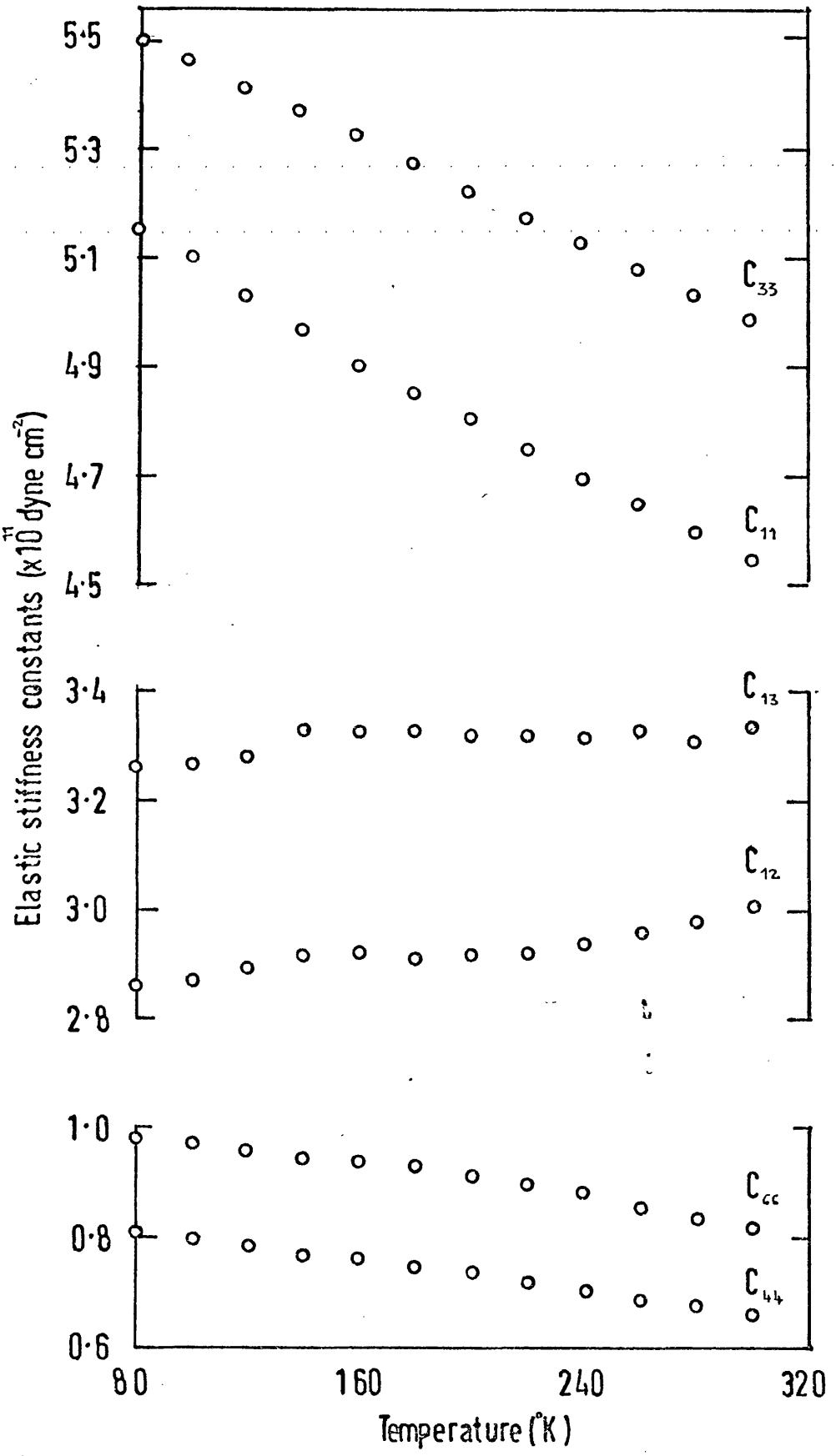

Figure 8.3 : Temperature dependences of the elastic stiffness constants of In ~ 17 at% Pb (fct c/a < 1).

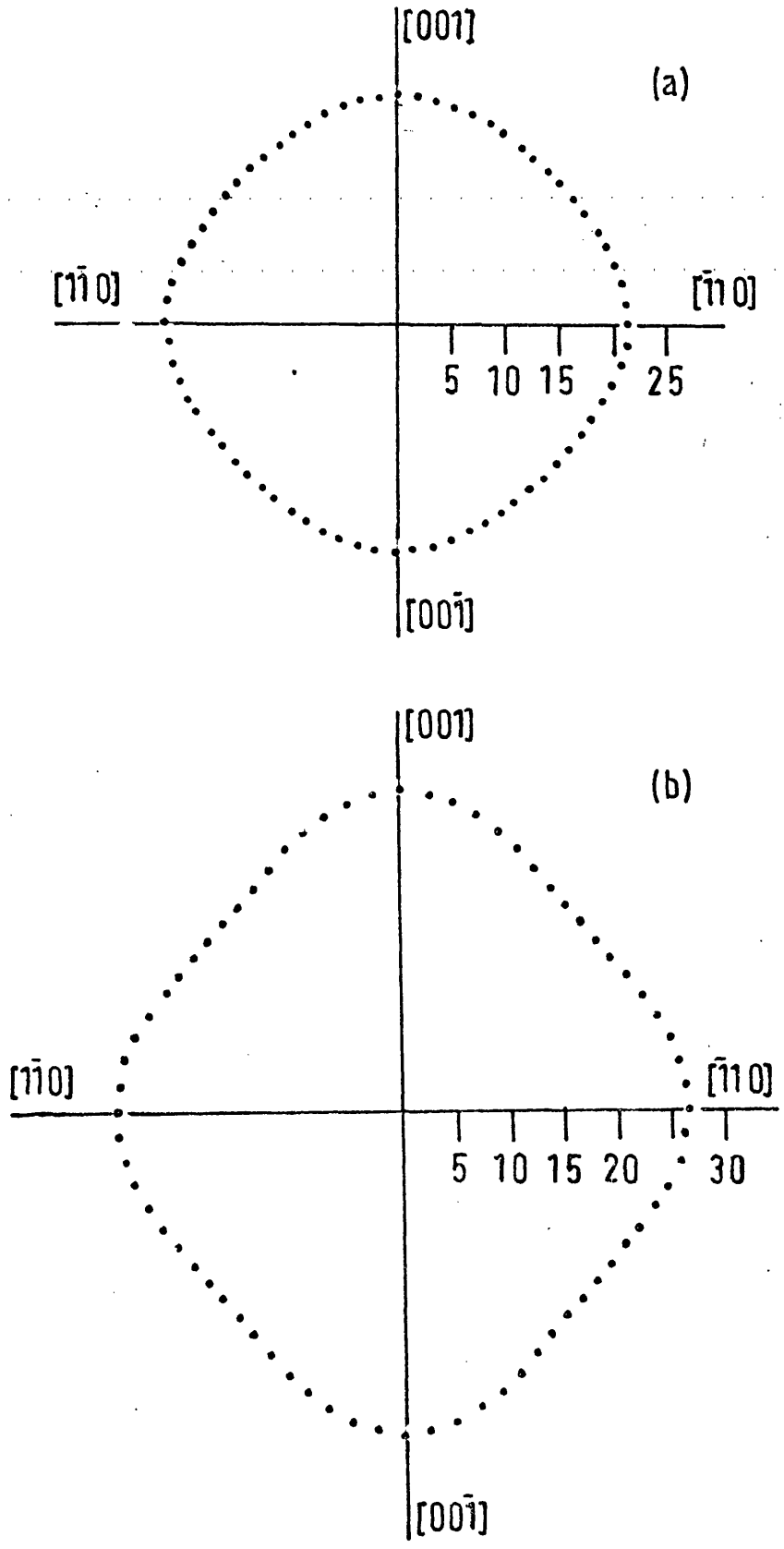

Figure 8.4: The (110) plane cross-section of the Young's modulus surface of In - 17 at% Pb at (a) 300°K and (b) 80°K. Units: 10^{10} dyne/cm^2.

$\frac{1}{2}(C_{11} - C_{12})$ of this fcc alloy have been obtained from ultrasonic wave velocity measurements made on a [110] oriented sample (see Table 3.3). The temperature dependences of C_{ℓ}, C_{44} and C' are plotted in Figure 8.5. In the absence of thermal expansion data for Pb-rich In-Pb alloys, α_{ij} values of pure Pb (Nix and McNair 1942) have been used for correcting ultrasonic wave path length and sample density changes with temperature. The three independent elastic constants C_{11}, C_{12} and C_{44} obtained from the experimental results plotted in Figure 8.5 are given at selected temperatures in Table 8.2 along with related parameters. For comparison this table includes the previously reported results for Pb (Waldorf and Alers 1962) and Pb-rich In-Pb alloys (van der Planken, Greiner and Smith 1971) - the present results somewhat extend the range of the fcc phase studied by van der Planken et al. From Figure 8.5 and Table 8.2 it can be seen that the elastic behaviour of the 75 at% Pb alloy is strongly influenced by the shear moduli C_{44} and C'. At 300°K, for this alloy C' has a value 4.5 times that of pure Pb whereas C_{44} remains essentially the same - it is stiffer by a factor of only 1.2. Also, this pattern is maintained throughout the temperature range 80-300°K. This means that while Pb remains highly anisotropic in its elastic behaviour - the anisotropy ratio $A(= C_{44}/C')$ varies from 3.9 to 4.1 over the temperature range 80 - 300°K - the 75 at% Pb alloy displays a remarkable isotropic behaviour as the A value stays close to unity (0.96 - 1.1) throughout. This feature is at once seen in the near sphericity of the Young's modulus surfaces - the (110) plane cross-section shown in Figure 8.6 is almost circular and should be compared with that of the highly anisotropic fcc In - 6.5 at% Cd alloy (plotted in Figure 6.13) which unlike the 75 at% Pb alloy displays pronounced softening of C'.

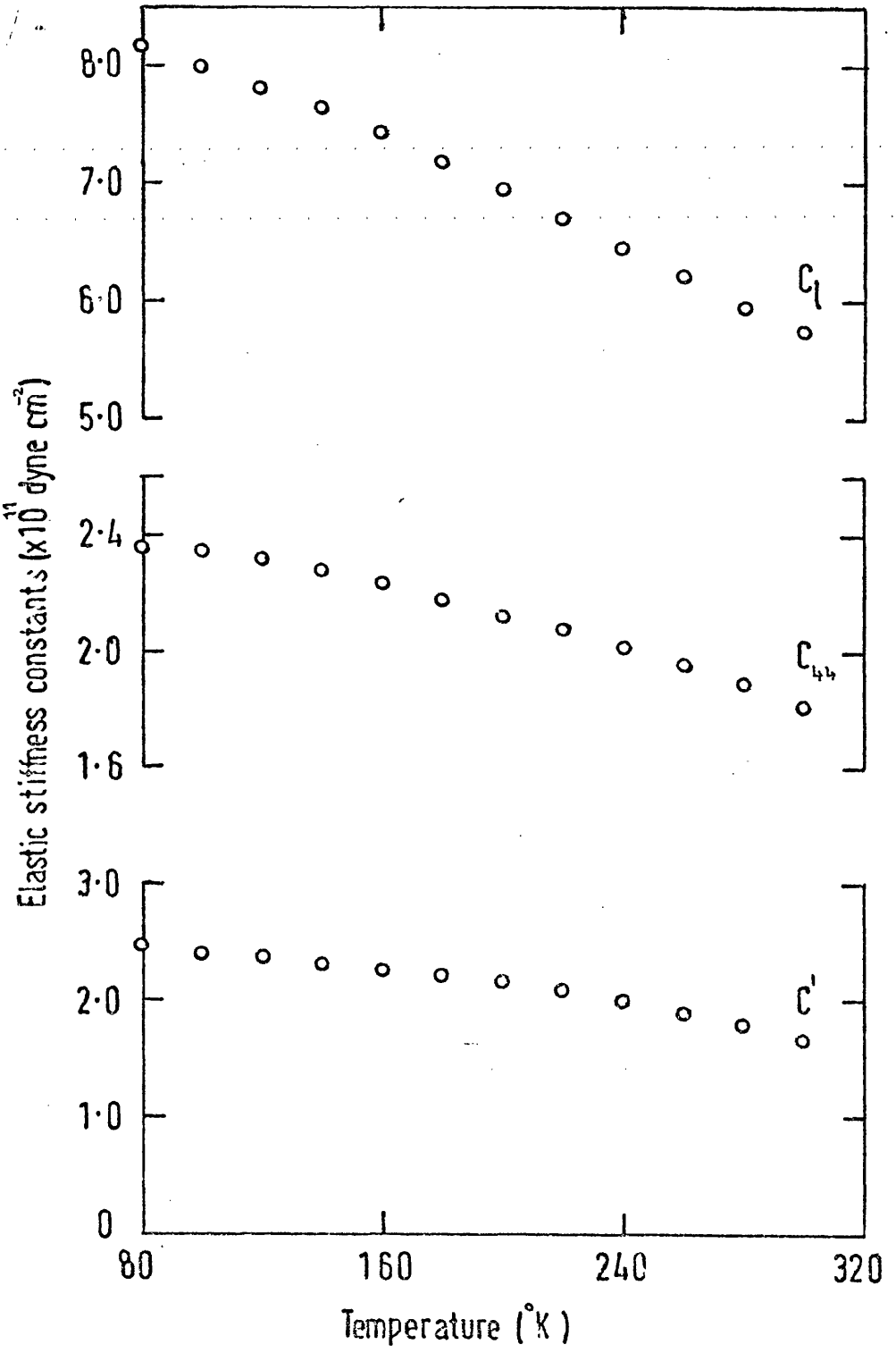

Figure 8.5 : Temperature dependences of the elastic stiffness constants of In - 75 at% Pb (fcc).

Table 8.2

Elastic constants and related parameters of fcc In-Pb alloys

Composition (at% In)	0*		5.5**		9**		20.7**		25	
Temperature (^{o}K)	300	78	300	78	300	78	300	78	300	80
Elastic stiffness constants (x 10^{11} dyne/cm^2):										
C_{11}	4.953	5.435	4.932	5.325	5.970	6.600	4.870	7.635	5.60	8.25
C_{12}	4.229	4.495	4.251	4.445	3.370	3.340	1.890	3.975	2.28	3.35
C_{44}	1.490	1.833	1.443	1.765	1.390	1.710	1.660	2.055	1.82	2.36
$C' = \frac{1}{2}(C_{11}-C_{12})$	0.362	0.47	0.340	0.44	1.3	1.63	1.49	1.83	1.66	2.45
Anisotropy ratio $A = C_{44}/C'$	4.12	3.9	4.24	4.01	1.07	1.05	1.11	1.12	1.1	0.96
$\bar{\theta}_D$	90.9	101.7	90	100.3	118.6	131.6	130.4	146.1	138.6	162.2
θ_1 Debye temperatures (^{o}K)	215.3	227.3	217	227.4	222.7	233.9	208.1	260	224.8	268.6
θ_2	100.3	111.4	99.7	110.5	106.3	118	118.8	132.1	125.8	146
θ_3	70.1	78.7	69.2	77.6	104.5	116.7	115.7	128.4	123	144.7

Continued

Table 8.2 Continued

Elastic compliance constants (x 10^{-11} cm^2/dyne):										
S_{11}	0.94	0.73	1.00	0.78	0.28	0.23	0.26	0.20	0.23	0.16
S_{12}	-0.43	-0.33	-0.46	-0.35	-0.10	-0.08	-0.07	-0.07	-0.07	-0.05
S_{44}	0.67	0.54	0.69	0.57	0.72	0.58	0.60	0.49	0.55	0.42
Bulk modulus (x 10^{12} dyne/cm^2)	0.447	0.481	0.448	0.474	0.424	0.443	0.288	0.52	0.339	0.498
Compressibilities (x 10^{-12} cm^2/dyne):										
β_v (volume)	2.24	2.08	2.23	2.11	2.36	2.26	3.47	1.92	2.95	2.01
$\beta_x=\beta_z$ (linear)	0.75	0.69	0.74	0.70	0.79	0.75	1.16	0.64	0.98	0.67

* Waldorf and Alers (1962)

** van der Planken et al (1971)

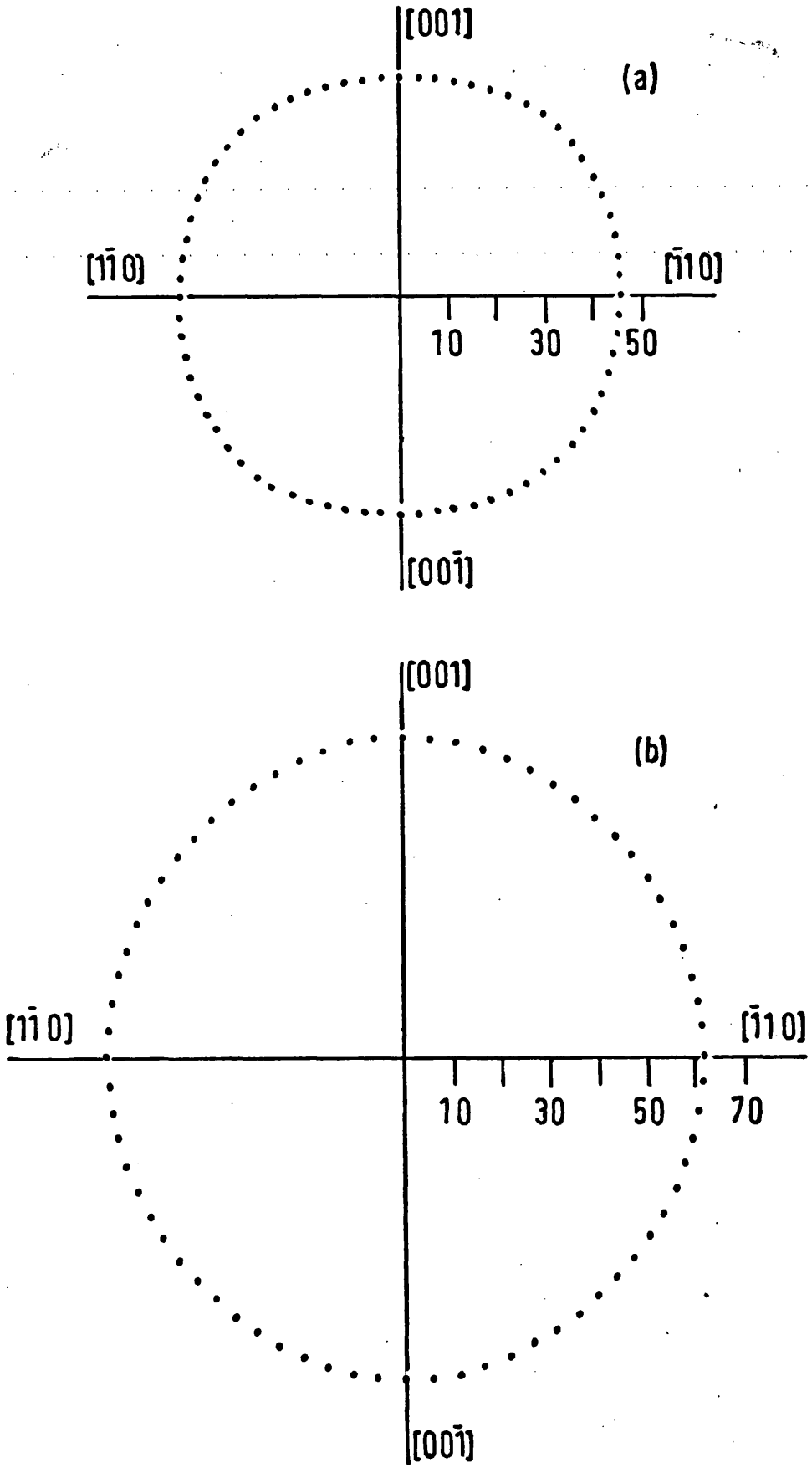

Figure 8.6: The (110) plane cross-section of the Young's modulus surface of In - 75 at% Pb at (a) 300°K and (b) 80°K. Units: 10^{10} dyne/cm^2.

8.3 Debye temperatures

$\theta_D(T)$ and the mode temperatures θ_i have been evaluated from the measured ultrasonic wave velocities using equations (6.15) and (6.16) respectively. The values thus obtained are given in Table 8.1 for the 5 and 17 at% Pb tetragonal alloys along with those of pure In and in Table 8.2 for the 75 at% Pb fcc alloy. Table 8.2 includes the Debye temperatures of pure Pb and 79.3, 91 and 94.5 at% Pb alloys calculated from the elastic constant results of Waldorf and Alers (1962) and van der Planken, Greiner and Smith (1971) respectively. There is no specific heat data for the tetragonal In-Pb alloys available at the present for comparison but such data exists for fcc Pb-rich alloys and some comments can be made. Culbert, Farrell and Chandrasekhar (1971) obtained the low temperature limit of the Debye temperature θ_o and the electronic specific heat coefficient γ of a series of In-Pb alloys containing from 0 to 60 at% In from low temperature heat capacity measurements. Their results show an increase in γ and a decrease in θ_o with increasing In concentration. More recent studies (Padamsee, Neighbor and Shiffman 1976) show a decrease in γ with increasing In concentration but the compositional dependence of θ_o is basically the same as that given by Culbert et al (1971). In contrast, the present results for $\theta_D(T)$ of the 75 at% Pb alloy and those studied by van der Planken et al (1971) indicate an increase in Debye temperature with increasing In concentration (Table 8.2) - this compositional dependence of $\theta_D(T)$ is maintained throughout the temperature range 80-300^{o}K. Although this is an interesting contradiction with the specific heat results, any further comparison at this stage cannot be justified in view of the lack of elastic constant data at temperatures close to $\theta_o/50$ - that is to say liquid helium temperatures.

8.4 Behaviour of shear elastic constants in relation to phase transformations in In alloys

The phase transformations in In-rich alloys with Cd, Tl and Pb may all be seen as changes in weak distortions of symmetrical crystalline structures resulting from homogeneous shear strains - volume changes on alloying are fairly small. The variations of shear elastic constants are therefore intimately related to alloy phase stabilities. In the case of In-Cd (Chapter 6) and In-Tl (Section 7.4, Pace and Saunders 1972, Gunton and Saunders 1974), alloying reduces the crystal stability of In to <110>, $\{1\bar{1}0\}$ shear stresses and leads to the fct-fcc structural transformation: the shear modulus $\frac{1}{2}(C_{11} - C_{12})$ tends to very small values as the transformation is approached from either the tetragonal or the cubic phase. Alloying changes on other elastic constants are small and do not reveal any physically significant effects. The elastic constant results of In-Pb alloys presented in Section 8.2 also show a strong dependence of $\frac{1}{2}(C_{11} - C_{12})$ on the solute concentration - there are also appreciable changes in other shear moduli in In-rich In-Pb alloys and their significance will be considered later. Unlike Tl, Cd (valency 2) and Pb (valency 4) both have a different valency from that of In (valency 3) and therefore their addition also results in a change in the electron/atom ratio z - the lesser valent Cd ($\Delta z = -1$) reduces the electron concentration and the higher valent Pb ($\Delta z = +1$) increases it. Previously, Tyzack and Raynor (1954a) found a correlation between the lattice spacing trends and the electron/atom ratio: for $z < 2.94$ the axial ratio c/a is equal to unity whereas for $z > 3.14$ c/a is less than one and for the tetragonal phase occurring for z between 2.94 and 3.14, the c/a ratio is greater

than one. Since changes in $\frac{1}{2}(C_{11} - C_{12})$ indicate impending phase transformations (and hence axial ratio changes) it is of interest to look at the variations of this modulus with the electron concentration z.

8.4.1 Variation of $\frac{1}{2}(C_{11} - C_{12})$ with the electron concentration z

A phenomenological description based on Landau's general theory of phase transformations (Landau and Lifshitz 1959) can be used to establish the values of the shear modulus $C' = \frac{1}{2}(C_{11} - C_{12})$ as a function of solute (e.g., Cd, Pb) and hence electron concentrations z. The details are as follows:

$$G = G_o + \tfrac{1}{2}C_{ij}u^2 + \frac{1}{3}pu^3 + \frac{1}{4}qu^4 \qquad (8.1)$$

where G_o is the free energy G at u = 0, u being the strain designated order parameter

$$u = 2(c/a - 1)/\sqrt{3} \qquad (8.2)$$

and p and q are constants. The concentration dependent elastic constant is mainly $C' = \frac{1}{2}(C_{11} - C_{12})$ and C_{ij} can be replaced by C' in equation (8.1). For the appearance of phase change, C' should then vary as a function of z. That is

$$C' = \beta(z - z_o) \qquad (8.3)$$

where $\beta = dC'/dz$ and z_o is a constant. The concentration z_c at which a phase transformation occurs can be found by equating free energies of the transforming and transformed phases and leads to

$$z_c = z_o + 2p^2/9q\beta \qquad (8.4)$$

The equilibrium condition is given by

$$dG/du = u(C' + pu + qu^2) = 0 \qquad (8.5)$$

and the spontaneous value of u in the different phases is given by

$$u = \left(-p \pm \sqrt{p^2-4C'q} \right)/2q \qquad (8.6)$$

Also

$$C' = (\partial^2 G/\partial u^2)_u \qquad (8.7)$$

From this approach and choosing appropriate values for p, q and β- making use of the available data for c/a changes with z and the elastic constants of In and Pb- Murakami and Kachi (1975) have calculated the values of C' as a function of z between 2.8 and 4. The elastic constant results of In-Cd and In-Pb alloys presented in this thesis provide a direct test of their phenomenological predictions. Figure 8.7 incorporates the comparison between the measured and predicted values of C'. The qualitative agreement between the experimental and predicted values of C' is satisfactory for In-Cd alloys (Figure 8.7); this is also borne in the extent of softening at the fcc-fct structural transformation. The calculated values for In-Pb alloys (z = 3 to 4) also show softening of C' at all the phase boundaries - this softening at both the fct (c/a > 1) - fct (c/a < 1) and fct (c/a < 1) - fcc transformations although similar to that of In-Cd alloys is less pronounced and the extent of softening is somewhat more at the fct (c/a < 1) - fcc transformation than at the other. Although the experimental value of C' for the 5 at% Pb alloy fits fairly well, the disagreement for the 17 at% Pb alloy with the calculated value is large - instead of softening, C' for this alloy is nearly three times stiffer than that of In.

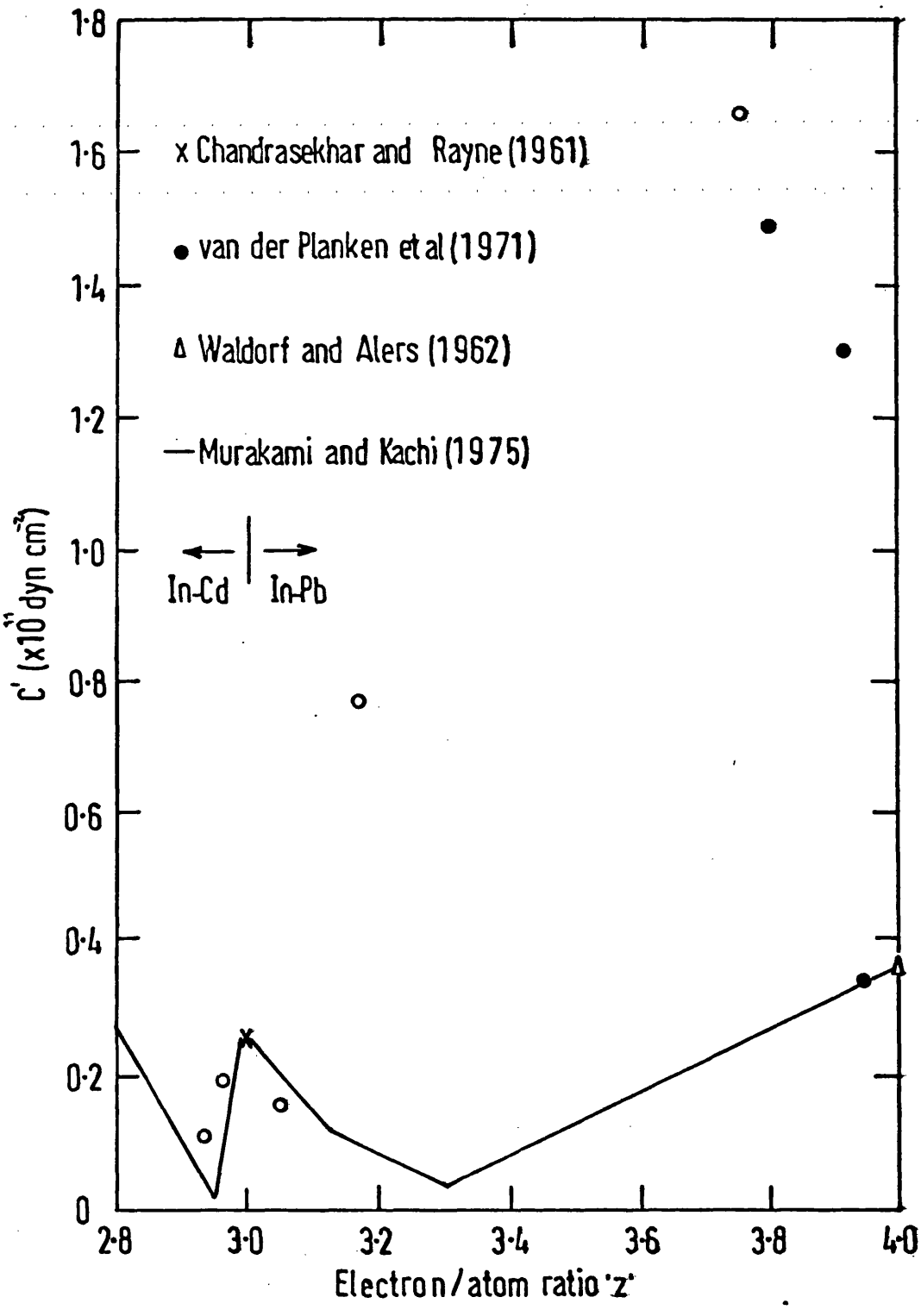

Figure 8.7: Shear elastic constant C' (300°K) of In-Cd and In-Pb alloys as a function of electron/atom ratio 'z'.

There are also large discrepancies between the predicted and experimental values for fcc Pb-rich alloys including those measured by van der Planken, Greiner and Smith (1971).

It appears unlikely that the softening of C' (if any) at the phase transformations in In-Pb alloys will be as pronounced as those depicted by the phenomenological calculations. As pointed out in Section 6.7, the presence of the cubic invariant in the Landau expansion should render the fcc-fct transformation in In alloys first order and as a result C' should have a finite value at the transformation. In the case of fct (c/a < 1) - fcc transformation in In-Pb alloys, the transformation is preceded by a fairly wide two phase region compared to that present in the In-Cd alloys and the transformation is therefore more strongly first order with a correspondingly larger magnitude for the cubic invariant. The softening of C' is therefore expected to be less pronounced. The fct (c/a > 1) - fct (c/a < 1) transformation also involves a wide two-phase region; in addition there is no change of symmetry and the implications of this will be considered in the next Section.

8.4.2 The fct (c/a > 1) - fct (c/a < 1) isomorphous transformation in In-Pb alloys

The transformation which occurs at the primary solid solubility limit of Pb in In ($\sim$ 13.7 at% Pb) involves no change of crystal symmetry - the primary solid solution fct structure remains the same but the c/a ratio changes from >1 to <1. This novel phase change in the In-Pb system comes under the category of isomorphous transformations of which the fcc (α) - fcc (α') transformation in Ce is the best known among the metallic systems (Ponyatovskii 1958, 1963).

In analogy with the liquid-gas transformation, isomorphous phase changes are also generally of the first order. But unlike the equilibrium curves of liquid-gas, the equilibrium curves of isomorphous crystalline phases are bound above by the fusion curve and if there occurs a convergence of the properties (e.g., unit cell volume or deformation) of isomorphous phases along the equilibrium curve, this curve can end both in a critical point and in a triple point, involving the intersection of the fusion curve with the equilibrium curve of the high temperature phase (Ponyatovskii 1963). Khmel'nitskii (1975) has examined the nonanalytic dependence of the acoustic velocity on the wave vector near critical points of isomorphous transformations and concludes that soft modes do not appear but the bulk modulus $\rightarrow 0$ as the critical point is approached. Although there is no indication of any acoustic phonon mode softening in the 17 at% Pb (fct, $c/a < 1$) alloy (Figure 8.3 and Table 8.1), the elastic constant results of this alloy do not provide a thorough and conclusive test of Khmel'nitskii's findings; as this composition - purposely chosen to improve chances of single crystal growth - remains well away from the fct ($c/a > 1$) - fct ($c/a < 1$) phase boundary (Figure 2.4) throughout the temperature range (80-300^{o}K) studied.

8.4.3. A comment on the elastic constant data of In-Pb alloys

The tetragonality of In itself and several properties of In-rich alloys with metals of differing valencies have in the past been discussed in terms of an interaction between the Fermi surface and faces or corners of the Brillouin zone boundary from a standpoint originated by Jones (1934) and Goodenough (1953). These include the thermoelectric power of In-Pb alloys (Tomasch and Reitz 1958),

lattice spacings and transport properties of In-Cd, In-Hg, In-Pb and In-Sn alloys (Yonemitsu 1966), axial ratios and superconducting transition temperatures of In-Pb alloys (Preece and King 1969) and heat capacities of In-Sn alloys (Lambert, Brock and Phillips 1971). An important contribution to the shear resistance of polyvalent metals come from the Fermi energy and since this is altered by heterovalent alloying additions (Leigh 1951a,b), the band structure considerations cited above should also in principle explain the shear elastic constants of In alloys. Although a Leigh type calculation of the shear elastic constants of pure In has been made (Winder and Smith 1958), lack of definite information regarding the alloying induced changes in the valence electron occupancy in In-rich alloys - at the present de Haas-van Alphen measurements give this information only for sufficiently dilute alloys and this is now available for In-Pb alloys of up to 1 at% Pb (Holtham and Parsons 1976) - make such an assessment largely a matter of conjecture. Nevertheless the substantial changes in C_{44} and C_{66} upon addition of 5 at% Pb, in C_{66} with the addition of 17 at% Pb and in C' in all the In-Cd and In-Pb alloys (Table 8.3) bring out the domineering effect of the valency of the solute on the alloy shear strengths. Band scheme alterations have also been held responsible for the anisotropy ($A = C_{44}/C'$) changes in fcc Pb-rich In-Pb alloys (van der Planken, Greiner and Smith 1971).

An optimised model potential calculation of the elastic constants of In-Pb alloys is at present being made by Professor G.A. Saunders (private communication). The present results provide the necessary experimental data with which to compare the findings of such a calculation. To conclude, the elastic constant results of

Table 8.3

Shear elastic constants of In alloys

Alloy Composition (at%)	Electron/ atom ratio z	Shear elastic constants at 300° K (units: 10^{11} dyne cm^{-2})		
		$C' = \frac{1}{2}(C_{11}-C_{12})$	C_{44}	C_{66}
100 In[+]	3	0.26	0.651	1.21
3.4 Cd	2.97	0.19_3	0.686	1.125
6.5 Cd	2.93	0.10_6	0.756	-
5 Pb	3.05	0.15_6	0.931	0.522
17 Pb	3.17	0.76_9	0.654	0.816
75 Pb	3.75	1.66	1.82	-
79.3 Pb[*]	3.79	1.49	1.660	-
91 Pb[*]	3.91	1.30	1.390	-
94.5 Pb[*]	3.94	0.34	1.443	-
100 Pb[**]	4	0.362	1.490	-

\+ Chandrasekhar and Rayne (1961)

* van der Planken, Greiner and Smith (1971)

** Waldorf and Alers (1962)

In-Pb alloys show that:

(i) in the fct ($c/a > 1$) phase, $C' = \frac{1}{2}(C_{11} - C_{12})$ softens in a manner similar to that found in In-rich In-Cd and In-Tl alloys

(ii) there is no softening of C' in the fct ($c/a < 1$) phase; the elastic behaviour of this phase is quite different from that of fct ($c/a > 1$)

(iii) the elastic behaviour of the Pb-rich fcc phase is isotropic and there is no softening of C'.

C H A P T E R 9

MELTING OF In-Cd AND In-Tl ALLOYS

9.1 Introduction

A number of mechanisms have been proposed for melting. Solid-liquid transformations have been discussed in terms of an absolute mechanical instability of the crystal lattice (Lindemann 1910), vanishing of the elastic constants (Born 1939, Ida 1969, 1971), generation of interstitials (Lennard-Jones and Devonshire 1939a,b), generation of vacancies (Gorécki 1974) and spontaneous generation of dislocations (Kuhlmann-Wilsdorf 1965). A major drawback with these mechanisms is their lack of wide scope and generality. This has already been demonstrated in the case of Born and Ida's melting hypotheses - the study of acoustic phonon mode softening in In-rich, In-Cd (Chapter 6) and In-Tl alloys (Chung, Gunton and Saunders 1976) through ultrasonic wave velocity measurements made near the melting point of these alloys produced results at variance with the suggested melting mechanisms. The present concern is to examine the implications, if any, of the acoustic phonon mode softening in In-rich, In-Cd and In-Tl alloys on an important thermodynamic parameter of the melting process; namely, the fusion entropy. Although this quantity can be readily obtained from calorimetric measurements of latent heat of fusion and melting point, very few fusion entropy data are available for alloy phases - none for In-based alloys.

9.2 Experimental details

The latent heat of fusion and the melting point of In-Cd alloys in the composition range 3.4 to 6.5 at% Cd and of In-Tl alloys between 10 and 31 at% Tl have been measured with a Perkin-Elmer Differential Scanning Calorimeter (Model DSC - 1B). A majority of

the alloy specimens used were prepared from single crystals used for ultrasonic studies (In-Cd alloys, Chapter 6 and In-Tl alloys, Pace and Saunders 1972, Gunton and Saunders 1974 and Chapter 7); others were from homogenised, polycrystalline samples cast in the form of buttons. No recognisable differences were found between measurements made on single crystal or polycrystalline specimens. For each alloy composition a number of specimens from different portions of the crystals were used. Crystal growth and characterisation procedures (Chapter 4) have already established the fact that the alloys studied here are homogeneous substitutional solid solutions.

In the scanning calorimeter, the latent heat of fusion and the melting point measurements are accomplished by electronically controlling the thermal equilibrium in the sample holder assembly consisting of two similar pans and covering lids (of Aluminium); one for the specimen under investigation and the other as reference. To start with, the instrument is calibrated with a substance of known melting point T_m. For this an In standard ($T_m = 429.5 \pm 1.5^{\circ}K$) available with the calorimeter was used. The specimen under investigation (a portion of the crystal weighing about 0.02 gm) is then firmly enclosed in the specimen pan and the lid hand-pressed on to it. The specimen and reference pans are then placed in the sample holder assembly which is held in an inert atmosphere of nitrogen. These procedures are adopted to minimise impurity inclusion and oxidation during the calorimeter run. Appropriate settings of the instrument control knobs lead to the desired rates of heating (0.5 to $64^{\circ}C$/min). The temperature of the sample holder assembly is recorded on the graph chart as the abscissa. This is

also registered on an instrument panel dial. When the specimen under investigation melts, more power will have to be supplied to the specimen pan than the reference pan to maintain thermal equilibrium in the sample holder assembly. This difference in power is recorded on the ordinate as the fusion peak and the area under this peak is a measure of the specimen latent heat of fusion (L_f). The temperature at which the abscissa base line starts deviating prior to the fusion peak gives the specimen melting point T_m.

9.3 Results

The fusion peak obtained for the In standard and typical fusion peaks of In-Cd and In-Tl alloys are shown in Figures 9.1 and 9.2 respectively. The fusion peak areas were measured with a planimeter and from these the latent heat of fusion L_f can be calculated as follows:

$$L_f(\text{Cal/gm}) = \frac{\text{Fusion peak area x Range setting x 60}}{\text{Area of rectangle x 1000x 2 x Specimen weight}} \quad (9.1)$$

where

Area of rectangle = ½(Chart width x one min. run of chart)

or

$$L_f = \frac{L_f' \times W' \times C' \times A}{A' \times C \times W \times R'} \quad (9.2)$$

where

L_f = Latent heat of fusin (Cal/gm)

W = Weight of the specimen or standard (gm)

C = Chart speed (mm/sec)

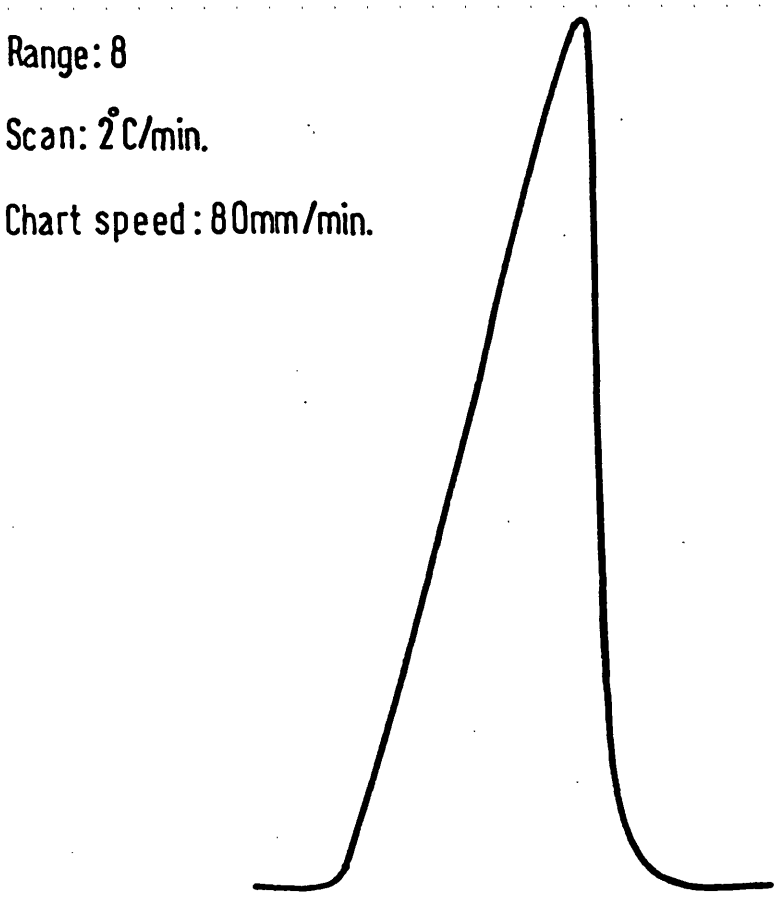

Figure 9.1: Fusion peak of Indium standard.

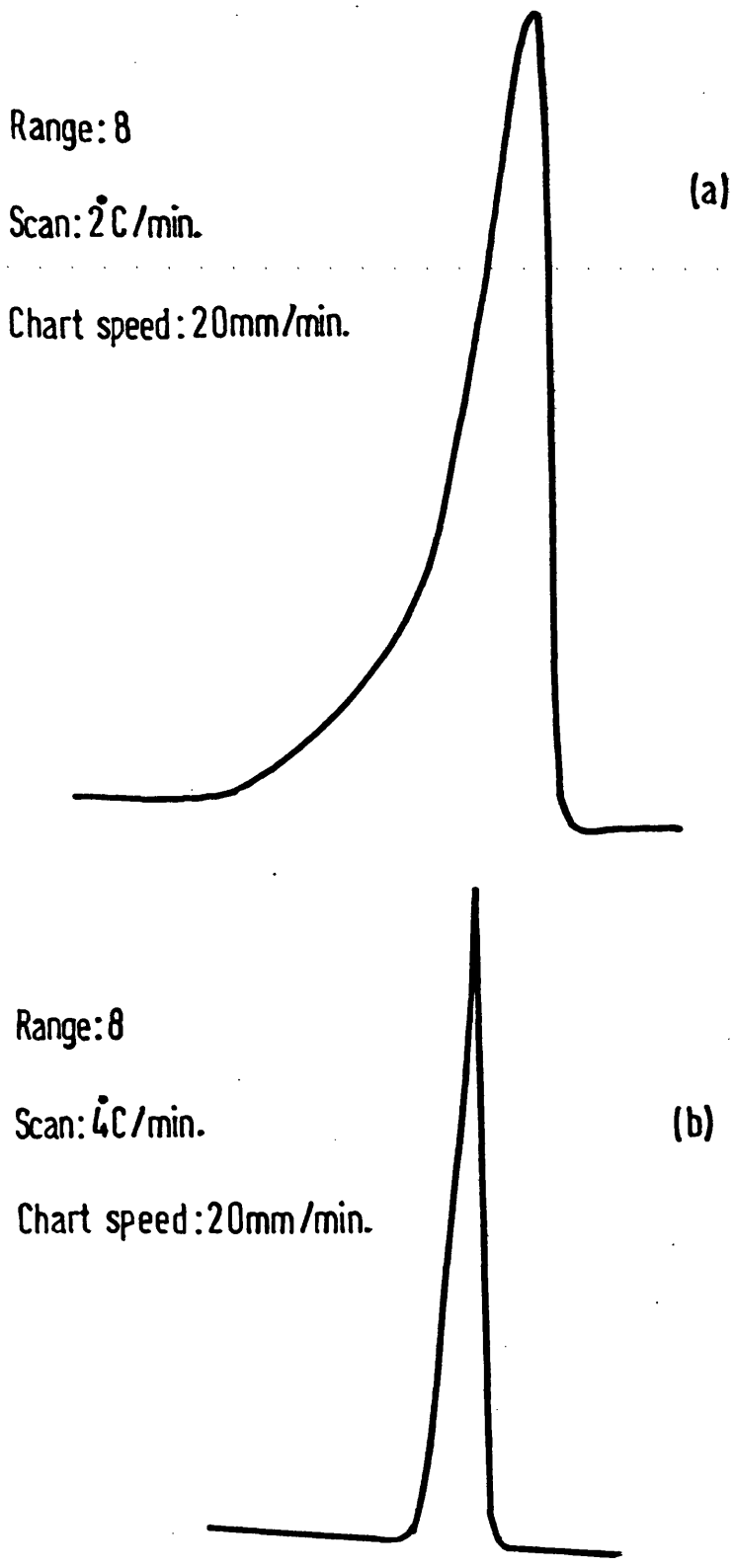

Figure 9.2: Fusion peaks of (a) In - 3.4 at% Cd and (b) In-18 at% Tl.

A = Area under the fusion peak (cm^2)

R = Calorimeter range setting

The unappended and the primed symbols refer respectively to the alloy specimens and the In standard. In the present study, L_f values have been calculated using equation (9.2) and with a value of 6.95 Cal/gm (= L'_f) for the In standard. All the results were reproducible to ±0.1 Cal/gm. The average for a number of runs made with different specimen weights and calorimeter settings (e.g., temperature scanning rate, range setting) was found for each alloy composition.

The L_f values for In-Cd alloys are plotted in Figure 9.3 (and also tabulated in Table 1); those for In-Tl alloys are plotted in Figure 9.4 (and given in Table 2).

9.4 Discussion

Important thermodynamic parameters that can be obtained from latent heat of fusion and melting point measurements are the fusion entropy $S_f = L_f/T_m$ and the volume change on melting $V_f = (V_\ell - V_s)/V_s$. The latter is related to the latent heat of fusion through the Clausius-Clapeyron equation $dT/dP = T(V_\ell - V_s)/L_f$. However, for melting at atmospheric pressure, volume changes are small for metallic systems and L_f gives directly the change in internal energy between the solid and liquid phases (Slater 1939). The entropy of fusion S_f is a measure of the state of order. For completely disordered alloys, Kubaschewski (1941, 1943) and Kubaschewski and Evans (1958) found that the S_f values vary according to $S_f(AB) = xS_f(A) + (1-x)\ S_f(B)$ where x is the atomic fraction of component A and (1-x) that of B. If the alloy is ordered, a disorder portion $\sigma = -R\{x \ln x + (1-x) \ln (1-x)\}$ will have to be

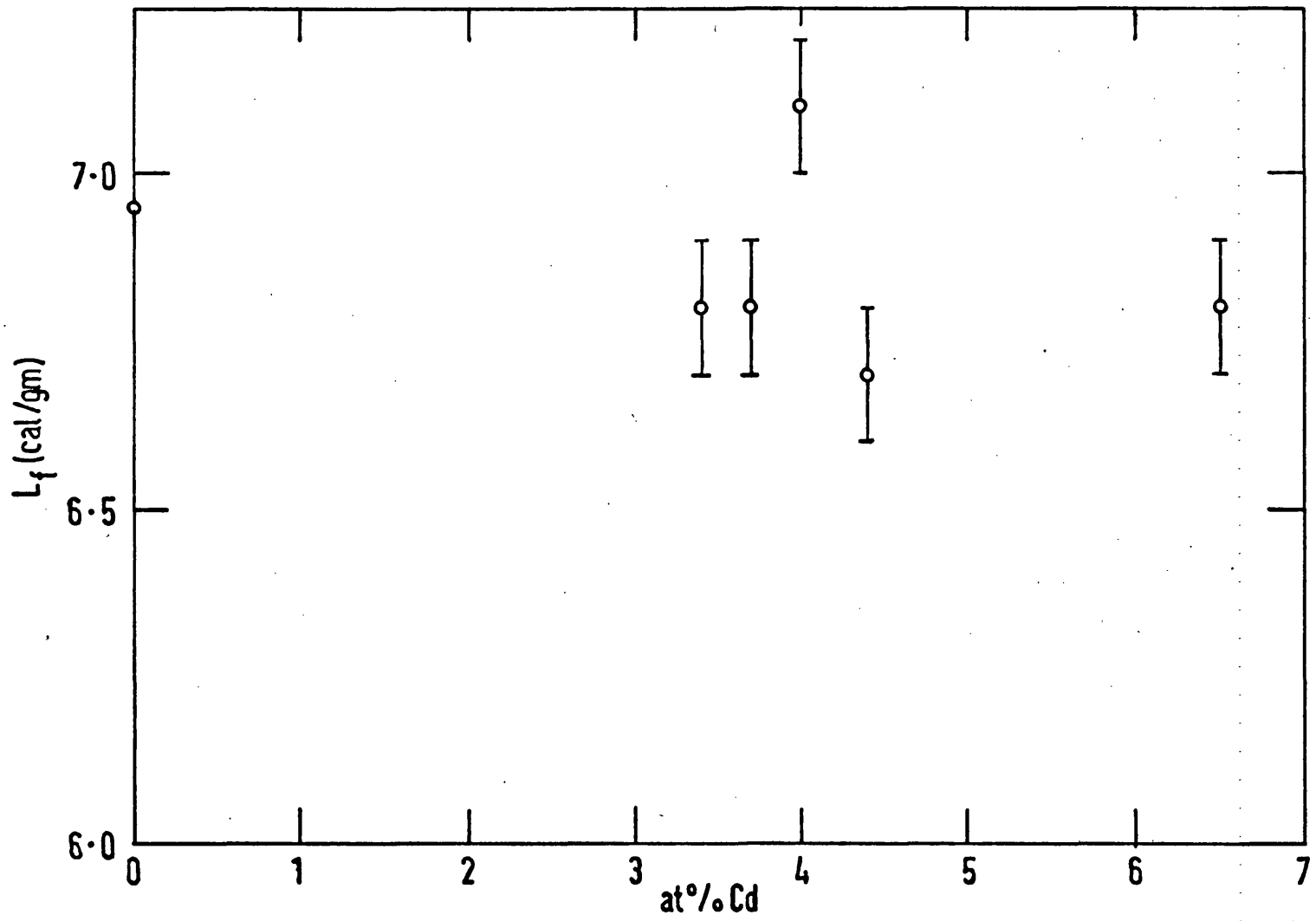

Figure 9.3: Latent heats of fusion (L_f) of In-Cd alloys as a function of Cd concentration.

Table 9.1

Latent heat and entropies of fusion of In-Cd alloys

Alloy composition (at% Cd)	Latent heat of fusion L_f (Cal/gm)	Entropy of fusion S_f ($\times 10^{-2}$ Cal/gm/^{o}K)
0	6.95	1.62
3.4	6.82	1.59
3.7	6.77	1.60
4.0	7.09	1.68
4.4	6.69	1.58
6.5	6.84	1.61
*100	12.9	2.17

* Weast R. C. (1976-77)

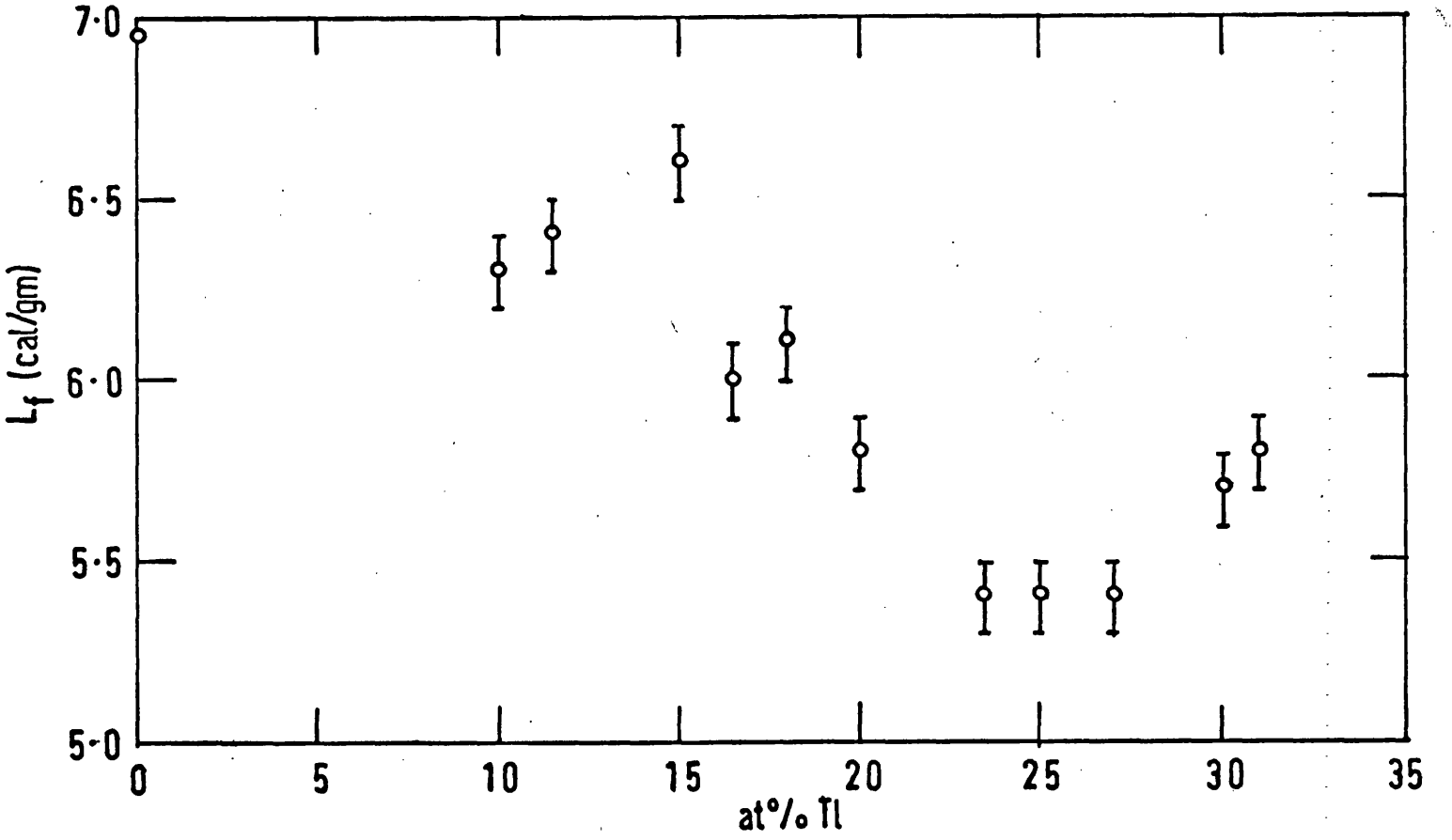

Figure 9.4: Latent heats of fusion (L_f) of In-Tl alloys as a function of Tl concentration.

Table 9.2

Latent heat and entropies of fusion of In-Tl alloys

Alloy composition (at% Tl)	Latent heat of fusion L_f (Cal/gm)	Entropy of fusion S_f ($\times 10^{-2}$ Cal/gm/^{o}K)
0	6.95	1.62
10	6.33	1.48
11.5	6.40	1.50
15	6.58	1.54
16.5	5.99	1.40
18.0	6.11	1.42
20.0	5.77	1.35
23.5	5.37	1.25
25	5.37	1.24
27	5.37	1.25
30	5.71	1.30
30.25	5.64	1.29
31	5.84	1.34
*100	5	0.866

* Weast R. C. (1976-77)

included in addition. σ is nothing but the positional entropy term and for the disordered In-Cd and In-Tl alloys its contribution to the S_f value is negligible. The fusion entropy variations in In-Cd (Table 9.1) and In-Tl (Table 9.2) alloys cannot be explained on these lines. The deviation from an additive behaviour is substantial in both the alloy systems. The fusion entropy data also indicate very little correlation with the crystal structure of the alloys. However, there is an interesting feature with the S_f values of the 4 at% Cd (Table 9.1) and the 15 at% Tl (Table 9.2) alloys. Both these alloys have larger fusion entropies than the other alloys of their respective system. Reference to the phase diagrams (In-Cd system, Figure 2.2 and In-Tl system, Figure 2.3) indicates that these fct alloys approach very close to the fcc - fct phase boundary near their melting points. They would have transformed to the fcc phase if melting had been suppressed. Present investigations (Chapter 6) have shown that the fcc - fct transformation in In-Cd alloys is accompanied by the softening of the $[110]$, $\underline{q}\,[1\bar{1}0]$ acoustic phonon mode. Similar results have previously been obtained for the fcc - fct martensitic transformation in In-Tl alloys (Pace and Saunders 1972, Gunton and Saunders 1974 and Chung, Gunton and Saunders 1976). The large fusion entropies of 4 at% Cd and 15 at% Tl alloys may then plausibly be due to the enhanced entropy contribution arising from the presence of the soft acoustic phonon mode just prior to melting in these alloys.

C H A P T E R 1 0

SOFT ACOUSTIC PHONON MODES IN INDIUM ALLOYS: CONCLUSIONS

The main theme of this thesis has been the ultrasonic study of elastic behaviour and phase stabilities of In (valency z = 3) alloys with neighbouring elements Cd (z = 2), Tl (z = 3) and Pb (z = 4) - alloy systems with many common features including the occurrence of diffusionless structural transformations. The primary concern was to examine whether acoustic phonon mode softening accompanies the structural transformations in In-Cd and In-Pb alloys-as it is in In-rich, In-Tl alloys (Pace and Saunders 1972, Gunton and Saunders 1973, 1974). Indeed, this has been found to be so in the case of In-Cd alloys. The fct-fcc transformation in these alloys is accompanied by softening of the $[110], \underline{q} // [1\bar{1}0]$ acoustic phonon mode near the Brillouin zone centre. Addition of Cd to In reduces the soft mode shear modulus $\frac{1}{2}(C_{11} - C_{12})$; this elastic constant further decreases as the phase transformation is approached from either the fct or the fcc phase. However, in contrast to its behaviour in In-rich, In-Tl alloys, $\frac{1}{2}(C_{11} - C_{12})$ does not go to zero at the transformation. This reflects the more recognisably first order character of the transformation in In-Cd than in the In-Tl alloys. Influence of acoustic phonon mode softening on the melting process is indicated by the enhancement of fusion entropies in In-rich alloys with Cd and Tl - in alloy compositions which approach very close to the fct/fcc phase boundary at the melting point and hence show marked mode softening just prior to melting. In so far as the metallurgy of the In-Cd system is concerned, the single crystal characterisation procedures have shown that all the alloys studied (0 - 6.5 at% Cd) are homogeneous substitutional solid solutions. The 6.5 at% Cd fcc alloy has been found to transform on cooling at T_c (= 232 ± 2°K) and this in effect has extended the low temperature limit of the fct/fcc phase boundary of the existing phase diagram.

Mode softening has also been found in the primary solid solution range (fct, c/a > 1) of In-Pb alloys. In this phase, addition of Pb - like Cd and Tl - reduces the shear modulus $\frac{1}{2}(C_{11} - C_{12})$. But there is no softening in the fct (c/a < 1) and fcc phases. In alloys belonging to these phases, $\frac{1}{2}(C_{11} - C_{12})$ is much larger than that of In. The elastic behaviour of the fct (c/a < 1) phase is markedly different to that of the fct (c/a > 1) phase and the elastic behaviour of the Pb-rich fcc phase is mainly isotropic.

Zener's prediction, namely that $\frac{1}{2}(C_{11} - C_{12})$ must be much smaller than C_{44} in bcc materials with closed ion shells, has been found valid for bcc Tl-rich, In-Tl alloys. These alloys correspond to solid solutions of In in the high temperature bcc polymorph of Tl and a linear extrapolation of the measured alloy elastic constants to vanishing In content has been used to estimate the elastic constants of bcc Tl itself. Results indicate that the stability of this polymorph is due to its lower Debye temperature and hence larger entropy than that of the low temperature hcp form.

REFERENCES

Adler P.N. and Margolin H. (1964) Trans. Met. Soc. A.I.M.E. 230, 1048

Adler P.N. and Margolin H. (1966) Acta Met. 14, 1645

Alers G.A. (1965) "Physical Acoustics" Vol. 3B, ed. W.P. Mason, Academic Press, New York

Auld B.A. (1973) "Acoustic Fields and Waves in Solids" Vol. 1, Wiley, New York

Barrett C.S. and Massalski T.B. (1966) "Structure of Metals" McGraw-Hill, New York

Basinski Z.S. and Christian J.W. (1954) Acta Met. 2, 148

Betteridge W. (1938) Proc. Phys. Soc. 50, 519

Boas W. and Mackenzie J.K. (1950) "Progress in Metal Physics" Vol. 2, ed. B. Chalmers, Pergamon Press, Oxford

Bond W.L. (1943) Bell Syst. Tech. J. 22, 1

Born M. (1939) J. Chem. Phys. 7, 591

Bowles J.S., Barrett C.S. and Guttman L. (1950) Trans. Met. Soc. A.I.M.E. 188, 1478

Bridgman P.W. (1925a) "A Condensed Collection of Thermodynamic Formulas" Harvard Univ. Press, Cambridge (U.S.A.)

Bridgman P.W. (1925b) Proc. Am. Acad. Art. Sci. 60, 305

Bridgman P.W. (1935) Phys. Rev. 48, 893

Bridgman P.W. (1955) Proc. Am. Acad. Art. Sci. 84, 1

Brugger K (1965) J. App. Phys. 36, 759

Buerger M.J. (1951) "Phase Transformations in Solids" eds. R. Smoluchowski, J.E. Mayer and W.A. Weyl, Chapman and Hall, London

Bunn C.W. (1961) "Chemical Crystallography" Clarendon Press, Oxford

Burkart M.W. and Read T.A. (1953) Trans. Met. Soc. A.I.M.E. 197, 1516

Campbell D.R., Tu K.N. and Robinson R.E. (1976) Acta Met. 24, 609

Carapella S.C. and Peretti E.A. (1949) Metal Progress 56, 666

Carapella S.C. and Peretti E.A. (1951) Trans. ASM. 43, 853

Chandrasekhar B.S. and Rayne J.A. (1961) Phys. Rev. 124, 1011

Christian J.W. (1965) "The Theory of Transformations in Metals and Alloys" Pergamon Press, Oxford

Chung D.Y., Gunton D.J. and Saunders G.A. (1976) Phys. Rev. B 13, 3239

Cochran W. (1960) Adv. Phys. 9, 387

Cochran W. (1961) Adv. Phys. 10, 401

Cottam R.I. (1973) Ph.D. Thesis, University of Durham

Cowley R.A. (1976) Phys. Rev. B 13, 4877

Culbert H.V., Farrell D.E. and Chandrasekhar B.S. (1971) Phys. Rev. B 3, 794

Debye P. (1914) Ann. Physik. 43, 49

Delaey R., Krishnan R.V., Tas H. and Warlimont H. (1974) J. Mater. Sci. 9, 1521

Dismukes J.P. and Ekstrom L. (1965) Trans. Met. Soc. A.I.M.E. 233, 672

Eckert R.G. and Drickamer H.G. (1952) J. Chem. Phys. 20, 13

Farley J.M. and Saunders G.A. (1972) J. Phys. C - Solid State Phys. 5, 3021

Farley J.M. (1973) Ph.D Thesis, University of Durham

Ferris R.W., Shepard M.L. and Smith J.F. (1963) J. App. Phys. 34, 768

Fisher E.S. and Dever D. (1970) Acta Met. 18, 265

Fleury P.A. (1972a) J. Acoust. Soc. Am. 49, 1041

Fleury P.A. (1972b) Comments Solid State Phys. 4, 149, 167

Fleury P.A. (1973) "Phase Transitions" ed. L. E. Cross, Pergamon Press, New York

Fleury P.A. (1976) "Annual Review of Materials Science" ed. R.A. Huggins, Annual Reviews Inc., Palo Alto (Calif.)

Folk R., Iro H. and Schwabl F. (1976) Z. Physik. B 25, 69

France L.K., Hartley C.S. and Reid C.N. (1967) Met. Sci. J. 1, 65

Friedel J. (1974) J. de Phys. 35, L59

Goodenough J.B. (1953) Phys. Rev. 89, 282

Gorécki T. (1974) Z. Metallkunde 65, 426

Goss A.J. and Vernon E.V. (1952) Proc. Phys. Soc. B 65, 905

Goss A.J. (1963) "The Art and Science of Growing Crystals" ed. J.J. Gilman, Wiley, New York.

Grimvall G. and Ebbsjö I. (1975) Physica Scr. 12, 168

Gunton D.J. and Saunders G.A. (1973) Solid State Commun. 12, 569

Gunton D.J. (1973) Ph.D Thesis, University of Durham

Gunton D.J. and Saunders G.A. (1974) Solid State Commun. 14, 865

Gutman E.J. and Trivisonno J. (1967) J. Phys. Chem. Solids 28, 805

Guttman L. (1950) Trans. Met. Soc. A.I.M.E. 188, 1472

Hansen M. and Anderko K. (1958) "Constitution of Binary Alloys" McGraw-Hill, New York

Henry N.F.M. and Lonsdale K. (1965) "International Tables for X-ray Crystallography" Vol. 1, Kynoch Press, Birmingham

Heumann T. and Predel B. (1959a) "The Physical Chemistry of Metallic Solutions and Intermetallic compounds" (N.P.L. Symposium No. 9, Paper 5B), H.M. Stationery Office, London

Heumann T. and Predel B. (1959b) Z. Metallkunde 50, 309

Heumann T. and Predel B. (1962) Z. Metallkunde 53, 240

Heumann T. and Predel B. (1966) Z. Metallkunde 57, 50

van der Hoeven B.J.C. and Keesom P.H. (1964) Phys. Rev. A135, 631

Hofman W. (1970) "Lead and Lead Alloys" Springer-Verlag, Berlin

Holder J. (1970) Rev. Sci. Instr. 41, 1355

Holtham P.M. and Parsons D. (1976) J. Phys. F - Metal Phys. 6, 1481

Hume-Rothery W. and Raynor G.V. (1962) "The Structure of Metals and Alloys" Institute of Metals, London

Ida Y. (1969) Phys. Rev. 187, 951

Ida Y. (1971) Phys. Rev. B 1, 2488

Ishizaki K., Bolsaitis P. and Spain I.L. (1973) Phys. Rev. B 7, 5412

Ishizaki K., Bolsaitis P. and Spain I.L. (1976) Phys. Lett. 57A, 180

Ishizaki K., Spain I.L. and Bolsaitis P. (1976) J. Acoust. Soc. Am. 59, 716

James R.W. (1962) "The Optical Principles of the Diffraction of X-rays" Bell, London

Jayaraman A., Klement W., Newton R.C. and Kennedy G.C. (1963) J. Phys. Chem. Solids 24, 7

Jones H. (1934) Proc. Roy. Soc. A 147, 396

Kaiser R.H. and Shuck F.O. (1970) Met. Trans. 1, 2336

Kammer E.W. (1964) J. Acoust. Soc. Am. 36, 1594

Khmel'nitskii D.E. (1975) Sov. Phys. - Solid State 16, 2079

Kollarits F.J. and Trivisonno J. (1968) J. Phys. Chem. Solids 29, 2133

Kubaschewski O. (1941) Z. Electrochem. 47, 475

Kubaschewski O. (1943) Z. Phys. Chem. 192, 292

Kubaschewski O. and Evans E. Ll. (1958) "Metallurgical Thermochemistry" Pergamon Press, Oxford

Kuhlmann-Wilsdorf D. (1965) Phys. Rev. A140, 1599

Lambert M.H., Brock J.C.F. and Phillips N.E. (1971) Phys. Rev. B 3, 1816

Landau L.D. (1937a) Phys. Z. Sowj. Un. 11, 26

Landau L.D. (1937b) Phys. Z. Sowj. Un. 11, 545

Landau L.D. and Lifshitz E.M. (1959) "Statistical Physics" Pergamon Press, London

Landau L.D. and Lifshitz E.M. (1975) "Theory of Elasticity" Pergamon Press, Oxford

Ledbetter H.M. and Moment R.L. (1976) Acta Met. 24,891

Leigh R.S. (1951a) Phil. Mag. 42, 139

Leigh R.S. (1951b) Phil Mag 42, 876

Lennard-Jones J.E. and Devonshire A.F. (1939a) Proc. Roy. Soc. A 169, 317

Lennard-Jones J.E. and Devonshire A.F. (1939b) Proc. Roy. Soc. A 170, 464

Lichnowski A.J.M. (1975) Ph.D. Thesis, University of Durham

Lindemann F.A. (1910) Z. Physik. 11, 609

Luo H.L., Hagen J. and Merriam M.F. (1965) Acta Met. 13, 1012

Luo H.L. and Willens R.H. (1967) Phys. Rev. 154, 436

McSkimin H.J. (1961) J. Acoust. Soc. Am. 33, 12

McSkimin H.J. and Andreatch P. (1962) J. Acoust. Soc. Am. 34, 609

McSkimin H.J. and Andreatch P. (1967) J. Acoust. Soc. Am. 41, 1052

Massalski T.B. and King H.W. (1962) J. Inst. Metals 90, 486

Massalski T.B. (1970) "Physical Metallurgy" ed. R.W. Cahn, North-Holland, Amsterdam

Maynell C.A. (1972) Ph.D Thesis, University of Durham

Meyerhoff R.W. and Smith J.F. (1963) Acta Met. 11, 529

Moore A., Graham J., Williamson G.K. and Raynor G.V. (1955) Acta Met. 3, 579

Murakami Y. and Kachi S. (1975) Trans. Japan Inst. Metals 16, 29

Murtha M.J., Jensen H.J. and Burnet G. (1973) J. Cryst. Growth 19, 58

Musgrave M.J.P. (1970) "Crystal Acoustics" Holden-Day, San Francisco

Nakanishi N. (1972) Mem. Konan Univ. (Sci. Ser.) No. 15, Art. 77

Nakanishi N. (1975) "Shape Memory Effects in Alloys" ed. J. Perkins, Plenum, New York

Nelson J.B. and Riley D.P. (1945) Proc. Phys. Soc. 57, 160

Nix F.C. and McNair D. (1942) Phys. Rev. 61, 74

Novotny D.B. and Smith J.F. (1965) Acta Met. 13, 881

Nye J.F. (1972) "Physical Properties of Crystals" Clarendon Press, Oxford

Olander A. (1932) J. Am. Chem. Soc. 54, 3819

Pace N.G. (1970) Ph.D Thesis, University of Durham

Pace N.G. and Saunders G.A. (1972) Proc. Roy. Soc. A 326, 521

Pace N.G. and Saunders G.A. (1972a) Nature- Phys. Sci. 237, 47

Padamsee H., Neighbor J.E. and Shiffman C.A. (1976) Phys. Rev. B 13, 5125

Pahlman J.E. and Smith J.F. (1968) J. Less-Common Metals 16, 397

Papadakis E.P. (1966) J. Acoust. Soc. Am. 40, 863

Pearson W.B. (1967) "Handbook of Lattice Spacings and Structures of Metals and Alloys" Pergamon Press, Oxford.

Pelton A.D. and Thompson W.T. (1975) "Progress in Solid State Chemistry" Vol. 10, eds. J. McCaldin and G. Somorjai, Pergamon Press, Oxford.

Pfann W.G. (1959) "Zone Melting" Wiley, New York

van der Planken J., Greiner J.D. and Smith J.F. (1971) J. Mater. Sci. 6, 1331

Pollock J.T. and King H.W. (1968) J. Mater. Sci. 3, 372

Polovov V.M. and Ponyatovskii E.G. (1973) Sov. Phys.-J.E.T.P. 37, 476

Ponyatovskii E.G. (1958) Sov. Phys. - Doklady 3, 498

Ponyatovskii E.G. (1959) Sov. Phys. - Cryst. 4, 237

Ponyatovskii E.G. (1963) Sov. Phys. - Cryst. 8, 221

Predel B. (1964) Z. Metallkunde 55, 117

Predel B. and Sandig H. (1970) J. Less-Common Metals 21, 71

Preece C.M. and King H.W. (1969) Acta Met. 17, 21

Rehwald W. (1973) Adv. Phys. 22, 721

Rhines F.N. (1956) "Phase Diagrams in Metallurgy" McGraw-Hill, New York

Ridley N. (1965) J. Less-Common Metals 8, 354

Ridley N. (1968) J. Phys. D - App. Phys. 2, 955

Rutter J.W. and Chalmers B. (1953) Can. J. Phys. 31, 15

Rutter J.W. (1958) "Liquid Metals and Solidification" American Society for Metals, Cleveland (Ohio)

Schmid E. and Boas W. (1968) "Plasticity of Crystals" Chapman and Hall, London

Schwartz R.G. and Gerstein B.C. (1971) J. Chem. Phys. 55, 4034

Seddon T. (1972) M.Sc. Thesis, University of Durham

Shepard M.L. and Smith J.F. (1967) Acta Met. 15, 357

Shirane G. (1974) Rev. Mod. Phys. 46, 437

Slater J.C. (1939) "Introduction to Chemical Physics" McGraw-Hill, New York

Smith J.F. and Schneider V.L. (1964) J. Less-Common Metals 7, 17

Smithells C.J. (1976) "Metals Reference Book" Butterworths, London

Straumanis M.E., Rao P.B. and James W.J. (1971) Z. Metallkunde 62, 493

Swenson C.A. (1955) Phys. Rev. 100, 1607

Tiller W.A., Rutter J.W., Jackson K. and Chalmers B. (1953) Acta Met. 1, 428

Tomasch W.J. and Reitz J.R. (1958) Phys. Rev. 111, 757

Tong H.C. and Wayman C.M. (1975) Met. Trans. A 6, 29

Truell R., Elbaum C. and Chick B.B. (1969) "Ultrasonic Methods in Solid State Physics" Academic Press, New York

Tyzack C. and Raynor G.V. (1954a) Trans. Faraday Soc. 50, 675

Tyzack C. and Raynor G.V. (1954b) Acta Cryst. 7, 505

Valentiner S. (1940) Z. Metallkunde 32, 244

Valentiner S. (1943) Z. Metallkunde 35, 250

Vaygham R.W. and Drickamer H.G. (1965) J. Phys. Chem. Solids 26, 1549

Vereshchagin L.F., Kabalkina S.S. and Troitskaya Z.V. (1964) Sov. Phys. - Doklady 9, 894

Verkin B.I. and Svechkarev I.V. (1965) Sov. Phys. - J.E.T.P. 20, 267

Volotskaya V.G. and Fogel N. Ya. (1970) Sov. Phys.- J.E.T.P. 31, 205

Waldorf D.L. and Alers G.A. (1962) J. App. Phys. 33, 3266

Wallace D.C. (1972) "Thermodynamics of Crystals" Wiley, New York

Weast R.C. (1976-77) "Handbook of Chemistry and Physics" CRC Press, Cleveland, (Ohio)

Weil R.B. (1965) Ph.D Thesis, University of California (Riverside)

Werner M. (1913) Z. Anorg. Chem. 83, 275

Wilson C.L. and Wick O.J. (1937) Industr. Engg. Chem. 29, 1164

Winder D.R. and Smith C.S. (1958) J. Phys. Chem. Solids 4, 128

Wooster W.A. (1973) "Tensors and Group Theory for the Physical Properties of Crystals" Clarendon Press, Oxford.

Yonemitsu K. (1966) J. Phys. Soc. Japan 21, 1231

Zener C. (1947) Phys. Rev. 71, 846

Zener C. (1948) "Elasticity and Anelasticity of Metals" University of Chicago Press, Chicago

Zener C. (1967) "Phase Stability in Metals and Alloys" eds. P.S. Rudman, J. Stringer and R.I. Jaffee, McGraw-Hill, New York